

# **Modelling and Simulation of the Laboratory Low Temperature Proton Exchange Membrane Fuel Cells**

Lei Xing

and

Keith Scott

## About the authors

Prof. Lei Xing obtained his PhD degree in 2014 at Newcastle University, UK, under the supervision of Prof. K. Scott. He worked as a postdoc research fellow at the University of Birmingham, UK, from 2014 to 2016. Then he was appointed a professorship at Jiangsu University, China. His research activities include multi-scale, multi-physics and multi-phase flow modelling and multi-variable optimisation of proton exchange membrane fuel cells and lithium ion batteries, chemical reaction engineering aspect scale-up of direct methanol fuel cells, photocatalytic process in pollution treatment, coating and controlled release of functional particles.

Prof. Keith Scott is a professor of electrochemical engineering of Newcastle University, UK. His research activities include electrochemical power sources, electrochemical environmental engineering, photochemical processes, membrane materials and membrane separations. He plays as leaders of several academic and industrial projects, such as Supergen and energy storage and BioFC Supergen funded by EPSRC, UK.

## Abstract

Proton exchange membrane fuel cells (PEMFCs) have been considered as the most promising solution that would enable both of efficiency improvement and emissions reduction in portable and transportation applications, as well as the energy conversion from sustainable resources to electrical energy. Among the PEMFC family, the medium and low temperature PEMFCs are considered as promising candidates as portable and automotive power sources. However, they can experience certain operating difficulties associated with water transport and flooding during their operation, especially at a high current density. Therefore, water management is of vital importance to achieve the maximum performance and durability of PEMFCs. Mathematical models are developed to fully couple majority of the physical and electrochemical processes occurred during PEMFC operation, which is capable of revealing the mass transport resistance, optimising the electrode composition and improving the cell performance at different operating conditions. By better understanding the water formation mechanisms and transport behaviours, the output power of PEMFCs can be enhanced by establishing effective water removal and distribution strategies.

Following a brief introduction of hydrogen energy and fuel cell technology summarised in Chapter 1, an overview of a variety of fuel cell modelling activities is given in Chapter 2. A detailed description of the fundamentals, principles and governing equations are shown in Chapter 3. Based on the theory described in Chapter 3, several models, from single-phase flow model to two-phase flow model, from isothermal model to non-isothermal model, were developed in the following chapters.

In Chapter 4, a single-phase flow, along-the-channel, two-dimensional, steady-state and isothermal model is developed, and validated against experimental data. This model is applied to a fuel cell with a counter-flow mode of hydrogen and air along parallel flow channels. In the flow channel and porous media, reactant flow is modelled using the continuity and Navier-Stokes equation. Reactant diffusion is modelled by the Maxwell-Stefan equation. Water transport through the membrane is described by the combinational mechanism in which electro-osmotic drag, back diffusion and hydraulic permeation are all included. The catalyst layer is modelled as a spherical agglomerate structure in which ionomer partially occupy the void space to form an ionomer film surrounding the agglomerate. This model is used to study the effects of the catalyst

layer properties on fuel cell performance. Based on the analysis of the polarisation curves and the distributions of oxygen mole fraction, effectiveness factor, the model indicates that the rapid decrease in current density at lower cell voltage is due to an increased oxygen diffusion resistance through the ionomer film.

In Chapter 5, a two-phase flow, across-the-channel, two-dimensional, steady-state and isothermal model is developed. The water phase transfers between water vapour, dissolved water and liquid water are taken into account in this model. The catalyst layer is also modelled as a spherical agglomerate structure. Liquid water formation and transport are introduced into the model. Liquid water occupies the secondary pores of the cathode catalyst layer to form a liquid water film on the outer boundary of the ionomer film. The liquid water film thickness is calculated by coupling the two-phase flow model with the agglomerate model. This model is used to study the influence of catalyst layer parameters and operating conditions on the performance of the cell. The model provides useful guidance for optimisation of the ionomer volume fraction in the cathode catalyst layer and the relative humidity of the cathode gas inlet.

In Chapter 6, a two-phase flow, across-the-channel, two-dimensional, steady-state and non-isothermal model is developed. The model considered the non-uniform temperature distribution within the fuel cell. The modelling results show that heat accumulates within the cathode catalyst layer under the channel. Higher operating temperatures improved the fuel cell performance by increasing the kinetic rate, reducing the liquid water saturation on the cathode and increasing the water carrying capacity of the anode gas. Applying higher temperature on the anode and enlarging the width ratio of the channel/rib could improve the cell performance.

In Chapter 7, a two-phase flow, along-the-channel, two-dimensional, steady-state and non-isothermal model is developed. Liquid water formation and transport at the anode is taken into account. The properties of gas diffusion layer and channel geometries are numerically studied and optimised. The interactive effects of operation conditions, including relative humidity, stoichiometric flow ratio and channel length are investigated. Results reveal low liquid water saturation with large contact angle, low electrode porosity and platinum loading, and short and deep channel. An optimal channel length of 1 cm is found to maximise the current densities at low cell voltages. Results also indicate that higher anode relative humidity is required to the improved cell performance. As the decrease in the anode relative humidity and increase in channel

length, the optimal cathode relative humidity is increased. The initial increase in stoichiometric flow ratio improved the limiting current densities. However, the further increases lead to limited contributions. The Peclet number indicated that the liquid water transport through the electrode is mainly determined by the capillary diffusion mechanism. A novel channel design featured with multi-outlets and inlets along-the-channel is proposed to mitigate the effect of water flooding and improve the cell performance.

In Chapter 8, a multi-variable optimisation of the cathode catalyst layer composition is represented by a surrogate modelling. This optimisation is based on the geometry and assumptions developed in the single-phase flow, along-the-channel, two-dimensional, steady-state and isothermal model. Five design parameters, platinum loading, platinum mass ratio to carbon, ionomer volume fraction, catalyst layer thickness and agglomerate radius, are optimised by a multiple surrogate model and their sensitivities are analysed by a Monte Carlo method based approach. The optimisation results are validated by the agglomerate model to confirm the effectiveness of the proposed methodologies. Two optimisation strategies, maximising the current density at a fixed cell voltage and within a specific range, are implemented for the optima prediction. The results show that the optimal catalyst composition depends on the cell voltages. At higher current densities, mass transport is more important. The performance is improved by reducing the ionomer volume fraction and increasing the catalyst layer porosity. At lower current densities, reaction kinetics and proton transport are more important. The performance is improved by increasing the ionomer volume fraction and decreasing catalyst layer porosity.

At the end of this book, main conclusions are summarised and future research trends and perspectives are recommended in Chapter 9.

## Table of Content

List of Figures.....	ix
List of Tables.....	xvi
Nomenclature.....	xviii
Acknowlegement.....	xxiii
Chapter 1. Introduction.....	1
1.1 Hydrogen, the next generation energy source.....	1
1.2 Fuel cells .....	3
1.2.1 Types of fuel cells .....	4
1.2.2 Proton exchange membrane fuel cell (PEMFC) .....	5
1.3 Fuel cells modelling.....	8
1.4 Objectives and structure of the book .....	8
1.5 References.....	9
Chapter 2. Overview of water management, optimisation and performance of PEMFCs ....	13
2.1 Introduction.....	13
2.2 Overview of water transport and flooding in the PEMFC .....	13
2.3 Overview of modelling of water transport in PEMFC.....	18
2.3.1 Modelling of water transport through the membrane .....	20
2.3.2 Modelling of water transport in porous electrodes .....	23
2.4 Flow field design .....	28
2.5 Experimental measurement and visualisation of liquid water .....	31
2.6 Overview of PEMFC numerical optimisation .....	33
2.7 Anode flooding and effect of operating conditons on cell performance.....	37
2.8 Conclusions.....	39
2.9 References.....	40
Chapter 3. Fundamentals, principles and governing equations .....	53
3.1 Introduction.....	53
3.2.1 Buter-Volmer kinetics.....	53
3.2.2 Agglomerate kinetics .....	56
3.3 Catalyst layer property.....	61
3.3.1 Porosity of the catalyst layer.....	61
3.3.2 Agglomerate density .....	63
3.3.3 Thicknesses of the ionomer and liquid water films .....	64
3.3.4 Specific area.....	67
3.4 Water phase transfer and transport through the membrane .....	67

---

3.4.1	Phase transfer and transport through the membrane .....	67
3.4.2	Liquid water transport in the porous electrode .....	70
3.4.3	Water vapour transport in porous electrode.....	72
3.4.4	Membrane and ionmer swelling.....	74
3.5	Governing equations .....	76
3.5.1	Conservation of mass.....	76
3.5.2	Conservation of momentum.....	77
3.5.3	Conservation of species .....	79
3.5.4	Conservation of energy .....	81
3.5.5	Conservation of charge .....	84
3.6	Constitutive relations and model parameters.....	87
3.6.1	Kinetic parameters .....	87
3.6.2	Open circuit potential.....	90
3.6.3	Reactant solubility and diffusivity in Nafion® .....	94
3.6.4	Oxygen diffusion coefficient in liquid water .....	96
3.6.5	Multicomponent diffusivity .....	96
3.6.6	Knudsen diffusion.....	98
3.6.7	Ionic conductivity .....	99
3.6.8	Electronic conductivity .....	101
3.6.9	Specific heat capacity and thermal.....	102
3.6.10	Water diffusivity through the membrane .....	106
3.6.11	Gas permeability in porous electrode and through membrane.....	108
3.6.12	Viscosity .....	109
3.7	Conclusions.....	110
3.8	References.....	111
Chapter 4.	Single-phase flow isothermal model.....	117
4.1	Introduction.....	117
4.2	Model description .....	119
4.2.1	Computational domain and assumption .....	119
4.2.2	Governing equations .....	121
4.2.3	Electrochemical reactions kinetics.....	122
4.2.4	Polarisation curves .....	124
4.2.5	Gas transport within the catalyst layers .....	124
4.2.6	Property of the catalyst layer .....	125
4.2.7	Water transport through the membrane .....	126
4.2.8	Stoichiometric flow ratio .....	126
4.2.9	Boundary conditions and source terms .....	127

---

---

4.2.10	Numerical solution.....	127
4.3	Results and discussion .....	129
4.3.1	Model validation .....	129
4.3.2	Property of the catalyst layer .....	130
4.3.3	Reactant gas distribution.....	134
4.3.4	Effectiveness factor.....	138
4.3.5	Distribution of membrane water content .....	140
4.3.6	Distribution of current density .....	141
4.3.7	Effect of platinum and carbon loading.....	143
4.3.8	Effect of agglomerate radius .....	145
4.3.9	Effect of gas inlet pressure.....	146
4.4	Conclusions.....	147
4.5	References.....	147
Chapter 5.	Two-phase flow isothermal model.....	150
5.1	Introduction.....	150
5.2	Model description .....	152
5.2.1	Computational domain and assumption.....	152
5.2.2	Governing equations .....	153
5.2.3	Electrochemical reactions kinetics.....	154
5.2.4	Gas transport within catalyst layers .....	155
5.2.5	Thickness of the liquid water film .....	155
5.2.6	Liquid water transport.....	156
5.2.7	Dissolved water transport .....	156
5.2.8	Source terms .....	157
5.2.9	Boundary conditions .....	158
5.2.10	Numerical solution.....	158
5.3	Results and discussion .....	159
5.3.1	Model validation .....	159
5.3.2	Liquid water film thickness .....	161
5.3.3	Comparison of the membrane and ionomer swelling .....	162
5.3.4	Membrane and ionomer water content.....	163
5.3.5	Ionomer volume fraction in cathode catalyst layer.....	164
5.3.6	Liquid water saturation in cathode porous electrode .....	165
5.3.7	Optimal ionomer water content .....	167
5.3.8	Orthogonal array testing .....	170
5.3.9	Optimal platinum loading .....	171
5.3.10	Optimal platinum mass ratio.....	173

---

---

5.3.11	Optimal dry ionomer loading.....	174
5.3.12	Optimal relative humidity .....	176
5.4	Conclusions.....	177
5.5	References.....	178
Chapter 6.	Two-phase flow Non-isothermal model .....	182
6.1	Introduction.....	182
6.2	Model description .....	183
6.2.1	Computational domain and assumption .....	183
6.2.2	Governing equations .....	183
6.2.3	Thermal parameters .....	185
6.2.4	Boundary conditions .....	187
6.2.5	Numerical solution.....	187
6.3	Results and discussion .....	188
6.3.1	Temperature distribution.....	188
6.3.2	Effect of temperature on liquid water saturation.....	190
6.3.3	Effect of temperature on membrane/ionomer water content.....	191
6.3.4	Effect of temperature on fuel cell performance .....	193
6.4	Optimise the temperature distribution and improve the cell performance.....	194
6.4.1	Increasing the operating temperature on the anode .....	195
6.4.2	Increasing the width ratio of the channel/rib .....	197
6.5	Conclusions.....	199
6.6	References.....	199
Chapter 7.	Anode partial flooding model .....	203
7.1	Introduction.....	203
7.2	Model description .....	206
7.2.1	Computational domain and assumption .....	206
7.2.2	Governing equations .....	207
7.2.3	Boundary conditions .....	211
7.2.4	Numerical solution.....	212
7.3	Model verification and validation.....	213
7.3.1	Mesh independence.....	213
7.3.2	Model validation .....	214
7.4	Results and discussions.....	216
7.4.1	The effect of contact angle in GDL on liquid water saturation.....	216
7.4.2	The effect of GDL porosity on liquid water saturation.....	219
7.4.3	The effect of platinum loading on liquid water saturation and CCL effectiveness factor .....	221

---

---

7.4.4	The effect of the GDL thickness on temperature profiles and CCL effectiveness factor .....	222
7.4.5	The effect of flow channel length and depth on liquid water saturation.....	224
7.4.6	Parametric study.....	227
7.4.7	Effect of relative humidity .....	229
7.4.8	Effect of stoichiometric flow ratio .....	238
7.4.9	The novel flow channel desing .....	247
7.5	Conclusions.....	249
7.6	Reference .....	251
Chapter 8.	Cathode catalyst layer optimisation .....	256
8.1	Introduction.....	256
8.2	Mathematical model .....	257
8.3	Model verification and validation.....	258
8.3.1	Mesh independence.....	258
8.3.2	Model validation .....	259
8.4	Global sensitivity analysis and design optimisation .....	259
8.4.1	Kriging Surrogate models .....	260
8.4.2	Sobol' Global sensitivity analysis.....	261
8.5	Optimisation formulation.....	263
8.6	Implementation of the optimisation process .....	265
8.7	Optimisation at a fixed cell voltage .....	266
8.7.1	Base design .....	267
8.7.2	Optimisation at low cell voltage .....	268
8.7.3	Optimisation at medium cell voltage .....	270
8.7.4	Optimisation at high cell voltage .....	273
8.8	Optimisation during a specific cell voltage range.....	276
8.9	Global sensitivity analysis .....	279
8.10	Final remarks .....	280
8.11	Conclusions.....	281
8.12	References.....	282
Chapter 9.	Summary, Conclusions and Perspective .....	285

## List of Figures

Figure 1-1 World primary energy consumption from 1900 to 2000 [1] .....	1
Figure 1-2 Hydrogen as an energy carrier linking multiple hydrogen production methods, through storage to various end-users [5] .....	2
Figure 1-3 Schematic diagram and basic principle of operation of a PEMFC .....	6
Figure 1-4 Voltage losses in the fuel cell and the resulting polarisation curves [17] .....	7
Figure 2-1 Structure of catalyst layers in PEMFCs .....	14
Figure 2-2 Water transport mechanism inside the PEMFCs.....	14
Figure 2-3 Converging capillary tree water transport mechanism [89] .....	15
Figure 2-4 A typical water flooding pattern in a PEMFC operated at constant cell voltage [17]	16
Figure 2-5 Voltage reversal effect (VRE) in PEMFC [17].....	17
Figure 2-6 Transient liquid water discharging from GDL obtained from VOF model [80] .....	26
Figure 2-7 Schematic representation of the agglomerate catalyst layer.....	28
Figure 2-8 Four types of typical flow field designs [14] .....	29
Figure 2-9 Magnified view of flow patterns in channels captured by the high resolution Olympus video microscope and the illustrations of liquid water generation and distribution [90] .....	32
Figure 2-10 ESEM micrographs of vapour condensation and liquid water breakthrough in electrode [77] .....	33
Figure 2-11 Polarisation curves of the base design and optimal design at the cell voltage of 0.476 V [102].....	36
Figure 3-1 A simplified schematic diagram of the triple phase boundary (TPB) in a catalyst- electrolyte-pores interacted electrode [1].....	56
Figure 3-2 Sketch of the catalyst layer based on agglomerate assumption.....	57
Figure 3-3 Schematic representation of reactant gas diffusion through the ionomer film surrounding the agglomerate.....	58
Figure 3-4 Sketch of the membrane and ionomer swelling and the bulged MEA into flow channel .....	75
Figure 3-5 Temperature dependent transfer coefficient of anode and cathode.....	88
Figure 3-6 Temperature dependent cathode reference exchange current density .....	90
Figure 3-7 Temperature dependent open circuit potential (OCP) for hydrogen oxidation reaction .....	94
Figure 3-8 Relative humidity dependent oxygen diffusivity through Nafion® membrane/ ionomer .....	95

Figure 3-9 Water content dependent Henry's constant for O <sub>2</sub> solubility in Nafion® membrane/ionomer .....	95
Figure 3-10 Temperature dependent oxygen diffusion coefficients in liquid water and Nafion® membrane/ ionomer.....	96
Figure 3-11 Temperature dependent binary diffusion coefficients for all pairs of gas species at 1.0 atm .....	98
Figure 3-12 Temperature dependent oxygen diffusion coefficients through void space of porous electrode.....	99
Figure 3-13 Effect of ionomer film thickness on dimensionless effective ionic conductivity of cathode catalyst layer ( $m_{Pt} = 0.4 \text{ mg cm}^{-2}$ , $f = 0.3$ , $l_{CL} = 15\mu\text{m}$ , $r_{agg} = 1.0 \mu\text{m}$ ) ....	101
Figure 3-14 Temperature dependent platinum electronic conductivity .....	102
Figure 3-15 Temperature dependent specific heat capacities of hydrogen, oxygen, nitrogen and water vapour [50].....	104
Figure 3-16 Temperature dependent thermal conductivities of hydrogen, oxygen, nitrogen and water vapour [50].....	104
Figure 3-17 Temperature dependent platinum thermal conductivity [51] .....	105
Figure 3-18 Temperature dependent carbon black thermal conductivity [52].....	105
Figure 3-19 Water content dependent diffusion coefficient of water through Nafion® membrane .....	107
Figure 3-20 Relationship between water activity and membrane water content .....	107
Figure 3-21 Comparison of the fitted saturated water vapour pressure with the experimental data [50] .....	108
Figure 3-22 Temperature dependent gas viscosity.....	109
Figure 3-23 Temperature dependent liquid water viscosity [57] .....	110
Figure 4-1 Sketch of a typical PEMFC (a) 3D representation (b) 2D computational domain Z1 .....	120
Figure 4-2 Schematic of the computational process .....	128
Figure 4-3 Validation of the modelling results to the experimental data.....	129
Figure 4-4 Porosities of the catalyst layer with different platinum mass ratios in base case condition .....	132
Figure 4-5 Agglomerate densities with different platinum mass ratios in base case condition	132
Figure 4-6 Ionomer film thicknesses with different platinum mass ratios in base case condition .....	133
Figure 4-7 Dimensionless concentration of oxygen in gas diffusion layer (a) and catalyst layer (b) in base case condition ( $E^{cell} = 0.3, 0.6$ and $0.9$ from down up).....	135
Figure 4-8 Dimensionless concentration of hydrogen in anode gas diffusion layer and catalyst layer in base case condition ( $E^{cell} = 0.3, 0.6$ and $0.9$ from up down) .....	136

---

Figure 4-9 Dimensionless concentration of water vapour in the gas diffusion layer and catalyst layer of anode (a) and cathode (b) in base case condition ( $E^{\text{cell}} = 0.3, 0.6$ and $0.9$ from down up for case (a) and from up down for case (b)) .....	138
Figure 4-10 Effectiveness factor of cathode catalyst layer at three cell voltages in base case condition ( $E^{\text{cell}} = 0.3, 0.6$ and $0.9$ V from down up) .....	139
Figure 4-11 Water content distribution within the membrane at three cell voltages in base case condition ( $E^{\text{cell}} = 0.3, 0.6$ and $0.9$ V from down up) .....	140
Figure 4-12 Current density distribution within the membrane with different cell voltages in base case condition ( $E^{\text{cell}} = 0.4, 0.5$ and $0.6$ from up down) .....	141
Figure 4-13 Current density distributions with the catalyst layers of anode and cathode in base case condition ( $E^{\text{cell}} = 0.3, 0.4, 0.5, 0.6, 0.7$ from up down) .....	142
Figure 4-14 Polarisation curves for different platinum and carbon loadings in base case condition .....	143
Figure 4-15 Average effectiveness factors for different platinum and carbon loadings in base case condition.....	144
Figure 4-16 Polarisation curves for different agglomerate radius in base case condition .....	145
Figure 4-17 Average effectiveness factors for different agglomerate radius in base case condition .....	146
Figure 4-18 Polarisation curves for different inlet pressures compared to base case condition	147
Figure 5-1 Sketch of a typical PEMFC (a) 3D representation (b) 2D computational domain Y1 .....	153
Figure 5-2 Schematic of the computational process .....	159
Figure 5-3 Validation of the modelling results to the experimental data at $60\text{ }^{\circ}\text{C}$ and $80\text{ }^{\circ}\text{C}$ ... .....	160
Figure 5-4 Liquid water film thicknesses with different platinum mass ratios in base case condition .....	161
Figure 5-5 Comparison of the effect of membrane and ionomer swelling on fuel cell performance .....	163
Figure 5-6 Membrane and ionomer water contents at different current densities (a) $0.06\text{ A cm}^{-2}$ ; (b) $0.26\text{ A cm}^{-2}$ ; (c) $0.53\text{ A cm}^{-2}$ ; (d) $0.79\text{ A cm}^{-2}$ ; (e) $1.00\text{ A cm}^{-2}$ in base case condition .....	164
Figure 5-7 Ionomer volume fraction within cathode catalyst layer with dry ionomer volume fraction of 30% in base case condition at the cell voltage of $0.3\text{ V}$ .....	165
Figure 5-8 Liquid water saturation with dry ionomer volume fraction of 0.2 (a) and 0.4 (b) in base case condition at the cell voltage of $0.3\text{ V}$ .....	166
Figure 5-9 Average liquid water saturations and liquid water film thicknesses at different current densities and relative humidity in base case condition .....	166
Figure 5-10 Sketch of oxygen diffusion through the ionomer and liquid water film .....	167

---

---

Figure 5-11 Effect of ionomer water content on parameter v with different platinum loading (a), platinum mass ratio (b) and dry ionomer volume fraction (c) .....	169
Figure 5-12 Effect of platinum loading on fuel cell performance.....	172
Figure 5-13 Effect of platinum loading on effectiveness factor of cathode catalyst layer.....	172
Figure 5-14 Effect of platinum mass ratio on fuel cell performance .....	173
Figure 5-15 Effect of platinum mass ratio on effectiveness factor of cathode catalyst layer ...	174
Figure 5-16 Effect of dry ionomer loadings on fuel cell performance.....	175
Figure 5-17 Effect of dry ionomer loading on effectiveness factor of cathode catalyst layer ..	175
Figure 5-18 Effect of cathode relative humidity on fuel cell performance .....	176
Figure 6-1 Schematic of the computational process .....	187
Figure 6-2 Temperature profiles at the cell voltage of 0.3 V and at (a) 60 °C ( $0.73 \text{ A cm}^{-2}$ ), (b) 70 °C ( $0.87 \text{ A cm}^{-2}$ ) and (c) 80 °C ( $0.95 \text{ A cm}^{-2}$ ) .....	189
Figure 6-3 Liquid water saturation profiles at $0.7 \text{ A cm}^{-2}$ with fully humidified inlet gases at (a) 60 °C (0.32 V), (b) 70 °C (0.39V) and (c) 80 °C (0.42V) .....	190
Figure 6-4 Membrane/ionomer water content profiles at (a) 60 °C, $0.7 \text{ A cm}^{-2}$ (0.32 V), (b) 70 °C, $0.7 \text{ A cm}^{-2}$ (0.39 V), (c) 80 °C, $0.7 \text{ A cm}^{-2}$ (0.42 V) and (d) 80 °C, $0.2 \text{ A cm}^{-2}$ (0.61 V) with fully humidified inlet gases .....	192
Figure 6-5 Polarisation curves at three operating temperatures with fully humidified inlet gases .....	194
Figure 6-6 Polarisation curves at different anode and cathode temperatures with fully humidified inlet gases .....	195
Figure 6-7 Temperature profiles at two conditions: (a) $T_a = 70 \text{ }^\circ\text{C}$ , $T_c = 80 \text{ }^\circ\text{C}$ , (b) $T_a = 80 \text{ }^\circ\text{C}$ , $T_c = 70 \text{ }^\circ\text{C}$ with fully humidified inlet gases .....	197
Figure 6-8 Polarisation curves with different width ratios of channel/rib and fully humidified inlet gases.....	198
Figure 6-9 Temperature profiles with two different width ratios of channel/rib and fully humidified inlet gases .....	198
Figure 7-1 Computational domain and mesh of the studied PEM fuel cell .....	207
Figure 7-2 Schematic of the computational process .....	213
Figure 7-3 Comparison of modelling results with experimental data for two cases.....	216
Figure 7-4 Dimensional liquid water saturation in (a) anode and cathode GDLs and dimensionless liquid water saturation in (b) anode GDL and (c) cathode GDL with various contact angels at 0.3 V in base-case condition: $\theta = 100^\circ, 120^\circ, 140^\circ$ and $160^\circ$ from up down.....	219
Figure 7-5 Liquid water saturation in (a) anode GDL and (b) cathode GDL with various GDL porosities at 0.3 V in base-case condition: $\varepsilon_{GDL} = 80\%, 60\%, 40\%$ and 20% from up down.....	220

---

---

Figure 7-6 Liquid water saturation in CCL with various platinum loadings at 0.3 V in base-case condition: $m_{\text{Pt}} = 0.8, 0.6, 0.4$ and $0.2 \text{ mg cm}^{-2}$ from up down.....	222
Figure 7-7 CCL effectiveness factor with various platinum loadings at 0.3 V in base-case condition: $m_{\text{Pt}} = 0.2, 0.4, 0.6$ and $0.8 \text{ mg cm}^{-2}$ from up down. ....	222
Figure 7-8 Temperature profile at cathode CL-GDL interface at the cell voltages of (a) 0.4 V (b) 0.1 V with various GDL thickness in base-case condition: $\delta_{\text{GDL}} = 10, 20, 60, 100, 200$ and $260 \mu\text{m}$ from up down. ....	223
Figure 7-9 CCL effectiveness factor with various GDL thicknesses at 0.3 V in base-case condition: $\delta_{\text{GDL}} = 60, 100, 200$ and $380 \mu\text{m}$ from up down. ....	224
Figure 7-10 Liquid water saturation in (a) anode channel and (b) cathode channel with various channel lengths at 0.3 V in base-case condition: $L = 4.0, 2.0, 1.0$ and $0.5 \text{ cm}$ from up down.....	225
Figure 7-11 Liquid water saturation at cathode GDL-channel interface at 0.3 V: $X = 0$ is the cathode channel inlet, $X = 0.5, 1.0, 2.0, 3.0$ and $4.0$ is the outlet, respectively. ...	226
Figure 7-12 Liquid water saturation in (a) anode channel and (b) cathode channel with various channel depth at 0.3 V in base-case condition: $\delta_{\text{Ch}} = 0.5, 1.0, 1.5$ and $2.0 \text{ mm}$ from left to right. ....	227
Figure 7-13 Current densities at various anode and cathode relative humidity at (a) 0.8 V (b) 0.5 V and (c) 0.2 V, $L = 1 \text{ cm}$ , $\xi_a = 1.2$ , $\xi_c = 2.0$ .....	231
Figure 7-14 Ionomer water content in the anode catalyst layer at various anode relative humidity at 0.2 V: $L = 1 \text{ cm}$ , $\xi_a = 1.2$ , $\xi_c = 2.0$ . Solid line - the minimum ionomer water content within the anode catalyst layer; Dash line - average ionomer water content along the anode CL-GDL interface.....	232
Figure 7-15 Optimal cathode relative humidity ( $\text{RH}_c$ ) of a short channel at (a) low and (b) medium cell voltages: $\text{RH}_a = 100\%$ to $50\%$ with the step of $10\%$ from up down, $L = 1 \text{ cm}$ , $\xi_a = 1.2$ , $\xi_c = 2.0$ .....	233
Figure 7-16 Optimal cathode relative humidity ( $\text{RH}_c$ ) of a long channel at (a) low and (b) medium cell voltages: $\text{RH}_a = 100\%$ to $50\%$ with the step of $10\%$ from up down, $L = 10 \text{ cm}$ , $\xi_a = 1.2$ , $\xi_c = 2.0$ .....	233
Figure 7-17 Membrane/ionomer water content with various length of channel at 0.2 V with $\text{RH}_a = 50\%$ and $\text{RH}_c = 60\%$ : upper layer – $1 \text{ cm}$ channel; middle layer – $5 \text{ cm}$ channel; lower layer – $10 \text{ cm}$ channel. ....	234
Figure 7-18 Effect of anode relative humidity ( $\text{RH}_a$ ) on liquid water saturation with $\text{RH}_c = 90\%$ at 0.2 V: the current density predicted at each case is (a) 1.790, (b) 1.758 and (c) $1.576 \text{ A cm}^{-2}$ .....	234
Figure 7-19 Membrane/ionomer water content at various $\text{RH}_a$ with $\text{RH}_c = 90\%$ at 0.2 V.....	235
Figure 7-20 Effect of cathode relative humidity ( $\text{RH}_c$ ) on liquid water saturation with $\text{RH}_a = 100\%$ at 0.2 V: the current density predicted at each case is (a) 1.790, (b) 1.844 and (c) $1.920 \text{ A cm}^{-2}$ .....	236

---

---

Figure 7-21 Membrane/ionomer water content in (a) membrane and (b) cathode catalyst layer at various $RH_c$ with $RH_a = 100\%$ at 0.2 V: $RH_c = 70\%, 50\%, 30\%$ and 10% from up down.....	237
Figure 7-22 Effect of cathode stoichiometric flow ratio on cell performance at low cathode stoichiometric flow ratio at two levels of $RH_c$ : solid line - $RH_c = 60\%$ , dash line - $RH_c = 100\%$ . Operating condition: $RH_a = 100\%$ , $\xi_a = 2.0$ , $\xi_c = 0.2, 0.4, 0.6, 0.8, 1.0$ .....	239
Figure 7-23 Effect of cathode stoichiometric flow ratio on cell performance at two levels of $RH_c$ : solid line - $RH_c = 60\%$ , dash line - $RH_c = 100\%$ . Operating condition: $RH_a = 100\%$ , $\xi_a = 2.0$ , $\xi_c = 2.0, 3.0$ and 5.0.....	240
Figure 7-24 Effect of cathode stoichiometric flow ratio on limiting current density at various cathode relative humidity of a short channel: $\xi_a = 1.2$ , $RH_a = 100\%$ , $L=1$ cm ....	241
Figure 7-25 Liquid water saturation in cathode channel of (a) 4 cm and (b) 10 cm at various cathode stoichiometric flow ratios with fully humidified gases: $\xi_a = 1.2$ .....	243
Figure 7-26 Effect of cathode stoichiometric flow ratio on limiting current density at various channel length with fully humidified gases: $\xi_a = 1.2$ .....	244
Figure 7-27 Effect of cathode stoichiometric flow ratio on limiting current density at various cathode relative humidity of a long channel: $\xi_a = 1.2$ , $RH_a = 100\%$ , $L = 10$ cm ..	244
Figure 7-28 Effect of cathode stoichiometric flow ratio on temperature profiles with fully humidified gases: $\xi_a = 2.0$ .....	245
Figure 7-29 Average Paclet number ( $Pe$ ) of (a) liquid water transport and (b) heat transport within the GDL and CL of the cathode at various current densities with fully humidified gases.....	246
Figure 7-30 Velocity magnitudes of reactant gases at 0.3 V of three channel designs in base-case condition.....	248
Figure 7-31 Profiles of liquid water saturation of three channel designs at $1.2 \text{ A cm}^{-2}$ in base-case condition .....	248
Figure 7-32 Sketch of gas channel using multi- inlets and outlets design (a) double (b) triple	249
Figure 8-1 Influence of mesh characteristics on current density .....	259
Figure 8-2 Flowchart of the optimisation process.....	266
Figure 8-3 Polarisation curve (a), cathode overpotential (b), cathode volumetric current density (c) and oxygen mole fraction (d) for base design and optimal design at the cell voltage of 0.2 V.....	270
Figure 8-4 Polarisation curve (a), cathode overpotential (b), cathode volumetric current density (c) and oxygen mole fraction (d) for base design and optimal design at the cell voltage of 0.5 V .....	272
Figure 8-5 Polarisation curve (a), cathode overpotential (b), cathode volumetric current density (c) and oxygen mole fraction (d) for base design and optimal design at the cell voltage of 0.8 V .....	275

---

- Figure 8-6 Power density curves (a) and polarisation curves during the cell voltage range of 0.3-0.6 V (b), 0.5-0.7 V (c) and 0.6-0.9 V (d) for the base design and optimal design. 277
- Figure 8-7 Sensitivity indices of the five variables at 0.2V (a), 0.5V (b) and 0.8V (c) ..... 280

## List of Tables

Table 1-1 Description of major fuel cell types .....	5
Table 2-1 Development of modelling work on the PEMFC .....	20
Table 2-2 Comparison between the water transport models.....	23
Table 2-3 Water visualisation techniques and their applications.....	33
Table 3-1 Source terms of water vapour, liquid water and dissolved water .....	73
Table 3-2 Enthalpies and entropies of formation for reactants and products at standard condition [26] .....	93
Table 3-3 Empirical coefficients for temperature dependent specific heat [26] .....	93
Table 3-4 Lennard-Jones potential parameters [22].....	97
Table 3-5 Specific heat capacities of platinum, carbon black, membrane/ionomer and liquid water [14] .....	103
Table 3-6 Effective specific heat capacity and thermal conductivity of gas diffusion layer, catalyst layer and membrane .....	106
Table 3-7 Gas permeability of gas diffusion layer and catalyst layer [54, 55] .....	109
Table 4-1 Geometric parameters and material properties of a PEMFC .....	121
Table 4-2 Governing equations used in the single-phase flow and isothermal model.....	122
Table 4-3 Electrochemical parameters used in this model.....	124
Table 4-4 Boundary conditions and source terms in the single-phase flow and isothermal model .....	128
Table 4-5 Physical parameters used in the model.....	130
Table 5-1 Governing equations used in the two-phase flow and isothermal model .....	154
Table 5-2 Transport parameters .....	157
Table 5-3 Conservation of water in different phases .....	157
Table 5-4 Source terms .....	158
Table 5-5 Parameters for model validation and base case condition .....	160
Table 5-6 Orthogonal array $L_9(3^4)$ .....	170
Table 5-7 Orthogonal array testing result .....	170
Table 5-8 Average ionomer film thicknesses at different current densities and relative humidity in base case condition .....	177
Table 6-1 Governing equations used in the two-phase flow and non-isothermal model .....	184
Table 6-2 Conservation of heat in different computational domains.....	185
Table 6-3 Source terms of heat .....	185

---

Table 6-4 Effective specific heat capacity and thermal conductivity of GDL, CL and membrane .....	186
Table 6-5 Thermal parameters .....	186
Table 6-6 Temperature dependent heat capacity and thermal conductivity.....	186
Table 6-7 Dissolved water transport flux, water phase-change and thermal source terms at 0.7 A cm <sup>-2</sup> .....	191
Table 7-1 Structural parameters and material properties of the PEM fuel cells .....	208
Table 7-2 Specific expressions in the general convection-diffusion equation.....	208
Table 7-3 Conservation of water in different phases and heat within different computational domain .....	209
Table 7-4 Conservation of heat.....	209
Table 7-5 Source terms for mass and heat .....	211
Table 7-6 Effective specific heat capacity and thermal conductivity of GDL, CL and channel.....	211
Table 7-7 Predicted current densities and computing time with various mesh characters.....	214
Table 7-8 Parameters used for model validation and base case condition in the study .....	215
Table 7-9 Details of levels of various study parameters and the predicted current densities at 0.05 V .....	228
Table 7-10 Predicted current densities with various levels of study parameters at different cell voltages .....	228
Table 7-11 Limiting current densities predicted at various anode stoichiometric flow ratios with fully humidified gases.....	238
Table 8-1 Characters of mesh sizes.....	259
Table 8-2 Lower and upper bound of design variables for the optimisation .....	265
Table 8-3 Physical parameters for base-case conditions.....	267
Table 8-4 Parameters for base design and optimal designs at different cell voltages .....	276
Table 8-5 Parameters for base design and optimal designs for different cell voltage ranges ...	278
Table 8-6 Key parameters to optimal design at different cell voltages.....	278

## Nomenclature

$A$	cross-sectional area, m <sup>2</sup>
$A_s$	reaction surface area per unit platinum mass, m <sup>2</sup> kg <sup>-1</sup>
$a$	specific area, m <sup>-1</sup>
$C$	dimensionless concentration
$c$	concentration, mol m <sup>-3</sup>
$c_{p,i}$	specific heat capacity of species $i$ , J mol <sup>-1</sup> K <sup>-1</sup>
$D$	diffusivity, m <sup>2</sup> s <sup>-1</sup>
$D_c$	capillary diffusion coefficient, m <sup>2</sup> s <sup>-1</sup>
$D_{ij}$	Maxwell-Stefan diffusion coefficient matrix, m <sup>2</sup> s <sup>-1</sup>
$\tilde{D}_i$	partial variance
$d$	pore diameters, m
$E_r$	effectiveness factor
$\bar{E}_r$	average effectiveness factor
$E^0$	open circle potential, V
$E^{\text{cell}}$	cell voltage, V
$EW$	equivalent weight of Nafion® membrane, g mol <sup>-1</sup>
$F$	Farady's constant, 96485 C mol <sup>-1</sup>
$f$	platinum mass ratio to $Pt/C$
$\mathbf{f}$	column vector of length $n_s$
$H$	Henry's constant, Pa m <sup>3</sup> mol <sup>-1</sup>
$I$	dimensionless current density
$i$	current density, A m <sup>-2</sup>
$i_0$	exchange current density, A m <sup>-2</sup>
$J(s)$	Leverett function
$k$	rate coefficient, s <sup>-1</sup>
$k_i$	thermal conductivity of species $i$ , W m <sup>-1</sup> K <sup>-1</sup>
$k_r$	relative permeability
$k_p$	hydraulic permeability, m <sup>2</sup>
$L$	length of the flow channel, m
$l$	thickness, m
$L_i$	volume fraction of species $i$
$M_j$	molecular weight for specie j, kg mol <sup>-1</sup>
$M_n$	mean molecular weight, kg mol <sup>-1</sup>

---

$M_T$	Thieles's modulus
$m_{\text{Pt}}$	platinum loading, mg cm <sup>-2</sup>
$m_{\text{C}}$	carbon loading, mg cm <sup>-2</sup>
$N$	number per volume, m <sup>-3</sup>
$N_j$	molar flux of specie j, mol m <sup>-2</sup> s <sup>-1</sup>
$n$	number
$p$	pressure, Pa
$Q$	reactant gas flow rates, m <sup>3</sup> s <sup>-1</sup>
<b>R</b>	symmetric correlation matrix
$R$	reaction rate, mol m <sup>-3</sup> s <sup>-1</sup>
$R_g$	ideal gas constant, 8.314 J mol <sup>-1</sup> K <sup>-1</sup>
$R_M$	membrane resistance, Ω m <sup>-2</sup>
$RH$	relative humidity
$r$	radius, m
$S$	source term
$s$	liquid water saturation
$T$	temperature, K
$t$	time, s
<b>u</b>	velocity vector, m s <sup>-1</sup>
$V$	mole volume, m <sup>3</sup>
$w$	mass fraction
$X$	normalised distance ( $x/l_{\text{CL}}$ )
<b>x</b>	design matrix of sample
$x$	mole fraction
$\tilde{x}_i$	design variable $i$
$Y$	normalised distance ( $y/L$ )
<b>y</b>	column vector
$\%M$	volume fraction of primary pores occupied by ionomer

## Greek letters

$\alpha$	charge transfer coefficient
$\alpha_w$	water activity
$\beta$	$(1-\beta_3)F/R_gT = (1-\beta_4)F/R_gT$
$\lambda$	water content
$\mu$	viscosity, Pa s
$\rho$	density, kg m <sup>-3</sup>

$\varepsilon$	porosity
$\delta$	thickness of ionomer/liquid water coating, m
$\gamma$	oxygen diffusion rate through the coating, s <sup>-1</sup>
$\eta$	overpotential, V
$\sigma$	surface tension, N m <sup>-1</sup>
$\theta$	coverage ratio
$\theta_c$	contact angel, °
$\sigma_s$	electronic conductivity, S m <sup>-1</sup>
$\sigma_M$	ionic conductivity, S m <sup>-1</sup>
$\varphi$	potential, V
$\Psi_w$	association parameter for water (the value is 2.6)
$\varsigma$	dimensionless modulus, $\varsigma = a_{CL} i_0 l^2 / n F D_e c_M^0$
$\zeta$	dimensionless modulus, $\zeta = a_{CL} i_0 l^2 \beta / \sigma_s^{eff}$
$v$	$D_{O_2-M} / \delta_M$ , m s <sup>-1</sup>

## Superscripts

$0$	intrinsic
$d$	dissolved
$eff$	effective
$ref$	reference
$eq$	equilibrium
$l$	liquid
$g$	gas

## Subscripts

$a$	anode
$ads$	adsorption
$agg$	agglomerate
$C$	carbon
$c$	cathode
$CL$	catalyst layer
$des$	desorption
$GDL$	gas diffusion layer
$i$	species i
$j$	species j
$Kn$	Knudsen diffusion

<i>loc</i>	local
<i>M</i>	Membrane/ionomer in PEMFCs and methanol in DMFCs
<i>P</i>	void space
<i>Pt</i>	platinum
<i>Pt/C</i>	platinum dispersed carbon
<i>p</i>	primary pores
<i>r</i>	relative
<i>S</i>	GDL penetration
<i>s</i>	secondary pores
<i>T</i>	temperature or total
<i>w</i>	liquid water
<i>sat</i>	saturation
<i>tot</i>	total
<i>vl</i>	vapour to liquid
<i>vd</i>	vapour to dissolved
<i>dl</i>	dissolved to liquid

## Mathematical operators

$\nabla$	Nabla operator
$\frac{\partial}{\partial t}$	time derivative
$\sum$	summation
$  $	modulus
<i>exp</i>	exponential function
<i>ln</i>	natural logarithm function
<i>log</i>	10 base logarithm function

## Abbreviations

1D	one-dimensional
2D	two-dimensional
3D	three-dimensional
AFC	alkaline fuel cell
ACL	anode catalyst layer
ANN	artificial neural network
B-V	Bulter-Volmer
CCD	charge coupled device

CCL	cathode catalyst layer
CFD	computational fluid dynamics
CL	catalyst layer
CHP	combined heat and power
DC	direct electricity
DHE	dynamic hydrogen electrode
DMFC	direct methanol fuel cell
EOD	electro-osmotic drag
FCV	fuel cell vehicles
FEM	finite element method
HOR	hydrogen oxidation reaction
GDL	gas diffusion layer
GSA	global sensitivity analysis
KRG	Kriging model
LB	Lattice Boltzmann
M <sup>2</sup>	multi-phase mixture
MC	Monte Carlo
MCFC	molten carbonate fuel cell
MEA	membrane electrode assembly
MOR	methanol oxidation reaction
NMR	nuclear magnetic resonance
OCP	open circuit potential
ORR	oxygen reduction reaction
PAFC	phosphoric acid fuel cell
PDE	partial differential equation
PEMFC	proton exchange membrane fuel cell
RBF	radial basis function
RTD	residence time distribution
SHE	standard hydrogen electrode
SPE	solid polymer electrolyte
SOFC	solid oxide fuel cell
TPB	triple phase boundary
VHLC	variable heating and load control
VRE	voltage reversal effect
VOF	volume of fluid
WCC	water carrying capacity

## Acknowledgements

I would like to take this opportunity to thank my supervisor, Prof. Keith Scott, for the precious opportunity of working on the SUPERGEN project funded by EPSRC of UK government. Thanks a lot for colleagues and friends in the Fuel Cell Lab of Newcastle University, including Dr. M. Mamlouk, Dr. X. Liu, Dr. X. Wang, Dr. C. Xu, Dr. Y. Cao, and Dr. X. Wu.

Sepcial thanks to my father, mother, sister and nucel for supporting my decisions.

Last but not least, I dedicate this book to my wife, Mrs Yue Wang, and our baby Zhou Xing. We met in Newcastle and fell in love in this magic city. I am grateful for having you always by my side as you continuously make me better.

## Chapter 1. Introduction

### 1.1 Hydrogen, the next generation energy source

Energy is vital important to every aspect of modern society. The entire industrialised infrastructure of the world would collapse without energy. The rapid industrialisation and urbanisation lead to an increasing consumption of energy. As shown in Figure 1-1, the world's primary energy consumption increases more than ten times from 1900 to 2000. Today, the global energy requirements are mostly dependent on fossil fuels, which is about 80% of the present world energy demand [2]. This will eventually result in the depletion of limited fossil energy resources (for example coal and oil) and the environmental pollution. By 2050, oil and gas supply is unlikely to be able to meet the global energy demand [3]. The CO<sub>2</sub> content in the atmosphere has increased 30% since the industrial era begin, leading to a global warming [4]. In order to prevent the depletion of fossil fuels and decrease their negative effect on climate change, increasing focus is being placed on renewable energy to satisfy the growing energy demand [5]. According to the report of 2013 from the Renewable Energy Policy Network [6], the renewable power capacity (excluding the hydropower) worldwide has exceeded 1470 Giga watt (GW) in 2012, up about 8.5% from the previous year.

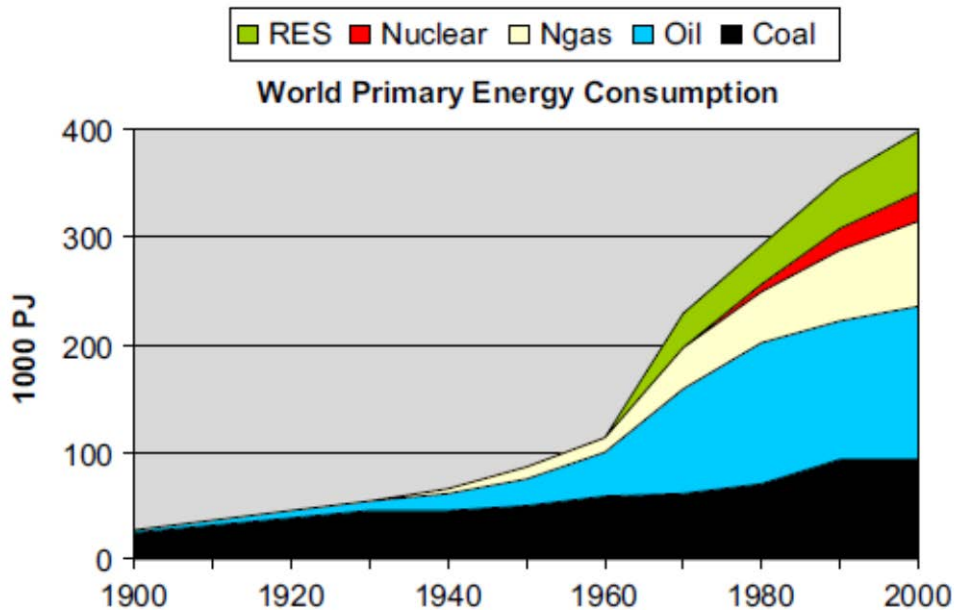


Figure 1-1 World primary energy consumption from 1900 to 2000 [1]

(RES: Renewable Energy Source; Ngas: Natural gas)

Hydrogen is suggested as the ideal energy carrier for the future. This is because hydrogen can be obtained from several resources, in particular, fossil, renewable and nuclear resources. Hydrogen is the lightest and one of the most plentiful elements in nature. Hydrogen makes up approximate 75% of all the matter in the universe and its density is 7.5% of air. Hydrogen has a range of excellent properties over the conventional power sources. However, hydrogen is not a primary energy source. It must be produced by other energy sources before using as a clean energy [6]. Figure 1-2 illustrates how hydrogen can be produced as an energy carrier by multiple hydrogen production methods and how hydrogen can be used as various end-user applications.

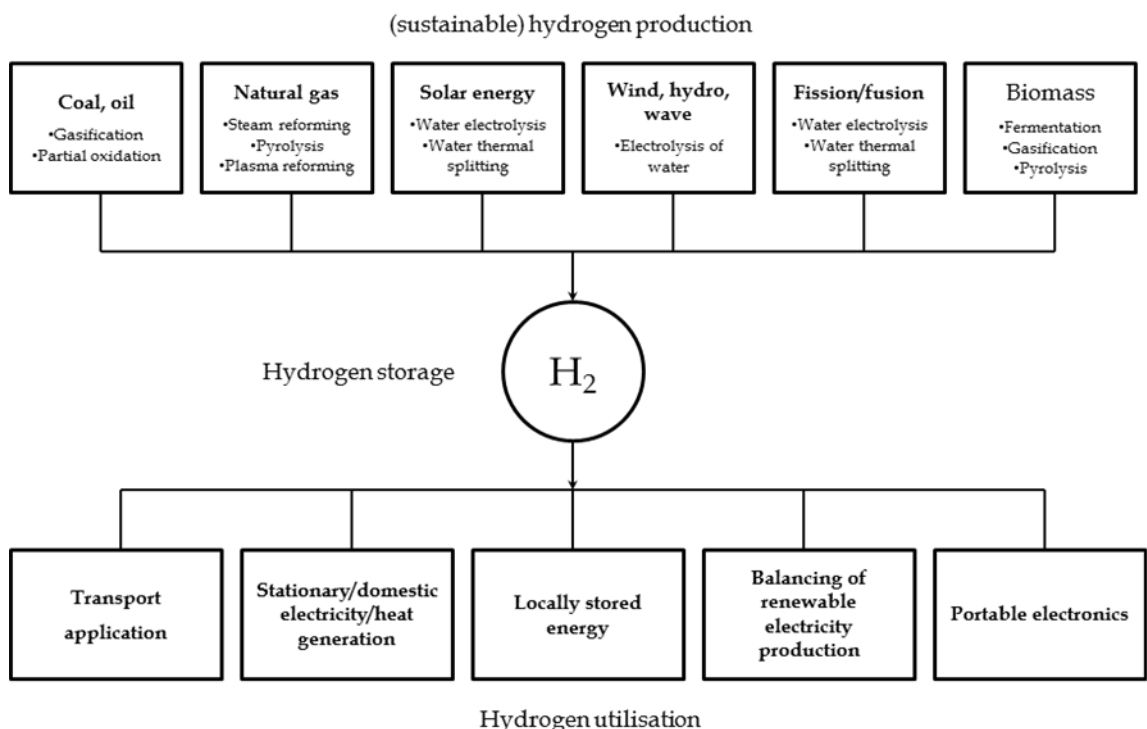


Figure 1-2 Hydrogen as an energy carrier linking multiple hydrogen production methods, through storage to various end-users [5]

Obviously, hydrogen can be produced from a variety of resources, contributing significant security to energy supply. Hydrogen will be in the long-term produced from renewable energy sources by developed technology, such as water electrolysis. However, in the short-term, hydrogen is produced in large quantities from fossil fuels reformation [7]. For example, in 2007, the annual production of hydrogen is about 0.1 Giga ton (Gton), 98% from the reforming of fossil fuels, such as oil refining and ammonia and methanol production [8]. The portion of hydrogen produced by renewable energy sources has increased in recent years. Renewable energy contributed 2.0% of

total global energy consumption in 2005 [9], and it increased to 19% in 2012[6]. For instant, renewable energy met 27% of the electricity demand of Italy in 2012 [6]. The expansion of combined heat and power (CHP) plants helps Denmark maintaining the same primary fuel consumption more than 30 years, which has so far saved 14 % of fossil fuels [10]. The European roadmap for the development of hydrogen and fuel cell technologies has now set a target of 1 GW of distributed power generation capacity from fuel cells by 2015 [3].

Researchers believed that the strong relationship between hydrogen and electricity provided an opportunity of achieving the sustainable use of energy. Fuel cells are considered as ideal devices capable of replacing traditional internal combustion engines as the primary way to convert chemical energy into electricity [11].

## 1.2 Fuel cells

A fuel cell is an electrochemical device that converts chemical energy of fuel (e. g. hydrogen or methanol) directly into direct current (DC) electricity. Unlike the traditional internal combustion engine, fuel cell produces electrical energy through electrochemical reaction, rather than through combustion. A single fuel cell consists of a pair of anode and cathode, and an electrolyte in between. Individual fuel cells can be connected in series to form a fuel cell stack, which can generate higher power for portable and stationary application.

The first observation of a fuel cell effect was made by Shoenberin in 1838 [12]. Based on this work, the first fuel cell was demonstrated and developed by Grove in 1839 [13] and 1842 [14]. The fuel cell used platinum strips and sulphuric acid as the electrodes and electrolyte, respectively. Electrical energy was produced by combining hydrogen and oxygen. In the following one hundred years, fuel cells were not practically used until the U.S. space program, Gemini and Apollo program, in 1960s. The first practical fuel cell applications were in the Gemini Program. In the following Apollo Program, fuel cells were used to provide electricity for life support, guidance and communications. In spite of the continued successful application in the U. S. space program, fuel cells were “forgotten” for terrestrial applications until the early 1990s. In 1993, Energy Partners demonstrated the first passenger car running on PEM fuel cells [15].

A typical process of electricity generation from fuels involves several energy conversion steps. The efficiency of the traditional combustion engines is limited by the Carnot efficiency because the energy conversion steps are not 100% efficient [16]. Fuel cells circumvent all the energy conversion steps and generate electricity in a single step. This makes fuel cells more efficient than the combustion systems. Moreover, fuel cell operating on hydrogen is zero emission; the only exhausts are water and heat. A variety of advantages make them promising candidates as power sources for portable and stationary applications.

Although fuel cells have a variety of advantages, some disadvantages, such as high cost and low durability, remain big barriers that slow down their commercialisation [16]. In order to make the fuel cells economically competitive, new technological solutions must be developed.

### ***1.2.1 Types of fuel cells***

Depending on the different electrolyte used, fuel cells can be categorised in five groups, namely:

- a. Alkaline fuel cells (AFC)
- b. Proton exchange membrane or polymer electrolyte membrane fuel cells (PEMFC)
- c. Phosphoric acid fuel cells (PAFC)
- d. Molten carbonate fuel cells (MCFC)
- e. Solid oxide fuel cells (SOFC)

AFCs adopt an immobilised liquid KOH, while PEMFCs use a perfluorinated membrane, such as Nafion<sup>®</sup>, and PAFCs apply an immobilised liquid H<sub>3</sub>PO<sub>4</sub> as the electrolyte, respectively. Hydrogen and oxygen (air) are the fuel and oxidant used in AFCs, PEMFCs and PAFCs, which typically operated under 220 °C. MCFCs are high-temperature (approximate 600 °C) fuel cells that use an electrolyte composed of a molten carbonate salt mixture suspended in a porous, chemically inert ceramic matrix. MCFCs use natural gas, biogas as well as hydrogen as the fuel. The operating temperature of SOFCs (800-1000 °C) is higher than that of MCFCs. SOFCs use a solid oxide materials, such as ceramic, as the electrolyte which conducts negative oxygen

ions from the cathode to anode. Oxygen or air is used at cathode while hydrogen or hydrocarbon, such as methane, is used as the fuel at anode. Note that in the PEMFC group, fuel cells used methanol as the fuel is categorised as another type of fuel cell, direct methanol fuel cell (DMFC). Although all types of fuel cells are based on the same electrochemical principles, they all operate at different temperature ranges, incorporate different materials, and differ in the performance characteristics and fuel tolerance. The main characteristics of each types of fuel cell are shown in [Table 1-1 \[17, 18\]](#).

Table 1-1 Description of major fuel cell types

	AFC	PEMFC	PAFC	MCFC	SOFC	DMFC
Electrolyte	Liquid KOH (immobilised)	Polymer membrane (e.g. Nafion®)	Liquid H <sub>3</sub> PO <sub>4</sub> (immobilised)	Molten carbonate	Ceramic (usually Y <sub>2</sub> O <sub>3</sub> -stabilised ZrO <sub>2</sub> )	Polymer membrane (e.g. Nafion®)
Charge carrier	OH <sup>-</sup>	H <sup>+</sup>	H <sup>+</sup>	CO <sub>3</sub> <sup>2-</sup>	O <sup>2-</sup>	H <sup>+</sup>
Operating temperature	60-220 °C	80-220 °C	150-220 °C	600-700 °C	800-1000 °C	50-120 °C
Catalyst	Ni, Ag, metal oxides and noble metals	Platinum	Platinum	Nickel	Perovskites (ceramic)	Platinum and Ruthenium
Cell components	Carbon based	Carbon based	Carbon based	Stainless based	Ceramic based	Carbon based
Fuel compatibility	Hydrogen	Hydrogen	Hydrogen	Hydrogen, methane	Hydrogen, methane, carbon monoxide	Methanol

The modelling activities included in this book are focused on PEMFC operating with Nafion® as electrolyte. Their operation, performance, design and application will be described in the next sections.

### 1.2.2 Proton exchange membrane fuel cell (PEMFC)

The first practical fuel cell was developed by General Electric Company (GE) in the 1950s. GE was awarded the contract for the Gemini space program in 1962. The fuel cell in the Gemini program is a 1 kW PEMFC system with a platinum loading of 35 mg Pt cm<sup>-2</sup>. The observed current density was 37 mA cm<sup>-2</sup> at 0.78 V [\[19\]](#). In the 1960s, improvements were made by incorporating Teflon in the catalyst layer directly adjacent to the electrolyte. Considerable improvements were made from the early 1970s onward with the adoption of the fully fluorinated Nafion® membrane [\[20\]](#).

A typical PEMFC unit (see Figure 1-3) consists of a membrane electrode assembly (MEA) sandwiched between the flow field plates of the anode and cathode in which flow channels are machined. The MEA includes three parts, gas diffusion layer (GDL) and catalyst layer (CL) on anode and cathode, respectively, and polymer electrolyte membrane in between. At anode, hydrogen flows into the anode flow channel and transport to the CL through the GDL, and then oxidises into protons and electrons in the anode CL (reaction 1-1). The protons pass through the polymer electrolyte membrane and reach to the cathode CL, while the electrons travel via an external circuit to the cathode. At the same time, at cathode, air or oxygen flows into the cathode flow channel and transport to the CL through the GDL. In the cathode CL, oxygen combines with the protons and electrons, which generated in the anode CL, to produce water (reaction 1-2).

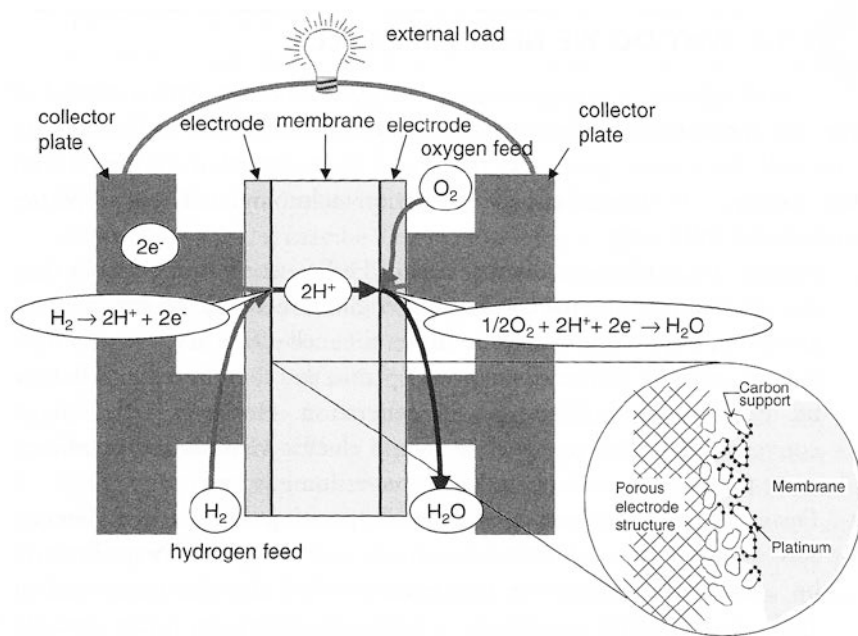
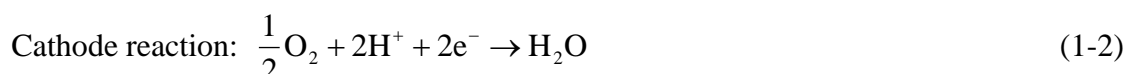


Figure 1-3 Schematic diagram and basic principle of operation of a PEMFC



The thermodynamic potential for the reaction (1-2) calculated from the standard chemical potentials at 25 °C and 1.0 atm is 1.23 V versus standard hydrogen electrode (SHE).

In the case of a fuel cell supplied with reactants gases without the closed electrical circuit, the observed practical cell potential is called the open circuit potential (OCP). The OCP is lower than the theoretical potential due to the activation losses, especially at the cathode, in the fuel cell even when no external current is generated [16]. The relationship between fuel cell potential and current density is called the polarisation curves, which is obtained by subtracting the activation polarisation losses, ohmic losses, and concentration polarisation losses from the equilibrium potential. Figure 1-4 shows the polarisation curve and different voltage losses in a PEMFC. Note that a majority of the voltage losses occur at the cathode due to the sluggish oxygen reduction reaction (ORR) [21].

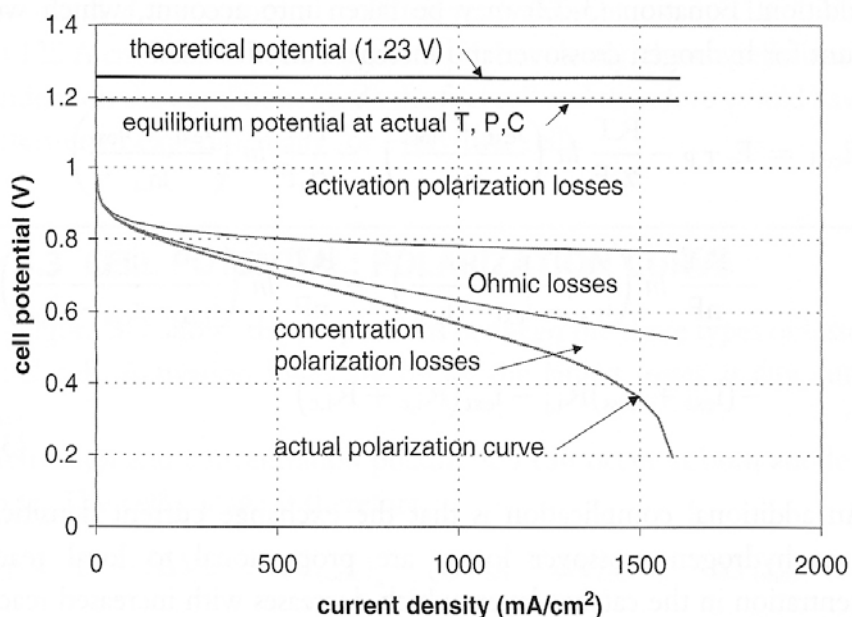


Figure 1-4 Voltage losses in the fuel cell and the resulting polarisation curves [17]

The major application of PEMFCs focuses on transportation due to their potential impact on the environment, e.g. the low emission. Stationary electricity plants and portable power sources are the other important applications. In the last decade, the interest and involvement of the scientific and engineering communities and companies in the PEMFC technology have continuously increased. The total number of the granted fuel cell patents increased approximate 350% during 2000 to 2010. In 2010, 1801 granted fuel cell patents were published by the U.S. and European patent offices, and this number increased to 2732 in 2011 [22, 23]. Automakers such as General Motors (GM), Honda, Toyota, have paid considerable attention on developing their fuel cell vehicles (FCV) and announced plans of commercialising their FCV by 2015 [24].

Intelligent Energy, an intellectual property rich company in UK, launched its first commercial off-grid hydrogen fuel cell, Upp<sup>TM</sup>, in 2013. Upp<sup>TM</sup> is a smart PEMFC device that can conveniently power and charge all the compatible hand-held electronic devices via universal serial bus (USB) [25].

### 1.3 Fuel cells modelling

Modelling plays a significant role in the process of fuel cell design and development. Normally, the fuel cell design and development process begins with a set of requirements, including power output, operating conditions, size limitation, safety specifications, and others. Based on the knowledge of materials and processes involved in the fuel cells, modelling is performed to predict the fuel cell performance. The modelling helps the designer to determine the best candidate designs or improve the existing designs that satisfy the requirement.

Modelling can provides a better understanding on the electrochemical reactions and mass transport occurred within the fuel cells, for example, the reactants profiles [26], temperature distribution [27], and polarisation curves obtained [28]. It can give a quick prediction of the fuel cell performance under various given operating conditions, material properties and fuel cell geometries. Modelling reduces the time, effort and cost associated with the experimental studies and provides a theoretical guidance on the development and optimisation of the fuel cells [29].

### 1.4 Objectives and structure of the book

A main objective of this book is to develop a fully coupled, multi-physics and multi-phase flow model of a typical Nafion® membrane based PEMFC unit in order to better understand the water formation and transport mechanisms, heat distributions and mass transport resistance at different cell loadings and various operating conditions. The aim is to develop a computational model which is capable of analysing and predicting the behaviour of a PEMFC equipped with a Nafion® membrane. This model will give guidance to enhance the PEMFC output by optimising the composition of the electrode and operating conditions.

This book is divided into nine chapters as follow:

Chapter 1. An overview of the hydrogen energy and fuel cell technology.

- Chapter 2. A literature review of the different fuel cell modelling approaches.
- Chapter 3. A detailed description of the fundamentals, principles and governing equations.
- Chapter 4. A single-phase flow isothermal model is developed to analyse the distribution of the reactant species in flow channel and porous electrode. This model is used to study the water content distribution within the membrane and the effect of catalyst layer parameters on fuel cell performance.
- Chapter 5. A two-phase flow isothermal model is developed to study the water phase transfer, dissolved water transport through the membrane and ionomer, and liquid water distribution in cathode catalyst layer and gas diffusion layer is represented.
- Chapter 6. A two-phase flow non-isothermal model is developed to investigate the temperature distribution in MEA, and the influence of temperature on membrane water content, liquid water saturation, and cell performance.
- Chapter 7. An anode partial flooding model is developed to study the water flooding at the anode and the initiated influence on the electrochemical reaction. Electrode parameters and channel geometries, as well as a variety of operation conditions are numerically investigated for an improved cell performance.
- Chapter 8. A multiple surrogate model is developed to optimise the cathode catalyst layer composition. Five design parameters are optimised and their sensitivities are analysed by a Monte Carlo method based approach.
- Chapter 9. Conclusions are summarised and future research trends and perspectives are recommended.

## 1.5 References

1. Lund, H., *Renewable energy strategies for sustainable development*. Energy, 2007. **32**: p. 912-919.
2. Das, D. and T.N. Veziroglu, *Hydrogen production by biological processes: a survey of literature*. International Journal of Hydrogen Energy, 2001. **26**: p. 13-28.

3. Edwards, P.P., V.L. Kuznetsov, W.I.F. David and N.P. Brando, *Hydrogen and fuel cells: Towards a sustainable energy future*. Energy Policy, 2008. **36**: p. 4356-4362.
4. Conte, M., A. Iacobazzi, M. Ronchetti and R. Vellone, *Hydrogen economy for a sustainable development: State-of-the-art and technological perspectives*. Journal of Power Sources, 2001. **100**: p. 171-187.
5. Dincer I., *Renewable energy and sustainable development: a crucial review*. Renewable and Sustainable Energy Review, 2000, **4**: p.157-175.
6. Network, R.E.P. *Renewables Global Status Report*. 2013; Available from: <http://www.ren21.net/REN21Activities/GlobalStatusReport.aspx>. (accessed Jan 2014).
7. Edwards, P.P., V.L. Kuznetsov and W.I.F. David, *Hydrogen energy*. Philosophical Transactions of the Royal Society A: Mathematical, Physical and Engineering Sciences, 2007. **365**: p. 1043-1056.
8. Marban, G. and T. Valdes-Solis, *Towards the hydrogen economy?* International Journal of Hydrogen Energy, 2007. **32**: p. 1625-1637.
9. Network, *Renewables Global Status Report*. 2005; Available from: <http://www.ren21.net/REN21Activities/GlobalStatusReport.aspx> (accessed Jan 2014).
10. Lund, H. and P.A. Ostergaard, *Electric grid and heat planning scenarios with centralised and distributed sources of conventional, CHP and wind generation*. Energy, 2000. **25**: p. 299-312.
11. Dunn, S., *Hydrogen futures: Toward a sustainable energy system*. International Journal of Hydrogen Energy, 2002. **27**: p. 235-264.
12. Bossel, U., *The birth of the fuel cell 1835-1845*. Oberrohrdorf, Switzerland: European Fuel Cell Forum, 2000.
13. Grove, W.R., *On voltaic series and the combination of gases by platinum*. London and Edinburgh Philosophical Magazine and Journal of Science, 1839. **14**: p. 127-130.
14. Grove, W.R., *On a gaseous voltaic battery*. London and Edinburgh Philosophical Magazine and Journal of Science, 1842. **21**: p. 417-420.

15. Nadal, M. and F. Barbir, *Development of a hybrid fuel cell/battery powered electric vehicle.* in D.L. Block and T.N. Veziroglu (editors), *Hydrogen Energy Progress X*, vol. 3. Coral Gables, FL: International Association for Hydrogen Energy, 1994. p. 1427-1440.
16. Weber, A.Z., S. Balasubramanian and P.K. Das. *Proton Exchange Membrane Fuel Cells.* in K. Sundmacher (editor), *Advances in Chemical Engineering Fuel Cell Engineering*, USA: Elsevier Inc; 2012. p. 66-143.
17. Barbir, F., *PEM fuel cells : theory and practice – 2<sup>nd</sup> Edition.* 2005, Oxford: Academic.
18. O'Hayre, R., S. Cha, W. Colella and F.B. Prinz, *Fuel cell fundamentals.* 2006, Hoboken, NJ: John Wiley & Sons, INC.
19. Appleby, A.J. and E.B. Yeager, *Solid polymer electrolyte fuel cells (SPEFCs).* Energy, 1986. **11**:137–52.
20. Wang, Y., K.S. Chen, J. Mishler, S.C. Cho and X.C. Adroher, *A review of polymer electrolyte membrane fuel cells: Thechology, applications, and needs on fundamental research.* Applied Energy, 2011. **88** : p. 981-1007.
21. Bernardi, D.M. and M.W. Verbrugge. *A mathematical model of the solid-polymer-electrolyte fuel cell.* Journal of Electrochemical Society, 1992. **139**: p. 2477-2491.
22. Stone, C. and Morrison A.E., *From curiosity to “power to change the world”.* Solid State Ionics, 2002. **152-153**: p.1-13.
23. Network, Fuel cell today patent review (2011 and 2012), Available from: [www.fuelcelltoday.com/analysis.patents](http://www.fuelcelltoday.com/analysis.patents) (accessed Jan 2014).
24. Gittleman C., D. Masten and S. Jorgensen. Automotive fuel cell R&D needs. in: DOE fuel cell pre-solicitation workshop. Department of Energy, Lakewood, Colorado, 2010.
25. Network, Intelligent energy launches Upp (TM) - Portable power for your connected devices (2013). Available from: [www.intellinet-energy/consumer-electronics](http://www.intellinet-energy/consumer-electronics) (accessed Jan 2014).
26. Guran, V., H. Liu and S. Kakac, *Two-dimensional model for proton exchange membrane fuel cells.* AIChE Journal, 1998, **44**: 2410-2422.

27. Hottinen, T. and O. Himanen, *PEMFC temperature distribution caused by inhomogeneous compression of GDL*. Electrochemistry Communications, 2007, **9**: 1047-1052.
28. Yan, W.M., C.Y. Soong, F. Chen and H.S. Chu, *Effect of flow distributor geometry and diffusion layer porosity on reactant gas transport and performance of proton exchange membrane fuel cells*. Journal of Power Source, 2004, **125**: 27-39.
29. Secanell, M, J. Wishart and P. Dobson, *Computational design and optimisation of fuel cells and fuel cell systems: A review*. Journal of Power Sources, 2011. **196**: 3690-3704.

## Chapter 2. Overview of water management, optimisation and performance of PEMFCs

### 2.1 Introduction

By now, research and development in fuel cell technology have resulted in a broad range of insights on aspects to material, design, manufacturing and operating of PEMFCs and DMFCs [1-4]. These variations indicate that there are a multitude of factors governing the performance of the PEMFCs and DMFCs, of which some physical design or operation can be optimised to improve the fuel cell performance, for example, the platinum and ionomer loadings of the catalyst layer [5-8], the relative humidity of the reactant gas inlet [9-10], as well as the flow field configuration [11-16].

This chapter reviews the state-of-art research and development on the modelling, design and optimisation of the PEMFCs and DMFCs. As a vital important issue of fuel cell operation, water management including water transport and liquid water flooding are reviewed. Following the review of modelling approach and experimental study for water transport, the overview of the PEMFCs optimisation is represented. At the end of this chapter, the anode behaviour of the DMFCs is reviewed.

### 2.2 Overview of water transport and flooding in the PEMFC

For PEMFCs, the perfluorinated membranes, such as Nafion<sup>®</sup>, are typically used as the electrolyte. Ionomer is required in the catalyst layers preparation for the purpose of proton transport from the anode catalyst layer, through the membrane, to the cathode catalyst layer. As shown in Figure 2-1, on the membrane-catalyst layer boundary, Nafion<sup>®</sup> membrane is connected with the ionomer in the catalyst layers, for both the anode and cathode. Water in PEMFCs acts as the lubricant which makes the fuel cell system running smoothly [17]. It can be fed into the PEMFCs system by the gas inlet or/and generated by the oxygen reduction reaction (ORR) at cathode. Water exists as water vapour in the gas mixture, which is absorbed by the Nafion<sup>®</sup> membrane as well as the ionomer in the catalyst layer becoming the dissolved water. When current is generated, the proton migration through the membrane is associated with a drag of water molecules from the anode to the cathode. This so-called electro-osmotic drag

(EOD), together with the electrochemical water production, leads to a water accumulation at the cathode.

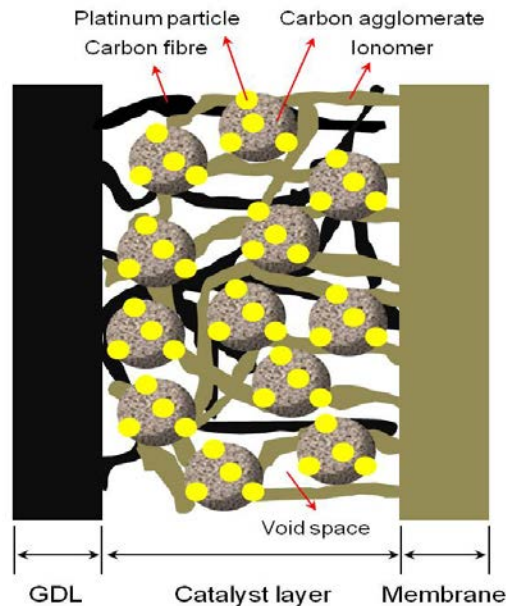


Figure 2-1 Structure of catalyst layers in PEMFCs

Due to the generated gradient of water concentration between the anode and cathode, a certain amount of water could diffuse back from the cathode to the anode, which is an opposite direction against the EOD. In addition, the pressure difference between the anode and cathode could drive a water transport through the membrane, which is called hydraulic permeation. The water transport occurred in a PEMFC is schematically shown in Figure 2-2.

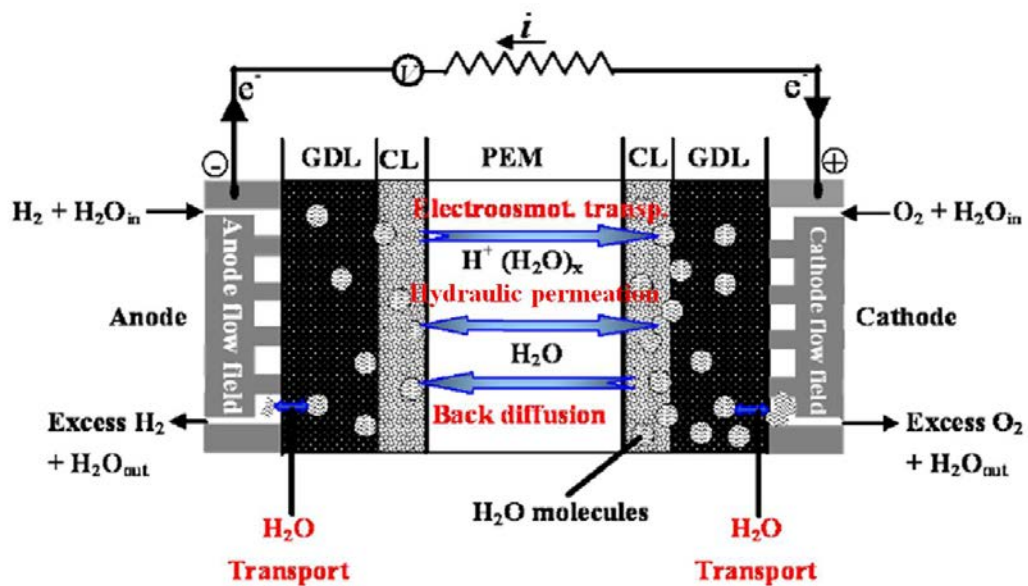


Figure 2-2 Water transport mechanism inside the PEMFCs

Maintaining a subtle equilibrium between membrane dehydration and liquid water flooding is the key issue to achieve maximum performance and durability for PEMFCs [18, 19]. On one hand, water is required to guarantee the good proton conductivity of the proton exchange membrane, where protons move in the hydrated parts of the ionomer via dissociation of sulfonic acid bonds. The protons cannot migrate in dry proton exchange membrane, where the sulfonic acid bond cannot be dissociated, lead to a decrease of ionic conductivity [20]. Furthermore, lower ionic conductivity hinders the access of protons to the active sites of catalyst layer, resulting in an increase in activation polarisation [21]. On the other hand, excess water formed within catalyst layers needs to be transported to flow channels through gas diffusion layers and removed by reactant gas out of the PEMFC system (see Figure 2-3) or else excess water will block the flow channel and the pores of the porous electrodes and then increase the mass transport resistance. This phenomenon, which can be considered as one of the most important limiting factor of PEMFC performance, is known as “flooding”.

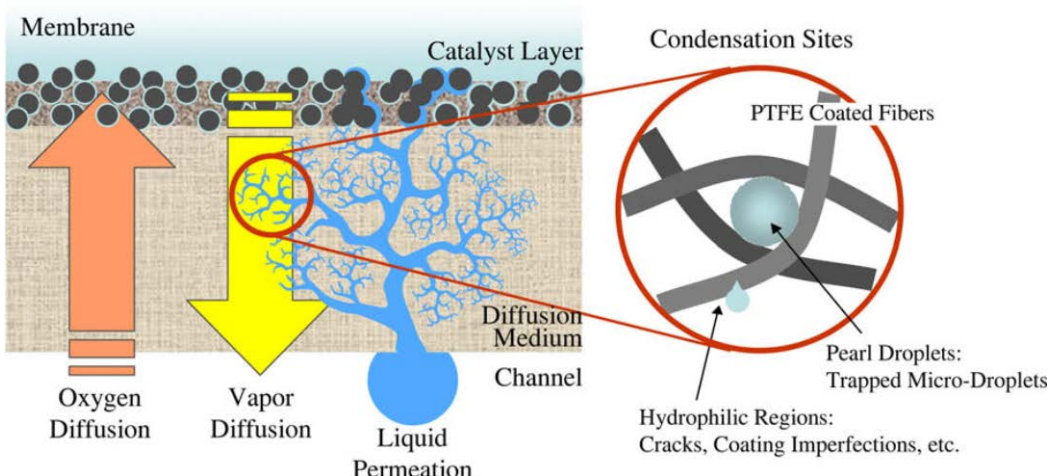


Figure 2-3 Converging capillary tree water transport mechanism [89]

Cathode flooding, anode flooding and flow channel flooding are the three main types of flooding included in the PEMFC system. They are determined by temperature, gas flow rate, pressure and humidity of the reactant gases. Generally, flooding of the cathode and the anode are linked to high current density that results in a greater water formation rate than the removal rate. Moreover, even if liquid water floods into both side of the electrodes [22, 23], water flooding is more prone to occur at the cathode, because water formed within the catalyst layer of the cathode, especially at higher current density [24]. The accumulation of liquid water in the channels is observed only after complete saturation of the gas with water vapour because the evaporation and

water vapour transport are relatively faster than liquid water transport [23]. The thickness of the membrane, water content of the membrane and humidity of the reactant gases in turn determine the concentration gradient of water between anode and cathode. Furthermore, membrane water content and reactant gas humidity are dependent on the gas inlet humidification and the temperature and pressure in the gas channels [24]. Besides, back diffusion prevails over electro-osmotic drag at lower current density; and electro-osmotic drag prevails over back diffusion while higher current density is achieved, thus the anode (including the membrane) tends to dry out, even the cathode is well hydrated at high current density [25].

Membrane dehydration is the most serious negative influence on the fuel cell performance. It is more likely to occur at the anode side of the membrane due to the dry reactant gas inlet and the effect of electro-osmotic drag. The pores of membrane shrink under the dehydrated condition, leading to lower water back diffusion, especially for the operating conditions such as higher temperature and higher current density. Consequently, the proton exchange membrane dehydrates, resulting in a remarkable decrease in the conductivity and a big increase in the ionic resistance [19, 25, 26]. In addition, severe drying condition leads to irreversible degradation of the membrane [27, 28]. All types of flooding lead to instant increase in mass transport losses, gas starvation and immediate drop of cell potential. As shown in Figure 2-4, the time dependent performance of current density at 0.6V vs. SHE (standard hydrogen electrode) is observed [29]. The gas flow path can be temporarily blocked by liquid water, giving rise to a sharp reduction in current density.

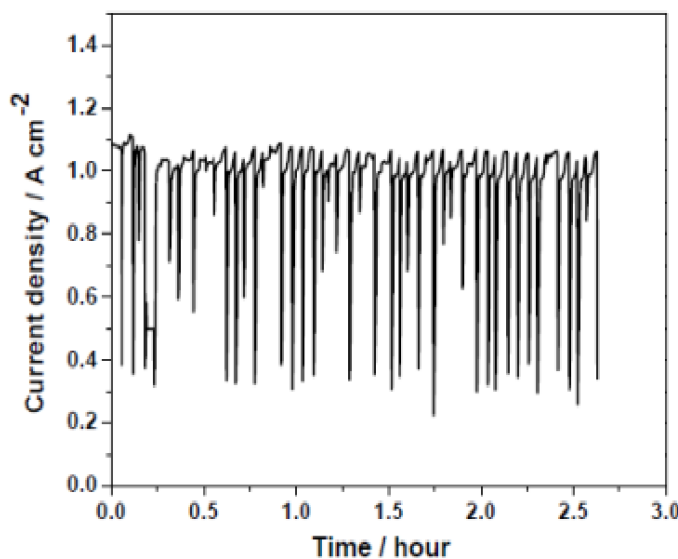
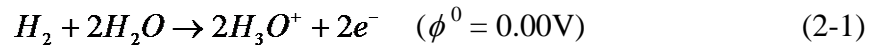
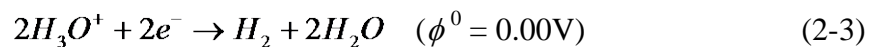
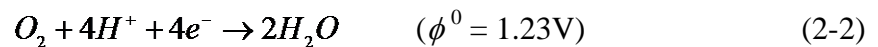


Figure 2-4 A typical water flooding pattern in a PEMFC operated at constant cell voltage [17]

It is important to note that one of the most serious negative effects of cathode flooding is the voltage reversal effect (VRE). In the case of oxygen starvation, not enough oxygen supplied at cathode.  $\text{H}_3\text{O}^+$ , which generated by water molecule and proton at cathode according to Eq. (2-1), would be reduced by electron instead of oxygen, resulting in a significant drop of potential.



The original electron consuming process of oxygen reduction reaction (Eq. 2-2) would be replaced by the new electron consuming process (Eq. 2-3) as follow:



Consequently, the cathode potential decreases from 1.23 V to 0.00 V at current off and from 0.80 V to -0.1 V at current on.

Polarisation occurs while current flows through the electrode. The cathode polarisation causes potential to change more negative and anode polarisation more positive [29], for example 0.1 V. As a result, the output voltage of the cell decreases from 0.7 V to -0.2 V under the effect of VRE (see Figure 2-5).

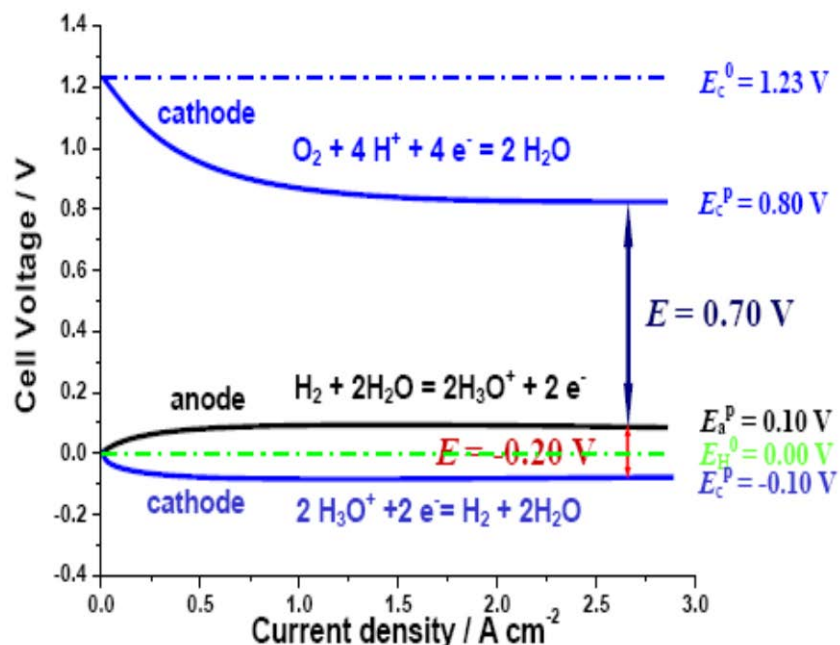


Figure 2-5 Voltage reversal effect (VRE) in PEMFC [17]

### 2.3 Overview of modelling of water transport in PEMFC

Numerical modelling of PEMFC is important for better understanding of the transport processes in PEMFC because of the experimental drawbacks such as difficulty of performing the different experimental measurements simultaneously, unrealistic operating conditions, and high cost of materials and testing instruments. Numerous models have been developed to describe water management and liquid water transport in PEMFCs over the last decade [30-34]. Depending on different descriptions on water formation and transport, the models can be mainly categorised into four groups: dynamic models, lumped models, flooding models and other models associated with the effect of geometrical configuration.

In early 1990s, some simple models have been developed. These models were all simplified models which all applied the assumption that the reactant and charge only transport along one direction. The numerical models developed by Springer *et al.* [35, 36] and Bernardi and Verbrugge [37, 38] are usually considered as the pioneering modelling works for PEMFC. These models are essentially one-dimensional models considering the membrane, catalyst layer and gas diffusion layer based on solving the conservations equations by assuming homogeneous materials and using effective transport properties. After that, Nguyen and White [39] and Fuller and Newman [40] developed pseudo two-dimensional models by further considering the flow channels, which considered the effect of water humidity inlet and temperature distributions, providing more detailed water and thermal management capability. However, the models developed in this period are too simple to simulate the very complex PEMFC system although they laid the foundation for PEMFC modelling.

More numerical models were developed in the late 1990s. Yi and Nguyen [41, 42] and Gurau *et al.* [43] developed two-dimensional models to explore more detailed transport phenomena in PEMFCs. These models illustrated the utility of multi-dimensional models in the understanding of the internal conditions of PEMFC, such as the reactant and water distribution. Gloaguen and Durand [44], Bultel *et al.* [45-47] and Marr and Li [48] developed the agglomerate models. These models applied simplified catalyst layer structures by assuming that the large agglomerates were formed by ionomer and platinum/carbon particles on the level of micrometre. Compared to the models developed earlier, more detailed mass and charge transport phenomena were

analysed more accurately because these models extended the one-dimensional or pseudo two-dimensional to the two-dimensional. It is important to note that all the models developed were based on the single phase assumption, which treated the water as vapour, including the water formed in the cathode catalyst layer and supplied along with the humidified gas inlet. The water condensation within the porous electrodes and the flow channels was not considered. Although there was not sufficient evidence to conform that water could be condensed in catalyst layers and gas diffusion layers while the PEMFC system operated in normal condition. However, condensed water in the flow channels has been observed by some instruments such as high-resolution camera [49, 50]. Generally, ideal single phase assumption is applied when reactant gases are oxidised or reduced at the surface of solid catalyst (Pt-Ru and other binary or ternary alloy). In reality, the condensed water could change the single-phase flow problem to a two-phase flow problem.

In the 2000s, multi-dimensional models have been developed by many researchers to solve a complete set of conservation equations (such as continuity and Navier-Stokes) coupled with electrochemical reactions (for example the kinetics of oxygen reduction at cathode). Computational fluid dynamics (CFD) code and some commercial software (such as Fluent, COMSOL) based on finite volume methods were adopted to develop such models, and more complicated geometry and transport phenomena were investigated. In the area of three-dimensional geometry, the models developed by Dutta *et al.* [51, 52], Zhou and Liu [53], Berning *et al.* [54], Mazumder and Cole [55], Lee *et al.* [56], Um and Wang [57] and Wang and Wang [58] were considered as the pioneering works in this field, these models mainly considered a single flow channel with the major components of reactant gases. Large scale simulations considering multi-channel or small stacks were also carried out [59-62]. Without doubt, these models give more accurate and more specific analysis on the distribution of reactant gases ( $H_2$  and  $O_2$ ), water vapour, and pressures. The main impediment to the widespread use of these multi-dimensional models is the requirement for the computer hardware.

In fact, reasonable simplification of the complex multi-dimensional models is considered as the practical way of modelling the complicate transportation and reaction inside of the PEMFC with lower computational requirement. In order to simplify the models and reduce the amount of computation for conservation equations, some modelling works neglected liquid water formation by assuming liquid water as super saturated water vapour [39-41]. The real two-phase flow models, which give more

accurate prediction than the previous models with single-phase assumption, have also been developed by Nguyen *et al.* [63-66], Djilali *et al.* [67-69], Mazumber and Cole [70], and Wang *et al.* [71, 72]. These two-phase flow models solved the mass, momentum and species transport conservation equations for the gas mixture, with an extra conservation equation for liquid water transport. However, the accurate and detailed water transport behaviour cannot be studied in these models because the interface tracking between liquid water and gas is not permitted. As a result, the volume of fluid (VOF) model, based on liquid water dynamics in order to investigate water flow in single serpentine flow channel, was developed by Quan *et al.* [73].

Overall, a large number of numerical models have been developed by researches around the world. The main difference between the models developed in different period is presented in [Table 2-1](#). In short, the development of these models is from simple to complex, from general to specific. In spite of the great changes of the equation forms in the models, all the processes are described based on some basic laws, for example, the laws of conservation of energy and momentum. Developing a comprehensive and comparatively simple model for the PEMFCs under practical load conditions by reasonably simplify the complex multi-dimensional models is our main objective of the modelling work. Furthermore, the experimental data will be obtained to validate the simulation results.

Table 2-1 Development of modelling work on the PEMFC

Models	Period of development	Dimensions of reactant, products and charge transportation	Accuracy of modelling process comparing to practical fuel cell	Complexity of the models and computer hardware requirement
1D and pseudo 2D	Early 1990s	One dimension	Crude	Simple and low
2D	Later 1990s	Two dimensions	Medium	Medium
3D and multi-dimensional	2000s	Three dimensions	Precise	Complex and high

### 2.3.1 Modelling of water transport through the membrane

The previous modelling efforts on water transport through the membrane can be classified into three types: diffusive, chemical potential and hydraulic models. The diffusive model can be explained with dilute solution theory by considering the

membrane as solvent while water and proton as solute. This theory assumes that the interaction between different solute species can be neglected, and only the interaction between solute (water and proton) and solvent (membrane) is considered. Then the flux of solute species in solvent can be described by using the Nernst-Planck equation. Nernst-Planck equation is a conservation of mass describing the flux of ions under the influence of both an ionic concentration gradient and an electric field. The general form of Nernst-Planck equation is:

$$\frac{dc_i}{dt} = \nabla(D_i \nabla c_i - \mathbf{u} c_i + \frac{D_i z_i e}{k_B} c_i \nabla \phi) \quad (2-4)$$

where  $t$  (s) is time,  $D_i$  ( $\text{m}^2 \text{s}^{-1}$ ) is the diffusivity of the solute specie  $i$ ,  $c_i$  ( $\text{mol m}^{-3}$ ) is the concentration of the solute specie  $i$ ,  $\mathbf{u}$  ( $\text{m s}^{-1}$ ) is the velocity of the fluid,  $z_i$  is the valence of ionic specie  $i$ ,  $e$  ( $1.60218 \times 10^{-19}$  C) is elementary charge,  $k_B$  ( $1.3806505 \times 10^{-23}$  J K $^{-1}$ ) is the Boltzmann constant,  $T$  (K) is temperature.

For water transport,  $\frac{D_i z_i e}{k_B} c_i \nabla \phi$  becomes zero because water is in zero valence. For proton transport,  $D_i \nabla c_i$  becomes zero by assuming constant concentration of proton through the membrane. Furthermore,  $uc_i$  becomes zero for both the water and proton transport due to the fact that the membrane does not move. Therefore, the Nernst-Planck equation for proton transport is simplified to Ohm's law [74],

$$i = -\sigma_M \nabla \phi \quad (2-5)$$

By further considering the effect of electro-osmotic drag, the water transport is simplified to [74]:

$$J_w = D_M \nabla c_w + n_{drag} \frac{i}{F} \quad (2-6)$$

where  $\sigma_M$  ( $\Omega^{-1}$ ) is the membrane conductivity,  $\nabla \phi$  (V) is the potential,  $D_M$  ( $\text{m}^2 \text{s}^{-1}$ ) is the diffusivity of water through the membrane,  $n_{drag}$  is electro-osmotic drag coefficient through membrane,  $c_w$  ( $\text{mol m}^{-3}$ ) is water concentration,  $F$  (C mol $^{-1}$ ) is Faraday's constant,  $i$  (A m $^{-2}$ ) is the current density.

The diffusive model is the most successful model for water transport through membrane since its initial application by Springer *et al.* [35, 36]. By further considering the interaction between different solute species, the chemical potential model is developed. The proton and water transport through membrane is therefore can be explained by concentrated solution theory [75, 76] as,

$$i = -\sigma_M \nabla \phi - \frac{n_{drag} \sigma_M}{F} \nabla \Pi_H \quad (2-7)$$

$$J_w = -\alpha_w \nabla \Pi_w + n_{drag} \frac{i}{F} \quad (2-8)$$

where  $\Pi_H$  ( $\text{J mol}^{-1}$ ) and  $\Pi_w$  ( $\text{J mol}^{-1}$ ) are the chemical potential of proton and water, respectively.  $\alpha_w$  is water transport coefficient through membrane.

Comparing Eq. (2-5) with Eq. (2-7) and Eq. (2-6) with Eq. (2-8), it can be noticed that the concentration ( $c$ ) is replaced by chemical potential ( $\Pi$ ), the diffusion coefficient ( $D$ ) is replaced by transport coefficient ( $\alpha$ ), and one more term is added in Eq. (2-7) to account for the multi-component interaction. The biggest obstacle of the widespread use of chemical potential model is the difficulty in obtaining the transport parameters. As a result, the chemical potential model is less popular than the diffusive model.

In the diffusive and chemical potential models, the convective transport caused by pressure gradient across membrane is not considered. However, the convective transport could happen when water enlarges the pores of the membrane. To fill the gap, the hydraulic model is developed [37, 38] according to two assumptions:

- (1) The membrane is assumed to be fully hydrated to allow the maximum possible convective transport.
- (2) Constant gas volume fraction in membrane is assumed.

Consequently, water flux due to pressure gradient and electro-osmotic drag can be calculated by Nernst-Planck equation. Generally, the hydraulic model neglects the diffusive transport, and the water flux can be represented by the follow equation

$$J_w = -c_w \frac{k_p}{\mu_w} \nabla p_w + n_{drag} \frac{i}{F} \quad (2-9)$$

where  $k_p$  ( $\text{m}^2$ ) and  $\mu_w$  (Pa s) are the permeability and dynamic viscosity of water in membrane. Due to the effect of electro-osmotic drag, the anode side of the membrane is often prone to dry out. Therefore, the fully hydrated membrane assumption remains questionable. In fact, water convective transport is only considerable while the pressure gradient exists between the anode and cathode. If the inlet gas pressure of anode is as same as that of cathode, the water convective transport could be neglect because diffusive transport and electro-osmotic drag have bigger influence on the water transport. The merits and demerits of these three types of models are summarised in [Table 2-2](#).

Table 2-2 Comparison between the water transport models

<i>Model</i>	<i>Merits</i>	<i>Demerits</i>
Diffusion model- Springer <i>et al.</i> [35, 36]	<ul style="list-style-type: none"> <li>1. Membrane conductivity was associated with water content.</li> <li>2. Capable of determining the membrane conductivity in moderate and high hydration cases.</li> </ul>	<ul style="list-style-type: none"> <li>1. Lack of accuracy at very low membrane water content.</li> <li>2. Failed to describe the water concentration through the membrane in case of saturation.</li> <li>3. Restricted to Nafion® membrane.</li> </ul>
Chemical potential model- Weber and Newman [75]	<ul style="list-style-type: none"> <li>1. The frictional forces on species motion were considered.</li> <li>2. The electrostatic interactions were taken into account.</li> <li>3. Both the pressure and activity are incorporated as the driving force.</li> <li>4. Bridging the gap between the single phase and two phase models</li> </ul>	<ul style="list-style-type: none"> <li>1. A multitude of parameters.</li> <li>2. Difficulty in obtaining the values of the parameters.</li> <li>3. Complicated boundary conditions.</li> <li>4. Only works on Nafion® membrane.</li> </ul>
Hydraulic model- Bernardi and Verbrugge [37, 38]	<ul style="list-style-type: none"> <li>1. Both the pressure and electric potential forces were included in the driving force.</li> <li>2. Electro-osmotic drag, back diffusion and hydraulic permeation were all considered for water transport through the membrane.</li> </ul>	<ul style="list-style-type: none"> <li>1. Requiring the values of the membrane parameters.</li> <li>2. Impossible to account for the membrane structure.</li> <li>3. The chemical interaction between water and membrane materials was not considered.</li> </ul>

### 2.3.2 Modelling of water transport in porous electrodes

A variety of different models have been developed for modelling the water transport in the porous electrodes, including gas diffusion layers and catalyst layers. Depending on the assumption of the morphology of the porous electrodes, the models can be categorised into two groups, namely homogenous and non-homogenous models. In the homogenous models, the porous electrodes are assumed to be constructed by

homogeneous materials, while the non-homogenous model applies real or simplified micro-structure of the porous electrodes. When the porous electrodes are assumed as homogeneous, the entire computational domain shares the same properties, such as conductivity, permeability and porosity. The overall effect of micro-structure is usually reflected by the effective coefficient. Thus, the geometry generation and model solving process are greatly simplified and result in an easier model development and lower requirement of the computer hardware. The drawback of this assumption is the lack of precision about the detailed process within the porous electrodes, such as nucleation water. The modelling works before 2000s usually adopts the homogeneous assumption [33-47].

The gas diffusion layer is typically made up of three-dimensional random carbon fibre and its real structure is highly anomalous [77-79]. In order to accurately simulate the electrochemical reactions and transport processes occurred in a real or simplified gas diffusion layer, e.g. the liquid water formation and transport, numerous models have been developed [16, 24, 27, 57, 58, 71, 72, 80-83]. The volume of fluid (VOF) model [24, 27, 57, 58, 71, 72, 80] and Lattice Boltzmann (LB) model [16, 81-84] are the two types of the most popular models for liquid water transport in the gas diffusion layers. In this literature review, the VOF model is presented as an example. Under isothermal condition, by omitting the phase change and electrochemical reaction, the VOF model with two phases, reactant gas and liquid water, can be presented by the following conservation equations.

Conservation of mass for the two-phase mixture:

$$\frac{\partial}{\partial t} \rho + \nabla(\rho \mathbf{u}) = 0 \quad (2-10)$$

Conservation of momentum for the two-phase mixture:

$$\frac{\partial}{\partial t} (\rho \mathbf{u}) + \nabla(\rho \mathbf{u} \mathbf{u}) = -\nabla p + \mu \nabla(\nabla \mathbf{u} + \nabla \mathbf{u}^T) - \frac{2}{3} \mu \nabla(\nabla \mathbf{u}) + S_u \quad (2-11)$$

Conservation of momentum for the liquid water only:

$$\frac{\partial}{\partial t} (\rho s_l) + \nabla(\rho s_l \mathbf{u}) = 0 \quad (2-12)$$

where  $\rho$  ( $\text{kg}\cdot\text{m}^{-3}$ ) and  $\mu$  ( $\text{kg}\cdot\text{m}^{-1}\cdot\text{s}^{-1}$ ) are the density and dynamic viscosity of the two-phase mixture, respectively, and they are the volume averaged values. The volume averaged density and viscosity can be described as follow:

$$\rho = s_g \rho_g + s_l \rho_l \quad (2-13)$$

$$\mu = s_g \mu_g + s_l \mu_l \quad (2-14)$$

$$s_g + s_l = 1 \quad (2-15)$$

where  $s$  is the volume fraction, and the subscript  $l$  and  $g$  represent the liquid and gas phases, respectively.

In the momentum equation Eq. (2-11),  $S_u$  ( $\text{kg m}^{-2} \text{s}^{-2}$ ) is the source term accounting for the surface tension effect, which can be calculated as

$$S_u = \gamma \frac{2\chi\rho\nabla s_g}{(\rho_g + \rho_l)} \quad (2-16)$$

where  $\gamma$  ( $\text{N}\cdot\text{m}^{-1}$ ) is the surface tension coefficient between the two phases, and  $\chi$  ( $\text{m}^{-1}$ ) is the surface curvature defined as

$$\chi = \nabla[\vec{v}_w \cos(\theta) + \vec{\tau}_w \sin(\theta)] \quad (2-17)$$

where  $\vec{v}_w$  and  $\vec{\tau}_w$  ( $\text{m s}^{-1}$ ) are the unit vectors normal and tangential to the wall surface, and  $\theta(^{\circ})$  is the contact angel.

Note that the shape of the interface between the two phases at the wall depends on the wettability of the wall. By using the VOF model in a micro-structure of the gas diffusion layers, the movement of liquid water under the effect of pressure gradient and contact angel can be observed [80]. Figure 2-6 shows the transient liquid water discharging from the gas diffusion layer with the pressure gradient of  $6.5\times 10^5 \text{ Pa m}^{-1}$  and contact angel of  $135^{\circ}$ . It can be observed that liquid water is removed under a pressure gradient and finally only a small amount of liquid water is left in the GDL.

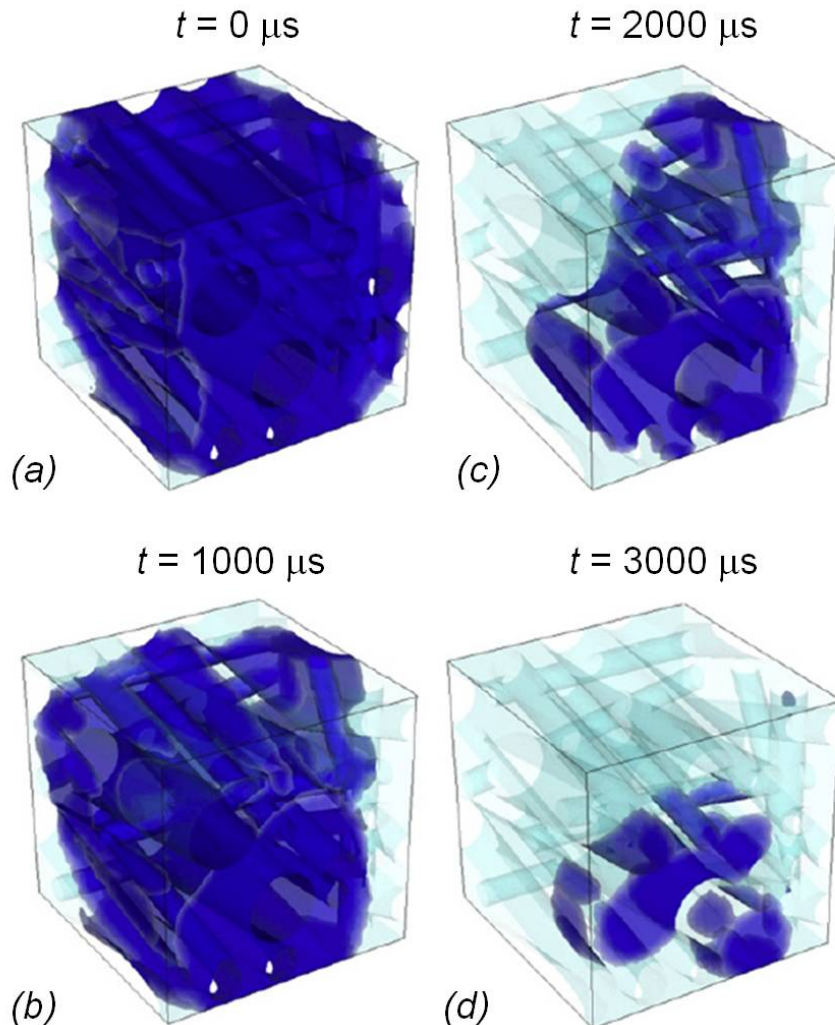


Figure 2-6 Transient liquid water discharging from GDL obtained from VOF model [80]

(Pressure gradient is  $6.5 \times 10^5 \text{ Pa m}^{-1}$  and the contact angle is  $135^\circ$ )

Catalyst layer is the core of the PEMFC in which electrochemical reaction occurred. The catalyst layers are prepared by spraying the catalyst particle (such as Pt-Ru alloy) contained ink onto the carbon paper. The difference between the catalyst layer and gas diffusion layer is that the catalyst particle is surrounded by the carbon fibre in the catalyst layers and result in much small pores than that of the gas diffusion layers. Therefore, the VOF model is hard to be applied to the micro-structure of the catalyst layers [77]. The general process of the electrochemical reaction includes two steps, diffusion and reaction. First of all, the reactants must transport through the porous media and reach the surface of the catalyst particles. Then the reactants are absorbed on the surface of the catalyst particle where products are generated via chemical reactions. Finally, the products generated on the surface of the catalyst particle must move away.

The models mentioned previously applied a variety of approaches to describe the catalyst layer. Depending on the degree of complexity, these approaches can be categorised into three groups. In the simplest approach, the catalyst layers are treated as reactive boundaries between the gas diffusion layer and membrane [54, 85]. For example, Jeng *et al.* [85] developed a simple two-dimensional across-the-channel model to study the mass transport of the reactant gases through the gas diffusion layers. The effectiveness of the gas diffusion layers was evaluated under different current densities and an optimal thickness of the cathode gas diffusion layer was suggested. Berning *et al.* [54] developed a three-dimensional, non-isothermal model to investigate the temperature distribution in the MEA. However, the catalyst layers were treated as one-dimensional boundaries in this model. It is important to notice that this kind of approach always over estimate the current density due to the ignorance of the mass transport resistance in the catalyst layer.

The second approach assumes the catalyst layer as a thin film fully flooded with liquid water or ionomer. This approach is adopted in the model developed by Marr and Li [48], in which the void space within the cathode catalyst layer was fully occupied by liquid water. This model can give a reasonable simulation on the cell performance during higher current densities. However, it underestimated the cell performance during lower current densities due to an increase in mass transport within the catalyst layer.

In the last approach, the catalyst layer is assumed as a porous two and a three-dimensional domain filled with catalyst particles agglomerate. The void spaces within the agglomerates (inter-agglomerate space) and between the agglomerates (outer-agglomerate space) are defined as the primary and secondary pores, respectively. Both the primary and secondary pores can be filled with ionomer, liquid water, and reactants. The models applied this approach is called the agglomerate models, which can be further subcategorised into three sub-groups namely slab, cylindrical and spherical agglomerate models [78] as shown in Figure 2-7.

In order to give a more accurate simulation on the diffusion-reaction process occurred in the catalyst layer, agglomerate models are usually preferred. In the agglomerate models, the catalyst particles, ionomer and void space are assumed to be homogeneously mixed to form the micrometre agglomerates. In the spherical agglomerate model, the diameter of the agglomerate is less than 10  $\mu\text{m}$  [79].

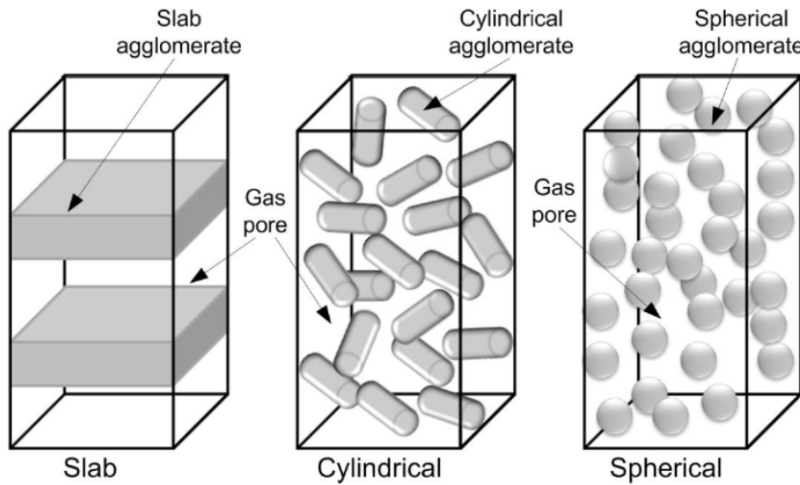


Figure 2-7 Schematic representation of the agglomerate catalyst layer

Due to the fact that the sluggish oxygen reduction reaction (ORR) occurred at the cathode, the agglomerate models are therefore usually adopted in the cathode catalyst layer. At cathode, the rate expression of oxygen reduction can be presented as:

$$R_{O_2} = k_{O_2} c_{O_2} \quad (2-18)$$

In order to account for the mass transport from the outer boundary to the centre of the agglomerates, the effectiveness factor,  $E_r$ , is introduced into Eq. (2-18) as follow:

$$R_{O_2} = E_r k_{O_2} c_{O_2} \quad (2-19)$$

where

$$E_r = \frac{1}{\Phi_L} \left( \frac{1}{\tanh(3\Phi_L)} - \frac{1}{\Phi_L} \right), \quad \Phi_L = \frac{R_{agg}}{3} \sqrt{\frac{k_{O_2}}{D_{eff}}} \quad (2-20)$$

The effectiveness factor can be considered as an indicator of catalyst utilisation.

By the effort of the agglomerate model, the ORR kinetics is simulated quantitatively. As the production of ORR, the amount of water can be therefore calculated.

## 2.4 Flow field design

There are mainly four types of typical flow fields, namely parallel (conventional), serpentine, interdigitated and pin-type, employed in the practical applications. The features and differences are shown in Figure 2-8 as follow:

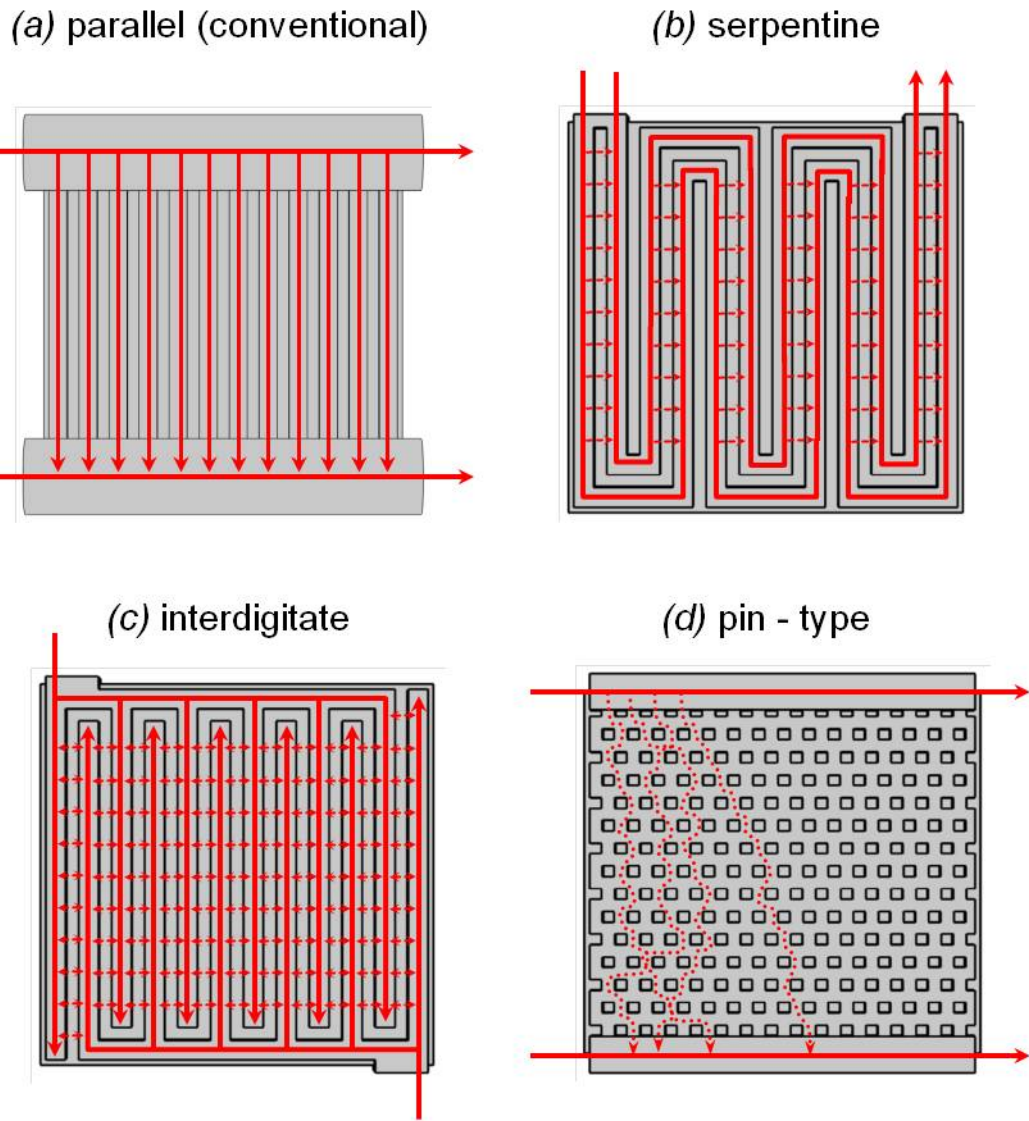


Figure 2-8 Four types of typical flow field designs [14]

In the parallel flow field, diffusion is the dominant mechanism for the transport of reactants and products. The conventional flow field is an energy saving design because very low inlet pressure is required for the gas flow at the inlet. However, the accumulation of reactant gas and liquid water are prone to occur because the transport rate is limited by diffusion. The parallel flow field is popular due to its simple mass transport mechanism and low inlet pressure requirement.

In the serpentine flow field, the pressure and concentration of the reactant gas decrease along the flow channel from the inlet to the outlet. If the channel cross-section is small while the channel length is very long, the pressure drop between the adjacent channels becomes substantial, significant pressure gradient is therefore set up across the porous electrode, much larger than the pressure gradient along the flow channel,

resulting in a considerable cross leakage flow between the adjacent channels. This significant cross leakage flow through the porous electrode induces a strong convection in the electrode, resulting in a reinforced transport of the reactant gas to the catalyst layer for electrochemical reaction and an accelerated moving of product water from the active sites of catalyst layer to the flow channels. Therefore, this flow field design with a convective feature is most widely used and shows the most interesting of industrial collaboration. However, serpentine flow channel design is not the ideal flow field configuration due to a number of problems. For example, the substantial pressure drop due to the relatively long reactant flow path in the serpentine flow channel, which is considered as a significant power loss.

The flow channel design is a dead-end mode in the interdigitated flow field. When the reactant gases feed into the flow channel, they cannot flow out along-the-channel directly but flow through the porous gas diffusion layers. Therefore, the transport mechanism is converted from a diffusion mechanism to a forced convection mechanism. The shear force resulted from the gas flow helps to flush liquid water out of the electrode, thus effectively reducing the water flooding and significantly improving the cell performance [86]. However, higher inlet pressure is needed for gas flowing through the gas diffusion layers, which leads to a significant power loss.

The pin-type flow filed is a commonly utilised configuration, which provides random and multiple flow paths to the reactant gases. Therefore, one of the outstanding advantages of the pin-type flow filed is the low pressure drop between the inlet and the outlet. However, non-uniform flow and stagnant areas tend to occur at various places of the channels [87]. This significantly decreases the reactants transport efficiency and thus the overall fuel cell performance.

As stated by Liu *et al.* [11], an appropriate flow field design improves the reactant transport and the efficiency of the thermal and water management. The optimised flow filed is capable of reducing the activation polarisation and internal ohmic losses. The fuel cells with a parallel and an interdigitated flow fields were firstly experimentally compared by Nguyen [12] in 1996 and numerically compared by Kazim *et al.* [13] in 1999, respectively. They found that, as a new flow filed design, the interdigitated flow fields improve the fuel cell performance by enhancing the oxygen transport and reinforcing the water removal from the catalyst layer under forced gas convection. Four different flow filed designs including parallel, interdigitated, serpentine and pin-type,

were numerically compared by a three-dimensional model developed by Sousa *et al.* [14]. The serpentine flow fields with different dimensions were further studied and optimised by the experiment and model of Liu *et al.* [11]. The effect of different channel shapes on pressure drop, oxygen distribution, liquid water formation and transport, as well as fuel cell performance were studied in recent years [15, 16].

## 2.5 Experimental measurement and visualisation of liquid water

Liquid water formation and transport can be observed directly or indirectly by experimental measurement including direct visualisation, nuclear magnetic resonance (NMR) imaging, beam interrogation and fluorescence microscopy.

Direct visualisation has the advantage of providing high resolution image of water transport in flow channels. Transparent flow channels are required when optical devices, such as high-speed camera [49, 50], infrared cameras [88] and charge-coupled device (CCD) cameras [89], are applied. It is useful to observe the effect of operating conditions on the formation, growth and movement of the droplet. For example, as shown in Figure 2-9, Hussaini and Wang [90] applied an operating fuel cell with a transparent flow channel of cathode to observe the liquid water flooding on the surface of the gas diffusion layer and in the flow channel. The two-phase transport, in the form of droplet, film and slug, is occurred in micro-channels of the PEMFC. However, the direct visualisation technique always provides images of liquid water in flow channels only because of the opaque materials of the gas diffusion layers and catalyst layers.

NMR is widely used in water visualisation by measuring the emitted signal from the excited H nuclei in an external magnetic field in PEMFC with opaque structures. This technique has successfully detected liquid water in the flow channels of an operating PEMFC. For example, Minard *et al.* [91] observed the dehydration of the membrane by employing the NMR technique. However, the NMR technique can only be used to observe water in the membrane rather than within paramagnetic materials like carbon. As a result, water content in the gas diffusion layers and catalyst layers is impossible to be detected by this technique.

Neutron imaging, electron microscopy and X-rays are the three frequently employed techniques included in the beam interrogation. The principle of neutron imaging is based on the sensitive response of neutrons to hydrogen-containing compounds such as water [92]. This technique provides in-situ analysis on an operating PEMFC, such as

visualisation of water accumulation and distribution of water in the cathode porous electrodes and flow channels. The drawback of this technique, which limits the widespread application, is the high cost and the availability of radiation equipment that provides a neutron source. As shown in [Figure 2-10](#), electron microscopy can be used to observe vapour condensation and liquid water morphology in porous gas diffusion layers and catalyst layers [77, 93]. Moreover, the X-ray image technique can give the temporal and spatial resolution of water formation and transport inside a PEMFC. These two techniques all show strong potential for the visualisation of water.

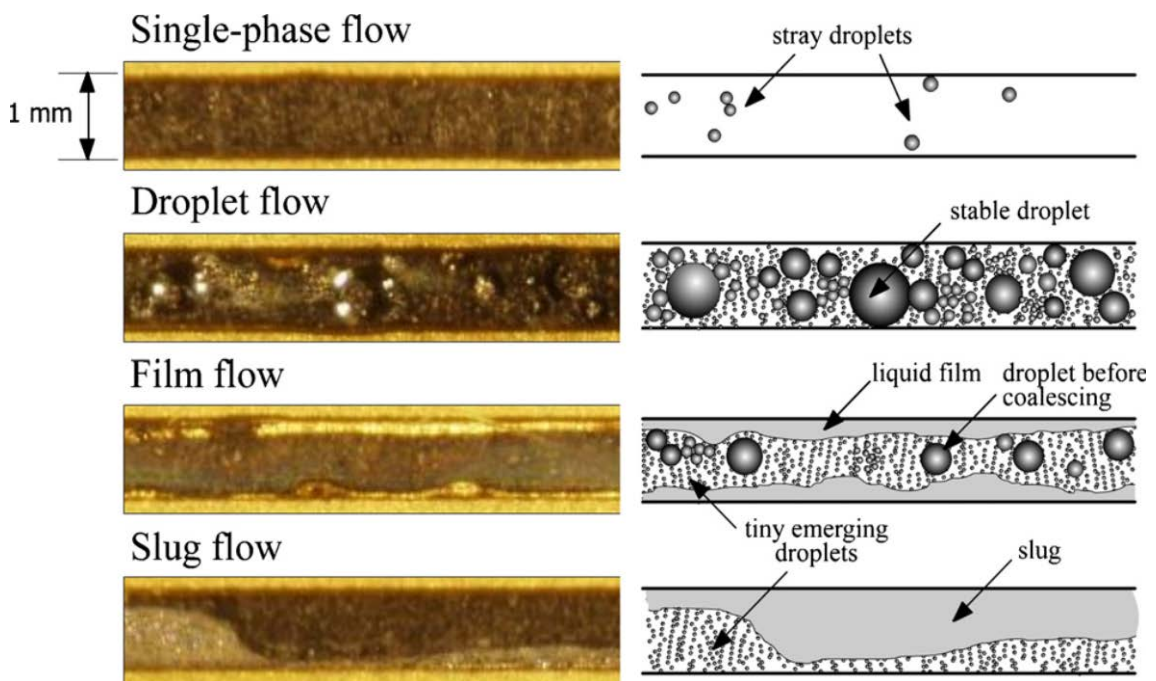
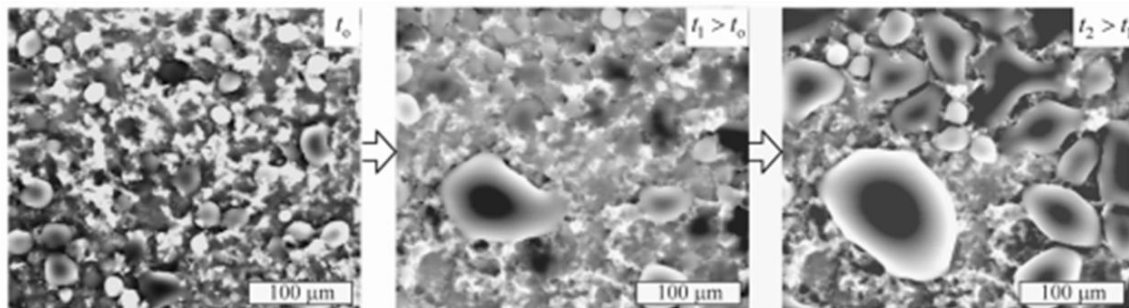


Figure 2-9 Magnified view of flow patterns in channels captured by the high resolution Olympus video microscope and the illustrations of liquid water generation and distribution [90]

Fluorescence microscopy is one of the important techniques for detecting the water in a PEMFC. This technique is based on the phenomenon that certain material, such as H nuclei, emits energy detectable as visible light when irradiated with the light of a specific wavelength. Fluorescence microscopy in conjunction with optical photography provides a method to visualise the micro-scale transport of liquid water on the surface of gas diffusion layers [94] and the dynamic water droplet behaviour emerging from the gas diffusion layers into flow channels [95].

(a) Water vapour condensation and liquid water breakthrough in catalyst layer



(b) Water vapour condensation and liquid water breakthrough in gas diffusion layer

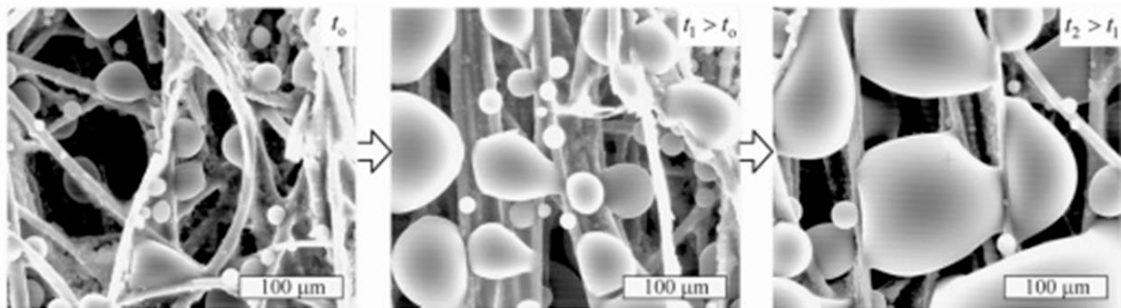


Figure 2-10 ESEM micrographs of vapour condensation and liquid water breakthrough in electrode [77]

The overview of the different visualisation techniques is summarised in [Table 2-3](#).

Table 2-3 Water visualisation techniques and their applications

Water visualisation techniques	Type of visualisation	Basic principle	Scope of application
Direct visualization	Direct	Optical photography	Transparent flow channels
NMR	Indirect	The spin of nuclei in an external magnetic field	Flow channels and membrane
Beam interrogation	Indirect	The sensitive response of neutrons to hydrogen-containing compounds	GDL, CL and membrane
Fluorescence microscopy	Indirect	Certain material emits energy detectable as visible light when irradiated with the light of a specific wavelength	GDL

## 2.6 Overview of PEMFC numerical optimisation

Numerical optimisation has been an active research area since 1960s [96]. It has been used in many applications, such as, structural [97], aerospace [98] and automotive engineering [99]. The common principle of the numerical optimisation is to efficiently

search for an optimal design in a coupled mathematical algorithm with the aid of a computational analysis tool. Only a few designs need to be evaluated using the optimisation algorithm, the computational time is therefore reduced. Optimal design helps the researchers to create a new design or improve an existing one. In order to account for the inter-relationship between various parameters and optimise several objectives simultaneously in a fuel cell design, a multi-objective optimisation is always used. A mathematical formulation of such a problem is given by:

$$\begin{aligned}
 & \text{Maximise or minimise} && \mathbf{J}(\mathbf{x}) = [J_1, J_2, J_3, \dots, J_n]^T \\
 & \text{W.R.T} && x_k \quad \text{for } k = 1, 2, 3, \dots, n \\
 & \text{Subject to:} && h_i(\mathbf{x}) = 0 \quad \text{for } i = 1, 2, 3, \dots, p \\
 & && g_i(\mathbf{x}) \leq 0 \quad \text{for } i = 1, 2, 3, \dots, q \\
 & && \mathbf{x}_L \leq \mathbf{x} \leq \mathbf{x}_U
 \end{aligned} \tag{2-21}$$

where  $\mathbf{J}(\mathbf{x})$  is the vector of objectives. In fuel cell design, the objective can be cost, performance, durability and others, which is represented by  $J_i$  individually.  $x_k$  is known as the design variables, which are related to objective vector,  $\mathbf{J}(\mathbf{x})$ .  $\mathbf{x}_L$  and  $\mathbf{x}_U$  are the lower and upper bounds of design variable  $x_k$ .  $h_i(\mathbf{x})$  and  $g_i(\mathbf{x})$  are the design constraints.

Design of fuel cells is a challenging endeavour because a multitude of physical and chemical phenomena need to be optimised simultaneously to achieve the best performance. Normally, it requires the evaluation of a set of possible designs. Due to the fact that the number of possible design increases sharply as the number of design variables increase. For example, the number of possible is  $10^5$  for a design with ten variables and five possibilities per variable. It is impossible to evaluate all possible designs. As a result, some design variables have to be constrained as constants to reduce the number of possible designs. This is the so-called sub-optimal design. The sub-optimal designs in fuel cell optimisation mainly focus on the following aspects: flow field design, electrode design, operating condition optimisation and fuel cell stack optimisation. Similarly, the optimisation has to mainly concentrate on limited important objectives, while ignoring other design objectives.

The first efforts in the flow field design and optimisation were published in 2004 by Grujicic *et al.* [100]. The unique optimisation objective was to maximise the current density at a cell voltage of 0.7 V with an interdigitated flow field. The design parameters included cathode pressure inlet, cathode gas diffusion layer thickness, the width and ratio of gas channel and current collector. However, all design variables reached the bounds in the optimal design. In 2006, Lin *et al.* [101] optimised the channel width ratio, porosities of gas diffusion layers and catalyst layers using a gradient-based optimisation algorithm (simplified conjugate gradient method). The optimal channel width ratio of 0.54, GDL porosity of 0.6 and CL porosity of 0.3 were obtained in the optimisation results.

Song *et al.* [5, 6] are considered as the pioneers of optimisation of the fuel cell electrode using numerical optimisation approach. The catalyst layer composition was optimised in order to achieve the maximum current density at the cell voltage of 0.6 V. The design variables were ionomer volume fraction, platinum loading and the thickness of the catalyst layer. The optimal distributions of Nafion® ionomer and platinum were obtained. The optimisation results indicated that the optimal ionomer loading was around 30 wt. % [5], and the electrode performance was improved by placing more ionomer and platinum near the membrane [6]. Secanell *et al.* optimised both platinum loading and performance of a complete MEA [7] based on the previously developed optimisation framework [102]. The design variables included platinum loading, ionomer loading, GDL porosity and platinum mass ratio. Figure 2-11 shows that the cell performance was improved using the parameters obtained from the optimal design. The optimisation results showed that the platinum loading had to be controlled within the range of 0.1 to 0.5 mg cm<sup>-2</sup>, as higher loading resulted in a waste of platinum rather than an increase in current density.

The improved cell performance can be achieved with higher operating temperature, inlet pressure and stoichiometric flow ratio [103-105]. Consequently, both an accurate fuel cell model and a complete fuel cell system model have to be coupled in the optimisation of operating conditions. Otherwise, the optimisation algorithm would always choose the higher values of the operating parameters [106]. The pioneering efforts in the operating conditions optimisation can be found in 2000 by Mawardi *et al.* [107]. The objective was to maximise the power density at a fixed current density. The design variables included operating temperature, pressures of anode and cathode, mole

fractions of the gas inlet, stoichiometry and relative humidity. Minimising membrane hydration, maximising temperature rise and cell voltage were the additional constraints. The optimisation results indicated that the optimal operating conditions strongly depend on the current densities. Wu *et al.* [108] optimised the efficiency of the fuel cell system at low, medium and high current densities. The design variables used were the operating temperature, pressure of cathode gas inlet, stoichiometry and relative humidity. The optimisation results suggested that, for a realistic system, the optimal cathode stoichiometry was between 1.25 and 2, cathode pressure between 1.5 and 3 atm, and cathode relative humidity between 10% and 15%.

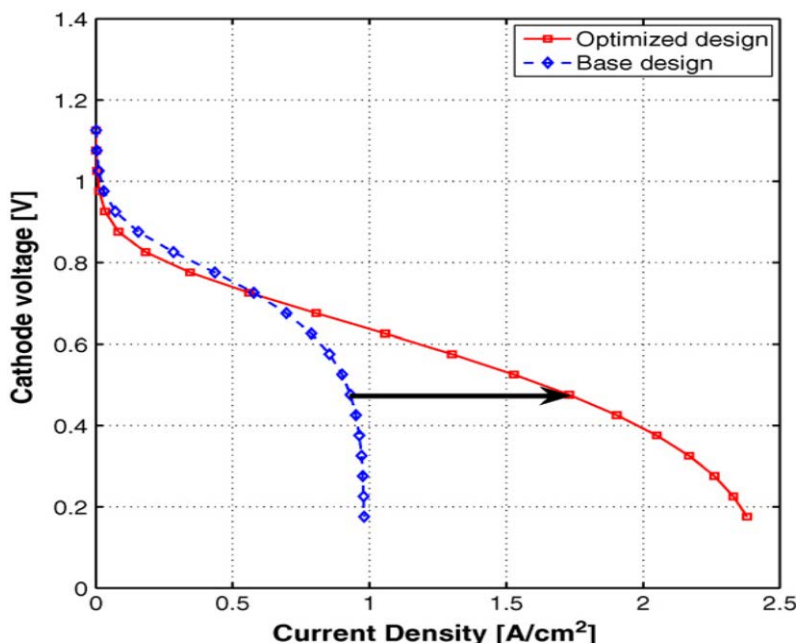


Figure 2-11 Polarisation curves of the base design and optimal design at the cell voltage of 0.476 V [102]

Fuel cell stack optimisation has received little attention compared with the flow field design, electrode design and operating condition optimisation. In the fuel cell stack, the clamping load applied to a PEM fuel cell stack is considered as the most important effect on fuel cell performance due to the influence on electron transfer, mass and thermal transport [109]. Zhou *et al.* [110] proposed a finite element method (FEM) in a developed two-phase flow model to study the effect of cathode gas diffusion layer deformation on the fuel cell polarisation curves. The modelling results showed that an optimal compression deformation exists when the contact resistance was considered. Mohamed and Jenkins [111] optimised the number of cells in series based on a simplified zero dimensional, isothermal fuel cell stack model, in which the optimisation objective was to maximise the power output. Recently, Zhou *et al.* [112] developed a

cold start model for PEM fuel cells aimed at optimising the start-up methods. As a novel method, the variable heating and load control (VHLC) was proposed.

Numerical optimisation is able to provide insight for fuel cell design including cost reduction, performance improvement, and efficiency increase. As a relative new research area, numerical optimisation of needed fuel cells has attracted the growing interest.

## 2.7 Anode flooding and effect of operating conditions on cell performance

Three phases of water co-exist in PEMFCs: as vapour and liquid in porous electrodes and channels, and as a dissolved phase absorbed by membrane and ionomer (membrane and ionomer water uptake). Among three phases, dissolved water can migrate between the anode and cathode through the membrane under the driving forces of EOD (electro-osmotic drag), back diffusion and hydraulic permeation [113-115]. Liquid water can be generated in terms of water vapour condensation and membrane/ionomer desorption when over-saturated. Simultaneously, liquid water is removed from the MEA (membrane electrode assembly) generally by reactant gases flowing along-the-channels. If water generation rate is faster than the removal rate, excess water will accumulate in the electrodes and flow channels, leading to a water flooding inside the cell. This flooding can reduce the effective porosity in the porous media and increase the pressure drop along-the-channel, inhibiting the gas transport to the active sites in CLs (catalyst layers), finally resulting in a decline in the cell performance [116, 117]. Water flooding is typically observed at the cathode side due to the fact that water is produced inside the CCLs (cathode catalyst layers) by the ORR (oxygen reduction reaction).

There have been numerous studies of water flooding at the cathode but less consideration of water transport related to the anode. However, hydrogen consumption at the anode could also result in the humidified anode reactant gas becoming supersaturated with water vapour, which can result in transfer to liquid water after condensation. Liquid water movement in hydrophilic and hydrophobic anode gas channel, as well as the effect of hydrogen inlet velocity, operating temperature and channel walls wettability, was numerically studied by Ferreira et al. [118]. Experimental studies have detected liquid water in the anode and that more liquid water was observed at a high anode relative humidity [119, 120]. An in-situ detection scheme of anode flooding, developed by O'Rourke et al. [121], showed that anode flooding could be

detected prior to a rapid cell voltage decline, which was considered as an early warning of cathode catalyst damage. As reported by Anderson et al. [122], AWR (anode water removal) could be used as a diagnostic tool to assess cathode water flooding in PEM fuel cells.

The operating conditions interactively affect the water balance in the fuel cell and ultimately the cell performance [123]. During PEM fuel cells operation, temperature, pressure, stoichiometric flow ratio and humidification condition are the most common parameters that can affect performance and thus need to be carefully considered when applying specific MEA (membrane electrode assembly) and flow field design. Without considering the durability of fuel cell component materials, higher operating temperature is desirable due to the positive impact of temperature on various transport, kinetic and phasetransfer processes [124, 125]. However, high temperature condition is a significant challenge for practical fuel cells as it can lead to the mechanical and chemical failure of Nafion® membrane [126]. In addition, the increased WCC (water carrying capacity) of gas at high operating temperature may lead to reactant gas starvation, especially in the case of fully humidified inlet gas at the cathode [127].

High operating pressure is capable of increasing the fuel cell open circuit potential (Nernst equation), exchange current density and gas-pair diffusivity due to the increased partial pressure of the reactant gases at both the anode and cathode [128, 129]. Therefore, improved fuel cell performance is normally achieved when operating at higher pressure, especially at higher cathode pressure [130]. High cell performance is obtainable at high operating pressures but the net system efficiency may be lower on account of the power needed for air compression. Moreover, high back pressure is a challenge of the mechanical strength and safety issues of fuel cell unit.

RH also significantly affects the electrode degradations. Specifically, Pt particle growth [131], effective Pt surface area loss [132], carbon corrosion rate [133], are generally accelerated under increased RH. On the contrary, the effect of humidification conditions on membrane degradation is complex. Increasing RH can increase the membrane gas crossover, which then accelerates electrode degradation due to partial fuel starvation [134, 135]. However, inadequate moisture membrane content at low RH also results in detrimental impacts on membrane degradation [136]. Thus, an optimal RH is required to prolong the dynamic lifetime of fuel cells. Generally, relative high stoichiometric flow ratio is required to avoid reactant gas dilution/starvation and to

guarantee the uniform distribution of the reactant gas at the GDL-channel boundary along-the-channel. Low cathode stoichiometric flow ratio may lead to oxygen starvation on the reaction zone, resulting in the cell voltage undershoot during load change which accelerates the electrode degradation [137]. Higher cathode stoichiometric flow ratio is also of benefit to improving the liquid water removal rate inside the channel [138]. The cell performance is therefore improved due to the increased volume fraction of reactant gas and reduced mass transport resistance.

## 2.8 Conclusions

Water formation and transport mechanisms and the negative effect of liquid water flooding on the fuel cell performance are overviewed and the mathematical models for water formation and transport are chronologically summarised in this chapter. Based on the water formation mechanism and the water transport processes described, the models for water transport through the Nafion® membrane are mainly categorised as three types: diffusion models, chemical potential models and hydraulic models. The merit and demerit of each type of models are compared in this chapter. For the water transport through the Nafion® membrane, a model accounted for the electro-osmotic drag (EOD), back diffusion and hydraulic permeation will be developed.

The oxygen oxidation reaction (ORR) at the cathode is one of the main sources for liquid water generation. In order to accurately simulate the ORR inside the porous catalyst layer, the agglomerate model has to be adopted. Liquid water movement through the porous electrodes, including catalyst layers and gas diffusion layers, can be simulated by the volume of fluid (VOF) model and Lattice Boltzmann (LB) model. The VOF model and the agglomerate model will be combined to provide an effective way for modelling the liquid water formation and transport through the porous electrodes.

Liquid water formation and movement can be experimentally detected and observed. The basic principles and scopes of each visualisation techniques are concluded and compared. In addition, different flow field designs are introduced and compared. Anode flooding may occur when hydrogen consumption rate is faster than the water migration rate. Because hydrogen consumption at the anode could lead to the humidified anode reactant gas supersaturated with water vapour, which transfers to liquid water after condensation. The effect of operation conditions, including temperature, pressure, relative humidity, stoichiometric flow ratio, is summarised.

The fuel cell performance can be improved by optimising the composition of the electrode and operating conditions. Fuel cell optimisations in terms of flow field design, electrode design, operating condition optimisation and fuel cell stack optimisation are overviewed. The property and composition of the cathode catalyst layer plays an important role in determining the fuel cell performance.

## 2.9 References

1. Mehta, V. and J.S. Cooper, *Review and analysis of PEM fuel cell design and manufacturing*. Journal of Power Sources, 2003. **114**: p. 32-53.
2. Sharma, S. and B.G. Pollet, *Support materials for PEMFC and DMFC electrocatalysts- A review*. Journal of Power Sources, 2012. **208**: 96-119.
3. Aiyejina, A. and M.K.S Sastry, *PEMFC flow channel geometry optimization: A review*. Journal of Fuel Cell Science and Technology, 2012. **9**: 011011-1-011011-24.
4. Scott, K. and A.K. Shukla, *Direct Methanol Fuel Cells: Fundamentals, problems and perspectives*. in R.E. White (editor), *Modern aspects of electrochemistry*, New York: Springer; 2007. **40**: p. 127-218.
5. Song, D., Q. Wang, Z. Liu, T. Navessin, M. Eikerling and S. Holdcroft, *Numerical optimisation study of the catalyst layer of PEM fuel cell cathode*. Journal of Power Sources, 2004. **126**: p. 104-111.
6. Song, D., Q. Wang, Z. Liu, T. Navessin and S. Holdcroft, *Numerical study of PEM fuel cell cathode with non-uniform catalyst layer*. Electrochimica Acta, 2004. **50**: p. 731-737.
7. Secanell, M., R. Songprakorp, A. Suleman and N. Djilali, *Multi-objective optimisation of a polymer electrolyte fuel cell membrane electrode assembly*. Energy & Environmental Science. 2008, 1: p.378-388.
8. Secanell, M., R. Sonprakorp, N. Djilali and A. Suleman, *Optimisation of a proton exchange membrane fuel cell membrane electrode assembly*. Structural and Multidisciplinary Optimisation. 2010, **40**: p. 563-583.
9. Jeon, D.H., K.N. Kim, S.M. Baek and J.H. Nam, *The effect of relative humidity of the cathode on the performance and uniformity of PEM fuel cells*. International Journal of Hydrogen Energy, 2011. **36**: 12499-12511.

10. Kim, Y.B., *Study on the effect of humidity and stoichiometry on the water saturation of PEM fuel cells.* International Journal of Energy Research, 2012. **36:** 509-522.
11. Liu, H., P. Li and K. Wang, *Optimization of PEM fuel cell flow channel dimensions- Mathematic modelling analysis and experimental verification.* International Journal of Hydrogen Energy, 2013. **38:** p. 9835-9846.
12. Nguyen, T.V., *A gas distributor design for proton exchange membrane fuel cells.* Journal of Electrochemical Society, 1996. **143:** L103-L105.
13. Kazim, A., H.T. Liu and P. Forges, *Modelling of performance of PEM fuel cells with conventional and interdigitated flow fields.* Journal of Applied Electrochemistry, 1999. **29:** 1409-1416.
14. Sousa, T., M. Mamlouk, K. Scott and C.M. Rangel, *Three-dimensional model of a high temperature PEMFC. Study of the flow field effect on performance.* Fuel Cells, 2012. **12:** 566-576.
15. Akhtar, N., A. Qureshi, J. Scholta, C. Hartnig, M. Messerschmidt and W. Lehnert, *Investigation of water droplet kinetics and optimisation of channel geometry for PEM fuel cell cathodes.* International Journal of Hydrogen Energy, 2009. **34:** 3104-3111.
16. Salah, Y.B., Y. Tabé and T. Chikahisa, *Gas channel optimisation for PEM fuel cell using the lattice Boltzmann method.* Energy Procedia, 2012. **28:** 125-133.
17. Ji, M. and Z. Wei, *A Review of Water Management in Polymer Electrolyte Membrane Fuel Cells.* Energies, 2009. **2:** p. 1057-1106.
18. Nguyen, T.V. and M.W. Knobbe, *A liquid water management strategy for PEM fuel cell stacks.* Journal of Power Sources, 2003. **114:** p. 70-79.
19. Canut, J.M.L., R.M. Abouatallah and D.A. Harrington, *Detection of membrane drying, fuel cell flooding, and anode catalyst poisoning on PEMFC stacks by electrochemical impedance spectroscopy.* Journal of Electrochemical Society, 2006. **153:** p. A857-A864.
20. Hickner, M.A., C.H. Fujimoto and C.J. Cornelius, *Transport in sulfonated poly(phenylene)s: Proton conductivity, permeability, and the state of water.* Polymer , 2006. **47:** p. 4238-4244.

21. Stumper, J., M. Lohr and S. Hamada, *Diagnostic tools for liquid water in PEM fuel cells*. Journal of Power Sources, 2005. **143**: p. 150-157.
22. Barbir, F., H. Gorgun and X. Wang, *Relationship between pressure drop and cell resistance as a diagnostic tool for PEM fuel cells*. Journal of Power Sources, 2005. **141**: p. 96-101.
23. Natarajan, D. and T.V. Nguyen, *Current distribution in PEM fuel cells. Part I: Oxygen and fuel flow rate effects*. AIChE Journal, 2005. **51**: p. 2587-2598.
24. Meng, H. and C.Y. Wang, *New model of two-phase flow and flooding dynamics in polymer electrolyte fuel cells*. Journal of Electrochemical Society, 2005. **152**: p. A1733-A1741.
25. Janssen, G.J.M. and M.L.J. Overvelde, *Water transport in the proton-exchange-membrane fuel cell: measurements of the effective drag coefficient*. Journal of Power Sources, 2001. **101**: p. 117-125.
26. Sridhar, P., *Humidification studies on polymer electrolyte membrane fuel cell*. Journal of Power Sources, 2001. **101**: p. 72-78.
27. Wang, Y. and C.Y. Wang, *Dynamics of polymer electrolyte fuel cells undergoing load changes*. Electrochimica Acta, 2006. **51**: p. 3924-3933.
28. Li, C.C. and P.G. Pickup, *Dependence of electrode overpotentials in PEM fuel cells on the placement of the reference electrode*. Electrochemical and Solid-State Letters, 2006. **9**: p. A249-A251.
29. Okada, T., *Theory for water management in membranes for polymer electrolyte fuel cells: Part I. The effect of impurity ions at the anode side on the membrane performances*. Journal of Electroanalytical Chemistry, 1999. **465**: p. 1-17.
30. Knights, S.D., K.M. Colbow, J. St-Pierre and D.P. Wilkinson, *Aging mechanisms and lifetime of PEFC and DMFC*. Journal of Power Sources, 2004. **127**: p. 127-134.
31. Sinha, P.K. and C.Y. Wang, *Probing effects of GDL microstructure on liquid water transport by pore network modeling*. ECS Transactions, 2006. **3**: p. 387-396.
32. Kumbur, E.C., K.V. Sharp and M.M. Mench, *Validated Leverett approach for multiphase flow in PEFC diffusion media: III. temperature effect and unified approach*. Journal of Electrochemical Society, 2007. **154**: p. B1315-B1324.

33. Natarajan, D. and T.V. Nguyen, *A two-dimensional, two-phase, multicomponent, transient model for the cathode of a proton exchange membrane fuel cell using conventional gas distributors*. Journal of Electrochemical Society, 2001. **148**: p. A1324–A1335.
34. Berg, P., K. Promislow, J. St-Pierre, J. Stumper and B. Wetton, Water management in PEM fuel cells. Journal of Electrochemical Society, 2004. **151**: p. A341-A353.
35. Springer, T.E., T.A. Zawodzinski and S. Gottesfeld, *Polymer electrolyte fuel cell model*. Journal of Electrochemical Society, 1991. **138**: p. 2334-2342.
36. Springer, T.E., M.S. Wilson and S. Gottesfeld, *Modeling and experimental diagnostics in polymer electrolyte fuel cells*. Journal of Electrochemical Society, 1993. **4**: p. 3513-3526.
37. Bernardi, D.M. and M.W. Verbrugge, *A mathematical model of the solid-polymer-electrolyte fuel cell*. Journal of Electrochemical Society, 1992. **139**: p. 2477–2491.
38. Bernardi, D.M. and M.W. Verbrugge, *Mathematical model of a gas diffusion electrode bonded to a polymer electrolyte*. AIChE Journal, 1991. **37**: p. 1151-1163.
39. Nguyen, T.V. and R. E. White, *A water and heat management model for proton-exchange-membrane fuel cells*. Journal of Electrochemical Society, 1993. **140**: p. 2178-2186.
40. Fuller, T.F. and J. Newman, *Water and thermal management in solid-polymer-electrolyte fuel cells*. Journal of Electrochemical Society, 1993. **140**: p. 1218-1225.
41. Yi, J.S. and T.V. Nguyen, *An along-the-channel model for proton exchange membrane fuel cells*. Journal of Electrochemical Society, 1998, **145**: p. 1149-1159.
42. Yi, J.S. and T.V. Nguyen, *Multicomponent transport in porous electrodes of proton exchange membrane fuel cells using the interdigitated gas distributors*. Journal of Electrochemical Society, 1999. **146**: p. 38-45.
43. Gurau, V, H. Liu and S. Kakac, *Two-dimensional model for proton exchange membrane fuel cells*. AIChE Journal, 1998. **44**: p. 2410-2422.
44. Gloaguen, F. and R. Durand, *Simulations of PEFC cathodes: an effectiveness factor approach*. Journal of Applied Electrochemistry, 1997. **27**: p. 1029-1035.

45. Bultel, Y., P. Ozil and R. Durand, *Modelling the mode of operation of PEMFC electrodes at the particle level: influence of ohmic drop within the active layer on electrode performance*. Journal of Applied Electrochemistry, 1998. **28**: p. 269-276.
46. Bultel, Y., P. Ozil and R. Durand, *Modified thin film and agglomerate models for active layers of P.E. fuel cells*. Electrochimica Acta, 1998. **43**: p. 1077-1087.
47. Bultel, Y., P. Ozil and R. Durand, *Modelling of mass transfer within the PEM fuel cell active layer: limitations at the particle level*. Journal of Applied Electrochemistry, 1999. **29**: p. 1025-1033.
48. Marr, C. and X. Li, *Composition and performance modelling of catalyst layer in a proton exchange membrane fuel cell*. Journal of Power Sources, 1999. **77**: p. 17-27.
49. Spernjak, D., A.K. Prasad and S.G. Advani, *Experimental investigation of liquid water formation and transport in a transparent single-serpentine PEM fuel cell*. Journal of Power Sources, 2007. **170**: p. 334-344.
50. Tuber, K., D. Pocza and C. Hebling, *Visualization of water buildup in the cathode of a transparent PEM fuel cell*. Journal of Power Sources, 2003. **124**: p. 403-414.
51. Dutta, S., S. Shimpalee and J.W. Van-Zee, *Three-dimensional numerical simulation of straight channel PEM fuel cells*. Journal of Applied Electrochemistry, 2000. **30**: p. 135-146.
52. Dutta, S., S. Shimpalee and J. W. Van-Zee, *Numerical prediction of mass-exchange between cathode and anode channels in a PEM fuel cell*. International Journal of Heat and Mass Transfer, 2001. **44**: p. 2029-2042.
53. Zhou, T. and H. Liu, *A general three-dimensional model for proton exchange membrane fuel cells*. International Journal of Transport Phenomena, 2001. **3**: p. 177-198.
54. Berning, T., D.M. Lu and N. Djilali, *Three-dimensional computational analysis of transport phenomena in a PEM fuel cell*. Journal of Power Sources, 2002. **106**: p. 284-294.
55. Mazumder, S. and J.V. Cole, *Rigorous 3-D mathematical modeling of PEM fuel cells: I model predictions without liquid water transport*. Journal of Electrochemical Society, 2003. **150**: p. A1503-1503.

56. Lee, W.K., S. Shimpalee and J.W. Van-Zee, *Verifying predictions of water and current distributions in a serpentine flow field polymer electrolyte membrane fuel cell*. Journal of Electrochemical Society, 2003. **150**: p. A341-A348.
57. Um S. and C.Y. Wang, *Three-dimensional analysis of transport and electrochemical reactions in polymer electrolyte fuel cells*. Journal of Power Sources, 2004. **125**: p. 40-51.
58. Wang, Y. and C.Y. Wang, *Transient analysis of polymer electrolyte fuel cells*. Electrochimica Acta, 2005. **50**: p. 1307-1315.
59. Liu, Z., Z. Mao, C. Wang, W. Zhuge and Y. Zhang, *Numerical simulation of a mini PEMFC stack*. Journal of Power Sources, 2006. **160**: p. 1111-1121.
60. Shimpalee, S., S. Greenway, D. Spuckler and J.W. Van-Zee. *Predicting water and current distributions in a commercial-size PEMFC*. Journal of Power Sources, 2004. **135**: p. 79-87.
61. Ju, H., H. Meng and C.Y. Wang, *A single-phase, non-isothermal model for PEM fuel cells*. International Journal of Heat and Mass Transfer, 2005. **48**: p. 1303-1315.
62. Wang, Y. and C.Y. Wang, *Ultra large-scale simulation of polymer electrolyte fuel cells*. Journal of Power Sources, 2006. **153**: p. 130-135.
63. He, W., J.S. Yi and T.V. Nguyen, *Two-phase flow model of the cathode of PEM fuel cells using interdigitated flow fields*. AIChE Journal, 2000. **46**: p. 2053-2064.
64. Lin, G. and T.V. Nguyen, *A two-dimensional two-phase model of a PEM fuel cell*. Journal of the Electrochemical Society, 2006. **153**: p. A372-A382.
65. Natarajan, D. and T.V. Nguyen, *Three-dimensional effects of liquid water flooding in the cathode of a PEM fuel cell*. Journal of Power Sources, 2003. **115**: p. 66-80.
66. Ye, Q. and T.V. Nguyen, *Three-dimensional simulation of liquid water distribution in a PEMFC with experimentally measured capillary functions*. Journal of the Electrochemical Society, 2007. **154**: p. B1242-B1251.
67. Sui, P.C., S. Kumar and N. Djilali, *Advanced computational tools for PEM fuel cell design: Part I. Development and base case simulations*. Journal of Power Sources, 2008. **180**: p. 410-422.

68. Sui, P.C., S. Kumar and N. Djilali, *Advanced computational tools for PEM fuel cell design: Part II. Detailed experimental validation and parametric study.* Journal of Power Sources, 2008. **180**: p. 423-432.
69. Berning, T. and N. Djilali, *A 3D, multiphase, multicomponent model of the cathode and anode of a PEM fuel cell.* Journal of Electrochemical Society, 2003. **150**: p. A1589-A1598.
70. Mazumder, S. and J.V. Cole, *Rigorous 3-D mathematical modeling of PEM fuel cells: II. model predictions with liquid water transport.* Journal of Electrochemical Society, 2003. **150**: p. A1510-A1517.
71. Basu, S., J. Li and C.Y. Wang, *Two-phase flow and maldistribution in gas channels of a polymer electrolyte fuel cell.* Journal of Power Sources, 2009. **187**: p. 431-443.
72. Wang, Y., S. Basu and C.Y. Wang, *Modeling two-phase flow in PEM fuel cell channels.* Journal of Power Sources, 2008. **179**: p. 603-617.
73. Quan, P., B. Zhou, A. Sobiesiak and Z. Liu, *Water behaviour in serpentine micro-channel for proton exchange membrane fuel cell cathode.* Journal of Power Sources, 2005. **152**: p. 131-145.
74. Newman, J.S., *Electrochemical system.* 2nd ed. Englewood Cliffs: Prentice Hall; 1991.
75. Weber, Z. and J. Newman, *Transport in polymer-electrolyte membranes. I. Pyhyssical Model.* Journal of Electrochemical society, 2003. **150**: p. A1108-A1115.
76. Pintauro, P.N. and D.N. Bennion, *Mass transport of electrolytes in membrane I: development of mathematical transport model.* Industrial and Engineering Chemistry Fundamentals, 1984. **23**: p. 230-234.
77. Nam, J.H. and M. Kaviany, *Effective diffusion and water-saturation distribution in single- and two-layer PEMFC diffusion medium.* International Journal of Heat and Mass Transfer, 2003. **46**: p.4595-4611
78. Sun, W., B.A. Peppley and K. Karan, *An improved two-dimensional agglomerate cathode model to study the influence of catalyst layer structural parameters.* Electrochimica Acta, 2005. **50**: p. 3359-3374.

79. Das, P.K., X. Li and Z.S. Liu, *A three-dimensional agglomerate model for the cathode catalyst layer of PEM fuel cells*. Journal of Power Sources, 2008. **179**: p. 186-199.
80. Park, J.W., K. Jiao and X. Li, *Numerical investigation on liquid water removal from the porous gas diffusion layer by reactant flow*. Applied Energy, 2010. **87**: p. 2180-2186.
81. Wang, L.-P. and B. Afsharpooya, *Modeling fluid flow in fuel cells using the lattice-Boltzmann approach*. Mathematics and Computer in Simulation, 2006. **72**: 242-248.
82. Park, J., M. Matsubara and X. Li, *Application of lattice Boltzmann method to a micro-scale flow simulation in the porous electrode of a PEM fuel cell*. Journal of Power Sources, 2007. **173**: 404-414.
83. Delavar, M.A., M. Farhadi and K. Sedighi, *Numerical simulation of direct methanol fuel cells using lattice Boltzmann method*. International Journal of Hydrogen Energy, 2010. **35**: 9306-9317.
84. Gao, Y., X.X. Zhang, P.Rama, Y. Liu, R. Chen, H. Ostadi and K. Jiang, *Modeling fluid flow in the gas diffusion layers in PEMFC using the multiple relaxation-time Lattice Boltzmann method*. Fuel Cells, 2012. **12**: p. 365-381.
85. Jeng, K.T., S.F. Lee, G.F. Tsai and C.H. Wang, *Oxygen mass transfer in PEM fuel cell gas diffusion layers*. Journal of Power Sources, 2004, **138**: p. 41-50.
86. Wood, D.L., J.S. Yi and T.V. Nguyen, *Effect of direct liquid water injection and interdigitated flow field on the performance of proton exchange membrane fuel cell*. Electrochimica Acta, 1998. **43**: p. 3795-3809.
87. Guo, N., M.C. Leu and U.O. Koju, *Network based optimization model for pin-type flow field of polymer electrolyte membrane fuel cell*. International Journal of Hydrogen Energy, 2013. **38**: 6750-6761.
88. Hakenjos, H. Muenter, U. Wittstadt and C. Hebling, *A PEM fuel cell for combined measurement of current and temperature distribution, and flow field flooding*. Journal of Power Sources, 2004. **131**: p. 213-216.
89. Zhang, F.Y., X.G. Yang and C.Y. Wang, *Liquid water removal from a polymer electrolyte fuel cell*. Journal of Electrochemical Society, 2006. **153**: p. A225-A232.

90. Hussaini, I.S. and C.Y. Wang, *Visualization and quantification of cathode channel flooding in PEM fuel cells*. Journal of Power Sources, 2009. **187**: p. 444-451.
91. Minard, K., V. Viswanathan, P. Majors, L. Wang and P. Rieke, *Magnetic resonance imaging (MRI) of PEM dehydration and gas manifold flooding during continuous fuel cell operation*. Journal of Power Sources, 2006. **161**: p. 856-863.
92. Satija, R., D. Jacobson, M. Arif and S. Werner, *In situ neutron imaging technique for evaluation of water management systems in operating PEM fuel cells*. Journal of Power Sources, 2004. **129**: p. 238-245.
93. Nam, J.H., K.J. Lee, G.S. Hwang, C.J. Kim and M. Kaviany, *Microporous layer for water morphology control in PEMFC*. International Journal of Heat and Mass Transfer, 2009. **52**: p. 2779-2791.
94. Bazylak, A., D. Sinton, Z.S. Liu and N. Djilali, *Effect of compression on liquid water transport and microstructure of PEMFC gas diffusion layers*. Journal of Power Sources, 2007. **163**: p. 784-792.
95. Bazylak, A., D. Sinton and N. Djilali, *Dynamic water transport and droplet emergence in PEMFC gas diffusion layers*. Journal of Power Sources, 2008. **176**: p. 240-246.
96. Arora, J.S. and Q. Wang, *Review of formulations for structural and mechanical system optimisation*. Structural and Multidisciplinary Optimization, 2005. **30**: p. 251-272.
97. Evgrafov, A., M. Patriksson and J. Petersson, *Stochastic structural topology optimisation: existence of solution and sensitivity analyses*. Journal of Applied Mathematics and Mechanics, 2003. **83**: p. 479-492.
98. Secanell, M. and A. Suleman, *Numerical evaluation of optimisation algorithms for low-Reynolds-number aerodynamic shape optimisation*. AIAA Journal, 2005. **43**: p. 2262-2267.
99. Bendsoe, M. and O. Sigmund, Topology Optimisation, 2<sup>nd</sup> edition, Springer-Verlag, 2003.
100. Grujicic, M. and K.M. Chittajallu, *Design and optimisation of polymer electrolyte membrane (PEM) fuel cells*. Applied Surface Science, 2004. **227**: p. 56-72.

101. Lin, H.-H., C.-H. Cheng, C.-Y. Soong, F. Chen and W.-M. Yan, *Optimisation of key parameters in the proton exchange membrane fuel cell*. Journal of Power Sources, 2006. **162**: 246-254.
102. Secanell, M., K. Karan, A. Suleman and N. Djilali, *Multi-variable optimization of PEMFC cathodes using an agglomerate model*. Electrochimica Acta, 2007. **52**: p. 6318-6337.
103. Kazim, A., P. Forges and H.T. Liu, *Effects of cathode operating conditions on performance of a PEM fuel cell with interdigitated flow field*. International Journal of Energy Research, 2003. **27**: p. 401-414.
104. Kim, S., S. Shimpalee and J.W. Van-Zee, *The effect of stoichiometry on dynamic behaviour of a proton exchange membrane fuel cell (PEMFC) during load change*. Journal of Power Sources, 2004. **135**: p. 110-121.
105. Amirinejad, M., S. Rowshanzamir and M.H. Eikani, *Effect of operating parameters on performance of a proton exchange membrane fuel cell*. Journal of Power Sources, 2006. **161**: p. 872-875.
106. Wishart, J., Z. Dong and M. Secanell, *Optimisation of a PEM fuel cell system based on empirical data and a generalised electrochemical semi-empirical model*. Journal of Power Sources, 2006. **161**: p. 1041-1055.
107. Mawardi, A., F. Yang and R. Pitchumani, *Optimisation of the operating parameters of a proton exchange membrane fuel cell for maximum power density*. Journal of Fuel Cell Science and Technology, 2005. **2**: p. 121-135.
108. Wu, J., Q. Liu and H. Fang, *Toward the optimisation of operating conditions for hydrogen polymer electrolyte fuel cells*. Journal of Power Sources, 2006. **156**: p. 388-399.
109. Zhang, W. and C.-W. Wu, *Effect of clamping load on the performance of proton exchange membrane fuel cell stack and its optimisation design: A review of modelling and experimental research*. Journal of Fuel Cell Science and Technology, 2014. **11**: p. 021012-1 - 021012-11.
110. Zhou, P., C.W. Wu and G.J. Ma, *Numerical study on the compression effect of Gas Diffusion Layer on PEMFC Performance*. Journal of Power Sources, 2007. **170**: p. 93-100.

111. Mohamed, I. and N. Jenkins, *Proton exchange membrane (PEM) fuel cell stack configuration using genetic algorithms*. Journal of Power Sources, 2004. **131**: p. 142-146.
112. Zhou, Y., Y. Luo, S. Yu and K. Jiao, *Modelling of cold start processes and performance optimisation for proton exchange membrane fuel cell stacks*. Journal of Power Sources, 2014. **247**: p. 738-748.
113. Ge, S., X. Li, B. Yi and I.M. Hsing, *Absorption, desorption, and transport of water in polymer electrolyte membranes for fuel cells*. Journal of Electrochemistry Society, 2005. **152**: p. A1149-A1157.
114. Wu, H., P. Berg and X. Li, *Steady and unsteady 3D non-isothermal modeling of PEM fuel cells with the effect of non-equilibrium phase transfer*. Applied Energy, 2010. **87**: p. 2778-2784.
115. Yang, X.G., Q. Ye and P. Cheng, *Matching of water and temperature fields in protonexchange membrane fuel cells with non-uniform distributions*. International Journal of Hydrogen Energy, 2011. **36**: p. 12524-12537.
116. Das, P.K., X. Li and Z.S. Liu, *Analysis of liquid water transport in cathode catalyst layer of PEM fuel cells*. International Journal of Hydrogen Energy, 2010. **35**: p. 2403-2416.
117. Meng, H. and C.Y. Wang, *Model of two-phase flow and flooding dynamics in polymer electrolyte fuel cells*. Journal of Electrochemistry Society, 2005. **152**: p. A1733-A1741.
118. Ferreira R.B., D.S. Falcao, V.B. Oliveira and A.M.F.R. Pinto, *Numerical simulation of twophase flow in an anode gas channel of a proton exchange membrane fuel cell*. Energy, 2015. **82**: p. 619-628.
119. Wong, K.H., K.H. Loo, Y.M. Lai, S.C. Tan and C.K. Tse, *A theoretical study of inlet relative humidity control in PEM fuel cell*. International Journal of Hydrogen Energy, 2011. **36**: p. 11871-11885.
120. Iranzo, A., P. Boillat, J. Biesdorf and A. Salva, *Investigation of the liquid water distribution in a 50 cm<sup>2</sup> PEM fuel cell: effects of reactants relative humidity, current density, and cathode stoichiometry*. Energy, 2015. **82**: p. 914-921.
121. O'Rourke, J., M. Ramani and M. Arcak, *In situ detection of anode flooding of a PEM fuel cell*. International Journal of Hydrogen Energy, 2009. **34**: p. 6765-6770.

122. Anderson, R., M. Blanco, X. Bi and D.P. Wilkinson, *Anode water removal and cathode gas diffusion layer flooding in a proton exchange membrane fuel cell*. International Journal of Hydrogen Energy, 2012. **37**: p. 16093-16103.
123. Li, H., Y. Tang, Z. Wang, Z. Shi, S. Wu, D. Song et al., *A review of water flooding issues in the proton exchange membrane fuel cell*. Journal of Power Sources, 2008. **178**: p. 103-117.
124. Djilali, N., *Computational modelling of polymer electrolyte membrane (PEM) fuel cells: challenges and opportunities*. Energy, 2007. **32**: p. 269-280.
125. Siegel, C., *Review of computational heat and mass transfer modelling in polymer-electrolyte-membrane (PEM) fuel cells*. Energy, 2008. **33**: p.1331-1352.
126. Shao, Y., G. Yin, Z. Wang and Y. Gao, *Proton exchange membrane fuel cell from low temperature to high temperature: material challenges*. Journal of Power Sources, 2007. **167**: p. 235-242.
127. Xing, L., X. Liu, T. Alaje, R. Kumma, M. Mamlouk, K. Scott, *A two-phase flow and non-isothermal agglomerate model for a proton exchange membrane (PEM) fuel cell*. Energy, 2014. **73**: p. 618-634.
128. Wang, L., A. Husar, T. Zhou and H. Liu, *A parametric study of PEM fuel cell performances*. International Journal of Hydrogen Energy, 2003. **28**: p. 1263-1272.
129. Berning, T and N. Djilali, *Three-dimensional computational analysis of transport phenomena in a PEM fuel cell e a parametric study*. Journal of Power Sources, 2003. **124**: p. 440-452.
130. Xing, L., M. Mamlouk and K. Scott, *A two-dimensional agglomerate model for a proton exchange membrane fuel cell*. Energy, 2013. **61**: p. 196-210.
131. Borup, R.L., J.R. Davey, F.H. Garzon, D.L. Wood and M.A. Inbody, *PEM fuel cell electrocatalyst durability measurements*. Journal of Power Sources, 2006. **163**: p. 76-81.
132. Bi, W., Q. Sun, Y. Deng and T.F. Fuller, *The effect of humidity and oxygen partial pressure on degradation of Pt/C catalyst in PEM fuel cell*. Electrochimica Acta, 2009. **54**: p. 1826-1833.

133. Lim, K.H., H.S. Oh, S.E. Jang, Y.J. Ko, H.J. Kim and H. Kim H, *Effect of operating conditions on carbon corrosion in polymer electrolyte membrane fuel cells*. Journal of Power Sources, 2009. **193**: p. 575-579.
134. Inaba, M., T. Kinumoto, M. Kiriakie, R. Umebayashi, A. Tasaka and Z. Ogumi, *Gas crossover and membrane degradation in polymer electrolyte fuel cells*. Electrochimica Acta, 2006. **51**: p. 5746-5753.
135. Chen, J., J.B. Siegel, T. Matsuura and A.G. Stefanopoulou, *Carbon corrosion in PEM fuel cell dead-ended anode operation*. Journal of Electrochemistry Society, 2011. **158**: p. B1164-B1174.
136. Panha, K., M. Fowler, X. Yuan and H. Wang, *Accelerated durability testing via reactants relative humidity cycling on PEM fuel cells*. Applied Energy, 2012. **93**: p. 90-97.
137. Qu, S., X. Li, M. Hou, Z. Shao and B. Yi, *The effect of air stoichiometry change on the dynamic behaviour of a proton exchange membrane fuel cell*. Journal of Power Sources, 2008. **185**: p. 302-310.
138. Zhang, F.Y., X.G. Yang and C.Y. Wang, *Liquid water removal from a polymer electrolyte fuel cell*. Journal of Electrochemistry Society, 2006. **153**: p. A225-A232.

## Chapter 3. Fundamentals, principles and governing equations

### 3.1 Introduction

The electrochemical and physical phenomena occurred in PEMFCs, including the polarisation curves, profiles of the reactant and product species, velocities of species, as well as the temperature distributions, can be described by coupling the electrode kinetics with the conservation equations of mass, momentum, energy and charge. In this chapter, the fundamentals, principles are given and the governing equations used in the model are presented.

### 3.2 Electrode kinetics

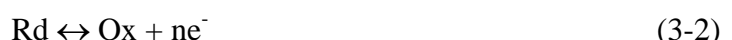
#### 3.2.1 Butler-Volmer kinetics

Fuel cells operation is based on the electrochemical reactions occurring simultaneously at the anode and cathode, which have been presented by Eq. (1-1) to Eq. (1-6) in Chapter 1. The reaction rate of an electrochemical reaction is defined as the speed of the electrochemical reaction proceeds on the electrode surface. Electrical current is generated by the electrons released and consumed in the electrochemical reaction processes. Current density is the current per unit surface area. According to Faraday's law, current density is proportional to the charge transferred and the consumption of reactants per unit area:

$$i = nFN_i \quad (3-1)$$

where  $n$  is the amount of substance,  $F$  (96385 C mol<sup>-1</sup>) is the Faraday's constant,  $N_i$  (mol m<sup>-2</sup> s<sup>-1</sup>) is the flux of reactant per unit area,  $i$  (A m<sup>-2</sup>) is the current density.

An electrochemical reaction involves either oxidation or reduction of reactant species. Typically, the oxidation process produces electrons while the reduction process consumes the electrons as follow:



On an electrode at equilibrium conditions (no external current is generated), both the oxidation and reduction processes occur at equal rates. The net current generated is the difference between the electrons released and consumed:

$$i = nF(k_f c_{Ox} - k_b c_{Rd}) \quad (3-3)$$

where  $k_f$  and  $k_b$  ( $s^{-1}$ ) are the forward (reduction) and backward (oxidation) reaction rate coefficient,  $c_{Ox}$  and  $c_{Rd}$  ( $\text{mol m}^{-2}$ ) are the surface concentration of the oxidised and reduced species, respectively. The reaction rate coefficient for an electrochemical reaction is a function of the Gibbs free energy as follow:

$$k_{f/b} = \frac{k_B T}{h} \exp\left(\frac{-\Delta G}{R_g T}\right) \quad (3-4)$$

where  $k_B$  ( $1.38 \times 10^{-23} \text{ J K}^{-1}$ ) is the Boltzmann's constant,  $h$  ( $6.626 \times 10^{-34} \text{ J s}$ ) is the Planck's constant,  $R_g$  ( $8.314 \text{ J mol}^{-1} \text{ K}^{-1}$ ) is the universal gas constant,  $T$  (K) is the temperature, and  $\Delta G$  ( $\text{J mol}^{-1}$ ) is the Gibbs free energy, which is considered to consist of both chemical and electrical terms. Consequently, for a reduction reaction:

$$\Delta G = \Delta G_{ch} + \alpha_{Rd} F \phi \quad (3-5)$$

and for an oxidation reaction:

$$\Delta G = \Delta G_{ch} - \alpha_{Ox} F \phi \quad (3-6)$$

where  $\Delta G_{ch}$  ( $\text{J mol}^{-1}$ ) is the Gibbs free energy of the chemical component,  $\phi$  (V) is the potential, and  $\alpha_{Rd}$  and  $\alpha_{Ox}$  are the transfer coefficient for reduction and oxidation reactions, respectively.

Note that in the case of multi-step electrochemical reactions,  $\alpha_{Rd} + \alpha_{Ox}$  is generally equal to  $n/v$ , where  $n$  is the number of electrons transferred in the overall reaction and  $v$  is the stoichiometric number. The forward and backward reaction rate coefficients in Eq. (3-3) are represented, respectively:

$$k_f = k_{0,f} \exp\left(\frac{-\alpha_{Rd} F \phi}{R_g T}\right) \quad (3-7)$$

$$k_b = k_{0,b} \exp\left(\frac{\alpha_{Ox} F \phi}{R_g T}\right) \quad (3-8)$$

Therefore, from Eq. (3-3) to Eq. (3-8), the net current expression is obtained:

$$i = nF[k_{0,f}c_{Ox} \exp\left(\frac{-\alpha_{Rd}F\phi}{R_gT}\right) - k_{0,b}c_{Rd} \exp\left(\frac{\alpha_{Ox}F\phi}{R_gT}\right)] \quad (3-9)$$

At equilibrium, the forward and backward reactions proceed simultaneously, generating zero net current. In this case, the current densities for both forward and backward reaction are equal.

$$i_0 = nFk_{0,f}c_{Ox} \exp\left(\frac{-\alpha_{Rd}F\phi_{eq}}{R_gT}\right) = k_{0,b}c_{Rd} \exp\left(\frac{-\alpha_{Ox}F\phi_{eq}}{R_gT}\right) \quad (3-10)$$

where  $i_0$  ( $\text{A m}^{-2}$ ) is the exchange current density,  $k_{0,f}$  and  $k_{0,b}$  ( $\text{s}^{-1}$ ) are the reaction rate constant of the forward and backward reaction at standard conditions (25 °C and atmospheric pressure),  $\phi_{eq}$  (V) is the equilibrium or reversible potential.

As described in [Chapter 1](#), the equilibrium potential for a hydrogen PEMFC anode is 0 V and for a DMFC is 0.03V, while the equilibrium potential for the cathode operated with oxygen is 1.229 V at standard conditions. By combining [Eq. \(3-9\)](#) and [Eq. \(3-10\)](#), a relationship between the current density and the overpotential is obtained, which is known as the Butler-Volmer (B-V) equation.

$$i = i_0[\exp\left(\frac{-\alpha_{Rd}F\eta}{R_gT}\right) - \exp\left(\frac{\alpha_{Ox}F\eta}{R_gT}\right)] \quad (3-11)$$

where  $\eta$  (V) is the overpotential, defined as the difference between the electrode potential and the equilibrium potential. The B-V equation is valid for both anode and cathode reaction in a PEMFC:

$$i_a = i_{0,a}[\exp\left(\frac{-\alpha_{Rd,a}F\eta_a}{R_gT}\right) - \exp\left(\frac{\alpha_{Ox,a}F\eta_a}{R_gT}\right)] \quad (3-12)$$

$$i_c = i_{0,c}[\exp\left(\frac{-\alpha_{Rd,c}F\eta_c}{R_gT}\right) - \exp\left(\frac{\alpha_{Ox,c}F\eta_c}{R_gT}\right)] \quad (3-13)$$

The anode overpotential is positive, which makes the first term in the bracket of [Eq. \(3-12\)](#) negligible and results in a negative sign of the anode current density obtained. Similarly, the cathode overpotential is negative, which makes the second term in the

bracket of Eq. (3-13) negligible and leads to a positive sign of the cathode current density.

### 3.2.2 Agglomerate kinetics

The electrochemical reactions, in which electrons, protons and gas are involved, only take place on the surface of the catalyst. Reactant gas transport through the micro pores within the catalyst layer, electrons travel through the electrically conductive solid, and protons migrate through the electrolyte. According to the functions of different component within the catalyst layer, the existence of triple phase boundaries (TPB) is needed [1], where the content of electrolyte (for proton transfer), void space (for gas transport) and platinum dispersed carbon (for catalysis and electron transfer) interact (see Figure 3-1).

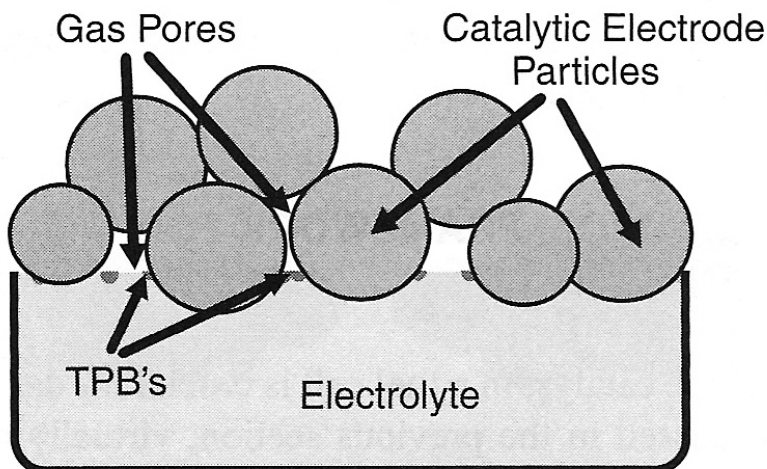


Figure 3-1 A simplified schematic diagram of the triple phase boundary (TPB) in a catalyst-electrolyte-pores interacted electrode [1]

In order to provide a more accurate description of the catalyst layer structure, the spherical agglomerate model is adopted, in which each agglomerate is assumed to consist of three components: platinum dispersed on carbon ( $Pt/C$ ), ionomer and void space. The void space within the agglomerate is defined as the primary pores and the void space between the agglomerate is defined as the secondary pores. The primary pores are partially occupied by the ionomer, whereas the secondary pores are partially occupied by the ionomer and liquid water surrounding the agglomerate. The structure of the catalyst layer is schematically represented in Figure 3-2. Reactant gas has to dissolve in the ionomer/water film before reaching the catalyst particles. Thus, the

simple Butler-Volmer relationship can't describe the kinetics, as the transport of the dissolved species in the ionomer/water film should be taken into account.

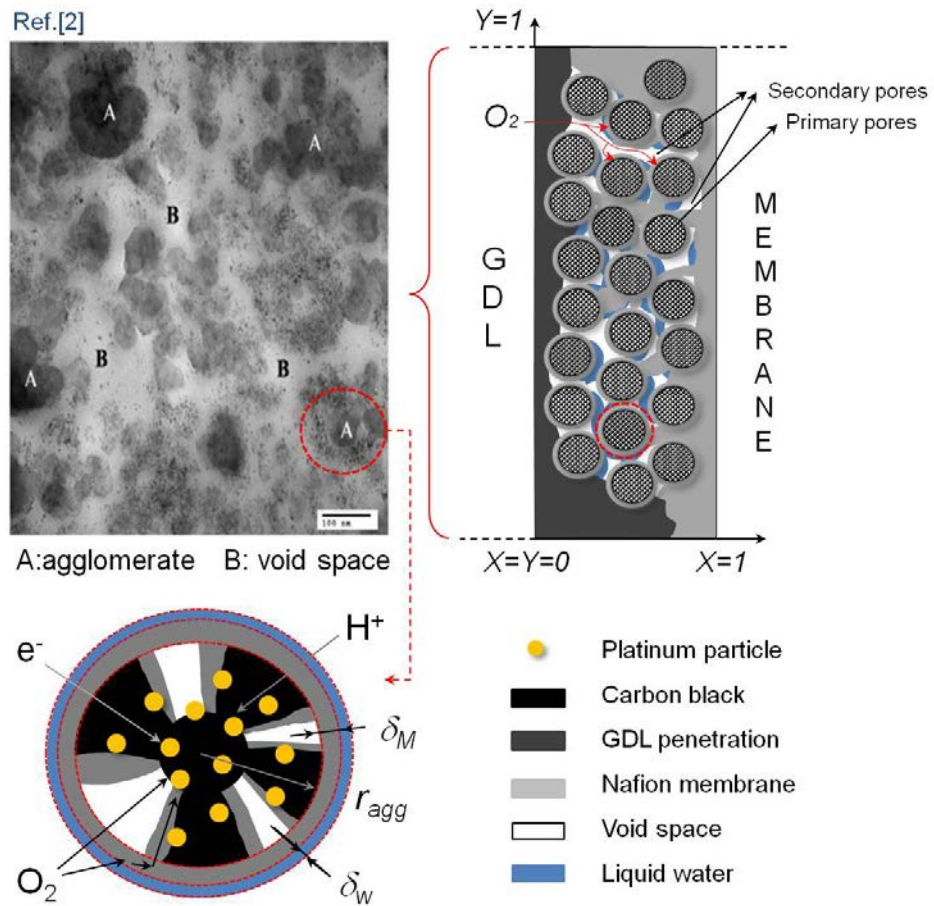


Figure 3-2 Sketch of the catalyst layer based on agglomerate assumption

In the agglomerate assumption, six key processes were included:

- Multicomponent diffusion of reactant gases;
- Reactant gases dissolution at the electrolyte/water film outer boundary;
- Diffusion of dissolved reactant gases through the electrolyte/water film;
- Diffusion of dissolved reactant gases within the agglomerate;
- Electrochemical reactions occurred on the *Pt/C* surface.
- Electrons and proton transport through the solid and electrolyte phases, respectively.

As shown in Figure 3-3, the concentration of the dissolved species at the outer and inner boundary of the ionomer/water film are represented by  $c_{i,out}$  and  $c_{i,in}$  ( $\text{mol m}^{-3}$ ),

respectively. The concentration of the dissolved species at the outer interface is described by Henry's law as:

$$c_{i,out} = \frac{p_i}{H_i} \quad (3-14)$$

where  $p_i$  (Pa) and  $H_i$  ( $\text{Pa m}^3 \text{ mol}^{-1}$ ) are the partial pressure and Henry's constant of reactant species  $i$ , respectively.

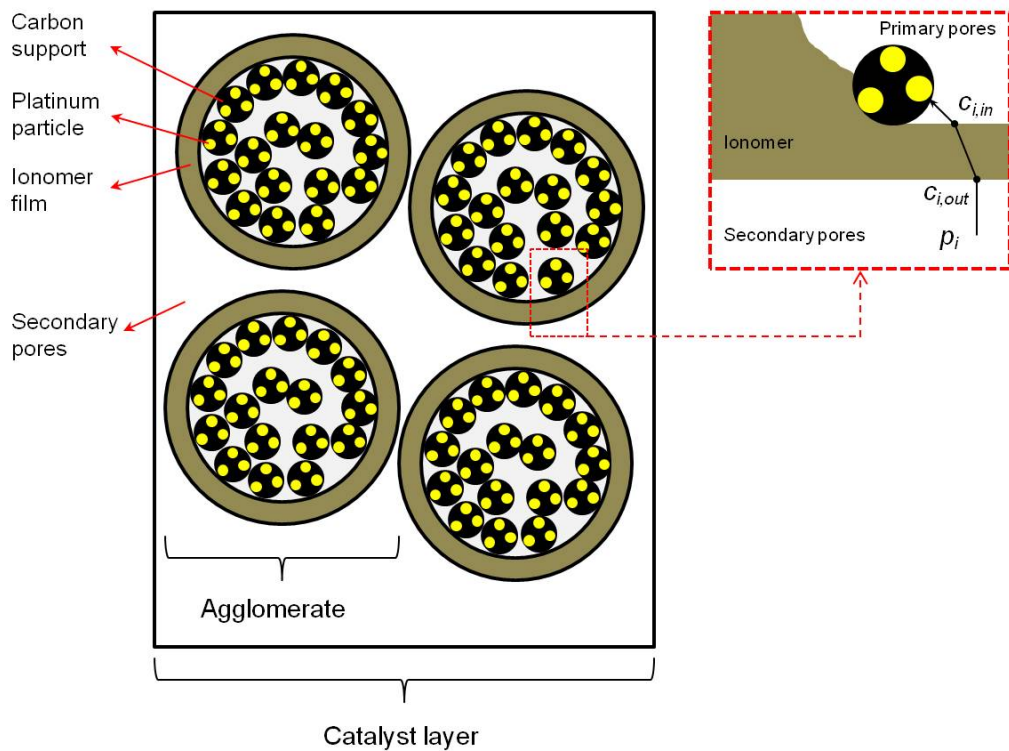


Figure 3-3 Schematic representation of reactant gas diffusion through the ionomer film surrounding the agglomerate

The diffusion of reactant through the ionomer/water film can be described by Fick's law:

$$N_i = -D_i^{eff} \frac{\partial c_i}{\partial r} \quad (3-15)$$

where  $N_i$  ( $\text{mol m}^{-2} \text{ s}^{-1}$ ) is the reactants mole flux through the ionomer/water film,  $D_i^{eff}$  ( $\text{m}^2 \text{ s}^{-1}$ ) is the effective diffusion coefficient of reactants,  $c_i$  ( $\text{mol m}^{-3}$ ) is the reactant concentration, and  $r$  (m) is the radius.

It is assumed that the ionomer/water film is present in the agglomerate evenly, and the film is much thinner than the size of the agglomerate, and the molar rate is conserved in

the ionomer/water film, namely the molar rate is constant at the outer boundary of the ionomer/water film. Thus, the reactants mole flux through the ionomer/water film can be derived as follow:

$$C = -(4\pi r^2) D_i^{eff} \frac{\partial c_i}{\partial r} \quad (3-16)$$

Boundary conditions:  $r = r_{agg}$ ,  $c_i = c_{i,in}$

$$r = r_{agg} + \delta, \quad c_i = c_{i,out} \quad (3-17)$$

where  $C$  (mol s<sup>-1</sup>) is a constant. Integrating Eq. (3-16) and applying the boundary conditions in Eq. (3-17) leading to:

$$C = -D_i^{eff} \left( \frac{c_{i,out} - c_{i,in}}{\delta} \right) 4\pi r_{agg} (r_{agg} + \delta) \quad (3-18)$$

where  $r_{agg}$  (m) is the radius of the agglomerate,  $\delta$  (m) is the thickness of the ionomer/water film. Combing Eq. (3-16) and Eq. (3-18), the reactants mole flux is obtained as follow:

$$N_i = D_i^{eff} \frac{r_{agg}}{(r_{agg} + \delta)} \frac{c_{i,out} - c_{i,in}}{\delta} \quad (3-19)$$

According to mass balance, at steady-state, the amount of the species consumed equals to the species diffusion to the active surface.

$$a_{agg} N_i = R_i \quad (3-20)$$

where  $a_{agg}$  (m<sup>-1</sup>) is the specific area of the agglomerate, defining as the surface area per agglomerate volume, and  $R_i$  (mol m<sup>-3</sup> s<sup>-1</sup>) is the reaction rate.

Assuming the reactions of either hydrogen oxidation, oxygen reduction or methanol oxidation as the first-order kinetics with respect to the reactant concentration [3, 4] gives:

$$R_i = k_{agg} c_i \quad (3-21)$$

where  $k_{agg}$  ( $\text{s}^{-1}$ ) is the reaction rate coefficient representing the reactions occurred in the agglomerate. By introducing the effectiveness factor into Eq. (3-21), the overall reaction rate only depends on the reactant concentration at the outer boundary of the agglomerate, obtained as:

$$R_{i,agg} = E_{agg} k_{agg} c_{i,out} \quad (3-22)$$

where  $R_{i,agg}$  ( $\text{mol m}^{-3} \text{ s}^{-1}$ ) is the reaction rate based on the agglomerate volume and,  $E_{agg}$  is the effectiveness factor of the agglomerate, which represents the geometry of the agglomerate and the reactant mass transport resistance within the agglomerate. For the spherical agglomerates, the effectiveness factor can be described as follow [3]:

$$E_{agg} = \frac{1}{M_{T,agg}} \left[ \frac{1}{\tanh(3M_{T,agg})} - \frac{1}{3M_{T,agg}} \right] \quad (3-23)$$

where  $M_{T,agg}$  the Thiele's modulus, a dimensionless parameter [3].

$$M_{T,agg} = \frac{r_{agg}}{3} \sqrt{\frac{k_{agg}}{D_{i,agg}^{eff}}} \quad (3-24)$$

where  $D_{i,agg}^{eff}$  ( $\text{m}^2 \text{ s}^{-1}$ ) is the reactant effective diffusion coefficient inside the agglomerate.

According to Faraday's law, the volumetric current density is related to the reactants consumption rate via the following equation:

$$i_{i,agg} = nFE_{agg} k_{agg} c_{i,in} \quad (3-25)$$

$i_{i,agg}$  ( $\text{A m}^{-3}$ ) is the volumetric current density based on the agglomerate volume, and the subscript  $i$  refers to anode or cathode, respectively. Combining equations from Eq. (3-19) to Eq. (3-22) the concentration of the dissolved species at the inner boundary of the ionomer/water film is obtained as:

$$c_{i,in} = \left[ 1 + \frac{E_{agg} k_{agg} (r_{agg} + \delta) \delta}{a_{agg} r_{agg} D_i^{eff}} \right]^{-1} c_{i,out} \quad (3-26)$$

Substituting Eq. (3-26) into Eq. (3-25), gives

$$i_{i,agg} = nF \left[ \frac{1}{E_{agg} k_{agg}} + \frac{(r_{agg} + \delta)\delta}{a_{agg} r_{agg} D_i^{eff}} \right]^{-1} c_{i,out} \quad (3-27)$$

Substituting Eq. (3-14), the Henry's law, into Eq. (3-27):

$$i_{i,agg} = nF \frac{p_i}{H_i} \left[ \frac{1}{E_{agg} k_{agg}} + \frac{(r_{agg} + \delta)\delta}{a_{agg} r_{agg} D_i^{eff}} \right]^{-1} \quad (3-28)$$

The current density obtained from Eq. (3-11) could transfer to volumetric current density after corrected by the specific area of the electrode. The agglomerate volumetric current therefore can be related to the Butler-Volmer kinetics as:

$$i_{i,agg} = a_{agg} i_0 \left[ \exp\left(\frac{-\alpha_{Rd} F \eta}{RT}\right) - \exp\left(\frac{\alpha_{ox} F \eta}{RT}\right) \right] \quad (3-29)$$

On the inner boundary of the agglomerate, the intrinsic volumetric current density is obtained as:

$$i_{i,agg} = nFk_{agg}c_{i,in} \quad (3-30)$$

Comparing Eq. (3-25) with Eq. (3-30), the reaction rate is obtained:

$$k_{agg} = \frac{a_{agg} i_0}{nFc_{i,in}} \left[ \exp\left(\frac{-\alpha_{Rd} F \eta}{RT}\right) - \exp\left(\frac{\alpha_{ox} F \eta}{RT}\right) \right] \quad (3-31)$$

Thus the volumetric current densities generated inside the electrodes of anode and cathode can be calculated by Eq. (3-29).

### 3.3 Catalyst layer property

#### 3.3.1 Porosity of the catalyst layer

Most previous works assume the agglomerate as a solid nucleus in which no primary pores exist. However, in practice, both primary pores and secondary pores exist within the agglomerate and between agglomerate, respectively [6, 7].

The total volume of the catalyst layer consists of five components including iomomer (M), platinum (Pt), carbon black (C), void space (P) and solid portion(S).

$$V_{tot} = V_M + V_{Pt} + V_C + V_P + V_S \quad (3-32)$$

where the volume of the void space consists of two parts: primary pores ( $V_{P,p}$ ) and secondary pores ( $V_{P,s}$ ).

As shown in [Figure 3-2](#), the primary pores are the void space within the agglomerates and the secondary pores are the void space between the agglomerates, thus we have:

$$V_P = V_{P,p} + V_{P,s} \quad (3-33)$$

The platinum dispersed carbon ( $Pt/C$ ) is constructed by platinum and carbon, thus

$$V_{Pt/C} = V_{Pt} + V_C \quad (3-34)$$

Dividing both sides of [Eq. \(3-34\)](#) by the total volume of catalyst layer ( $V_{tot}$ ), the sum of volume fractions of all components is equal to unity. [Eq. \(3-32\)](#) and [Eq. \(3-33\)](#) becomes to

$$1 = L_M + L_{Pt} + L_C + L_S + \varepsilon_{CL} \quad (3-35)$$

$$\varepsilon_{CL} = \varepsilon_p + \varepsilon_s \quad (3-36)$$

where the terms on the right side of [Eq. \(3-35\)](#) represent the volume fraction of ionomer ( $L_M$ ), platinum ( $L_{Pt}$ ) carbon ( $L_C$ ), solid portion ( $L_S$ ), primary pores ( $\varepsilon_p$ ), and secondary pores ( $\varepsilon_s$ ), respectively, which are written as:

$$L_M = \frac{V_M}{V_{tot}}, \quad L_{Pt} = \frac{V_{Pt}}{V_{tot}}, \quad L_C = \frac{V_C}{V_{tot}}, \quad L_S = \frac{V_S}{V_{tot}}, \quad \varepsilon_p = \frac{V_{P,p}}{V_{tot}}, \quad \varepsilon_s = \frac{V_{P,s}}{V_{tot}} \quad (3-37)$$

The volume fraction of platinum, carbon and ionomer were related to their mass loading and densities and the thickness of the catalyst layer as

$$L_{Pt} = \frac{m_{Pt}}{\rho_{Pt} l_{CL}}, \quad L_C = \frac{m_C}{\rho_C l_{CL}}, \quad L_M = \frac{m_M}{\rho_M l_{CL}} \quad (3-38)$$

Normally, platinum is dispersed in carbon black to construct the catalyst particles. Therefore, the volume fraction of platinum dispersed on carbon ( $Pt/C$ ) is the sum of the volume fractions of platinum and carbon, which is given as follow:

$$L_{Pt/C} = \frac{m_{Pt}}{l_{CL}} \left( \frac{1}{\rho_{Pt}} + \frac{1-f}{f} \frac{1}{\rho_C} \right) \quad (3-39)$$

where the platinum mass ratio to that of carbon (abbreviated as platinum mass ratio) is introduced as:

$$f = \frac{m_{Pt}}{m_{Pt} + m_C} \quad (3-40)$$

Due to the clamping force of the membrane electrode assembly (MEA), the gas diffusion layer can penetrate into the catalyst layer. The volume fraction of the solid portion of the catalyst layer is defined as:

$$L_S = L_{GDL} (1 - \varepsilon_{GDL}) \quad (3-41)$$

where  $L_{GDL}$  is the percentage of gas diffusion layer penetrating into catalyst layer and,  $\varepsilon_{GDL}$  is the porosity of the gas diffusion layer. The porosity of the catalyst layer is therefore being written as:

$$\varepsilon_{CL} = 1 - L_M - L_{GDL} (1 - \varepsilon_{GDL}) - \frac{m_{Pt}}{l_{CL}} \left( \frac{1}{\rho_{Pt}} + \frac{1-f}{f} \frac{1}{\rho_C} \right) \quad (3-42)$$

### 3.3.2 Agglomerate density

The ionomer firstly partially fills up the primary pores within the agglomerate then covers the agglomerate to form a thin film. The total volume of ionomer is:

$$V_M = V_{M,agg} + V_{M,\delta} \quad (3-43)$$

where  $V_{M,agg}$  ( $m^3$ ) is the volume of ionomer within the agglomerate and,  $V_{M,\delta}$  ( $m^3$ ) is the volume of ionomer existed as the thin film surrounding the agglomerate. Due to the fact that the agglomerate particles consists of platinum dispersed carbon ( $Pt/C$ ), ionomer and primary pores, the total volume of the agglomerate is:

$$V_{agg,tot} = V_{Pt/C} + V_{M,agg} + V_{P,p} \quad (3-44)$$

The volume fraction of ionomer within the agglomerate ( $\varepsilon_{agg,M}$ ) and the volume fraction of primary pore space within the agglomerate ( $\varepsilon_{agg,p}$ ) are introduced as:

$$\varepsilon_{agg,M} = \frac{V_{M,agg}}{V_{agg,tot}}, \quad \varepsilon_{agg,p} = \frac{V_{P,p}}{V_{agg,tot}} \quad (3-45)$$

By substituting Eq. (3-45) into Eq. (3-44), the total volume of the agglomerate becomes to:

$$V_{agg,tot} = \frac{V_{Pt/C}}{1 - \varepsilon_{agg,M} - \varepsilon_{agg,p}} \quad (3-46)$$

The volume of the individual agglomerate particle (without the ionomer film) is

$$V_{agg,i} = \frac{4}{3}\pi r_{agg}^3 \quad (3-47)$$

Dividing Eq. (3-47) by Eq. (3-46), the total number of the agglomerate particles can be calculated as follow:

$$n_{agg} = \frac{3V_{Pt/C}}{4(1 - \varepsilon_{agg,M} - \varepsilon_{agg,p})\pi r_{agg}^3} \quad (3-48)$$

Assuming the platinum is homogenously dispersed in carbon black, the volume fraction of the primary pores of the agglomerate (before filled with ionomer) equals to the volume fraction of the total void space (including primary and secondary pores) of the entire catalyst layer, leading to

$$\varepsilon_{agg,M} + \varepsilon_{agg,p} = \varepsilon_{CL} \quad (3-49)$$

Substituting Eq. (3-49) into Eq. (3-48) and dividing Eq. (3-48) by the total volume ( $V_{tot}$ ), the agglomerate density can be obtained, which is defined as the number of agglomerate particles per volume of catalyst layer, as follow:

$$N_{agg} = \frac{3L_{Pt/C}}{4(1 - \varepsilon_{CL})\pi r_{agg}^3} \quad (3-50)$$

### 3.3.3 Thicknesses of the ionomer and liquid water films

The volume of agglomerate with the ionomer film is equal to the volume of platinum dispersed carbon, ionomer and primary pores, leading to:

$$n_{agg} \frac{4}{3} \pi (r_{agg} + \delta_M)^3 = V_M + V_{Pt/C} + V_{P,p} \quad (3-51)$$

Substituting Eq. (3-51) into Eq. (3-32):

$$V_{tot} = n_{agg} \frac{4}{3} \pi (r_{agg} + \delta_M)^3 + V_{P,s} + V_S \quad (3-52)$$

Substituting Eq. (3-48) into Eq. (3-52) then dividing both side by  $V_{tot}$  gives

$$1 = \frac{L_{Pt/C} (r_{agg} + \delta_M)^3}{(1 - \varepsilon_{CL}) r_{agg}^3} + \varepsilon_s + L_S \quad (3-53)$$

From Eq. (3-37) and Eq. (3-45), we have

$$\frac{\varepsilon_p}{\varepsilon_{agg,p}} = \frac{V_{agg,tot}}{V_{tot}} \quad (3-54)$$

Substituting Eq. (3-46) and Eq. (3-49) into Eq. (3-54) gives

$$\frac{\varepsilon_p}{\varepsilon_{CL} - \varepsilon_{agg,M}} = \frac{L_{Pt/C}}{1 - \varepsilon_{CL}} \quad (3-55)$$

Then the volume fractions of the primary and secondary pores can be obtained as:

$$\varepsilon_p = \frac{L_{Pt/C} (\varepsilon_{CL} - \varepsilon_{agg,M})}{1 - \varepsilon_{CL}} \quad (3-56)$$

$$\varepsilon_s = \varepsilon_{CL} - \frac{L_{Pt/C} (\varepsilon_{CL} - \varepsilon_{agg,M})}{1 - \varepsilon_{CL}} \quad (3-57)$$

By substituting Eq. (3-57) into Eq. (3-53), the thickness of the ionomer thin film can be calculated by the following equation:

$$\delta_M = r_{agg} \left[ \sqrt[3]{\frac{(1 - \varepsilon_{CL})(1 - \varepsilon_{CL} - L_S) + L_{Pt/C} (\varepsilon_{CL} - \varepsilon_{agg,M})}{L_{Pt/C}}} - 1 \right] \quad (3-58)$$

Defining the volume fraction of the primary pores occupied by the ionomer as:

$$\%M = \frac{\varepsilon_{agg,M}}{\varepsilon_{agg,M} + \varepsilon_{agg,p}} \quad (3-59)$$

Then Eq. (3-58) becomes to:

$$\delta_M = r_{agg} \left[ \sqrt[3]{\frac{(1 - \varepsilon_{CL})(1 - \varepsilon_{CL} - L_S) + L_{Pt/C} \varepsilon_{CL} (1 - \%M)}{L_{Pt/C}}} - 1 \right] \quad (3-60)$$

If the primary pores are completely occupied by the ionomer ( $\%M = 1$ ), Eq. (3-60) changes to:

$$\delta_M = r_{agg} \left[ \sqrt[3]{\frac{(1 - \varepsilon_{CL})(1 - \varepsilon_{CL} - L_S)}{L_{Pt/C}}} - 1 \right] \quad (3-61)$$

It is important to note that the volume fraction of the ionomer with the agglomerate ( $\varepsilon_{agg,M}$ ) is impossible to bigger than the porosity of the catalyst layer ( $\varepsilon_{CL}$ ).

Assuming that the ionomer is hydrophilic, any liquid water is assumed to coat the entire surface of the individual agglomerate to generate a liquid water film adjacent to the outer boundary of the ionomer film. The total volume of the liquid water generated can be obtained as:

$$V_w = s \varepsilon_{CL} V_{tot} \quad (3-62)$$

where  $s$  is the liquid water saturation, which is defined as the volume fraction of the void space occupied by liquid water.

Averaging the total volume of the liquid water to each individual agglomerate, the volume of the liquid water surrounding each agglomerate is:

$$V_{w,i} = \frac{s \varepsilon_{CL}}{N_{agg}} \quad (3-63)$$

Then the liquid water film thickness is given as:

$$\delta_w = \sqrt[3]{(r_{agg} + \delta_M)^3 + \frac{3s \varepsilon_{CL}}{4\pi N_{agg}}} - (r_{agg} + \delta_M) \quad (3-64)$$

Substituting Eq. (3-50) into Eq. (3-64):

$$\delta_w = \sqrt[3]{(r_{agg} + \delta_M)^3 + \frac{s \varepsilon_{CL} (1 - \varepsilon_{CL}) r_{agg}^3}{L_{Pt/C}}} - (r_{agg} + \delta_M) \quad (3-65)$$

where  $s'$  is the corrected liquid water saturation, defined as the volume fraction of the secondary pores occupied by the liquid water.

### 3.3.4 Specific area

The reaction surface area per unit platinum mass ( $\text{m}^2 \text{ kg}^{-1}$ ) can be calculated by an empirical equation as follow [8, 9]:

$$A_s = (227.79f^3 - 158.57f^2 - 201.53f + 159.5) \times 10^3 \quad (3-66)$$

The specific area of the catalyst layer ( $\text{m}^{-1}$ ), defined as the total active area per volume of catalyst layer, can be written as [8, 9]:

$$a_{CL} = \frac{m_{Pt}}{l_{CL}} A_s \quad (3-67)$$

The specific area of the agglomerate, defined as the total active area per volume of agglomerate, is

$$a_{agg} = \frac{a_{CL} V_{tot}}{V_{agg,tot}} \quad (3-68)$$

Substituting Eq. (3-46) and Eq. (3-49) into Eq. (3-68) leads to:

$$a_{agg} = \frac{m_{Pt} A_s}{l_{CL}} \frac{3}{4\pi r_{agg}^3 N_{agg}} \quad (3-69)$$

The specific area of the agglomerate covered by the ionomer is:

$$\dot{a}_{agg} = a_{agg} \left(1 + \frac{\delta_w}{r_{agg}}\right)^2 \quad (3-70)$$

## 3.4 Water phase transfer and transport through the membrane

### 3.4.1 Phase transfer and transport through the membrane

Water exists as three different phases in different solvents [10-12] including the dissolved water in the membrane and ionomer, water vapour and liquid water in the porous media and flow channels. The dissolved water is the membrane and ionomer absorbed water, which enters the membrane and ionomer from the water vapour during water uptake and leaves the membrane and ionomer in the liquid phase when the water

content of membrane and ionomer reaches complete saturation. The main phase transfer mechanisms include: phase transfer between liquid water and water vapour via condensation and evaporation, phase transfer between dissolved water and water vapour by membrane and ionomer absorption or water uptake, and phase transfer between liquid water and dissolved water during the process of membrane and ionomer desorption.

Water transport in the membrane plays an important role in determining the water content in the membrane/ionomer [10-14]. During fuel cell operation, water transport through the membrane occurs via three mechanisms: electro-osmotic drag (EOD) of water molecules carried by protons migrating from anode to cathode, back diffusion driven by the concentration gradient of water, and convection generated by the pressure gradient.

In order to mathematically describe the dissolved water transport through the membrane, a second order partial differential equation (PDE) is developed by following the traditional diffusive approach as follow:

$$\frac{\partial}{\partial t}(L_M c_w^d) + \nabla \cdot (n_d \frac{i_M}{F}) - \nabla \cdot (D_{w-M} \nabla c_w^d) - \nabla \cdot (\frac{k_{p,M} c_w^d}{\mu_w} \nabla p) = S_w^d \quad (3-71)$$

The term on the left hand side of the equation refers to the water accumulation, water migration by electro-osmotic drag (EOD), the back diffusion and the hydraulic permeation, respectively. where  $L_M$  is the volume fraction of ionomer ( $L_M = 1$  in membrane,  $0 < L_M < 1$  in catalyst layer),  $c_w^d$  (mol m<sup>-3</sup>) is the concentration of the dissolved water,  $n_d$  is the EOD coefficient, which is expressed as  $2.5\lambda/22$  [10-15],  $D_{w-M}$  (m<sup>2</sup> s) is the diffusion coefficient of water through the membrane,  $k_{p,M}$  (m<sup>2</sup>) is the hydraulic permeability of water in the membrane,  $\mu_w$  (Pa s) is the water viscosity,  $p$  (Pa) is the pressure.  $S_w^d$  (mol m<sup>-3</sup> s<sup>-1</sup>) is the source term. The concentration of the dissolved water depends on the water content of the membrane and ionomer, which can be calculated by the following equation [14]:

$$c_w^d = \frac{\rho_M}{EW} \frac{\lambda}{1+k_s\lambda} \quad (3-72)$$

where  $\rho_M$  ( $\text{kg m}^{-3}$ ) is the density of dry membrane,  $EW$  ( $\text{g mol}^{-1}$ ) is the equivalent weight of membrane, and  $k_s$  is the swelling coefficient, representing the volume increase of the membrane and ionomer.

Dissolved water is absorbed by the membrane and ionomer when the concentration of the dissolved water is smaller than the equilibrium concentration, which is the maximum dissolved water being carried by the membrane and ionomer. After reaching the equilibrium concentration, the dissolved water move away from the membrane and ionomer in the liquid water phase, during the process of membrane and ionomer desorption. The source terms regarding the process above are expressed as

$$S_{vd} = k_{ads}(c_w^{eq} - c_w^d) \quad c_w^d < c_w^{eq} \quad (3-73)$$

$$S_{dl} = k_{des}(c_w^d - c_w^{eq}) \quad c_w^d \geq c_w^{eq} \quad (3-74)$$

The subscripts  $vd$  and  $dl$  in the source term represent the water phase change from vapour to dissolved water and from dissolved water to liquid water, respectively.  $k_{ads}$  and  $k_{des}$  ( $\text{s}^{-1}$ ) are the adsorption and desorption rate coefficient, calculated by [15, 16]:

$$k_{ads} = \frac{1.14 \times 10^{-5} f_w}{\delta_{CL}} \exp \left[ 2416 \left( \frac{1}{303} - \frac{1}{T} \right) \right] \quad (3-75)$$

$$k_{des} = \frac{4.59 \times 10^{-5} f_w}{\delta_{CL}} \exp \left[ 2416 \left( \frac{1}{303} - \frac{1}{T} \right) \right] \quad (3-76)$$

$$f_w = \frac{\lambda V_w}{V_w + \lambda V_w} \quad (3-77)$$

where  $V_w$  and  $V_M$  ( $\text{m}^3 \text{ mol}^{-1}$ ) are the partial molar volume of water and the dry membrane, respectively.  $c_w^{eq}$  ( $\text{mol m}^{-3}$ ) is the equilibrium dissolved water concentration, which is determined by the equilibrium water content according to Eq. (3-72). The equilibrium water content is determined by empirical correlations based on water uptake measurements [10], given as

$$\lambda^{eq} = \begin{cases} 0.3 + 6\alpha_w [1 - \tanh(\alpha_w - 0.5)] + 3.9\sqrt{\alpha_w} [1 + \tanh(\frac{\alpha_w - 0.89}{0.23})] & \text{if } s \leq 0 \\ 16.8s + 14.0(1-s) & \text{if } s > 0 \end{cases} \quad (3-78)$$

The actual water content is proposed as a function of water activity:

$$\lambda = 0.043 + 17.81\alpha_w - 39.85\alpha_w^2 + 36.0\alpha_w^3 \quad \alpha_w \leq 1 \quad (3-79)$$

where  $\alpha_w$  is a function of both water vapour partial pressure and liquid water saturation [12], expressed as:

$$\alpha_w = x_w \frac{P}{P_{sat}} + 2s \quad (3-80)$$

### 3.4.2 Liquid water transport in the porous electrode

At a steady-state condition, applying the continuity equation on liquid water and gas phase, respectively, the following equations are obtained:

$$\nabla \cdot (\rho_w^l \mathbf{u}_w^l) = M_w S_l \quad (3-81)$$

$$\nabla \cdot (\rho_w^g \mathbf{u}_w^g) = M_w S_g \quad (3-82)$$

where  $M_w$  ( $\text{kg mol}^{-1}$ ) is the molecular weight of water and,  $\rho$  ( $\text{kg m}^{-3}$ ),  $\mathbf{u}$  ( $\text{m s}^{-1}$ ) and  $S$  ( $\text{mol m}^{-3} \text{ s}^{-1}$ ) are the density, velocity and source term of liquid water and water vapour, respectively. The subscript  $w$  represents water, and the superscripts  $l$  and  $g$  represent the liquid water and gas phase, respectively.

According to the Darcy's law, the velocity of the liquid water and gas phase can be related to their partial pressure as:

$$\mathbf{u}_w^l = -\frac{K^l}{\mu_w^l} \nabla p^l \quad (3-83)$$

$$\mathbf{u}_w^g = -\frac{K^g}{\mu_w^g} \nabla p^g \quad (3-84)$$

where  $K$  ( $\text{m}^2$ ),  $\mu$  ( $\text{Pa s}$ ) and  $p$  ( $\text{Pa}$ ) are the permeability, viscosity and partial pressure of the liquid water and gas phase, respectively.

The pressure difference between the wetting and non-wetting phase within the porous media is defined as the capillary pressure ( $p^c$ ), which is expressed as:

$$p^c = p^g - p^l \quad (3-85)$$

Substituting Eq. (3-85) into Eq. (3-83), the liquid water velocity becomes to:

$$\mathbf{u}_w^l = \frac{K^l}{\mu_w^l} \nabla p^c - \frac{K^l}{\mu_w^l} \nabla p^g \quad (3-86)$$

Introducing the liquid water saturation into the expression above, gives

$$\mathbf{u}_w^l = \frac{K^l}{\mu_w^l} \frac{dp^c}{ds} \nabla s - \frac{K^l}{\mu_w^l} \nabla p^g \quad (3-87)$$

where  $s$  is the liquid water saturation, defined as the volume fraction of the liquid water in the porous media.

Capillary pressure can be related to the liquid water saturation via [17]:

$$p^c = \sigma \cos(\theta_c) \left( \frac{\varepsilon}{K} \right)^{1/2} J(s) \quad (3-88)$$

where  $J(s)$  is the Leverett function, and is given by [17]:

$$J(s) = \begin{cases} 1.417(1-s) - 2.120(1-s)^2 + 1.263(1-s)^3 & \theta_c < 90^\circ \\ 1.417s - 2.120s^2 + 1.263s^3 & \theta_c > 90^\circ \end{cases} \quad (3-89)$$

Normally, the porous electrode is hydrophobic, therefore the Leverett function is expressed in terms of the liquid water saturation and the contact angel,  $\theta_c$ , is between  $90^\circ$  and  $180^\circ$ . The surface tension  $\sigma$ , for liquid water - air system, is taken as 0.0625 N/m. Combing Eq. (3-87) and Eq. (3-88), the liquid water velocity is expressed in terms of liquid water saturation as:

$$\mathbf{u}_w^l = \sigma \cos(\theta_c) \frac{K^l}{\mu_w^l} \left( \frac{\varepsilon}{K} \right)^{1/2} \frac{dJ(s)}{ds} \nabla s - \frac{K^l}{\mu_w^l} \nabla p^g \quad (3-90)$$

The permeability of liquid water and gas phase can be associated with the permeability of the porous media via:

$$K^l = k_r^l K, \quad K^g = k_r^g K \quad (3-91)$$

where  $k_{rl}$  and  $k_{rg}$  are the relative permeability of liquid water and gas phase, which are proportional to the cube of liquid water saturation as:

$$k_r^l = s^3, \quad k_r^g = (1-s)^3 \quad (3-92)$$

Substituting Eq. (3-84) and Eq. (3-91) into Eq. (3-90) leads to:

$$\mathbf{u}_w^l = \frac{\sigma \cos(\theta_c) k_r^l}{\mu_w^l} (\varepsilon K)^{1/2} \frac{dJ(s)}{ds} \nabla s - \frac{k_r^l \mu_w^g}{k_r^g \mu_w^l} \mathbf{u}_w^g \quad (3-93)$$

Substituting Eq. (3-93) into Eq. (3-81) and taking the liquid water accumulation into account, the liquid water saturation can be calculated by the as follow:

$$\frac{\partial}{\partial t} (\varepsilon \rho_w^l s) + \nabla \cdot (\rho_w^l D_c \nabla s - \frac{\rho_w^l k_r^l \mu_w^g}{k_r^g \mu_w^l} \mathbf{u}_w^g) = M_w S_w^l \quad (3-94)$$

where  $D_c$  ( $\text{m}^2 \text{ s}^{-1}$ ) is the capillary diffusion coefficient, which is calculated using the following expression:

$$D_c = \frac{\sigma \cos(\theta_c) k_r^l}{\mu_w^l} (\varepsilon K)^{1/2} \frac{dJ(s)}{ds} \quad (3-95)$$

At a steady-state, if the velocity of the gas phase can be neglected, Eq. (3-94) becomes a second order partial differential equation with respect to the liquid water saturation, shown as follow:

$$\nabla^2 s = \frac{M_w}{\rho_w^l D_c} S_w^l \quad (3-96)$$

The source term,  $S_{vl}$  ( $\text{mol m}^{-3} \text{ s}^{-1}$ ), is introduced for the interfacial mass transfer rate of water by condensation and evaporation, which is defined as:

$$S_{vl} = \begin{cases} k_{con} \frac{\varepsilon(1-s)x_w^g}{RT} (x_w^g p^g - p_{sat}) & x_w^g p^g \geq p_{sat} \\ k_{eva} \frac{\varepsilon s \rho_w^l}{M_w} (p_{sat} - x_w^g p^g) & x_w^g p^g < p_{sat} \end{cases} \quad (3-97)$$

where  $k_{con}$  ( $\text{s}^{-1}$ ) and  $k_{eva}$  ( $\text{atm}^{-1} \text{ s}^{-1}$ ) are the condensation and evaporation rate coefficient, respectively.

### 3.4.3 Water vapour transport in porous electrode

The transport of all involved gas species, including water vapour, within the porous electrode is described by the Maxwell-Stefan equation shown as follow:

$$\rho^g \mathbf{u}^g \cdot \nabla w_i^g - \nabla \cdot [-\rho^g \sum_{j=1}^N (1-s^j) D_{ij} (\nabla x_j^g - w_j^g) \frac{\nabla p}{p} + D_i^T \frac{\nabla T}{T}] = M_i S_i^g \quad (3-98)$$

where  $w_i^g$ ,  $w_j^g$  and  $M_i$  ( $\text{kg mol}^{-1}$ ) are the mass fraction, mole fraction and molecular weight of species  $i$ , respectively.  $D_{ij}$  ( $\text{m}^2 \text{s}^{-1}$ ) and  $D_i^T$  ( $\text{m}^2 \text{s}^{-1}$ ) are the multi-component diffusion coefficient and the thermal diffusion coefficient, which will be discussed in detail in [Section 3.5.7](#), respectively,  $T$  is the temperature,  $S_i^g$  ( $\text{mol m}^{-3} \text{s}^{-1}$ ) is the source terms, which account for the electrochemical reactions taken place within the porous catalyst layer shown as follow:

$$S_{H_2}^g = \frac{i_a}{2F}, S_{O_2}^g = -\frac{i_c}{4F}, S_w^g = \frac{i_c}{2F} \quad (3-99)$$

Note that  $\rho^g$  ( $\text{kg m}^{-3}$ ) is the density of the gas mixture, which is given by the ideal gas law:

$$\rho^g = \frac{p^g M_n}{RT} \quad (3-100)$$

where  $p^g$  (Pa) is the pressure of the gas mixture and  $M_n$  ( $\text{kg mol}^{-1}$ ) is the mean molecular weight of the gas mixture, which can be related to the mole fraction of the component as follow:

$$M_n = \sum_{i=1}^n x_i M_i \quad (3-101)$$

where  $n$  is the number of component gas in the gas mixture and,  $M_i$  ( $\text{kg mol}^{-1}$ ) is the molecular weight of the species  $i$ .

In the practical condition, the fuel cell anode typically dehydrates. Therefore, assuming no liquid water exists at the anode [\[10\]](#). The water phase transfer mechanism is only from vapour to dissolved water in the anode catalyst layer. The relationship between the sources terms of water in different phase within different region of the fuel cell are listed in [Table 3-1](#), shown as follow:

Table 3-1 Source terms of water vapour, liquid water and dissolved water

	Anode GDL	Anode CL	Cathode CL	Cathode GDL
Water vapour	$S_w^v = 0$	$S_w^v = -S_{vd}$	$S_w^v = S_w^g - S_{vd} - S_{vl}$	$S_w^v = -S_{vl}$
Liquid water	$S_w^l = 0$	$S_w^l = 0$	$S_w^l = S_{dl} + S_{vl}$	$S_w^l = S_{vl}$
Dissolved water	$S_w^d = 0$	$S_w^d = S_{vd}$	$S_w^d = S_{vd} - S_{dl}$	$S_w^d = 0$

Note: The unit for every source term is ( $\text{mol m}^{-3} \text{s}^{-1}$ )

### 3.4.4 Membrane and ionmer swelling

The polymeric matrix of the membrane and ionomer expands leading to an increase in their volume when membrane/ionomer water absorption (water uptake) occurs. Normally a dry Nafion® membrane/ionomer swells approximately 20% when fully hydrated by water vapour [14, 18]. The membrane penetrates into the gas diffusion layer combined with the platinum catalyst to form the catalyst layer. The membrane in the catalyst layer co-exists with the ionomer. Membrane and ionomer swellings have two effects on fuel cell performance. For the membrane, higher swelling increases the ionic conductivity and the water diffusion coefficient, while for the ionomer higher swelling increases the thickness of the ionomer film surrounding the agglomerate and decreases the void space within the catalyst layer leading to an increase in species transport resistance, specifically oxygen diffusion [14].

Depending on the directions of membrane swelling, there are two types of membrane deformation: the through-plane membrane thickness increasing and the in-plane membrane buckling. The through-plane membrane thickness increase is caused by the zero or low fastening force from gas flow fields to the MEA [19]. Due to the fact that the membrane is fixed between the bipolar plates under a relative high clamping force, the thickness of the portion of the membrane under the current collector ribs is impossible to change during membrane water absorption (water uptake). However, the in-plane buckling occurs within channel portions at grooved gas flow field as shown in Figure 3-4. Compared to the through-plane thickness increasing, the in-plane buckling is more important as the in-plane stress is the major stress component in the membrane [20]. The in-plane buckling could have a significant impact on the channel flow as the MEA bulges into the channel. The bulged gas diffusion layer into the flow channels increases the mass transport resistance and can lead to pinhole formation of the membrane under the channel [21].

Because the catalyst layer is very thin compared with the gas diffusion layer and membrane, the volume increase of the catalyst layer therefore can be neglected while the ionomer swelling occurs. It is reasonable to assume that ionomer swelling only increases the thickness of the ionomer film surrounding the agglomerate and decreases the volume fraction of the void space.

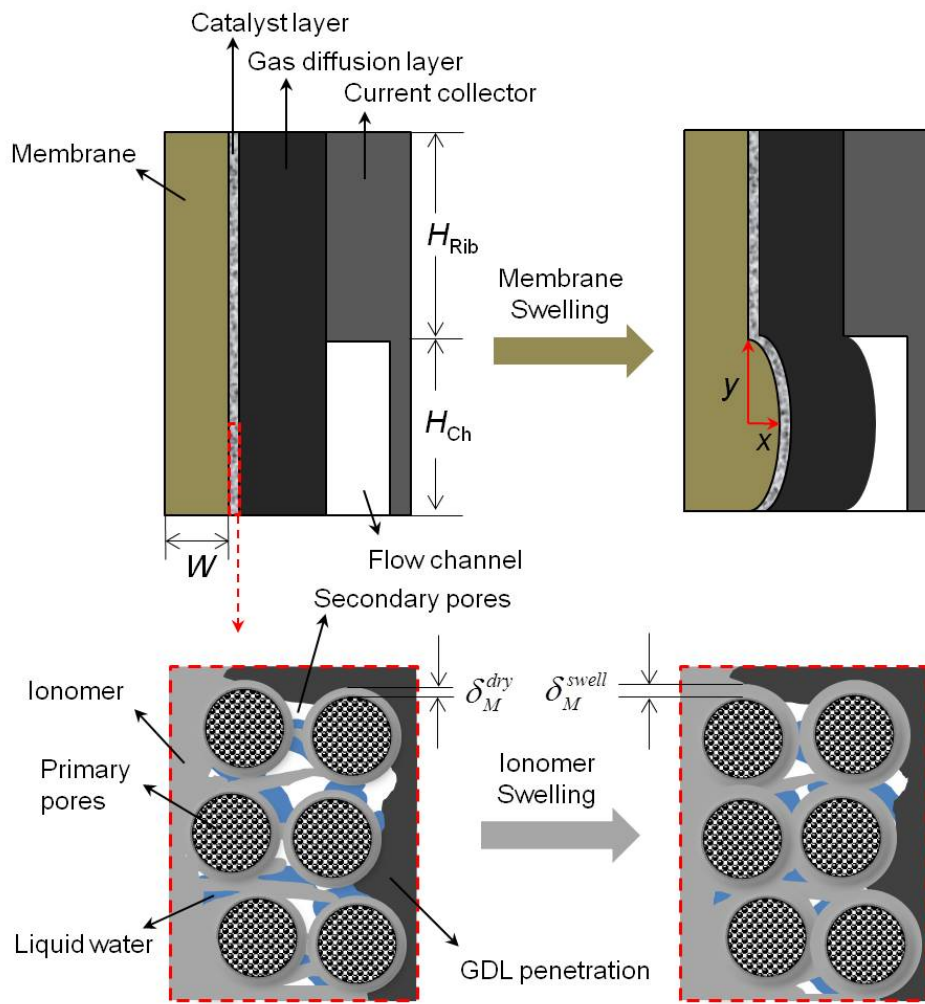


Figure 3-4 Sketch of the membrane and ionomer swelling and the bulged MEA into flow channel

By further assuming the shape of the swelled membrane is a half ellipse as shown in Figure 3-4, the major radius and the minor radius can be calculated as follow:

$$\frac{\pi xy}{2} = A_M^{swell} \quad (3-102)$$

where  $x$  (m) and  $y$  (m) are the major radius and the minor radius, respectively.  $A_M^{swell}$  ( $\text{m}^2$ ) is the increased area of the swelled membrane, which is related to the membrane water content by:

$$A_M^{swell} = (H_{Rib} + H_{Ch}) \cdot W \cdot (1 + k_s \lambda) \quad (3-103)$$

Note that the major radius of the ellipse is equal to the half height of the flow channels, gives:

$$y = \frac{H_{Ch}}{2} \quad (3-104)$$

By combining Eq. (3-102) and Eq. (3-104), the minor radius of the ellipse can be obtained as:

$$x = \frac{4(H_{Rib} + H_{Ch}) \cdot W \cdot (1 + k_s \lambda)}{\pi H_{Ch}} \quad (3-105)$$

And the volume fraction of the ionomer after swelling is calculated by the following equation:

$$L_M^{swell} = L_M (1 + k_s \lambda) \quad (3-106)$$

### 3.5 Governing equations

By coupling the conservation equations of mass, momentum, species, energy and charge, the complicated physical and chemical phenomena occurred within the fuel cells can be described in details. In this section, a general form of the governing equations used from Chapter 4 to Chapter 7 is represented.

#### 3.5.1 Conservation of mass

The mass balance within a volume element can be described by the following equation:

$$\left\{ \begin{array}{l} \text{rate of mass} \\ \text{accumulation} \end{array} \right\} = \left\{ \begin{array}{l} \text{rate of} \\ \text{mass inlet} \end{array} \right\} - \left\{ \begin{array}{l} \text{rate of} \\ \text{mass outlet} \end{array} \right\} \quad (3-107)$$

Applying Eq. (3-107) on the fluid continuously flowing in a porous media following the methodology developed by Bird *et al.* [22]:

$$\frac{\partial(\varepsilon\rho)}{\partial t} + \nabla \cdot (\rho\mathbf{u}) = Q_c \quad (3-108)$$

where  $\varepsilon$  is the porosity of the porous media,  $\rho$  ( $\text{kg m}^{-3}$ ) is the density of the fluid,  $t$  (s) is the time,  $\mathbf{u}$  ( $\text{m s}^{-1}$ ) is the velocity vector,  $Q_c$  ( $\text{kg m}^{-3} \text{ s}^{-1}$ ) is the general fluid sources, and  $\nabla$  is the nabla operator.

Note that the porosity equals unity if the flow media is non-porous. The vector  $\rho\mathbf{u}$  ( $\text{kg m}^{-2} \text{ s}^{-1}$ ) is the mass flux, and its divergence  $\nabla \cdot (\rho\mathbf{u})$  ( $\text{kg m}^{-3} \text{ s}^{-1}$ ) is the mass flux net rate per unit of volume. Consequently, Eq. (3-108) means that the rate increase in density within a small volume element is equal to the mass flux net rate divided by its volume.

This equation is valid for all the flowing and diffusion processes, such as fluid flow, mass transport and electrochemical reactions, occurred inside the fuel cell.

Eq. (3-108) can be expanded for a multi-component mixture consisting of  $n$  species by applying the law of conservation of mass for each species  $i$  ( $i = 1, 2, 3, \dots, n$ ):

$$\frac{\partial(\varepsilon\rho_i)}{\partial t} + \nabla \cdot (\rho_i \mathbf{u} + \mathbf{j}_i) = Q_{c,i} \quad (3-109)$$

where  $\mathbf{j}_i$  ( $\text{kg m}^{-2} \text{ s}^{-1}$ ) is the mass flux vector of species  $i$ . This equation describes the change of density of species  $i$  with time. The addition of all  $n$  equations results in Eq. (3-108), where

$$\sum_{i=1}^n \rho_i \mathbf{u} = \rho \mathbf{u}, \quad \sum_{i=1}^n \mathbf{j}_i = 0, \quad \sum_{i=1}^n Q_{c,i} = 0 \quad (3-110)$$

### 3.5.2 Conservation of momentum

The momentum balance within a volume element can be described by the following equation:

$$\left\{ \begin{array}{l} \text{rate of} \\ \text{momentum} \\ \text{accumulation} \end{array} \right\} = \left\{ \begin{array}{l} \text{rate of} \\ \text{momentum} \\ \text{in} \end{array} \right\} - \left\{ \begin{array}{l} \text{rate of} \\ \text{momentum} \\ \text{out} \end{array} \right\} + \left\{ \begin{array}{l} \text{sum of forces} \\ \text{acting on} \\ \text{system} \end{array} \right\} \quad (3-111)$$

The momentum flow through the volume element can be described by two mechanisms: convection and molecular transfer. By considering the fact that the fluid flows through all faces of the volume element, Eq. (3-111) can be written as follow [22]:

$$\frac{\partial(\rho \mathbf{u})}{\partial t} = -\nabla \cdot (\rho \mathbf{u} \mathbf{u}) - \nabla \cdot p - \nabla \cdot \tau + \rho \mathbf{g} \quad (3-112)$$

where  $\nabla p$  ( $\text{Pa m}^{-1}$ ) is the pressure gradient,  $\tau$  ( $\text{kg m}^{-1} \text{ s}^{-2}$ ) is the shear stress tensor, and  $\mathbf{g}$  ( $\text{m s}^{-2}$ ) is the gravitational acceleration vector.

The term on the left hand side of Eq. (3-112) means the rate of momentum increase per unit of volume while on the right hand side of Eq. (3-112) the first term is the rate of momentum gain by convection per unit of volume, the second term is the pressure force on element per unit of volume, the third term describes the rate of momentum gain by viscous transfer per unit of volume, and the last term is the gravitational force on the

element per unit of volume. This equation, which is valid for any continuous medium, is the general form of the motion equation. If the behaviour of the fluids obeys Newton's law of viscosity, in which the shear force per unit of area is proportional to the negative of the local velocity gradient, the shear stress tensor is therefore being expressed as [22]:

$$\boldsymbol{\tau} = \mu[\nabla \mathbf{u} + (\nabla \mathbf{u})^T - \frac{2}{3}(\nabla \cdot \mathbf{u})\mathbf{I}] \quad (3-113)$$

where  $\mathbf{I}$  is the identity matrix,  $\begin{bmatrix} 1 & 0 & 0 \\ 0 & 1 & 0 \\ 0 & 0 & 1 \end{bmatrix}$ .

In order to describe the momentum balance in the porous media, the Brinkman equation [23] is used. This equation was developed based on Darcy's law by Brinkman in 1949. An additional term was added into Darcy's law accounting for the viscous transport in the momentum balance. And both the pressure and flow velocity vector were treated as independent variables in the Brinkman equation shown as follow:

$$(\frac{\rho}{\varepsilon})\frac{\partial \mathbf{u}}{\partial t} = -\mathbf{u}\frac{\mu^{eff}}{K} - \nabla \cdot p - \nabla \cdot \boldsymbol{\tau} + \rho \mathbf{g} \quad (3-114)$$

where  $K$  ( $m^2$ ) and  $\varepsilon$  are the permeability and porosity of the porous media, respectively.  $\mu^{eff}$  (Pa s) is the effective viscosity of the fluid. The shear stress tensor is similar to that in Eq. (3-113) but the porosity of the porous media is included:

$$\boldsymbol{\tau} = \frac{\mu}{\varepsilon}[\nabla \mathbf{u} + (\nabla \mathbf{u})^T - \frac{2}{3}(\nabla \cdot \mathbf{u})\mathbf{I}] \quad (3-115)$$

For a multi-component mixture the motion equation is very similar to the equations developed for single fluid represented by Eq. (3-112) and Eq. (3-114). The difference is that the last term,  $\rho \mathbf{g}$  is replaced by  $\sum \rho_i \mathbf{g}_i$ , which accounts for the fact that each species may be affected by different external force per unit of mass. Simultaneously, a unit tensor  $\boldsymbol{\delta}$  is introduced to the pressure term shown as follow:

$$\frac{\partial(\rho \mathbf{u})}{\partial t} = -\nabla \cdot (\rho \mathbf{u} \mathbf{u}) - \nabla \cdot (p \boldsymbol{\delta}) - \nabla \cdot \boldsymbol{\tau} + \sum_{i=1}^n \rho_i \mathbf{g}_i, \quad i = 1, 2, 3, \dots, n \quad (3-116)$$

$$\left(\frac{\rho}{\varepsilon}\right)\frac{\partial \mathbf{u}}{\partial t} = -\mathbf{u}\frac{\mu^{eff}}{K} - \nabla \cdot (p\boldsymbol{\delta}) - \nabla \cdot \boldsymbol{\tau} + \sum_{i=1}^n \rho_i \mathbf{g}_i, \quad i = 1, 2, 3, \dots, n \quad (3-117)$$

Note that the flow velocity in equations from Eq. (3-112) to Eq. (3-117) is the superficial averaged velocity, which is defined as the volume rate of flow through a unit cross-sectional area including both pores and solid matrix. This definition makes the velocity field continuous across the boundaries between the porous and free flow regions. The flow therefore can be described by the same velocity in the entire domain.

### 3.5.3 Conservation of species

The mass balance of species  $i$  in a multi-component mixture can be obtained by applying the law of conservation of mass on species  $i$  to the volume element, through which a multi-component mixture. For species  $i$ , the mass balance is described as follow:

$$\left\{ \begin{array}{l} \text{rate of mass} \\ \text{accumulation} \end{array} \right\} = \left\{ \begin{array}{l} \text{rate of} \\ \text{mass in} \end{array} \right\} - \left\{ \begin{array}{l} \text{rate of} \\ \text{mass} \end{array} \right\} + \left\{ \begin{array}{l} \text{rate of production} \\ \text{or consumption} \end{array} \right\} \quad (3-118)$$

By considering the species transport through convection and diffusion, Eq. (3-118) could be written as follow:

$$\frac{\partial(\rho_i w_i)}{\partial t} = -\rho_i \mathbf{u} \nabla \cdot \mathbf{w}_i - \nabla \cdot \mathbf{j}_i + r_i \quad (3-119)$$

where  $w_i$ ,  $\mathbf{j}_i$  ( $\text{kg m}^{-2} \text{ s}^{-1}$ ) and  $r_i$  ( $\text{kg m}^{-3} \text{ s}^{-1}$ ) are the mass fraction, mass flux vector and source or sink term of species  $i$ , respectively.

Eq. (3-119) describes the change of mass fraction of species  $i$  with respect to time in a fixed volume element. On the right hand side of this equation, the first term represents the mass change resulting from convection, the second term represents the mass change due to diffusion, and the third term is the chemical reaction dependent mass change.

Bird *et al.* [22] states that four driving forces have to be considered for the mass flux vector in a multi-component system. Thus the mass flux vector of species  $i$  is written as follow:

$$\mathbf{j}_i = \mathbf{j}_i^x + \mathbf{j}_i^p + \mathbf{j}_i^g + \dot{\mathbf{j}}_i^T \quad (3-120)$$

where each term on the right hand side represent the contribution of ordinary diffusion ( $\mathbf{j}_i^x$ ), pressure diffusion ( $\mathbf{j}_i^p$ ), forced diffusion ( $\mathbf{j}_i^g$ ) and thermal diffusion ( $\mathbf{j}_i^T$ ), respective.

According to the approach proposed by Curtiss and Bird [24], the mass flux vector can be rearranged as follow:

$$\mathbf{j}_i = -D_i^T \nabla \ln T - \rho_i \sum_{j=1}^v D_{ij}^{eff} \mathbf{d}_j, \quad i = 1, 2, 3, \dots, n \quad (3-121)$$

where  $D_i^T$  ( $\text{m}^2 \text{s}^{-1}$ ) is the thermal diffusion coefficient,  $T$  (K) is the temperature,  $D_{ij}$  ( $\text{m}^2 \text{s}^{-1}$ ) is the Fick diffusion coefficient matrix for species  $i$  diffusing through species  $j$  in the multi-component mixture, and  $\mathbf{d}_j$  ( $\text{m}^{-1}$ ) is the driving force for diffusion through concentration, pressure and external forces. If gravity is the only external force,  $\mathbf{d}_j$  can be expressed as [25]:

$$\mathbf{d}_j = \nabla x_j + (x_j - w_j) \frac{\nabla p}{p} \quad (3-122)$$

The mole fraction of species  $j$  ( $x_j$ ) and its gradient ( $\nabla x_j$ ) can be related to the mass fraction of species  $j$  ( $w_j$ ) by the following equation:

$$x_j = \frac{w_j}{M_j} M_n \quad (3-123)$$

$$\nabla x_j = \frac{M_n^2}{M_j} \sum_{\substack{j=1 \\ k \neq j}}^n \left[ \frac{1}{M_j} + w_k \left( \frac{1}{M_k} + \frac{1}{M_j} \right) \right] \nabla w_k \quad (3-124)$$

where  $M_n$  ( $\text{kg mol}^{-1}$ ) is the mean molecular weight of the mixture.

In a porous media, the Fick's diffusion coefficient matrix needs to be corrected by the porosity and tortuosity of the porous media. Bruggman correction [26] shown as follow is the most common relationship used.

$$D_{ij}^{eff} = D_{ij} \mathcal{E}^\tau \quad (3-125)$$

Normally,  $\tau = 1.5$  is selected.

The source term for species conservation is associated with the chemical reaction. The source term for species  $i$  is zero unless species  $i$  is involved in the chemical reactions. As discussed in [Section 3.1.1](#), the reaction rate is negative in the anode catalyst layer and positive in the cathode catalyst layer. Consequently, the source terms for hydrogen, oxygen, nitrogen and water vapour are given as follow:

$$r_{H_2} = i_a \frac{M_{H_2}}{2F}, \quad r_{O_2} = -i_c \frac{M_{O_2}}{4F}, \quad r_{N_2} = 0, \quad r_{H_2O} = i_c \frac{M_{H_2O}}{2F} \quad (3-126)$$

where  $i_a$  and  $i_c$  ( $A\ m^{-3}$ ) are the volumetric current densities for the anode and cathode, respectively. It is important to note that the source terms for hydrogen and oxygen are negative due to the chemical reaction consumption, while the source term for water vapour is positive because water is the production. As nitrogen is not involved in the chemical reaction, the source term for nitrogen is zero.

### 3.5.4 Conservation of energy

By applying the same principle, which is used to develop the equation of motion, on energy, the law of conservation of energy for the fluid contained in the volume element can be written as follow:

$$\begin{aligned} \left\{ \begin{array}{l} \text{rate of} \\ \text{internal and} \\ \text{kinetic energy} \\ \text{accumulation} \end{array} \right\} &= \left\{ \begin{array}{l} \text{rate of} \\ \text{internal and} \\ \text{kinetic energy} \\ \text{in by convection} \end{array} \right\} - \left\{ \begin{array}{l} \text{rate of} \\ \text{internal and} \\ \text{kinetic energy} \\ \text{out by convection} \end{array} \right\} \\ &+ \left\{ \begin{array}{l} \text{net rate of} \\ \text{heat addition} \\ \text{by conduction} \end{array} \right\} + \left\{ \begin{array}{l} \text{net rate of} \\ \text{work done by} \\ \text{system on} \\ \text{surroundings} \end{array} \right\} \end{aligned} \quad (3-127)$$

In Eq. (3-127) the kinetic energy is associated with the fluid motion, and the internal energy is related to the random translational and internal motion of the molecules. The equation of energy for a multi-component mixture is given by using the methodology developed by Bird *et al.* [22]:

$$\begin{aligned} \frac{\partial}{\partial t} \rho(U + \frac{1}{2} u^2) &= -\nabla \cdot [\rho(U + \frac{1}{2} u^2) \mathbf{u}] - \nabla \cdot \mathbf{q} - \nabla \cdot (\boldsymbol{\tau} \cdot \mathbf{u}) \\ &+ \nabla \cdot (p \boldsymbol{\delta} \cdot \mathbf{u}) + \sum_{i=1}^n (\rho_i \mathbf{u} \cdot \mathbf{g}_i) + Q_e \end{aligned} \quad (3-128)$$

where  $U$  ( $\text{J kg}^{-1}$ ) is the internal energy per unit of mass of fluid in the volume element,  $Q_e$  ( $\text{J m}^{-3} \text{s}^{-1}$ ) is the heat source term, and  $\mathbf{q}$  ( $\text{J m}^{-2} \text{s}^{-1}$ ) is the heat flux vector.

The term on the left hand side of Eq. (3-128) is the rate of energy gained per unit of volume, while on the right hand side of Eq. (3-128), the first term is the rate of energy input per unit of volume by convection; the second term is the rate of energy input per unit of volume by thermal conduction; the third term is the rate of work done on the fluid per unit of volume by viscous forces; the fourth term is the rate of work done on the fluid per unit of volume by pressure forces; the fifth term is the rate of work done on the fluid per unit of volume by gravitational forces; and the last term is the heat source which accounts for heat generation and consumption due to chemical reactions and Joule heating.

According to Fourier's law, the heat flux vector is expressed in terms of temperature gradients as follow:

$$\mathbf{q} = -k\nabla T \quad (3-129)$$

This equation represents the energy transport by heat conduction, which is used to describe the molecular transport of heat in isotropic media. Expanding Eq. (3-129) to a multi-component mixture gives:

$$\mathbf{q} = -k_i \nabla T + \sum_{i=1}^n \frac{H_i}{M_i} \mathbf{j}_i, \quad i = 1, 2, 3, \dots, n \quad (3-130)$$

where  $k_i$  ( $\text{W m}^{-1} \text{K}^{-1}$ ) and  $H_i$  ( $\text{J mol}^{-1}$ ) are the thermal conductivity and partial molar enthalpy of species  $i$ . The second term on the right hand side represents the heat transport by species diffusion.

Combing the equations of motion and continuity with the equation of energy, the equation of thermal energy can be obtained as follow [22]:

$$\rho \left( \frac{\partial U}{\partial t} + \mathbf{u} \cdot \nabla U \right) = -\nabla \cdot \mathbf{q} - p \nabla \cdot \mathbf{u} - \boldsymbol{\tau} \nabla \cdot \mathbf{u} + Q_e \quad (3-131)$$

The term on the left hand side of the equation above represents the rate of internal energy gained per unit of volume; the first term on the right hand is the rate of internal energy input per unit of volume by conduction; the second term on the right hand is the

reversible rate of internal energy increase per unit of volume by compression; the third term on the right hand is the irreversible rate of internal energy increase per unit of volume by viscous dissipation; and the fourth term on the right hand is the heat source.

Instead of internal energy, Eq. (3-131) can be written in terms of the temperature and heat capacity of the fluid, which becomes more convenient for calculating the temperature profiles. At a constant pressure, the internal energy can be related to the temperature and heat capacity via the following equation:

$$\frac{\partial U}{\partial t} = -p \frac{\partial V}{\partial t} + c_p \frac{\partial T}{\partial t} \quad (3-132)$$

where  $V$  ( $\text{m}^3 \text{ kg}^{-1}$ ) is the volume per unit of mass, and  $c_p$  ( $\text{J mol}^{-1} \text{ K}^{-1}$ ) is the averaged heat capacity of the multi-component mixture at a constant pressure, which can be calculated by the heat capacity and mole fraction of the species of the multi-component mixture:

$$c_p = \sum_{i=1}^n c_{p,i} x_i, \quad i = 1, 2, 3, \dots, n \quad (3-133)$$

With the aid of the equation of continuity  $\rho(dV/dt) = \nabla \cdot \mathbf{v}$ , then multiplying both sides of Eq. (3-132) by the averaged density (could be calculated follow the method shown in Eq. (3-133)) of the multi-component mixture and combining Eq. (3-131) gives:

$$\rho c_p \frac{\partial T}{\partial t} + \rho c_p \mathbf{u} \cdot \nabla T = -\nabla \cdot \mathbf{q} - \boldsymbol{\tau} \nabla \cdot \mathbf{u} + Q_e \quad (3-134)$$

Due to the fact that the second term on the right hand side of the equation above ( $\boldsymbol{\tau} \nabla \cdot \mathbf{v}$ ) is only significant in high speed flow system in which the velocity gradient is large [22], it is reasonable to neglect this term on the purpose of simplification. By simply substituting Eq. (3-129) into Eq. (3-134), a secondary order partial differential equation for temperature profiles can be obtained as follow:

$$\rho c_p \frac{\partial T}{\partial t} + \rho c_p \mathbf{u} \cdot \nabla T - \nabla \cdot (k \nabla T) = Q_e \quad (3-135)$$

For a multi-phase heat transfer process occurred in the porous media, Eq. (3-135) becomes to:

$$\frac{\partial}{\partial t} \left[ \sum_{i=g,l,s} (\varepsilon \rho_i c_{p,i}) T \right] + \nabla \cdot \left[ \sum_{i=g,l} (\varepsilon \rho_i c_{p,i} \mathbf{u}_i) T \right] - \nabla \cdot \left( \sum_{i=g,l,s} k_i \nabla T \right) = Q_e \quad (3-136)$$

where  $\varepsilon$  is the porosity of the porous media, the subscript  $g$ ,  $l$ , and  $s$  refer to phases of gas, liquid and solid, respectively.

It is important to note that the solid phase is not included in the second term on the left hand side of the equation above. This is because the solid phase (porous electrode) does not move. The source term  $Q_e$  ( $\text{J m}^{-3} \text{ s}^{-1}$ ) is responsible for the heat generation and sink due to chemical reaction, latent heat due to phase change, and Joule heating. The heat generation in terms of Joule heating is expressed by the following equation:

$$q_{\text{Joule}} = \sigma \phi^2 \quad (3-137)$$

where  $\sigma$  ( $\text{S m}^{-1}$ ) is the ionic conductivity,  $\phi$  (V) is the potential.

For a fuel cell unit, Joule heating is taken into account in the gas diffusion layer, catalyst layer and membrane. Especially for the catalyst layer where hydrogen or methanol oxidation reaction and oxygen reduction reaction occurred, Joule heating is much significant, which can be calculated by the entropy changes of the reactant and the activation overpotential for each electrode. For a hydrogen fuel cell, Joule heating on both the anode and cathode is expressed as [27]:

$$q_{\text{reaction}}^a = -|i_a| \left( \frac{T \Delta S_a}{2F} \right) \quad (3-138)$$

$$q_{\text{reaction}}^c = -|i_c| \left( |\eta_c| - \frac{T \Delta S_c}{4F} \right) \quad (3-139)$$

where  $\Delta S_a$  and  $\Delta S_c$  ( $\text{J mol}^{-1} \text{ K}^{-1}$ ) are the entropy change for the reaction on anode and cathode, respectively. From the study of Lampinen and Fomino [27], the hydrogen oxidation reaction on anode is endothermic whereas the oxygen reduction reaction is exothermic. The entropy change is  $161.2 \text{ J mol}^{-1} \text{ K}^{-1}$  for the hydrogen oxidation reaction and  $-324.0 \text{ J mol}^{-1} \text{ K}^{-1}$  for the oxygen reduction reaction.

### 3.5.5 Conservation of charge

It is assumed that a finite volume  $dV$  ( $\text{m}^3$ ) carries an amount of charge  $dG_v$  (C). The charge density  $g_v$  ( $\text{C m}^{-3}$ ) is:

$$g_v = \frac{dG_v}{dV} \quad (3-140)$$

Then the total charge of the volume  $V$  is expressed as follow:

$$\int dG_v = \int dV g_v \quad (3-141)$$

The change of total charge in time generates current flow in and/or out of the surface  $dS$  ( $\text{m}^2$ ) surrounding the volume  $dV$ . The expression of conservation of charge is therefore:

$$\frac{d}{dt} \int dV g_v = - \oint dS \cdot \mathbf{i} \quad (3-142)$$

where  $\mathbf{i}$  ( $\text{A m}^{-2}$ ) is the current density vector. By using the Gauss divergence theorem and assuming that the volume  $V$  did not change with time, Eq. (3-142) can be rewritten as:

$$\frac{d}{dt} \int dV g_v = - \nabla \cdot \mathbf{i} \quad (3-143)$$

Assuming the charge density at any location does not change with time and adding a source term  $Q_i$  ( $\text{A m}^{-3}$ ), Eq. (3-142) can be simplified as follow:

$$\nabla \cdot \mathbf{i} = Q_i \quad (3-144)$$

If no external source applied,  $Q_i$  is equal to the volume current density  $i_v$  ( $\text{A m}^{-3}$ ). At stationary condition, the current density does not depend on time.

$$\nabla \cdot \mathbf{i} = 0 \quad (3-145)$$

The current density vector  $\mathbf{i}$  can be related to the electric field  $\mathbf{E}$  ( $\text{V m}^{-1}$ ) and conductivity  $\sigma$  ( $\text{S m}^{-1}$ ) by Ohm's law as:

$$\mathbf{i} = \sigma \mathbf{E} \quad (3-146)$$

At a specific point within the electric field, the voltage is equal to the negative gradient of the potential shown as follow:

$$\mathbf{E} = -\nabla \phi \quad (3-147)$$

Substituting Eq. (3-146) and Eq. (3-147) into Eq. (3-144) gives:

$$\nabla \cdot \mathbf{i} = \nabla(-\sigma \nabla \phi) = Q_i \quad (3-148)$$

Applying Eq. (3-148) on the solid (electrode) and electrolyte (membrane and ionomer) phases, respectively, two sub-equations are obtained [28]:

$$\nabla \cdot \mathbf{i}_s = \nabla(-\sigma_s^{eff} \nabla \phi_s) = Q_s \quad (3-149)$$

$$\nabla \cdot \mathbf{i}_M = \nabla(-\sigma_M^{eff} \nabla \phi_M) = Q_M \quad (3-150)$$

where  $\sigma_s^{eff}$  and  $\sigma_M^{eff}$  ( $S m^{-1}$ ) are the effective electrical conductivity for the solid phase and electrolyte conductivity for the membrane and ionomer, respectively. For any volume of the computational domain the electronic and the ionic currents generated are equal, leading to:

$$\nabla \cdot \mathbf{i}_s + \nabla \cdot \mathbf{i}_M = 0 \quad (3-151)$$

In a porous media, the source terms  $Q_s$  and  $Q_M$  can be expressed in terms of the volumetric current for the electrode and electrolyte, respectively. The total current generated in the anode must be equal to the total current consumed in the cathode. In the situation of no external resource the conservation of charge requires that:

$$Q_s = -Q_M \quad (3-152)$$

$$\int_{V_{CL,a}} i_a dV = - \int_{V_{CL,c}} i_c dV \quad (3-153)$$

The average volumetric current density  $i_{avg}$  ( $A m^{-3}$ ) is expressed as:

$$i_{avg} = \frac{1}{V_{CL,a}} \int_{V_{CL,a}} i_a dV = - \frac{1}{V_{CL,c}} \int_{V_{CL,c}} i_c dV \quad (3-154)$$

where  $V_{CL,a}$  and  $V_{CL,c}$  ( $m^3$ ) are the volume of the catalyst layer of anode and cathode, respectively. The surface overpotential, the driving force for the transfer current density in an electrochemical reaction, is defined as [26]:

$$\eta = \phi_s - \phi_M - E^{eq} \quad (3-155)$$

where  $E^{eq}$  (V) is the equilibrium potential, which is zero on the cathode and is equal to the theoretical cell potential at a given temperature and pressure on the cathode side calculated by the Nernst equation. The surface overpotential accounts for activation and concentration losses, the related thermodynamics will be explained in the next section, Section 3.5.2 in particular.

### 3.6 Constitutive relations and model parameters

It is necessary and important to estimate and select the parameters rigorously in a particular model as the parameters input may have a strong influence on the final simulation results. Sometimes, the unreasonable parameters make errors in the simulation process. The parameters represent the physical and chemical properties of the materials and reactants involved, therefore it is important to fully understand the relationships between every parameter and the operating conditions, such as temperature, pressure and relative humidity. The model can be simplified by defining some insensitive parameters as constants. In this section a detailed description on the parameters obtained is presented.

#### 3.6.1 Kinetic parameters

The electrochemical reaction kinetics described by both the Butler-Volmer equation and the agglomerate model have been given in Section 3.1. Two important kinetic parameters, the transfer coefficient and exchange current density, are investigated in this section. At this point, it is important to highlight that the kinetics parameters used in this work are identical to that in an acid system.

##### *Transfer coefficient*

The transfer coefficients are first shown in Eq. (3-5) and Eq. (3-6) to account for the electrical effects on the change of Gibbs free energy in an electrochemical reaction. As shown in Eq. (3-12) and Eq. (3-13), forward and backward reactions co-exist in the oxidation reaction on anode and the reduction reaction on cathode. The transfer coefficient for reduction reaction,  $\alpha_{Rd}$ , is assumed to be equal to the transfer coefficient for oxidation reaction,  $\alpha_{Ox}$ , for both anode and cathode by Sousa *et al.* [29], leading to  $\alpha_{Rd,a} = \alpha_{Ox,a} = \alpha_a$  and  $\alpha_{Rd,c} = \alpha_{Ox,c} = \alpha_c$ . In this study,  $\alpha_{Rd} + \alpha_{Ox}$  is set to unity according to the assumption in the paper of Sun *et al.* [3]. For oxygen reduction reaction on

cathode:  $\alpha_{Rd,c} = \alpha_c$ ,  $\alpha_{Ox,c} = 1 - \alpha_c$ ; for hydrogen oxidation reaction on anode:  $\alpha_{Ox,a} = \alpha_a$ ,  $\alpha_{Rd,a} = 1 - \alpha_a$ .

It is well known that the transfer coefficient have a significant influence on the current density. However, it is very difficult to predict the accurate value of the transfer coefficient for a particular system as it is a function of numerous conditions, such as temperature, pressure, catalyst structure, and reactant impurity. Parthasarathy *et al.* [30] found that the Tafel slope is lower at higher cell voltages and higher at lower at lower cell voltages. Based on the experimental measurement of Parthasarathy *et al.* [30], the cathode transfer coefficient was regressed by Sun *et al.* [3] as follow:

$$\alpha_c = 0.495 + 2.3 \times 10^{-3}(T - 300) \quad (3-156)$$

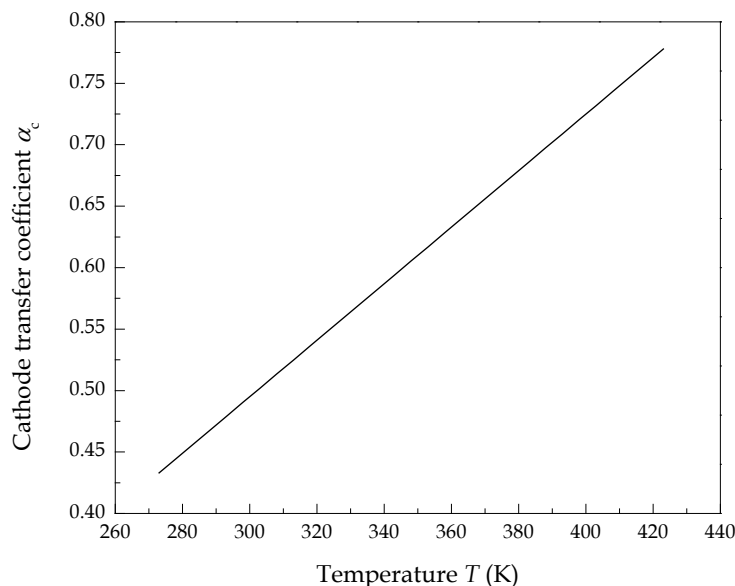


Figure 3-5 Temperature dependent transfer coefficient of anode and cathode

In comparison with the cathode transfer coefficient, the anode transfer coefficient changes slightly as the operating condition changed. Therefore, we applied the value reported by Bernardi and Verbrugge [31] of  $\alpha_a = 0.5$ . The effect of temperature on the cathode transfer coefficient is plotted in Figure 3-5.

### Exchange current density

As shown in Section 3.1.1, the exchange current density is the current densities for anode and cathode in case of both the forward and backward reactions are equally. It is analogous to the rate constant in chemical reactions and is a function of operating

temperature and partial pressure of the reactant. The exchange current density can be expressed by the following equation [26]:

$$i_0 = i_0^{\text{ref}} a_{\text{CL}} \left( \frac{p_r}{p_r^{\text{ref}}} \right)^\gamma \exp \left[ -\frac{E}{RT} \left( 1 - \frac{T}{T^{\text{ref}}} \right) \right] \quad (3-157)$$

where  $i_0^{\text{ref}}$  ( $\text{A m}^{-2}$ ) is the reference exchange current density per unit catalyst surface area obtained at the reference temperature of 25 °C and pressure of 1.0 atm,  $a_{\text{CL}}$  ( $\text{m}^{-1}$ ) is the specific area of the catalyst layer, which was given in Section 3.2.3,  $p_r$  (kPa) is the reactant partial pressure,  $p_r^{\text{ref}}$  (kPa) is the reference pressure,  $\gamma$  (0.5 for hydrogen oxidation reaction and 1.0 for oxygen reduction reaction [32-34]) is the pressure dependency coefficient,  $T^{\text{ref}}$  (298K) is the reference temperature,  $E$  ( $\text{kJ mol}^{-1}$ ) is the activation energy, it was found to be 72.4  $\text{kJ mol}^{-1}$  for oxygen reduction on cathode [35], and 16.9  $\text{kJ mol}^{-1}$  for hydrogen oxidation on anode [33].

Exchange current density is a reflection of the activity of the surface of the electrode. Higher exchange current density means lower energy barrier that the charge must overcome in moving from electrolyte to the catalyst surface. In a hydrogen/oxygen fuel cell, the exchange current density of the anode is several orders of magnitude larger than that of the cathode. In other words, more current is generated at a fixed overpotential with a higher exchange current density, and the cathode overpotential is much larger than the anode overpotential. For this reason, the polarisation curve is mainly determined by the oxygen reduction reaction (ORR) at cathode. According to the literatures [31, 36, 37], the reference exchange current density ( $i_0^{\text{ref}}$ ) for anode is 1.0  $\text{A cm}^{-2}$  whereas it is much small for cathode and can be related with temperature as follow:

$$i_0^{\text{ref}} = 10^{(3.507 - \frac{4001}{T})} \quad (3-158)$$

The relationship between the operating temperature and cathode reference exchange current density is shown in Figure 3-6.

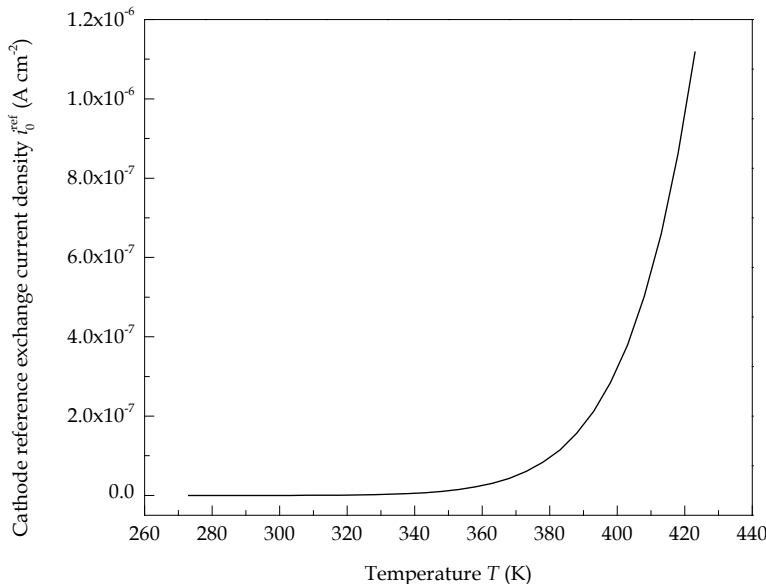


Figure 3-6 Temperature dependent cathode reference exchange current density

### 3.6.2 Open circuit potential

The open circuit potential is the theoretical or equilibrium potential of an electrode in absence of external current flow to or from the electrode, which can be calculated based on the knowledge of thermodynamics shown as follow. The portion of the reaction enthalpy that can be converted to electricity in a fuel cell corresponds to Gibbs free energy given by the following equation:

$$\Delta G = \Delta H - T\Delta S \quad (3-159)$$

As demonstrated in the equation above, Gibbs free energy  $\Delta G$  is not equal to the total reaction enthalpy  $\Delta H$  because there are some irreversible losses in energy conversion due to creation of entropy  $\Delta S$ . According to the stoichiometry of the reactions, the changes of enthalpy and entropy are calculated as follow:

$$\Delta H = \Delta H^0 + \int_{T_{\text{ref}}}^T c_{p,H_2O} dT - \int_{T_{\text{ref}}}^T c_{p,H_2} dT - \frac{1}{2} \int_{T_{\text{ref}}}^T c_{p,O_2} dT \quad (3-160)$$

$$\Delta S = \Delta S^0 + \int_{T_{\text{ref}}}^T \frac{1}{T} c_{p,H_2O} dT - \int_{T_{\text{ref}}}^T \frac{1}{T} c_{p,H_2} dT - \frac{1}{2} \int_{T_{\text{ref}}}^T \frac{1}{T} c_{p,O_2} dT \quad (3-161)$$

where  $\Delta H^0$  ( $\text{J mol}^{-1}$ ) and  $\Delta S^0$  ( $\text{J mol}^{-1} \text{K}^{-1}$ ) are the enthalpy and entropy at standard conditions (1.0 atm, 25 °C), respectively. In general, electrical work is a product of charge and potential:

$$W_{el} = qE \quad (3-162)$$

where  $W_{el}$  ( $\text{J mol}^{-1}$ ) is the electrical work,  $q$  is the charge ( $\text{C mol}^{-1}$ ) and  $E$  (V) is the potential.

The total charge transferred in a fuel cell reaction per mole of  $\text{H}_2$  consumed is equal to:

$$q = nNq_{el} \quad (3-163)$$

where  $n$  is the number of electrons per molecule of hydrogen ( $n = 2$ ),  $N$  is the Avogadro's number ( $N = 6.022 \times 10^{23}$  molecules  $\text{mol}^{-1}$ ),  $q_{el}$  is the charge per electron ( $q_{el} = 1.602 \times 10^{-19} \text{ C electron}^{-1}$ ). Because  $q_{el}N = 9.65 \times 10^{23} \text{ C mol}^{-1}$  is the Faraday's constant  $F$ , the electrical work is therefore becomes to:

$$W_{el} = nFE \quad (3-164)$$

As mentioned previously, the maximum amount of electrical energy generated in a fuel cell is equal to the Gibbs free energy.

$$W_{el} = -\Delta G \quad (3-165)$$

The theoretical potential of fuel cell is then changed to:

$$E = -\frac{\Delta G}{nF} \quad (3-166)$$

The temperature dependent theoretical cell potential can be calculated by substituting Eq. (3-159) into Eq. (3-166) yields:

$$E = -\frac{\Delta H - T\Delta S}{nF} \quad (3-167)$$

The theoretical cell potential also varies with reactant pressure. Assuming the reactants and product behave like ideal gas, the change in Gibbs free energy in an isothermal condition is expressed by the following equation:

$$dG = RT \frac{dp}{p} \quad (3-168)$$

After integration:

$$G = G^0 + RT \ln\left(\frac{p}{p^0}\right) \quad (3-168)$$

where  $G^0$  ( $\text{J mol}^{-1}$ ) is the Gibbs free energy at standard condition ( $25^\circ\text{C}$  and  $1.0 \text{ atm}$ ), and  $p^0$  ( $1.0 \text{ atm}$ ) is the reference or standard pressure. For any chemical reaction:



The change in Gibbs free energy is the change between products and reactants:

$$\Delta G = mG_C + nG_D - jG_A - kG_B \quad (3-170)$$

Substituting the equation above into Eq. (3-168):

$$G = G^0 + RT \ln\left[\frac{\left(\frac{p_C}{p^0}\right)^m \left(\frac{p_D}{p^0}\right)^n}{\left(\frac{p_A}{p^0}\right)^j \left(\frac{p_B}{p^0}\right)^k}\right] \quad (3-171)$$

This is known as the Nernst equation. Assuming the water produced in gas phase in Eq. (1-3), for the hydrogen/oxygen fuel cell, the open circuit potential (OCP) can be calculated as:

$$E^{OCP} = -\frac{(\Delta H - T\Delta S)}{nF} + \frac{RT}{nF} \ln\left[\frac{p_{H_2} p_{O_2}^{0.5}}{p_{H_2O}}\right] \quad (3-172)$$

For the hydrogen oxidation process, the enthalpy is the difference between the heats of formation of products and reactants, which can be expressed as follow:

$$\Delta H = h_{f,H_2O} - h_{f,H_2} - 1/2 h_{f,O_2} \quad (3-173)$$

Similarly, the entropy is the difference between entropies of products and reactants:

$$\Delta S = s_{f,H_2O} - s_{f,H_2} - 1/2 s_{f,O_2} \quad (3-174)$$

where  $h_{f,H_2O}$ ,  $h_{f,H_2}$  and  $h_{f,O_2}$  ( $\text{J mol}^{-1}$ ) are the enthalpies of water, hydrogen and oxygen, and  $s_{f,H_2O}$ ,  $s_{f,H_2}$  and  $s_{f,O_2}$  ( $\text{J mol}^{-1} \text{ K}^{-1}$ ) are the entropies of water, hydrogen and oxygen respectively. The values of enthalpies and entropies for reaction reactants and products at standard condition ( $25^\circ\text{C}$ ,  $1.0 \text{ atm}$ ) are shown in Table 3-2.

Table 3-2 Enthalpies and entropies of formation for reactants and products at standard condition [26]

	$h_f^0$ (kJ mol <sup>-1</sup> )	$s_f^0$ (kJ mol <sup>-1</sup> K <sup>-1</sup> )
Hydrogen	0	0.13066
Oxygen	0	0.20517
Liquid water	-286.02	0.06996
Water vapour	-241.98	0.18884

Assuming water is generated as liquid, the enthalpy and entropy for hydrogen oxidation reaction at standard condition are  $\Delta H^0 = -286.02$  kJ mol<sup>-1</sup> and  $\Delta S^0 = -0.1633$  kJ mol<sup>-1</sup> K<sup>-1</sup> according to Eq. (3-173) and Eq. (3-173).

The open circuit potential changes with temperature. The enthalpies and entropies of reaction reactants and products are functions of temperature, which are shown as:

$$h_f = h_f^0 + \int_{298.15}^T c_p dT \quad (3-175)$$

$$s_f = s_f^0 + \int_{298.15}^T \frac{1}{T} c_p dT \quad (3-176)$$

The specific heat of gas reactant and product can be calculated by the following empirical relationship [26]:

$$c_p = a + bT + cT^2 \quad (3-177)$$

where  $a$ ,  $b$ , and  $c$  are the empirical coefficients as shown in Table 3-3.

Table 3-3 Empirical coefficients for temperature dependent specific heat [26]

	$a$	$b$	$c$
Hydrogen	28.914	-0.00084	$2.01 \times 10^{-6}$
Oxygen	25.845	0.01298	$-3.90 \times 10^{-6}$
Water vapour	30.626	0.00962	$1.18 \times 10^{-6}$

Note: the unit of the specific heat is (J mol<sup>-1</sup> K<sup>-1</sup>)

The open circuit potential is therefore can be calculated by Eq. (3-172). As shown in Figure 3-7, the open circuit potential (OCP) decreases with temperature and the OCP is higher when the production generated as liquid water in comparison with water vapour.

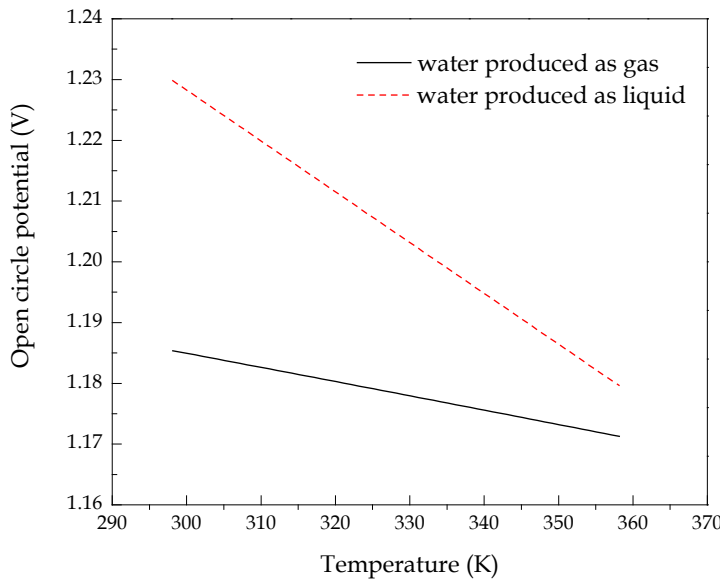


Figure 3-7 Temperature dependent open circuit potential (OCP) for hydrogen oxidation reaction

### 3.6.3 Reactant solubility and diffusivity in Nafion®

As described in [Section 3.1.2](#), reactant gases must transport through the ionomer film surrounding the agglomerate before reacted on the surface of platinum catalyst particles inside the agglomerate. Due to the fact that the solubility and diffusivity of hydrogen through Nafion® is several times larger than that of oxygen, oxygen solubility and diffusivity through Nafion® therefore attracts more attentions [31, 36]. For oxygen diffusivity through the Nafion® membrane and ionomer, Marr and Li [36] developed a temperature dependent equation by fitting the experimental data published by Parthasarathy *et al.* [30]. Suzuki *et al.* [38] reported that the oxygen diffusion coefficient is proportional to the power of the membrane water content. Combining these two equations will account for both the effects of temperature and water content of membrane and ionomer. Therefore, we have adopted an equation to obtain the oxygen diffusion coefficient as follow:

$$D_{O_2-M} = 1.3926 \times 10^{-10} \lambda^{0.708} \exp\left(\frac{T - 273.15}{106.65}\right) - 1.6461 \times 10^{-10} \lambda^{0.708} + 5.2 \times 10^{-10} \quad (3-175)$$

The oxygen diffusion coefficient obtained by Eq. (3-175) is validated by the experimental data by Takamura *et al.* [39] in [Figure 3-8](#).

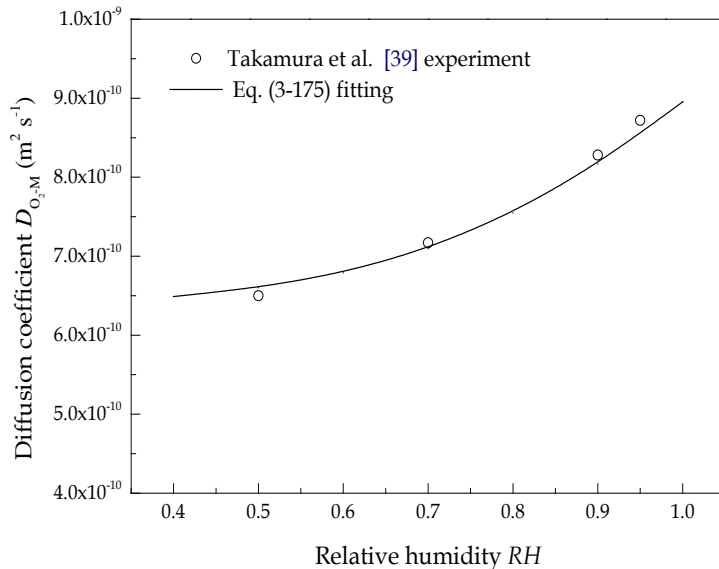


Figure 3-8 Relative humidity dependent oxygen diffusivity through Nafion® membrane/ ionomer

Nonoyama *et al.* [40] found that the Henry's constant for oxygen solubility in the Nafion® ionomer depends on the relative humidity. In order to investigate the effect of water content on the Henry's constant, we develop an equation by fitting the results of Suzuki *et al.* [38] based on the equation of Marr and Li [36].

$$H_{O_2} = 0.11552 \exp(14.1 + 0.0302\lambda - \frac{666}{T}) \quad (3-176)$$

The Henry's constant for oxygen dissolving in Nafion® ionomer, which is calculated by Eq. (3-176), is validated by the simulation results of Suzuki *et al.* [38] in Figure 3-9.

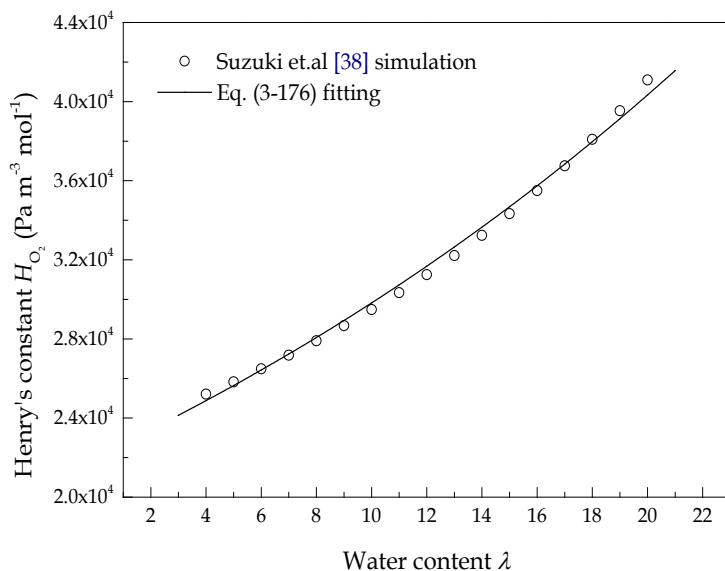


Figure 3-9 Water content dependent Henry's constant for O<sub>2</sub> solubility in Nafion® membrane/ionomer

### 3.6.4 Oxygen diffusion coefficient in liquid water

The intrinsic diffusion coefficient of oxygen diffusing through the liquid water is calculated by the following empirical equations [40, 41]:

$$D_{O_2-w} = 7.4 \times 10^{-8} T \frac{\sqrt{\psi_w M_w}}{\mu_w (V_{O_2})^{0.6}} \quad (3-177)$$

$V_{O_2}$  ( $\text{cm}^3 \text{ mol}^{-1}$ ) is the mole volume of the solute (dissolved oxygen) as liquid at its normal boiling point,  $\psi_w$  is the association parameter for the solvent (2.6 for water),  $\mu_w$  ( $\text{mPa s}$ ) is the temperature dependent viscosity of the solvent,  $T$  (K) is the operating temperature,  $M_w$  is the molar mass of the solvent ( $18 \text{ g mol}^{-1}$  for water).

Figure 3-10 shows the oxygen diffusion coefficient in liquid water in comparison with that in Nafion® membrane and ionomer. It is clear that oxygen diffusion coefficient increases as the temperature increases. Oxygen diffusing in liquid water is much faster than in Nafion® membrane and ionomer, for example at 340 K, the oxygen diffusion coefficient in liquid water is almost ten times larger than that in Nafion® membrane and ionomer. As a result, the thickness of the ionomer film has a greater impact on oxygen transport than the liquid water film.

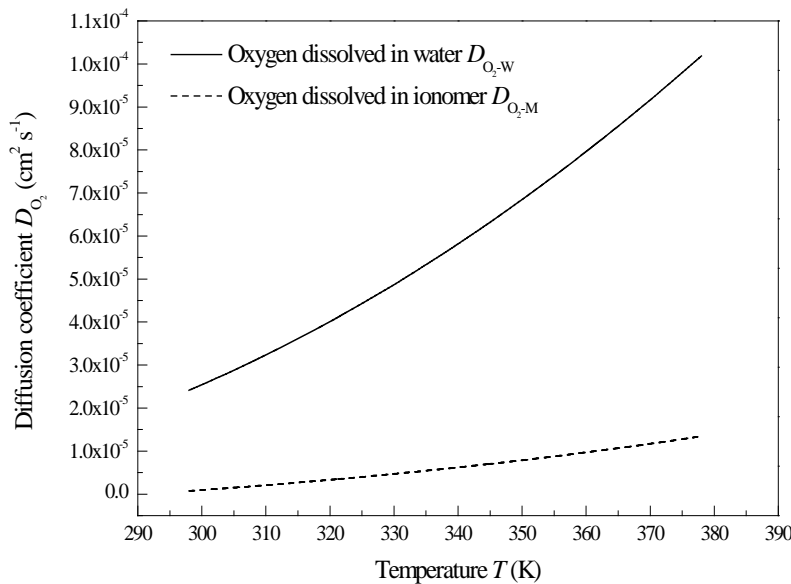


Figure 3-10 Temperature dependent oxygen diffusion coefficients in liquid water and Nafion® membrane/ ionomer

### 3.6.5 Multicomponent diffusivity

The intrinsic binary diffusion coefficients for all pairs of gas species  $D_{ij}$  ( $\text{m}^2 \text{s}^{-1}$ ) can be calculated using the equation developed by Bird *et al.* [22] as follow:

$$D_{ij}^0 = 1.8583 \times 10^{-7} \sqrt{T^3 \left( \frac{1}{M_i} + \frac{1}{M_j} \right)} \frac{1}{p \sigma_{ij}^2 \Omega_{ij}} \quad (3-178)$$

where

$$\sigma_{ij} = \frac{1}{2} (\sigma_i + \sigma_j), \quad \varepsilon_{ij} = \sqrt{\varepsilon_i \varepsilon_j} \quad (3-179)$$

$\Omega_i$  and  $\Omega_{ij}$  are functions of the reduced temperature  $T_i^*$  and  $T_{ij}^*$ .

$$T_i^* = \frac{\kappa}{\varepsilon_i} T, \quad T_{ij}^* = \frac{\kappa}{\varepsilon_{ij}} T \quad (3-180)$$

There are empirical expressions for calculating  $\Omega_i$  and  $\Omega_{ij}$  written as:

$$\Omega_i = A / (T_i^*)^B + C / \exp(T_i^* D) + E / \exp(T_i^* F) \quad (3-181)$$

$$\Omega_{ij} = A / (T_{ij}^*)^B + C / \exp(T_{ij}^* D) + E / \exp(T_{ij}^* F) + G / \exp(T_{ij}^* H) \quad (3-182)$$

The parameters are listed in Table 3-4.

Table 3-4 Lennard-Jones potential parameters [22]

Species $i$	$M_i$	$\sigma_i$	$\varepsilon_i / \kappa$
H <sub>2</sub>	2.016	2.915	38.0
O <sub>2</sub>	32.000	3.433	113.0
N <sub>2</sub>	28.013	3.667	99.8
H <sub>2</sub> O	18.000	2.641	809.1
$\Omega_i$	A=1.16145; B=0.14874; C=0.52487; D=0.77320; E=2.16178; F=2.43787		
$\Omega_{i,j}$	A=1.06036; B=0.15610; C=0.19300; D=0.47635; E=1.03587; F=1.52996; G=1.76474; H=3.89411		

The temperature dependent binary diffusion coefficients for all pairs of gas species at 1.0 atm are shown in Figure 3-11.

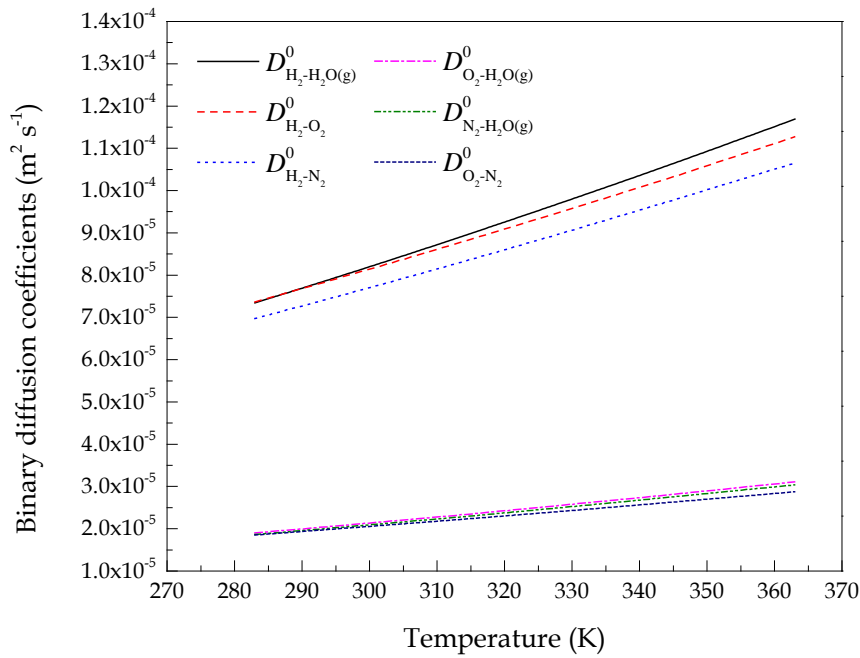


Figure 3-11 Temperature dependent binary diffusion coefficients for all pairs of gas species at 1.0 atm

### 3.6.6 Knudsen diffusion

Knudsen diffusion is a means of diffusion that occurs when the scale length of a system is comparable to or smaller than the mean free path of the particles involved. Knudsen effect on reactant gas diffusion is taken into account when the Knudsen number ( $K_n$ ) is greater than 0.1 [42, 43]. The Knudsen number and Knudsen diffusion coefficient of oxygen diffusion in porous media is [7, 9]:

$$K_n = \frac{k_B T}{\sqrt{2\pi p} \sigma_{ii} d_{avg}} \quad (3-183)$$

$$D_{K_n, O_2} = \frac{d_{avg}}{3} \sqrt{\frac{8RT}{\pi M_{O_2}}} \quad (3-184)$$

where  $k_B$  ( $1.38065 \times 10^{-23}$  J K<sup>-1</sup>) is the Boltzmann constant,  $\sigma_{ii}$  (m) is the particle diameter, and  $d_{avg}$  (m) is the average pore diameter in the catalyst layer, which can be calculated as [7, 9]:

$$d_{avg} = \frac{4}{3} \frac{\varepsilon_{CL}}{1 - \varepsilon_{CL}} r_{agg} \quad (3-185)$$

where  $\varepsilon_{CL}$  and  $r_{agg}$  (m) are the porosity of the catalyst layer and the radius of the agglomerate, respectively.

The intrinsic oxygen diffusion coefficient in the gas mixture is:

$$D_{O_2-g}^0 = \frac{1 - x_{O_2}}{\frac{x_{N_2}}{D_{O_2-N_2}^0} + \frac{x_{H_2O}}{D_{O_2-H_2O}^0}} \quad (3-186)$$

where the intrinsic binary diffusion coefficients  $D_{O_2-N_2}^0$  and  $D_{O_2-H_2O}^0$  are shown in [Section 3.5.5](#). Then the equivalent diffusion coefficient of oxygen in the porous media is:

$$\frac{1}{D_{O_2-g,e}^0} = \frac{1}{D_{O_2-g}^0} + \frac{1}{D_{K_n,O_2}} \quad (3-187)$$

The oxygen diffusion coefficients through the void space of porous electrode at various temperatures, which is obtained from [Eq. \(3-187\)](#), are shown in [Figure 3-12](#). It is clear the Knudsen effect cannot be neglected, especially at higher temperature.

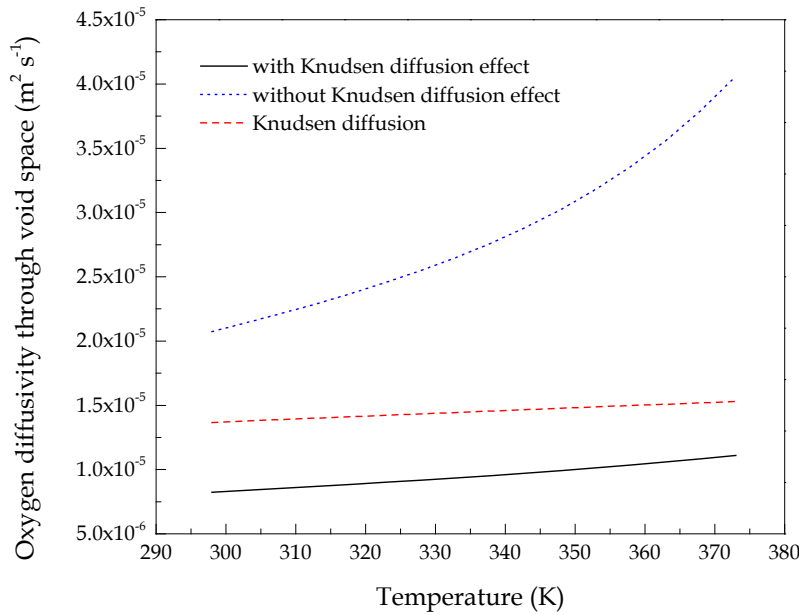


Figure 3-12 Temperature dependent oxygen diffusion coefficients through void space of porous electrode

### 3.6.7 Ionic conductivity

Proton transport between agglomerate requires sufficient ionomer films surrounding agglomerates. As the thickness of the ionomer film decreases, the contact between agglomerates decreases, which leads to a decrease in proton transport. The effective ionic conductivity of the catalyst layer,  $\sigma_M^{eff}$  ( $S\ m^{-1}$ ), can be obtained using the equation of Kamarajugadda *et al.* [44] instead of Bruggeman correction shown as follow:

$$\sigma_M^{eff} = (1 - \varepsilon_{CL}) \left[ 1 + \frac{(\varepsilon_{agg,M} - 1)}{(1 + \delta_M / r_{agg} + a_0)^3} \right] \sigma_M \quad (3-188)$$

where  $\varepsilon_{agg,M}$  is the volume fraction of ionomer in agglomerate,  $\delta_M$  (m) is the thickness of the ionomer film,  $r_{agg}$  (m) is the radius of agglomerate. The values of the parameters of  $\varepsilon_{agg,M}$ ,  $\delta_M$  and  $r_{agg}$  are associated with the structure of catalyst layer, which are shown in Section 3.2. Note that Eq. (3-188) is developed by improving the previous equation of Jaouen *et al.* [41]. In order to capture the trend of the relationship between  $\delta_M$  and  $\sigma_M^{eff}$  ( $\delta_M \rightarrow 0, \sigma_M^{eff} \rightarrow 0$ ), the dimensionless parameter  $a_0$  is added, which is given by:

$$a_0 = \min[0, (\frac{\delta_M}{r_{agg}} + \sqrt[3]{(1 - \varepsilon_{agg,M})} - 1)] \quad (3-189)$$

The intrinsic ionic conductivity,  $\sigma_M$  ( $S\ m^{-1}$ ), strongly depends on temperature and water content, which is expressed as:

$$\sigma_M = \exp \left[ 1268 \left( \frac{1}{303} - \frac{1}{T} \right) \right] (0.5139\lambda - 0.326) \quad (3-190)$$

The dimensionless effective ionic conductivity of cathode catalyst layer with different ionomer film thicknesses is shown in Figure 3-13.

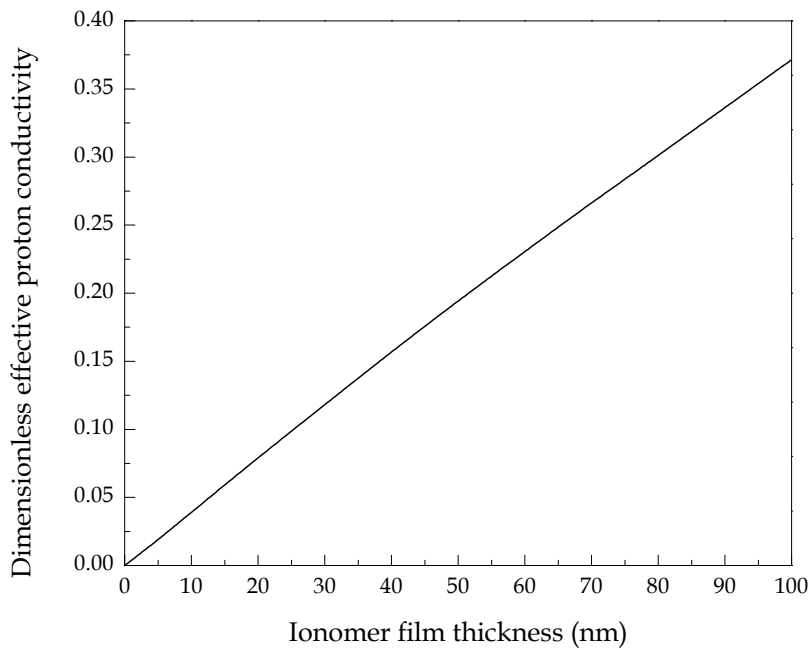


Figure 3-13 Effect of ionomer film thickness on dimensionless effective ionic conductivity of cathode catalyst layer ( $m_{\text{Pt}} = 0.4 \text{ mg cm}^{-2}$ ,  $f = 0.3$ ,  $l_{\text{CL}} = 15 \mu\text{m}$ ,  $r_{\text{agg}} = 1.0 \mu\text{m}$ )

### 3.6.8 Electronic conductivity

The electronic conductivities for gas diffusion layer and catalyst layer are given in this section. For gas diffusion layer, a constant value of  $1250 \text{ S m}^{-1}$  is adopted [45]. For catalyst layer, the electronic conductivity depends on the composition, e.g. the volume fractions of the components responsible for the conductivity. The effective electronic conductivity is therefore obtained using the following equation [46]:

$$\sigma_s^{\text{eff}} = \sigma_s \frac{2 - 2\varepsilon_e}{\varepsilon_e + 2} \quad (3-191)$$

where  $\sigma_s$  ( $\text{S m}^{-1}$ ) is the electronic conductivity of the solid phase (platinum dispersed carbon in the catalyst layer),  $\varepsilon_e$  is the volume fraction of the non-conductor materials, e.g. ionomer and void space in the catalyst layer.

The electronic conductivity of Vulcan XC-72 carbon black is  $450 \text{ S m}^{-1}$  reported by Pantea *et al.* [47], and the electronic conductivity of platinum is regressed from the experimental data provide by Powel and Tye [48] shown as follow:

$$\sigma_{\text{Pt}} = 1.7209 \times 10^9 T^{(-0.9259)} \quad (3-192)$$

The electronic conductivity calculated by Eq. (3-192) is validated by the experimental data in Figure 3-14.

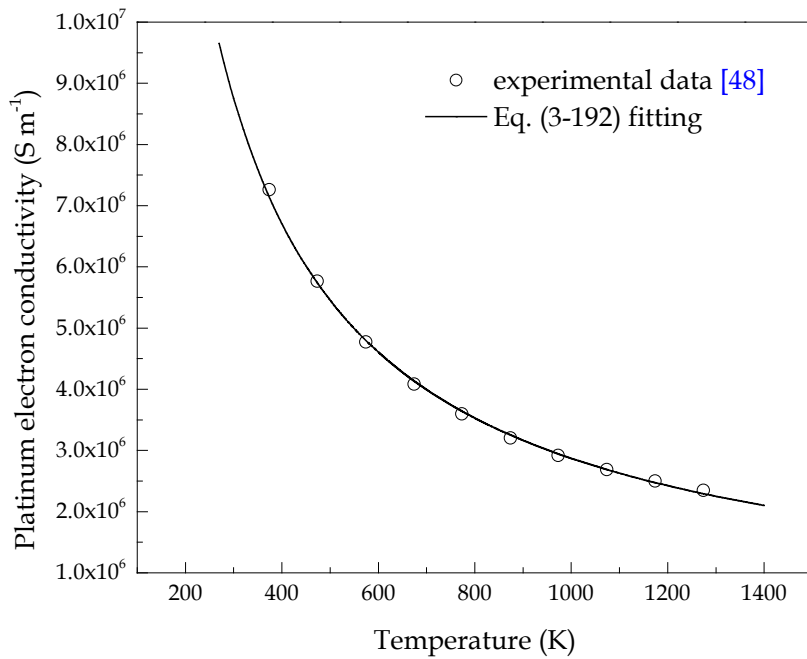


Figure 3-14 Temperature dependent platinum electronic conductivity

### 3.6.9 Specific heat capacity and thermal conductivity

The specific heat capacity and the thermal conductivity of the gas mixture are obtained by using an empirical equation developed by Wike [49],

$$c_p^g = \sum_i x_i c_{p,i}^g, \quad k^g = \sum_i \frac{x_i k_i}{\sum_j x_j \Phi_{ij}} \quad (3-193)$$

in which

$$\Phi_{ij} = \frac{1}{\sqrt{8}} \left(1 + \frac{M_i}{M_j}\right)^{-0.5} \left[1 + \left(\frac{k_i}{k_j}\right)^{0.5} \left(\frac{M_j}{M_i}\right)^{0.25}\right]^2, \quad \Phi_{ji} = \frac{k_j}{k_i} \frac{M_i}{M_j} \Phi_{ij} \quad (3-194)$$

where  $c_p^g$  ( $\text{J mol}^{-1} \text{ K}^{-1}$ ) is the specific heat capacity of the gas mixture,  $x_i$  is the mole fraction of species  $i$  in gas mixture,  $c_{p,i}^g$  ( $\text{J mol}^{-1} \text{ K}^{-1}$ ) is the specific heat capacity of species  $i$  in gas mixture,  $k^g$  ( $\text{W m}^{-1} \text{ K}^{-1}$ ) is the thermal conductivity of the gas mixture,  $k_i$  ( $\text{W m}^{-1} \text{ K}^{-1}$ ) is the thermal conductivity of species  $i$  in gas mixture,  $M_i$  ( $\text{kg mol}^{-1}$ ) is the molecular weight of species  $i$ .

The expressions for the specific heat capacities of each gas component including hydrogen, oxygen, nitrogen and water vapour are obtained by fitting the experimental data, which are compared in Figure 3-15.

$$c_{p,H_2}^g = 1.914 \times 10^{-6} T^2 - 8.314 \times 10^{-4} T + 28.890 \quad (3-195)$$

$$c_{p,O_2}^g = -4.281 \times 10^{-6} T^2 + 1.371 \times 10^{-2} T + 25.431 \quad (3-196)$$

$$c_{p,N_2}^g = 1.788 \times 10^{-5} T^2 + 2.924 \times 10^{-3} T + 27.848 \quad (3-197)$$

$$c_{p,H_2O}^g = 1.180 \times 10^{-6} T^2 + 9.621 \times 10^{-3} T + 30.326 \quad (3-198)$$

The specific heat capacities of solid and liquid phases changes slightly with temperature. Consequently, the specific heat capacities of platinum, carbon black, liquid water and membrane/ionomer are assumed as temperature independent constants shown in Table 3-5.

Also, the expressions for the thermal conductivities of hydrogen, oxygen, nitrogen and water vapour are obtained by fitting the experimental data shown in Figure 3-16.

$$k_{H_2} = 3.777 \times 10^{-4} T + 7.444 \times 10^{-2} \quad (3-199)$$

$$k_{O_2} = 6.204 \times 10^{-5} T + 8.83 \times 10^{-3} \quad (3-200)$$

$$k_{N_2} = 5.453 \times 10^{-5} T + 1.088 \times 10^{-2} \quad (3-201)$$

$$k_{H_2O}^g = 1.188 \times 10^{-4} T - 2.404 \times 10^{-2} \quad (3-202)$$

Table 3-5 Specific heat capacities of platinum, carbon black, membrane/ionomer and liquid water [14]

$c_p$ (J kg <sup>-1</sup> K <sup>-1</sup> )	
platinum	$1.3 \times 10^2$
carbon black	894.4
membrane/ionomer	1090.0
liquid water	4187.0

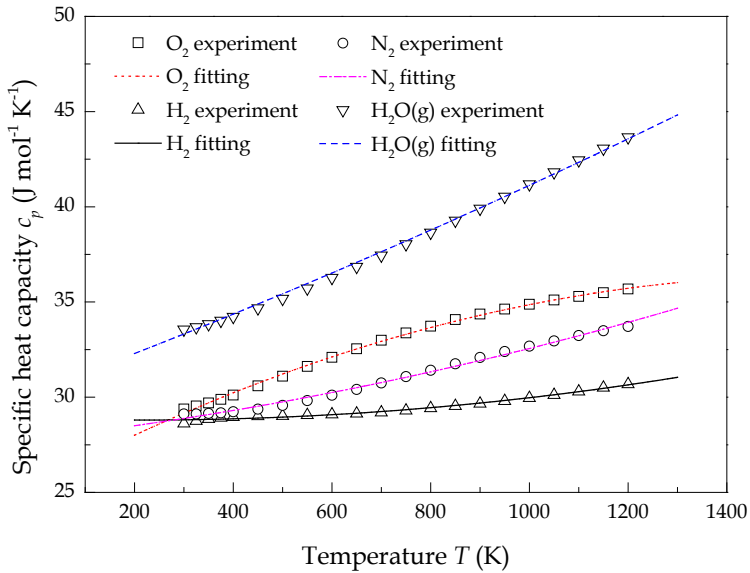


Figure 3-15 Temperature dependent specific heat capacities of hydrogen, oxygen, nitrogen and water vapour [50]

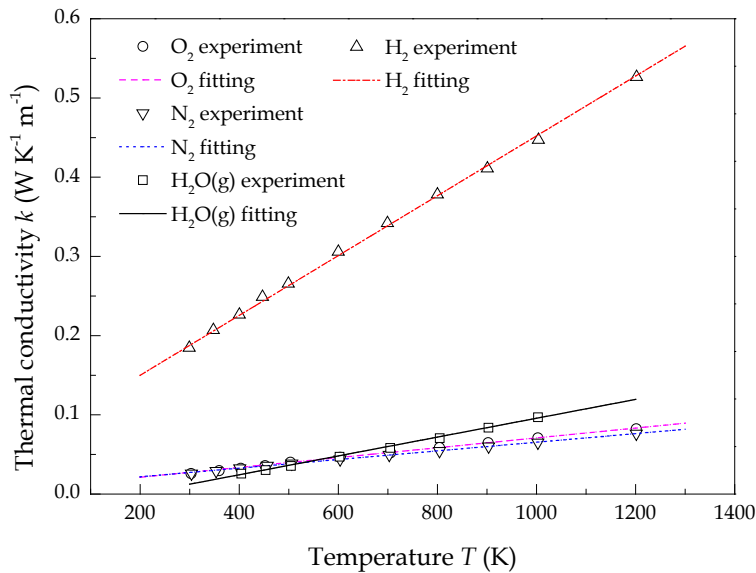


Figure 3-16 Temperature dependent thermal conductivities of hydrogen, oxygen, nitrogen and water vapour [50]

For the solid components, e.g. platinum, carbon black and liquid water, the expressions for the thermal conductivities are also obtained by fitting the experimental data.

$$k_{Pt} = -5.037 \times 10^{-9} T^3 + 2.483 \times 10^{-5} T^2 - 2.282 \times 10^{-2} T + 77.80 \quad (3-203)$$

$$k_C = 1.048 \times 10^{-6} T^2 - 2.869 \times 10^{-3} T + 2.979 \quad (3-204)$$

$$k_{H_2O}^l = -1.118 \times 10^{-5} T^2 + 8.388 \times 10^{-3} T - 0.9004 \quad (3-205)$$

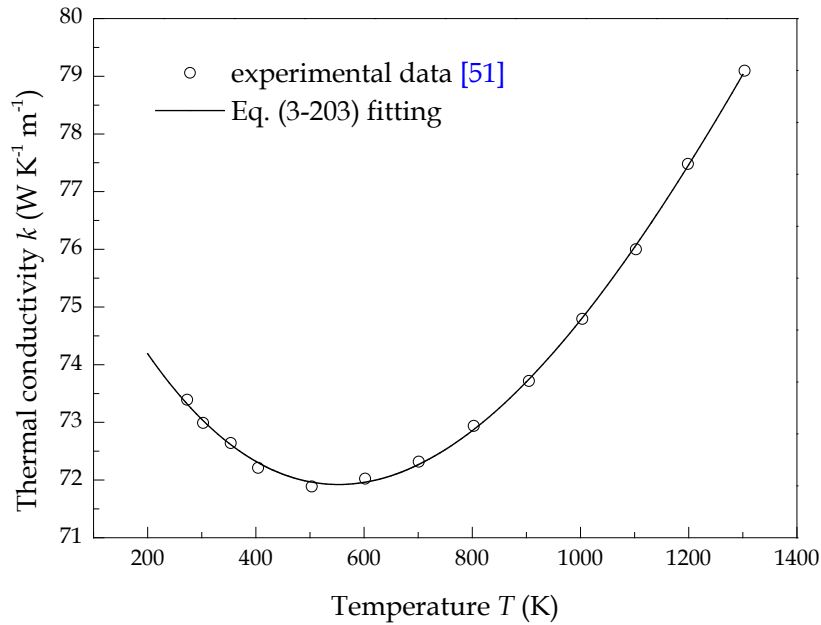


Figure 3-17 Temperature dependent platinum thermal conductivity [51]

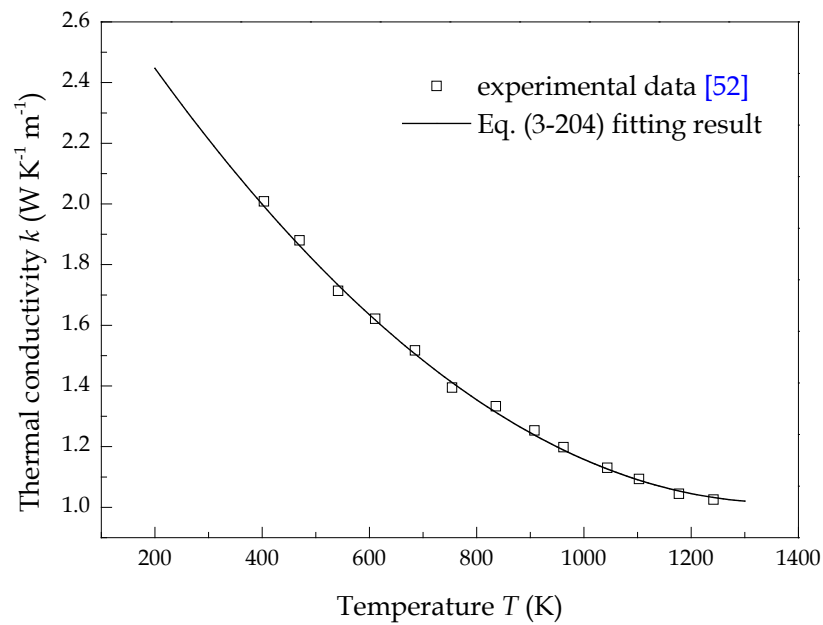


Figure 3-18 Temperature dependent carbon black thermal conductivity [52]

The thermal conductivity of membrane/ionomer is assumed to be a temperature independent constant of  $0.25 \text{ W m}^{-1} \text{ K}^{-1}$  [12, 18]. The thermal diffusion coefficient of species  $i$  in gas mixture,  $D_i^T$  ( $\text{m}^2 \text{ s}^{-1}$ ), in Section 3.3.3 can be expressed as the quotient of the thermal conductivity and specific heat capacity as follow:

$$D_i^T = M_i k_i / c_{p,i} \quad (3-206)$$

Figure 3-15 to Figure 3-18 show that the fitted expressions agree very well with the experimental data. The effective thermal conductivity and specific heat capacity depend on the volume fractions of the species within a chosen domain. Without a doubt, the cathode catalyst layer is the most complicated domain in which gas mixture, liquid water, ionomer, platinum dispersed carbon, gas diffusion layer penetration are all involved. The detailed expressions for the effective thermal conductivity, specific heat capacity of gas diffusion layer, catalyst layer and membrane/ionomer are listed in Table 3-6. The volume fractions of the component can be known from Section 3.2.

Table 3-6 Effective specific heat capacity and thermal conductivity of gas diffusion layer, catalyst layer and membrane

<i>Gas diffusion layer</i>	<i>Catalyst layer</i>	<i>Membrane</i>
$c_p^{\text{eff}}$	$\varepsilon_{GDL} c_{p,C}$	$L_{Pt} c_{p,Pt} + (L_C + L_S) c_{p,C} + L_M c_{p,M} + s \varepsilon_{CL} c_{p,w}^l + (1-s) \varepsilon_{CL} c_p^g$
$k^{\text{eff}}$	$\varepsilon_{GDL} k_C$	$L_{Pt} k_{Pt} + (L_C + L_S) k_C + L_M k_M$

### 3.6.10 Water diffusivity through the membrane

Nafion® membrane is an ideal media for dissolved water transport, the diffusion coefficient of water through the membrane is a piecewise function which is determined by both temperature and membrane water content as follow [7-14, 17, 18, 31]:

$$D_{H_2O-M} = \begin{cases} D_0(2.563 - 0.33\lambda + 0.0264\lambda^2 - 0.000671\lambda^3) & \lambda > 4 \\ D_0(-1.25\lambda + 6.65) & 3 < \lambda \leq 4 \\ D_0(2.05\lambda - 3.25) & 2 \leq \lambda \leq 3 \end{cases} \quad (3-207)$$

$$D_0 = 1.0 \times 10^{-10} \exp[2416(\frac{1}{303} - \frac{1}{T})] \quad (3-208)$$

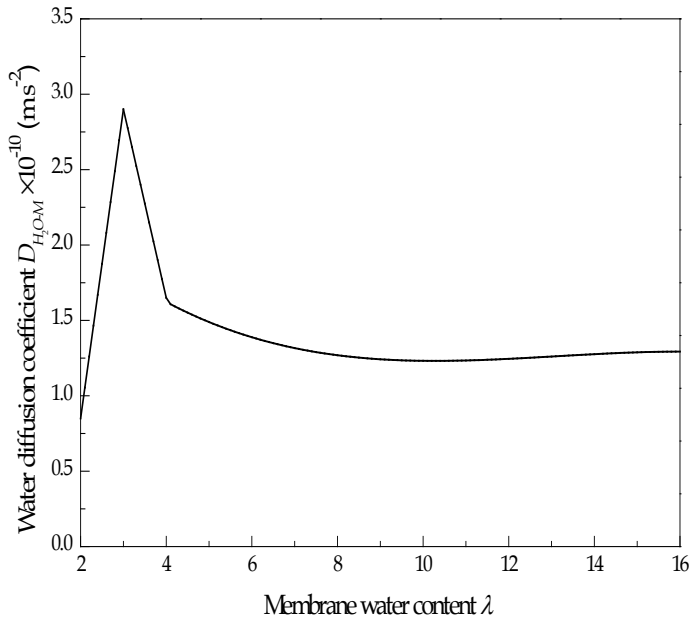


Figure 3-19 Water content dependent diffusion coefficient of water through Nafion® membrane

As shown in Figure 3-19, when the membrane water content increasing, the diffusion coefficient initially increases then decrease to a constant. In Eq. (3-207), the membrane water content can be expressed as a function of water vapour activity as follow:

$$\lambda = \begin{cases} 0.043 + 17.81\alpha_{H_2O} - 39.85\alpha_{H_2O}^2 + 36.0\alpha_{H_2O}^3 & \alpha_{H_2O} < 1 \\ 14.0 + 1.4(\alpha_{H_2O} - 1) & 1 \leq \alpha_{H_2O} \leq 3 \\ 16.8 & \alpha_{H_2O} > 3 \end{cases} \quad (3-209)$$

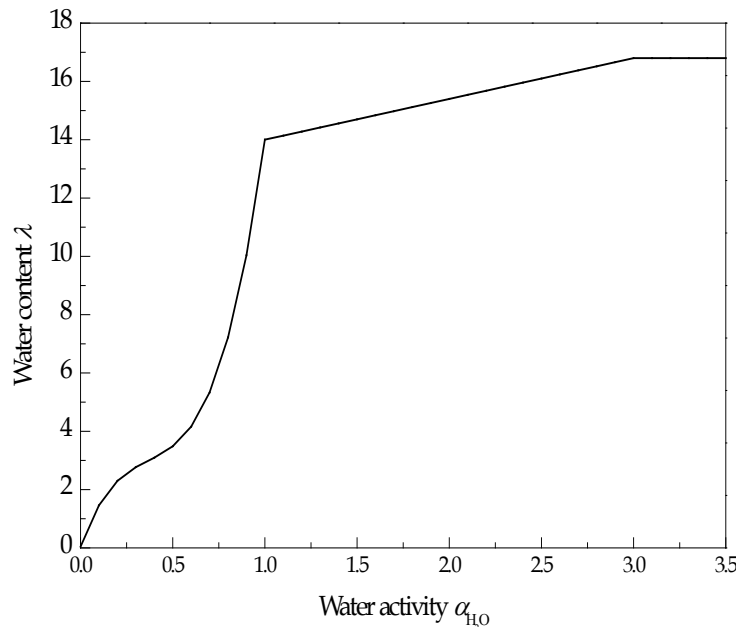


Figure 3-20 Relationship between water activity and membrane water content

As shown in Figure 3-20, the membrane water content increases up to 16.8 as water activity increases. Water activity can be associated with the partial pressure of water vapour as follow [53]:

$$\alpha_{H_2O} = \frac{p_{H_2O}}{p_{H_2O}^*} = RH \quad (3-210)$$

where  $p_{H_2O}$  (Pa) is the partial pressure of water vapour,  $p_{H_2O}^*$  (Pa) it the saturated water vapour pressure, which is the water vapour pressure at saturation temperature, and  $RH$  is the relative humidity. As shown in Figure 3-21, the saturated water pressure is obtained by fitting the experimental data as follow:

$$p_{sat} = 9.531 \times 10^{-4} (T - 237)^4 - 3.123 \times 10^{-2} (T - 237)^3 + 3.451 (T - 237)^2 + 20.96 (T - 237) + 611.0 \quad (3-211)$$

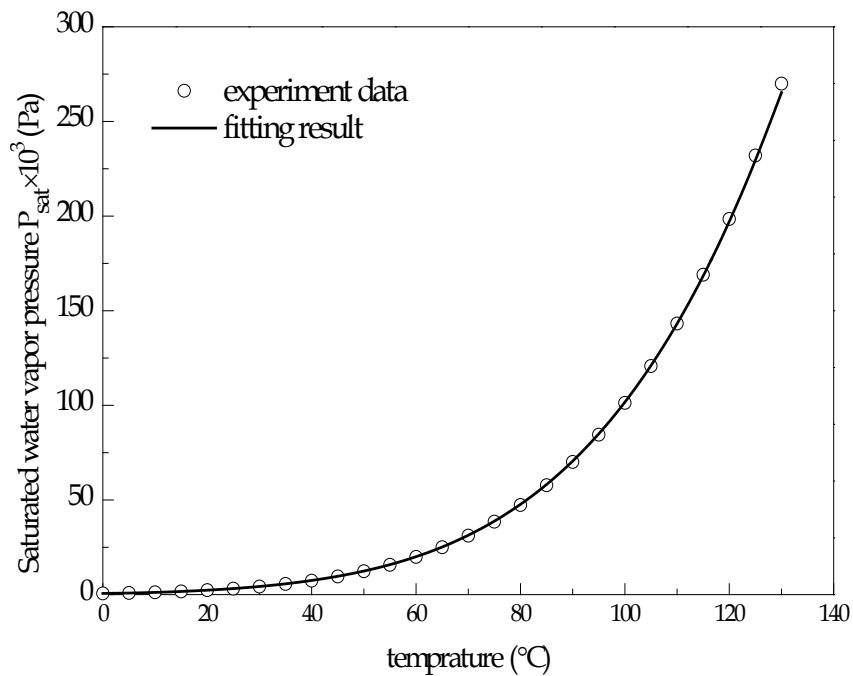


Figure 3-21 Comparison of the fitted saturated water vapour pressure with the experimental data [50]

### 3.6.11 Gas permeability in porous electrode and through membrane

Water could diffusion through the Nafion® membrane under a pressure force, the hydraulic permeability of water through Nafion® membrane is associated with the membrane water content as follow [31]:

$$k_{p,M} = 2.86 \times 10^{-20} \lambda \quad (3-212)$$

The through-plane and in-plane permeability of gas diffusion in porous gas diffusion layer is obtained by the studies of Ismail *et al.* [54, 55], which is given in Table 3-7.

Table 3-7 Gas permeability of gas diffusion layer and catalyst layer [54, 55]

	Gas diffusion layer	Catalyst layer
Through-plane permeability ( $\text{m}^2$ )	$4.97 \times 10^{-13}$	$4.97 \times 10^{-13} (\varepsilon_{CL}/\varepsilon_{GDL})^{1.5}$
In-plane permeability ( $\text{m}^2$ )	$1.87 \times 10^{-12}$	$1.87 \times 10^{-12} (\varepsilon_{CL}/\varepsilon_{GDL})^{1.5}$

### 3.6.12 Viscosity

According to Bird [22], the viscosity of single species  $i$  can be calculated by the following equation:

$$\mu_i = 2.669 \times 10^{-6} \frac{\sqrt{M_i T}}{\sigma_i^2 \Omega_i} \quad (3-213)$$

The viscosities of hydrogen, oxygen, nitrogen and water vapour are shown in Figure 3-22. As studied by Yaws [56], the viscosity of gas mixture  $\mu_m$  ( $\text{Pa s}$ ) at anode and cathode are given as:

$$\mu_m = \frac{\sum_{i=1}^n x_i \mu_i M_i^{0.5}}{\sum_{i=1}^n x_i M_i^{0.5}} \quad (3-214)$$

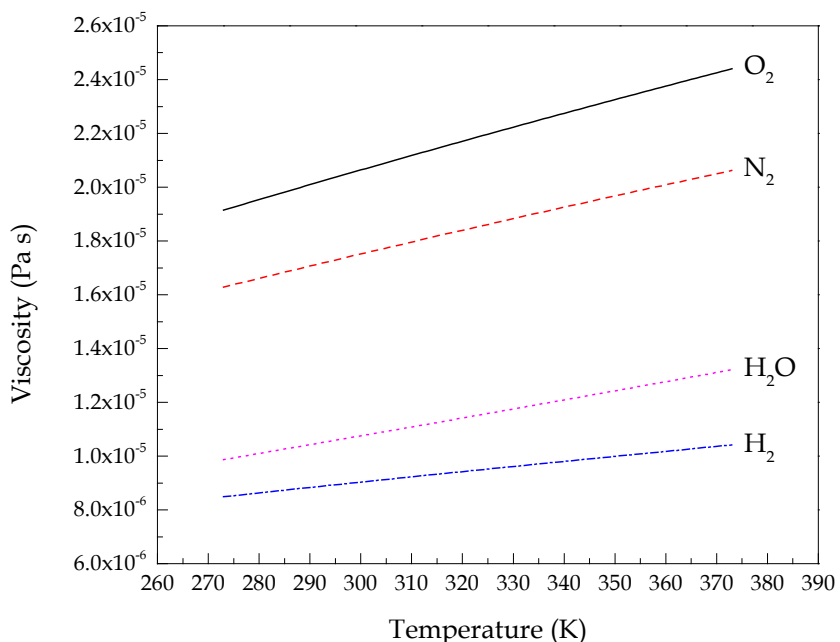


Figure 3-22 Temperature dependent gas viscosity

The temperature dependent viscosity of liquid water can be calculated by the empirical equation developed by Kestin *et al.* [57] as follow:

$$\log\left[\frac{\mu_w}{\mu_w(293K)}\right] = \frac{293-T}{T-177} [1.2378 - 1.303 \times 10^{-3}(293-T) + 3.06 \times 10^{-6}(293-T)^2 + 2.55 \times 10^{-8}(293-T)^3] \quad (3-215)$$

where  $\mu_w(293K) = 1.002 \text{ mPa s.}$

$\mu_w(T)/\mu_w(293K)$  obtained by Eq. (3-215) is shown in Figure 3-23. It is clear that the effect of temperature on liquid water viscosity is apparent.

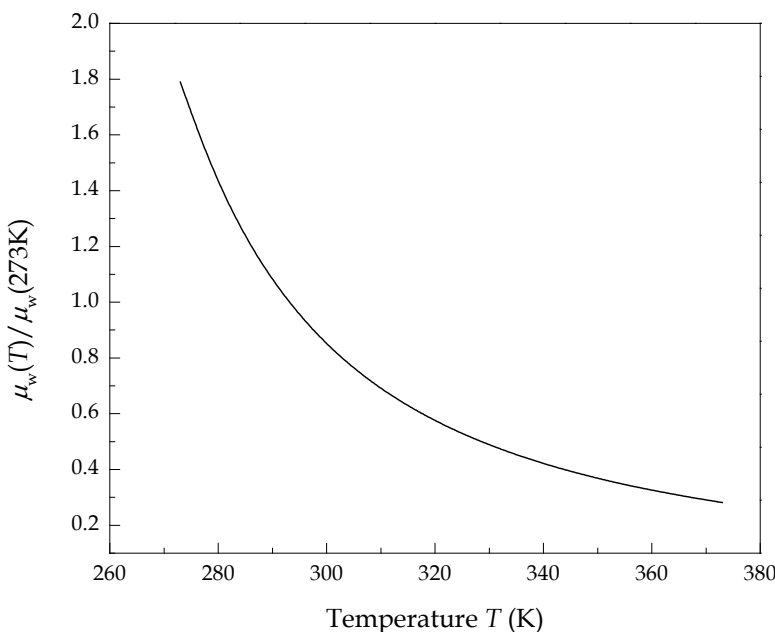


Figure 3-23 Temperature dependent liquid water viscosity [57]

### 3.7 Conclusions

All chemical and physical processes involved in the fuel cell can be described by proper differential and algebraic equations. In this chapter, the fundamentals and principles of a typical fuel cell are represented and the governing equations are derived.

A series of equations are developed to represent the properties of the catalyst layer, in which the porosity, agglomerate density, thicknesses of ionomer film and liquid water film, specific area can be quantitatively obtained. Both the Butler-Volmer and agglomerate structure based equations are developed for the reaction kinetics. For the most important transport process in PEMFC operation, the water phase transfer and

transport processes are described by a second order partial differential equation (PDE). The membrane and ionomer swelling is associated with their water content.

The majority of the parameters used are treated as dependent variables, which expand the model limits of applicability as the model will be valid at different operating conditions.

### 3.8 References

1. O'Hare R., D.M. Barnett, F.B. Prinz, *The triple phase boundary - A mathematical model and experimental investigations for fuel cells*. Journal of Electrochemistry Society, 2005. **152**: p. A439-A444.
2. Xie, Z., T. Navessin, K. Shi, R. Chow, Q. Wang, D. Song, B. Andreus, M. Eikerling, Z. Liu and S. Holdcroft, *Functionally graded cathode catalyst layer for polymer electrolyte fuel cells II. Experimental study of the effect of Nafion distribution*. Journal of Electrochemical Society, 2005. **152**: p. A1171-A1179.
3. Sun, W., B.A. Peppley, and K. Karan, *An improved two-dimensional agglomerate cathode model to study the influence of catalyst layer structural parameters*. Electrochimica Acta, 2005. **50**: p. 3359-3374.
4. Karan, K., *Assessment of transport-limited catalyst utilization for engineering of ultra-low Pt loading polymer electrolyte fuel cell anode*. Electrochemistry Communications, 2007. **9**: p. 747-753.
5. Thomas, J.M. and W.J. Thomas, *Introduction to the principles of heterogeneous catalysis*. 1967, London; New York: Academic Press.
6. Morais, R.F., P. Sautet, D. Loffreda and A.A. Franco, *A multiscale theoretical methodology for the calculation of electrochemical observables from ab initio data: Application to the oxygen reduction reaction in a Pt(1 1 1)-based polymer electrolyte membrane fuel cell*. Electrochimica Acta, 2011. **56**: p. 10842-10856.
7. Xing, L., X. Song, K. Scott, V. Pickert, W. Cao, *Multi-variable optimisation of PEMFC cathodes based on surrogate modelling*. International Journal of Hydrogen Energy, 2013. **38**: p. 14295-14313.
8. Khajeh-Hosseini-Dalasm N., M.J. Kermani, D.G. Moghaddam and J.M. Stockie, *A parametric study of cathode catalyst layer structural parameters on the*

- performance of a PEM fuel cell.* International Journal of Hydrogen Energy, 2013. **35:** p. 2417-2427.
9. Khajeh-Hosseini-Dalasm N., M. Fesanghary, K. Kushinobu and K. Okazaki, *A study of the agglomerate catalyst layer for the cathode side of a proton exchange membrane fuel cell: Modeling and optimization.* Electrochimica Acta, 2012. **60:** p. 55-65.
10. Wu, H., P. Berg and X. Li, *Modelling of PEMFC Transients with Finite-Rate Phase-Transfer Processes.* Journal of Electrochemistry Society, 2010. **157:** p. B1-B12.
11. Wu, H., P. Berg and X. Li, *Steady and unsteady 3D non-isothermal modelling of PEM fuel cells with the effect of non-equilibrium phase transfer.* Applied Energy, 2010. **87:** p. 2778-2784.
12. Yang, X.G., Q. Ye and P. Cheng, *Matching of water and temperature fields in proton exchange membrane fuel cells with non-uniform distributions.* International Journal of Hydrogen Energy, 2011. **36:**p. 12524-12537.
13. Springer, T.E., T.A. Zawodzinski and S. Gottesfeld, *Polymer Electrolyte Fuel Cell Model.* Journal of Electrochemistry Society, 1991. **138:** p. 2234-2242.
14. Shah, A.A., G.S. Kim, P.C. Sui and D. Harvey, *Transient non-isothermal model of a polymer electrolyte fuel cell.* Journal of Power Sources, 2007. **163:** p. 793-806.
15. Weber, A.Z. and J. Newman, *Transport in polymer-electrolyte membranes I. Physical model.* Journal of Electrochemistry Society, 2003. **150:** p. A1008-A1015.
16. Ge, S.H., X.G. Li, B.L. Yi and I.M. Hsing, *Absorption, Desorption, and Transport of Water in Polymer Electrolyte Membrane for Fuel Cells.* Journal of Electrochemistry Society, 2005. **152:** p. A1149-A1157.
17. Pasaogullari, U. and C.Y. Wang, *Two-phase transport and the role of micro-porous layer in polymer electrolyte fuel cells.* Electrochimica Acta, 2004. **49:** p. 4359-4369.
18. Weber A.Z. and J. Newman, *Transport in polymer-electrolyte membranes II. Mathematical model.* Journal of Electrochemistry Society, 2004. 151: p. A311-A325.

19. Uchiyama, T., M. Kato and T. Yoshida, *Buckling deformation of polymer electrolyte membrane and membrane electrode assembly under humidity cycles*. Journal of Power Sources, 2012. **206**: p. 37-46.
20. Kusoglu, A., A.M. Karlsson, M.H. Santare, S. Cleghorn and W.B. Johnson, *Mechanical behaviour of fuel cell membranes under humidity cycles and effect of swelling anisotropy on the fatigue stresses*. Journal of Power Sources, 2007. **170**: p. 345-358.
21. Silberstein, M.N. and M.C. Boyce, *Hydro-thermal mechanical behaviour of Nafion during constrained swelling*. Journal of Power Sources, 2011. **196**: p. 3452-3460.
22. Bird, R.B., W.E. Stewart, and E.N. Lightfoot, *Transport phenomena*. 2<sup>nd</sup> edition. 2002, New York: John Wiley.
23. Brinkman, H.C., *A calculation of the viscous force exerted by a flowing fluid on a dense swarm of particles*. Applied Scientific Research, 1949. **1**: p. 27-34.
24. Curtiss, C.F. and R. Byron Bird, *Multicomponent diffusion*. Industrial and Engineering Chemistry Research, 1999. **38**: p. 2515-2522.
25. COMSOL, *Chemical Engineering Module User's Guide*. 2011.
26. Barbir, F., *PEM fuel cells: theory and practice*. 2005, Oxford: Academic.
27. Lampinen, M.J. and M. Fomino, *Analysis of free energy and entropy changes for half-cell reactions*. Journal of the Electrochemical Society, 1993. **140**: p. 3537-3546.
28. Cheddie, D. and N. Munroe, Three-dimensional modeling of high temperature PEM fuel cells. Journal of Power Sources, 2006. **160**: p. 215-223.
29. Sousa, T., Mamlouk, M. and Scott, K., An isothermal model of a Laboratory Intermediate Temperature Fuel Cell using PBI doped Phosphoric Acid Membranes. Chemical Engineering Science, 2010. **65**: p. 2513-2530.
30. Parthasarathy, A., S. Srinivasan, A.J. Appleby and C.R. Martin, *Temperature dependence of the electrode kinetics of oxygen reduction at platinum/Nafion interface- A microelectrode investigation*. Journal of Electrochemistry Society, 1992. **139**: p. 2530-2537.

31. Bernardi, D.M., and M.W. Verbrugge, *A mathematical model of the solid-polymer-electrolyte fuel cell*. Journal of Electrochemistry Society, 1992. **139**: p. 2477-2491.
32. Scharifker, B.R., P. Zelenay, and J.O.M. Bockris, *Kinetic of oxygen reduction in molten phosphoric acid at high temperatures*. Journal of the Electrochemical Society, 1987. **134**: p. 2714-2725.
33. Vogel, W., J. Lundquist, P. Ross, and P. Stonehart, *Reaction Pathways and Poisons - II The rate controlling step for electrochemical oxidation of hydrogen on Pt in acid and poisoning of reaction by CO*. Electrochimica Acta, 1974. **20**: p. 79-93.
34. Liu, Z., J.S. Wainright, M.H. Litt, and R.F. Savinell, *Study of the oxygen reduction reaction (ORR) at Pt interfaced with phosphoric acid doped polybenzimidazole at elevated temperature and low relative humidity*. Electrochimica Acta, 2006. **51**: p. 3914-3923.
35. Birgersson, E., M. Noponen, and M. Vynnycky, *Analysis of a two-phase non-isothermal model for a PEFC*. Journal of the Electrochemical Society, 2005. **152**: p. A1021-A1034.
36. Marr, C., X. Li, *Composition and performance modelling of catalyst layer in a proton exchange membrane fuel cell*. Journal of Power Sources, 1999. **77**: p. 17-27.
37. Liu, Z., Z. Mao and C. Wang, *A two-dimensional partial flooding model for PEMFC*. Journal of Power Sources, 2006. **158**: p. 1229-1239.
38. Suzuki, T., K. Kudo and Y. Morimoto, *Model for investigation of oxygen transport limitation in a polymer electrolyte fuel cell*. Journal of Power Sources, 2013. **222**: p. 379-389.
39. Takamura, Y., E. Nakashima, H. Yamada, A. Tasaka and M. Inaba, *Effects of temperature and relative humidity on oxygen permeation in Nafion® and sulfonated poly (Arylene Ether Sulfone)*. ECS Transaction, 2008. **16**: p. 881-889.
40. Nonoyama, N., S. Okazaki, A.Z. Weber, Y. Ikogiand and T. Yoshida, *Analysis of oxygen-transport diffusion resistance in proton-exchange-membrane fuel cells*. Journal of the Electrochemical Society, 2011. **158**: p. B416-B423.

41. Reid, R.C., J.M. Prausnitz and B.E. Poling, *The properties of gases and liquids.* 4th edition. 1987, New York: McGraw-Hill.
42. Jaouen, F., G. Lindbergh and G. Sundholm, *Investigation of Mass-Transport Limitation in the Solid Polymer Fuel Cell Cathode.* Journal of the Electrochemical Society, 2002. **149**: p. A437 – A447.
43. Jaouen, F., G. Lindbergh and K. Wiezell, *Transient Techniques for Investigating Mass-Transport Limitations in Gas Diffusion Electrodes.* Journal of the Electrochemical Society, 2003. **150**: p. A1711 – A1717.
44. Kamarajugadda, S. and S. Mazumder, *Numerical investigation of the effect of cathode catalyst layer structure and compositon on polymer electrolye membrane fuel cell performance.* Journal of Power Sources, 2008. **183**: p. 629-642.
45. Sousa, T., M. Mamlouk and K. Scott, *A non-isothermal model of a laboratory intermediate temperature fuel cell using PBI doped phosphoric acid membranes.* Fuel Cells, 2010. **10**: p. 993-1012.
46. Zhou, T. and H. Liu, *Effects of the electrical resistances of the GDL in a PEM fuel cell.* Journal of Power Sources, 2006. **161**: p. 444-453.
47. Pantea, D., H. Darmstadt, S. Kaliaguine, and C. Roy, *Electrical conductivity of conductive carbon blacks: Influence of surface chemistry and topology.* Applied Surface Science, 2003. **217**: p. 181-193.
48. Powell, R.W. and R.P. Tye, *The promise of platinum as a high temperature thermal conductivity reference material.* British Journal of Applied Physics, 1963. **14**: p. 662-666.
49. Wilke, C.R., *A Viscosity Equation for Gas Mixture.* The Journal of Chemical Physics, 1950. **18**: p. 517-519.
50. Poling, B.E., J.M. Prausnitz and J.P. O'Connell, *Properties of Gases and Liquids.* 5<sup>th</sup> edition. 2001, New York: Mc Graw-Hill Education.
51. Haynes, W.M., editor, *CRC handbook of chemistry and physics.* 94<sup>th</sup> edition (Internet version 2014).CRC Press/Taylor and Francis, Boca Raton, FL.
52. Pierson, H.O., *Handbook of carbon, graphite, diamond, and fullerenes properties, processing, and applications.* Materials science and process

- technology series. Electronic materials and process technology. 1993, Park Ridge, N.J.: Noyes Publications.
53. Weng, D., J.S. Wainright, U. Landau, and R.F. Savinell, *Electro-osmotic drag coefficient of water and methanol in polymer electrolytes at elevated temperatures*. Journal of the Electrochemical Society, 1996. **143**: p. 1260-1263.
54. Ismail M.S., D. Borman, T. Damjanovic, D.B. Ingham, M. Pourkashanian, *On the through-plane permeability of microporous layer-coated gas diffusion layers used in proton exchange membrane fuel cells*. International Journal of Hydrogen Energy, 2011. **36**: p. 10392-103402.
55. Ismail, M.S., K.J. Hughes, D.B. Ingham, L. Ma, M. Pourkashanian, *Effects of anisotropic permeability and electrical conductivity of gas diffusion layers on the performance of proton exchange membrane fuel cells*. Applied Energy, 2012. **95**: p. 50-63.
56. Yaws, C.L., *Handbook of transport property data: viscosity, thermal conductivity, and diffusion coefficients of liquid and gases*. 1995, Houston: Gulf Pub. Co.
57. Kestin, J., M. Sokolov and W.A. Wakeham, *Viscosity of liquid water in the range -8 °C to 150 °C*. Journal of Physical and Chemical Reference Data, 1978. **7**: p. 941-948.

## Chapter 4. Single-phase flow isothermal model

In this chapter, the aim is to develop a two-dimensional, along-the-channel, single-phase flow, isothermal, steady-state model based on a spherical-agglomerate catalyst structure combined with the comprehensive water transport mechanism, to investigate the effect of catalyst layer parameters and operating conditions on the effectiveness factor of the catalyst layer and the performance of the fuel cell. This model can give guidance for optimisation of the catalyst layer composition.

### 4.1 Introduction

Proton exchange membrane fuel cells (PEMFCs) are promising candidates for automotive and small stationary applications due to their high electrical efficiency, power density and durability [1-3]. Although significant improvements with respect to cell performance, stability and cost have been achieved over the past decade, some barriers still hamper the commercial use of PEMFCs. The relatively poor oxygen reduction reaction (ORR) in the cathode catalyst layer is one of the biggest obstacles holding back the PEMFC performance [4-11].

Numerous models have been developed to investigate the effect of cathode catalyst layer on the fuel cell performance, for example, ultra-thin layer [4, 8], pseudo-homogeneous [7, 11] and agglomerate [6, 9] models. The ultra-thin layer model is the simplest model requiring the least computational resource because the catalyst layer is assumed to behave as merely an interface between the gas diffusion layer and the membrane. This model gives limited insight into the effect of composition on the performance of the catalyst layer. Due to the significant difference between the ultra-thin layer structure and the real three-dimensional structure of the catalyst layer, the ultra-thin layer model typically overestimates the current density output of the fuel cells.

An improved model developed by Marr and Li [7], based on the work of Bernardi and Verbrugge [5], applied a pseudo-homogeneous thin layer as the cathode catalyst structure and investigated the composition of the cathode catalyst layer, such as platinum and ionomer loading, on performance. This model indicated that good utilisation of the thin layer catalyst layer is difficult to achieve due to the greater ORR rate relative to the oxygen diffusion rate. However, this model, by assuming the void

space of the catalyst layer was fully occupied by liquid water, failed to simulate the fuel cell performance accurately under a wide range of operating condition. Broka and Ekdunge [6] compared the pseudo-homogeneous model with the agglomerate model and concluded that the latter gave a superior representation of the catalyst layers. Sun *et al.* [9] developed an improved two-dimensional, across-the-channel, spherical agglomerate model for the PEMFC cathode. They showed that in this model both electron and proton transport were important in determining the local cathode overpotential and the electrochemical reaction rate, and that the oxygen transport resistance through the ionomer film surrounding the agglomerates was the main factor controlling the observed limiting current density. However, the presence of liquid water was not considered in this model.

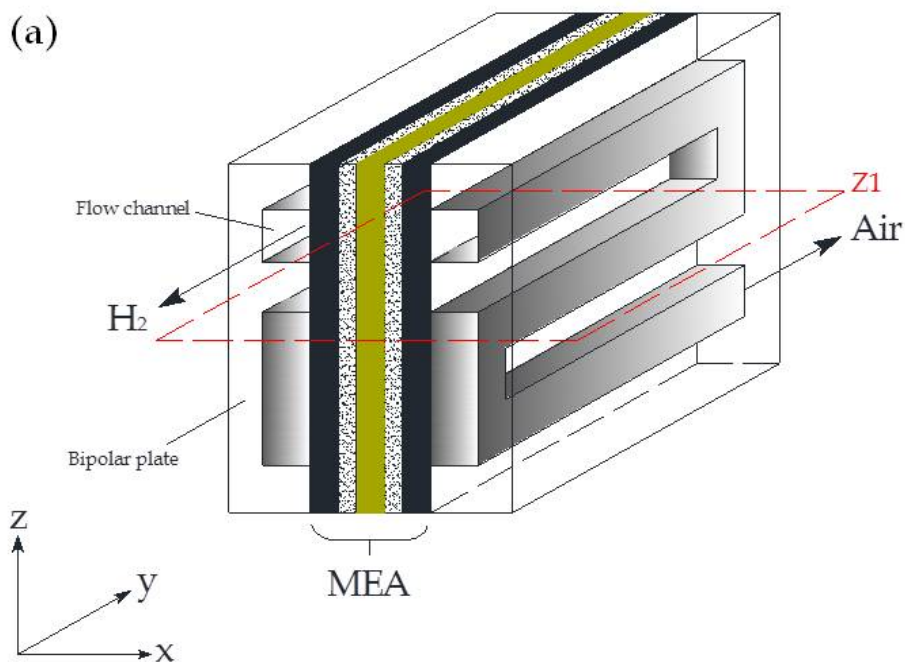
Water management is an important issue in PEMFCs that use perfluorinated membrane such as Nafion®. The earliest water management models were developed by Springer *et al.* [4], Bernardi and Vebrugge [5], and Nguyen and White [12]. The first one-dimensional steady-state model, developed by Springer *et al.* [4], described water diffusion coefficients, electro-osmotic drag coefficients and membrane conductivity as function of water content in the Nafion® 117 membrane. The model developed by Bernardi and Vebrugge [5] used a porous electrode instead of the ultrathin film electrode which was applied by Springer *et al.* [4]. Water transport through the membrane was associated with hydraulic pressure and the potential gradients. This model gave comprehensive profiles of concentration, pressures and water velocity through the membrane electrode assembly (MEA) including the catalyst layers and membrane. Heat management was combined with water management in the model developed by Nguyen and White [12]. The model focused on the effect of gas inlet humidity on the cell performance in which water migration and back diffusion accounted for the net water flux through the membrane. However, the effect of hydraulic permeation through the membrane was not included. Ge and Yi [13] developed a two-dimensional steady-state model to describe water transport through the membrane with fuel and oxidant gases in co-flow and counter-flow modes. In this model, three water transport mechanisms: electro-osmotic drag, back diffusion and hydraulic permeation were all considered. This so-called combinational model was successfully applied in previous work [14-18].

Although previous models have given several important insights for optimisation of the electrode composition and operating conditions, in order to improve the accuracy and reliability of the simulation results under various practical conditions, the hydrogen oxidation reaction (HOR) at anode need to be introduced into the model simultaneously when investigating the cathode.

## 4.2 Model description

### 4.2.1 Computational domain and assumption

The three-dimensional representation of a typical PEMFC unit is shown in Figure 4-1(a), which includes the bipolar plates, gas flow channels (domain 1), gas diffusion layers (domain 2) and catalyst layers (domain 3) on both the anode and cathode and a electrolyte membrane (domain 4) in between. The two-dimensional computational domain in this model, plane Z1 in Figure 4-1(a), is represented in detail in Figure 4-1(b). This plane is located in the middle of flow channels, on which the reactant flow direction is counter-flow. The geometric parameters and material properties of each layer are listed in Table 4-1.



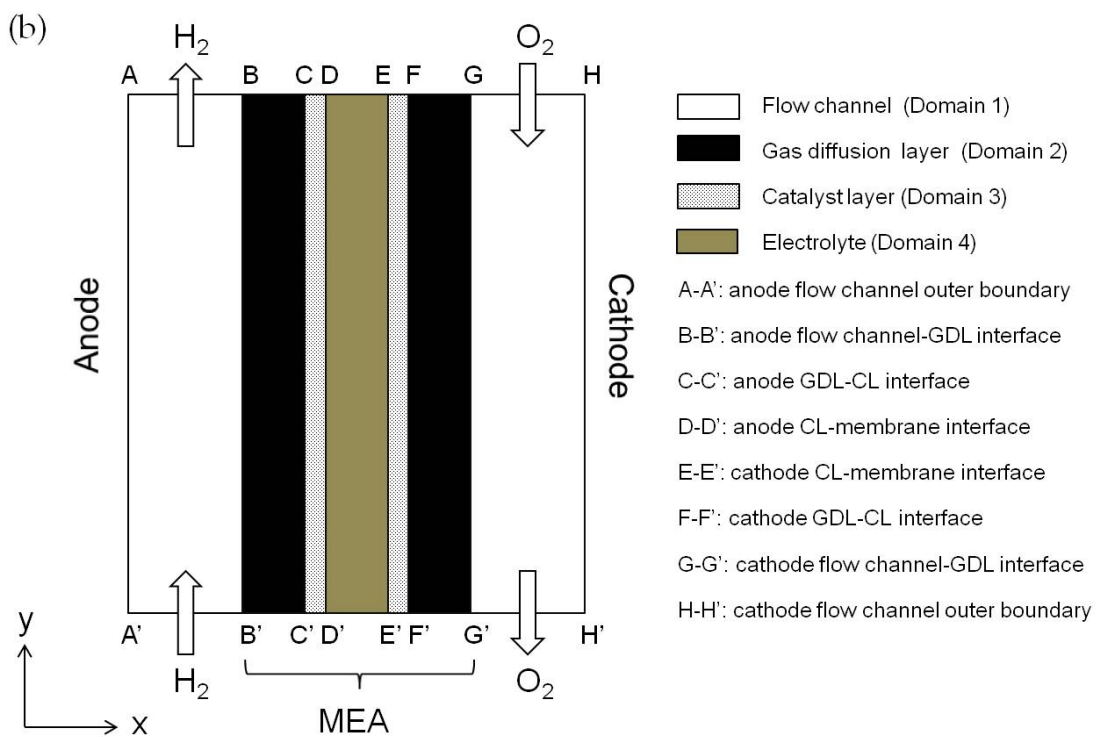


Figure 4-1 Sketch of a typical PEMFC (a) 3D representation (b) 2D computational domain Z1

In addition to the general assumption discussed in [Chapter 3](#), the model features and main assumptions in this particular model are listed as follows:

1. Reactant gases at both anode and cathode are treated as ideal gases and transport is by diffusion and convection.
2. The membrane is non-permeable to hydrogen, oxygen and nitrogen. Only dissolved water and protons for species transport are accounted for in the membrane.
3. Liquid water is not included in this model. The product water in the cathode catalyst layer is generated as water vapour.
4. Catalyst layers are constructed from spherical agglomerates, which are covered by ionomer films only.
5. Membrane/ionomer swelling is not addressed.
6. Counter-flow mode of reactant gases is applied.

Table 4-1 Geometric parameters and material properties of a PEMFC

Parameters	Value	Reference
Flow channels (Domain 1)		
Width, $w$ (mm)	1.0	assumed
Depth, $d$ (mm)	1.0	assumed
Length, $l$ (mm)	10.0	assumed
Gas diffusion layer (Domain 2)		
Thickness, $l_{GDL}$ ( $\mu\text{m}$ )	380	assumed
Porosity, $\varepsilon_{GDL}$	0.4	[11, 20]
Conductivity, $\sigma_{GDL}$ ( $\Omega^{-1} \text{ m}^{-1}$ )	1250	[21]
Permeability, $k_{p,GDL}$ ( $\text{m}^2$ )	$4.97 \times 10^{-13}$	[22]
Platinum density, $\rho_{Pt}$ ( $\text{kg m}^{-3}$ )	$2.145 \times 10^4$	[11]
Carbon density, $\rho_C$ ( $\text{kg m}^{-3}$ )	1800	[11]
Equivalent weight of ionomer, $EW$ ( $\text{g mol}^{-1}$ )	1100	[12]
Density of the dry membrane, $\rho_M$ ( $\text{kg m}^{-3}$ )	$2.0 \times 10^3$	[12]
Catalyst layer (Domain 3)		
Thickness, $l_{CL}$ ( $\mu\text{m}$ )	15.0	assumed
Porosity, $\varepsilon_{CL}$	Eq. (3-42)	calculated
Specific area, $a_{CL}$ ( $\text{m}^{-1}$ )	Eq. (3-67)	calculated
Conductivity, $\sigma_{CL}$ ( $\Omega^{-1} \text{ m}^{-1}$ )	Eq. (3-188)	calculated
Permeability, $k_{p,CL}$ ( $\text{m}^2$ )	$4.97 \times 10^{-13} (\varepsilon_{CL}/\varepsilon_{GDL})^{1.5}$	[22, 23]
Membrane (Domain 4)		
Thickness, $l_M$ ( $\mu\text{m}$ )	120	assumed
Conductivity, $\sigma_M$ ( $\Omega^{-1} \text{ m}^{-1}$ )	Eq. (3-190)	calculated
Permeability, $k_{p,M}$ ( $\text{m}^2$ )	Eq. (3-212)	calculated

#### 4.2.2 Governing equations

By taking all assumptions above into consideration, the governing equations described in Chapter 3 can be specified as follow to account for the particular processes in the selected domains (see Table 4-2).

Table 4-2 Governing equations used in the single-phase flow and isothermal model

Flow channels (Domain 1)	
Conservation of mass	$\nabla \cdot (\rho^s \mathbf{u}^s) = 0$ (4-1)
Conservation of momentum	$-\nabla \cdot (\rho^s \mathbf{u}^s \mathbf{u}^s) - \nabla \cdot p - \nabla \cdot \boldsymbol{\tau} + \rho^s \mathbf{g} = 0$ (4-2)
Conservation of species	$\rho^s \mathbf{u}^s \cdot \nabla w_i^s - \nabla \cdot [-\rho^s \sum_{j=1}^N D_{ij} (\nabla x_j^s - w_j^s) \frac{\nabla p}{p}] = 0$ (4-3)
Gas diffusion layers (Domain 2)	
Conservation of mass	$\nabla \cdot (\rho^s \mathbf{u}^s) = 0$ (4-4)
Conservation of momentum	$-\mathbf{u} \frac{\mu^{eff}}{K} - \nabla \cdot p - \nabla \cdot \boldsymbol{\tau} + \rho^s \mathbf{g} = 0$ (4-5)
Conservation of species	$\rho^s \mathbf{u}^s \cdot \nabla w_i^s - \nabla \cdot [-\rho^s \sum_{j=1}^N D_{ij} (\nabla x_j^s - w_j^s) \frac{\nabla p}{p}] = 0$ (4-6)
Conservation of charge	$\nabla (-\sigma_s^{eff} \nabla \phi_s) = \nabla (-\sigma_M^{eff} \nabla \phi_M) = 0$ (4-7)
Catalyst layers (Domain 3)	
Conservation of mass	$\nabla \cdot (\rho^s \mathbf{u}^s) = 0$ (4-8)
Conservation of momentum	$-\mathbf{u} \frac{\mu^{eff}}{K} - \nabla \cdot p - \nabla \cdot \boldsymbol{\tau} + \rho^s \mathbf{g} = 0$ (4-9)
Conservation of species	$\rho^s \mathbf{u}^s \cdot \nabla w_i^s - \nabla \cdot [-\rho^s \sum_{j=1}^N D_{ij} (\nabla x_j^s - w_j^s) \frac{\nabla p}{p}] = M_i S_i^s$ (4-10)
Conservation of charge	$\nabla (-\sigma_s^{eff} \nabla \phi_s) = Q_s$ (4-11)
Conservation of charge	$\nabla (-\sigma_M^{eff} \nabla \phi_M) = Q_M$ (4-12)
Membrane (Domain 4)	
Conservation of charge	$\nabla (-\sigma_M^{eff} \nabla \phi_M) = 0$ (4-13)

#### 4.2.3 Electrochemical reactions kinetics

##### Butler-Volmer kinetics

The volumetric current densities of both the anode and cathode based on the Butler-Volmer kinetics are obtained by substituting Eq. (3-157) into Eq. (3-12) and Eq. (3-13) as follow:

$$i_a = a_{CL} i_{0,a}^{ref} \left( \frac{P_{H_2}}{H_{H_2} c_{H_2}^{ref}} \right)^{0.5} \left[ \exp\left(-\frac{(1-\alpha_a)F\eta_a}{R_g T}\right) - \exp\left(\frac{\alpha_a F\eta_a}{R_g T}\right) \right] \quad (4-14)$$

$$i_c = a_{CL} i_{0,c}^{ref} \frac{P_{O_2}}{H_{O_2} c_{O_2}^{ref}} \left[ \exp\left(-\frac{\alpha_c F\eta_c}{R_g T}\right) - \exp\left(\frac{(1-\alpha_c)F\eta_c}{R_g T}\right) \right] \quad (4-15)$$

where  $c_{H_2}^{ref}$   $c_{O_2}^{ref}$  (mol m<sup>-3</sup>) are the reference molar concentration of hydrogen and oxygen, respectively.  $a_{CL}$  (m<sup>-1</sup>) is the specific area of the catalyst layer,  $i_{0,i}^{ref}$  (A m<sup>-2</sup>) is the exchange current density,  $\alpha_i$  is the transfer coefficient, and  $\eta_i$  (V) is the overpotential. The subscript  $i = a$  or  $c$ , refer to the anode and cathode, respectively.

### Agglomerate kinetics

The volumetric current densities based on the agglomerate kinetics are obtained by applying Eq. (3-28) for both the anode and cathode:

$$i_{a,agg} = 2F \frac{P_{H_2}}{H_{H_2}} \left[ \frac{1}{E_{agg,a} k_{agg,a}} + \frac{(r_{agg} + \delta_M) \delta_M}{a_{agg} r_{agg} D_{H_2-M}^{eff}} \right]^{-1} \quad (4-16)$$

$$i_{c,agg} = 4F \frac{P_{O_2}}{H_{O_2}} \left[ \frac{1}{E_{agg,c} k_{agg,c}} + \frac{(r_{agg} + \delta_M) \delta_M}{a_{agg} r_{agg} D_{O_2-M}^{eff}} \right]^{-1} \quad (4-17)$$

The first terms in the brackets of Eq. (4-16) and Eq. (4-17) represent the effect of mass transport within the agglomerate and the second terms represent the mass transport resistance resulting from the ionomer film surrounding the agglomerate. If no ionomer film is formed, the second terms are ignored then Eq. (4-16) and Eq. (4-17) can be simplified to:

$$i_{a,agg} = 2F E_{agg,a} k_{agg,a} \frac{P_{H_2}}{H_{H_2}} \quad (4-18)$$

$$i_{c,agg} = 4F E_{agg,c} k_{agg,c} \frac{P_{O_2}}{H_{O_2}} \quad (4-19)$$

Due to the weak dependence of the anode charge transfer coefficient, anode reference exchange current density and hydrogen solubility on temperature, these parameters are assumed as constant over the operating temperature range. The electrochemical parameters used in this model are listed in Table 4-3.

Table 4-3 Electrochemical parameters used in this model

Parameters	Anode	Cathode	Reference
Charge transfer coefficient	$\alpha_a = 0.5$	Eq. (3-156)	[5, 9, 24]
Reference exchange current density (A cm <sup>-2</sup> )	$i_{0,a}^{ref} = 1.0$	Eq. (3-158)	[5, 7, 24]
Equilibrium potential (V)	$\varphi_a^{eq} = RT \ln\left[\frac{p_{H_2}}{c_{H^+}^2}\right]$	Eq. (3-172)	[22, 24]
Henry's constant (Pa m <sup>3</sup> mol <sup>-1</sup> )	$H_{H_2} = 4.56 \times 10^3$	Eq. (3-176)	[5, 7]
Hydrogen reference concentration (mol cm <sup>-3</sup> )	$c_{H_2}^{ref} = 5.64 \times 10^{-5}$	-----	[5]
Oxygen reference concentration (mol cm <sup>-3</sup> )	-----	$c_{O_2}^{ref} = 3.39 \times 10^{-6}$	[5]

#### 4.2.4 Polarisation curves

The overpotential  $\eta_i$  (V) for each electrode is defined as:

$$\eta_i = \phi_s - \phi_M - E_i^{eq} \quad (4-20)$$

where  $\phi_s$  (V) is the solid phase potential,  $\phi_M$  (V) is the electrolyte phase (ionomer) potential and  $E_i^{eq}$  (V) is the reference potential of the electrode.  $E_a^{eq}$  is zero at standard condition ( $T = 25$  °C,  $p_{H_2} = 1.0$  atm,  $c_{H^+} = 1.0 \times 10^{-7}$  M) for the anode and  $E_c^{eq}$  equals the equilibrium cell potential for the cathode. Due to the relative high current conductivity of the electrode, the ohmic resistance is neglected. Therefore, the cell voltage  $E_{cell}$  (V) is obtained from the membrane resistance, current density and overpotential shown as follow:

$$E_{cell} = E^0 - \eta_a - |\eta_c| - i_M R_M \quad (4-21)$$

where  $E^0$  (V) is the open circuit potential (OCP) of the fuel cell.

#### 4.2.5 Gas transport within the catalyst layers

As described in Section 3.1.2, reactant gases firstly transport through the secondary pores to the outer boundary of the ionomer films surrounding the agglomerate. The

effective diffusion coefficient of species  $i$  through the secondary pores, corrected by the Bruggman relationship [4-7], is:

$$D_{i,s}^{eff} = \varepsilon_s^{1.5} D_{i-P}^0 \quad (4-22)$$

Secondly, reactant gases must diffuse through the ionomer films and reach the inner boundary of the films. Finally, reactant gases transport through the primary pores inside the agglomerates to the surface of the platinum particles. As assumed in Section 3.2, the agglomerates inside the catalyst layers consist of three components namely, platinum dispersed carbon ( $Pt/C$ ), ionomer and primary pores. As a consequence of the fact that ionomer and primary pores are the media for gas transport, the overall transport coefficient of gas species  $i$  within the agglomerates is:

$$D_{i,p}^{eff} = (\varepsilon_{agg,M})^{1.5} D_{i-M}^0 + (\varepsilon_{agg,p})^{1.5} D_{i-P}^0 \quad (4-23)$$

In Eq. (4-20) and Eq. (4-21),  $\varepsilon_s$  is the porosity of the secondary pores,  $\varepsilon_{agg,M}$  and  $\varepsilon_{agg,p}$  are the volume fractions of ionomer and primary pores within the agglomerate, respectively. Their expressions were given in Section 3.2. By taking the Knudsen diffusion into account, the equivalent diffusion coefficient of species  $i$  in the void space is:

$$\frac{1}{D_{i-P}^0} = \frac{1}{D_{i-g}^0} + \frac{1}{D_{Kn,i}} \quad (4-24)$$

where the intrinsic diffusion coefficient  $D_{i-g}^0$  and Knudsen diffusion coefficient  $D_{Kn,i}$  of species  $i$  were described in detail in Section 3.5.6.

#### 4.2.6 Property of the catalyst layer

The properties of the catalyst layer were studied in Section 3.2. In this section, the catalyst layer porosity ( $\varepsilon_{CL}$ ), agglomerate density ( $N_{agg}$ ), volume fraction of secondary pores ( $\varepsilon_s$ ), thickness of the ionomer film ( $\delta_M$ ), catalyst layer specific area ( $a_{CL}$ ) and agglomerate specific area ( $a_{agg}$ ) are summarised as follows:

$$\varepsilon_{CL} = 1 - L_M - L_{GDL}(1 - \varepsilon_{GDL}) - \frac{m_{Pt}}{l_{CL}} \left( \frac{1}{\rho_{Pt}} + \frac{1-f}{f} \frac{1}{\rho_C} \right) \quad (4-25)$$

$$N_{agg} = \frac{3L_{Pt/C}}{4(1-\varepsilon_{CL})\pi r_{agg}^3} \quad (4-26)$$

$$\varepsilon_s = \varepsilon_{CL} - \frac{L_{Pt/C}(\varepsilon_{CL} - \varepsilon_{agg,M})}{1 - \varepsilon_{CL}} \quad (4-27)$$

$$\delta_M = r_{agg} \left[ \sqrt[3]{\frac{(1 - \varepsilon_{CL})(1 - \varepsilon_{CL} - L_S) + L_{Pt/C}\varepsilon_{CL}(1 - \%M)}{L_{Pt/C}}} - 1 \right] \quad (4-28)$$

$$a_{CL} = \frac{m_{Pt}}{l_{CL}} (227.79f^3 - 158.57f^2 - 201.53f + 159.5) \times 10^3 \quad (4-29)$$

$$a_{agg} = \frac{m_{Pt}(1 - \varepsilon_{CL})}{L_{Pt/C}l_{CL}} (227.79f^3 - 158.57f^2 - 201.53f + 159.5) \times 10^3 \quad (4-30)$$

#### 4.2.7 Water transport through the membrane

In this single-phase flow model, the source term in Eq. (3-71), which is responsible for water phase transfer, is zero. In addition, membrane swelling is neglected. At a steady-state condition, Eq. (3-71) is therefore simplified to:

$$\nabla \cdot \left( \frac{2.5\lambda}{22} \frac{i_M}{F} \right) - \nabla \cdot \left( \frac{\rho_M D_{w-M}}{EW} \nabla \lambda \right) - \nabla \cdot \left( \frac{k_{p,M} \rho_M}{\mu_w EW} \frac{p_{c,M} - p_{a,M}}{\delta_M} \lambda \right) = 0 \quad (4-31)$$

where  $p_{a,M}$  and  $p_{c,M}$  (Pa) are the pressures at the anode side (boundary D-D' in Figure 4-1(b)) and cathode side (boundary E-E' in Figure 4-1(b)) of the membrane, respectively. Other parameters were discussed in Chapter 3. Eq. (4-31) is used to describe the dissolved water transport through the membrane under the driving forces of electro-osmotic drag, back diffusion and hydraulic permeation.

#### 4.2.8 Stoichiometric flow ratio

The stoichiometric flow ratio is defined as the amount of supplied reactants divided by the amount that is required by the electrochemical reaction. For the reactant gases at the anode and cathode, the stoichiometric flow ratios are given as follow:

$$\xi_a = \frac{p_a x_{H_2} Q_a}{R_g T} \frac{2F}{i^{ref} A} \quad (4-32)$$

$$\xi_c = \frac{p_c x_{O_2} Q_c}{R_g T} \frac{4F}{i^{ref} A} \quad (4-33)$$

where  $Q_a$  and  $Q_c$  ( $\text{m}^3 \text{s}^{-1}$ ) are the reactant flow rate of anode and cathode, respectively.  $i^{ref}$  ( $\text{A cm}^{-2}$ ) is the reference current density.

#### 4.2.9 Boundary conditions and source terms

The stoichiometric flow ratios at the anode and cathode inlet are defined as  $\xi_a$  and  $\xi_c$  at a reference current density of  $1.0 \text{ A cm}^{-2}$  while the inlet pressures at the anode and cathode are defined as  $p_a$  (Pa) and  $p_c$  (Pa), respectively. The water content on the catalyst layer-membrane boundaries of anode and cathode (D-D' and E-E' in Figure 4-1(b)) are defined as Dirichlet boundaries with the values according to Eq. (3-209). At the outlets, the species transport is assumed by convection only. The exterior boundaries of the domain are treated as solid walls. The detailed boundary conditions and source terms are defined in Tables 4-4.

#### 4.2.10 Numerical solution

The commercial software COMSOL Multiphysics 4.2 is used to implement the fully coupled equations in the mathematical model. The key issue of successfully solving of this model is the water content ( $\lambda$ ) due to its strong effect on all critical parameters, such as electro-osmotic drag coefficient, membrane ionic conductivity and water diffusion coefficient through the membrane. The numerical solution of all equations is based on the finite element method (FEM). The computational geometry consists of 19,672 elements, the distance between each element is known as the step. At each step, the equations accounting for different phenomena are fully coupled and computed following the schematic as shown in Figure 4-2. The calculating error is controlled lower than  $10^{-5}$ .

Table 4-4 Boundary conditions and source terms in the single-phase flow and isothermal model

Boundary or domain in Figure 4-1(b)	Condition expressions
Anode inlet (Boundary A'-B')	$x_{H_2O,a} = \frac{P_{sat}}{P_a} RH_a, x_{H_2,a} = 1 - x_{H_2O,a},$ $RH_a = 1.0, \xi_a = 2.0, p_a = 1.0 \text{ atm}$
Cathode inlet (Boundary G-H)	$x_{H_2O,c} = \frac{P_{sat}}{P_c} RH_c, x_{O_2,c} = 0.21(1 - x_{H_2O,c}),$ $x_{N_2,c} = 0.79(1 - x_{H_2O,c}), RH_c = 1.0,$ $\xi_c = 2.0, p_c = 1.0 \text{ atm}$
Gas diffusion layers (Domain 2)	$S_{H_2} = 0, S_{O_2} = 0, S_{H_2O} = 0$
Catalyst layer (Domain 3)	$S_{H_2} = \frac{i_a}{2F}, S_{O_2} = -\frac{i_c}{4F}, S_{H_2O} = \frac{i_c}{2F}$
Anode flow channel- gas diffusion layer interface (Boundary B-B')	$\phi_s = 0$
Cathode flow channel- gas diffusion layer interface (Boundary G-G')	$\phi_s = E^{cell}$
Anode outlet (Boundary A-B)	$w_{H_2} \rho u \cdot \mathbf{n} = 0$
Cathode outlet (Boundary G'-H')	$w_{O_2} \rho u \cdot \mathbf{n} = 0$

Note:  $\mathbf{n}$  is the normal vector to the boundary.

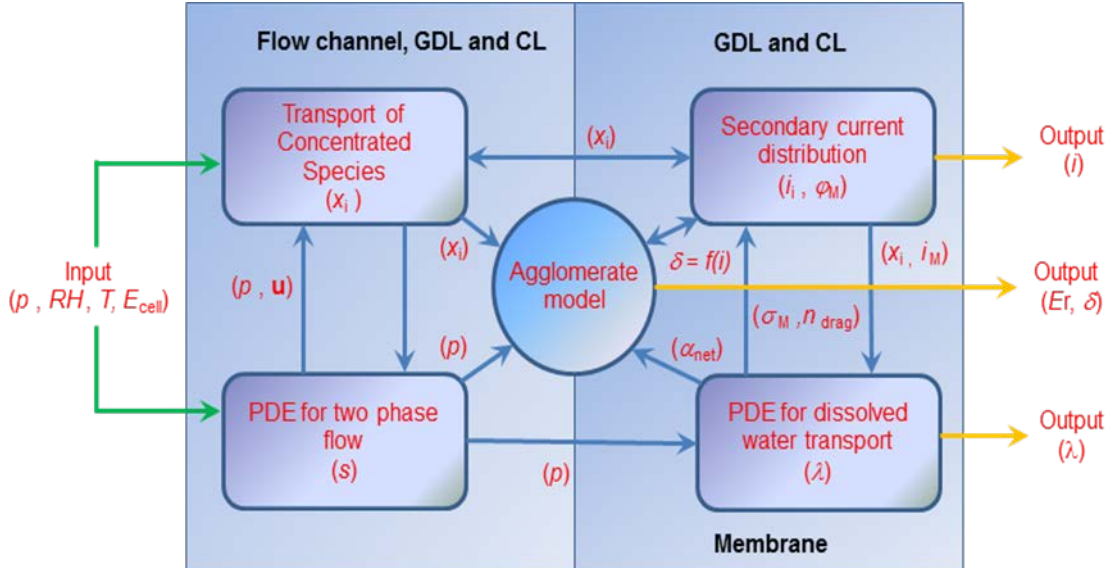


Figure 4-2 Schematic of the computational process

## 4.3 Results and discussion

### 4.3.1 Model validation

Figure 4-3 compares the experimental data with the results simulated by three models: the simple Butler-Volmer, agglomerate without a film and agglomerate with a film models. The experimental data is obtained using a single PEM fuel cell with an active area of  $1 \times 1 \text{ cm}^2$ . The catalyst layers are prepared with the platinum loadings of 0.1 and  $0.4 \text{ mg cm}^{-2}$  for anode and cathode, respectively. Both the mass ratios of platinum and ionomer are 20% in the catalyst layers of the anode and cathode. The operating condition is temperature at  $60^\circ\text{C}$ , pressure of 1.0 atm, gas humidity of 100%, hydrogen flow rate of 0.2 standard litre per minute (slpm), air flow rate of 0.5 slpm. The parameters used for model validation and base case are listed in Table 4-5.

It is apparent from Figure 4-3 that, due to weak mass transport resistance at higher cell voltages, all three models gives very close simulation in agreement with the experimental data. With increasing current density there is the typical fall in cell voltage. At higher current densities there is a more rapid decrease in current density which is caused by the increase in mass transport resistance.

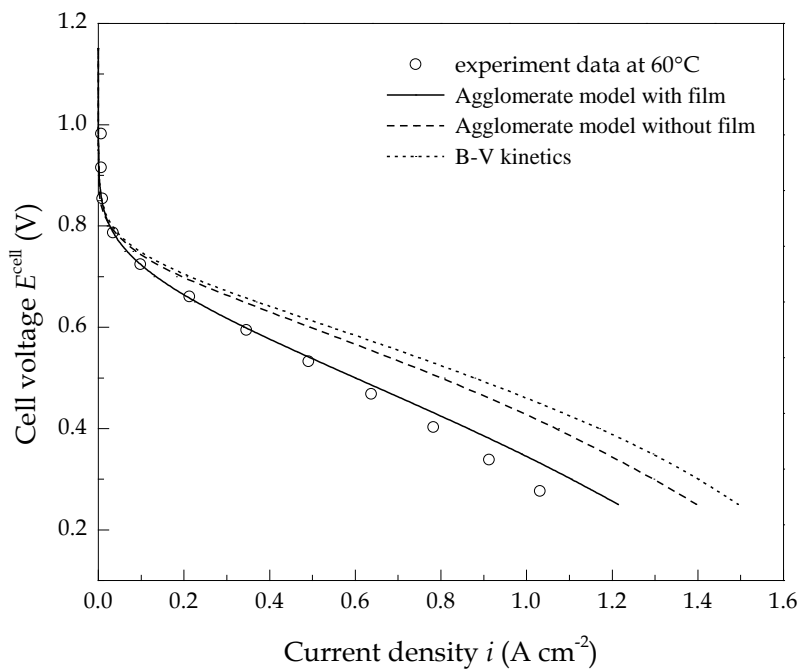


Figure 4-3 Validation of the modelling results to the experimental data

( $m_{\text{Pt},a} = 0.1 \text{ mg cm}^{-2}$ ,  $m_{\text{Pt},c} = 0.4 \text{ mg cm}^{-2}$ ,  $f_a = 20\%$ ,  $f_c = 20\%$ ,  $L_s = 6\%$ ,  $l_{\text{CL}} = 15 \mu\text{m}$ ,

$\varepsilon_{\text{GDL}} = 40\%$ ,  $L_M = 13.3\%$ ,  $T = 60^\circ\text{C}$ ,  $p = 1.0 \text{ atm}$ ,  $RH = 100\%$ ,  $\xi_a = 19.6$ ,  $\xi_c = 20.6$ )

By accounting for the resistance of oxygen transport to the platinum surface, the agglomerate with a film model gives more accurate predictions of the polarisation curve whilst the other two models overestimate the current density.

Table 4-5 Physical parameters used in the model

<i>Electrode parameters</i>	<i>Validation</i>	<i>Base case</i>
Anode platinum loading, $m_{Pt,a}$ (mg cm <sup>-2</sup> )	0.1	0.4
Cathode platinum loading, $m_{Pt,c}$ (mg cm <sup>-2</sup> )	0.4	0.4
Anode platinum mass ratio, $f_a$	0.2	0.4
Cathode carbon loading, $f_c$	0.2	0.4
Agglomerate radius, $r_{agg}$ (μm)	1.0	0.5
Catalyst layer thickness, $l_{CL}$ (μm)	15.0	15.0
GDL thickness, $l_{GDL}$ (μm)	300	380
Membrane thickness, $l_M$ (μm)	55	120
GDL porosity, $\varepsilon_{GDL}$	40%	40%
Ionomer volume fraction, $L_M$	13.3%	30%
Volume fraction of solid portion, $L_s$	6%	6%
Cathode transfer coefficient, $\alpha_c$	0.85	$0.495 + 2.3 \times 10^{-3}(T - 300)$
<i>Operating conditions</i>	<i>Validation</i>	<i>Base case</i>
Operating temperature, $T$ (K)	333	343
Anode pressure, $p_a$ (atm)	1.0	1.0
Cathode pressure, $p_c$ (atm)	1.0	1.0
Relative humidity, $RH$ (%)	100	100
Anode stoichiometric flow ratio, $\xi_a$	19.6	1.2
Cathode stoichiometric flow ratio, $\xi_c$	20.6	2.0

### 4.3.2 Property of the catalyst layer

Following the model validation, the effect of the composition of the catalyst layer without ionomer swelling is studied. Three important parameters of the catalyst layer are investigated, namely porosity ( $\varepsilon_{CL}$ ), agglomerate density ( $N_{agg}$ ), ionomer film thickness ( $\delta_M$ ). During this study, the thickness of the catalyst layer ( $l_{CL}$ ), agglomerate radius ( $r_{agg}$ ), ionomer volume fraction ( $L_M$ ), volume fraction of ionomer in primary

pores (% $M$ ), and volume fraction of gas diffusion layer penetration ( $L_s$ ) are held constant at 15  $\mu\text{m}$ , 0.5  $\mu\text{m}$ , 40%, 50% and 6%, respectively.

### ***Porosity and agglomerate density***

Figure 4-4 shows the porosity and Figure 4-5 shows the agglomerate density of the catalyst layer with varying platinum loading from 0.2 to 0.8  $\text{mg cm}^{-2}$  and platinum mass ratio from 0.1 to 1.0, respectively. It is clear that the porosity and agglomerate density of the catalyst layer are diametrically opposed with respect to how they change with platinum loading and platinum mass ratio. At fixed platinum loading, since the catalyst layer thickness is constant, the porosity increases as the platinum mass ratio increases. On the contrary, the agglomerate density decreases as the platinum mass ratio increases. The increase in porosity can be explained by the densities of the platinum particles with respect to the carbon particles. According to Eq. (3-39), the volume fraction of the solid phase ( $L_{Pt/C}$ ) is determined by two parts: the volume fraction of platinum and carbon, which are expressed as the quotient of their mass loadings and densities ( $m_{Pt}/(l_{CL}\rho_{Pt})$  and  $(1-f)m_{Pt}/(l_{CL}\rho_C f)$ ). As shown in Table 4-1, the density of platinum is approximate twelve times bigger than carbon. The volume fraction of the solid phase is therefore mainly determined by the volume fraction of carbon. If the catalyst layer consists of the platinum particles only ( $f = 1$ ), the volume fraction of the solid phase decreases to  $m_{Pt}/(l_{CL}\rho_{Pt})$ . For example, the increase in platinum mass ratio from 0.3 to 0.8 decreases the volume fraction of the solid phase from 35.8% to 5.0% when the platinum mass loading and the catalyst layer thickness are fixed at 0.4  $\text{mg cm}^{-2}$  and 15  $\mu\text{m}$ , respectively. In this condition, the decrease in volume fraction of the solid phase leads to an increase in the porosity from 18.2% to 49.1% and results in a decrease in the agglomerate density from  $8.4 \times 10^{17} \text{ m}^{-3}$  to  $2.7 \times 10^{17} \text{ m}^{-3}$ . On the other hand, at a fixed platinum mass ratio, the porosity of the catalyst layer decreases and the agglomerate density increases as the platinum loading increases. This is because, the volume of the solid phase varies linearly with the platinum loading when the platinum mass ratio and catalyst layer thickness are fixed as constant in Eq. (3-39). For example, the increase in the platinum loading from 0.2 to 0.8  $\text{mg cm}^{-2}$  results in the volume fraction of the solid phase increasing from 11.7% to 46.9% at fixed platinum mass ratio and catalyst layer thickness of 0.4 and 15  $\mu\text{m}$ , respectively. In this condition, the increase in the volume fraction of the solid phase result in a decrease in the porosity from 42.3% to 7.1%

according to Eq. (4-25) and an increase in the agglomerate density from  $3.9 \times 10^{17} \text{ m}^{-3}$  to  $9.6 \times 10^{17} \text{ m}^{-3}$  according to Eq. (4-26).

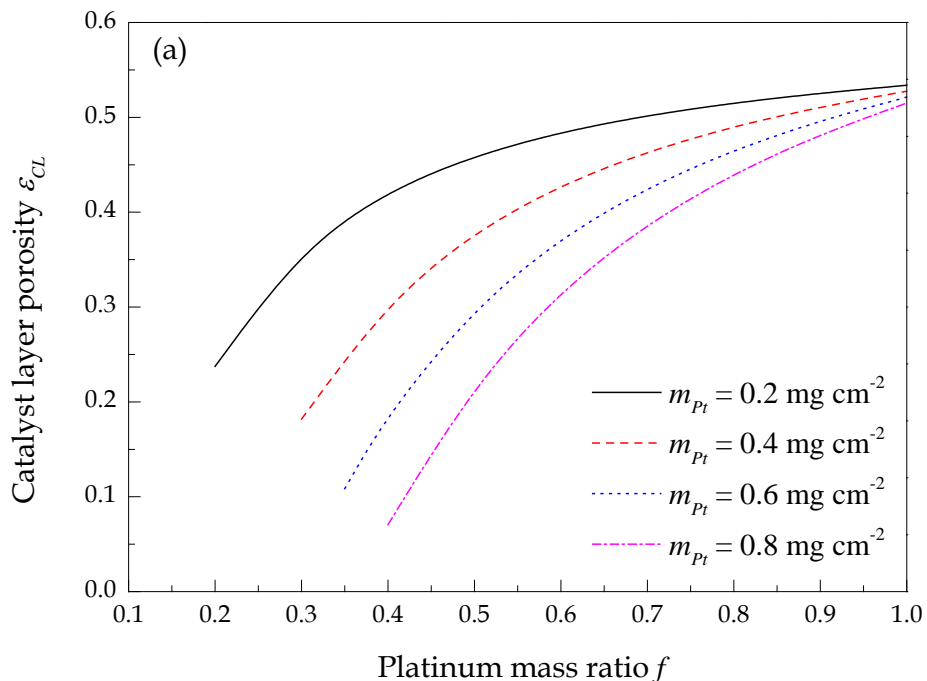


Figure 4-4 Porosities of the catalyst layer with different platinum mass ratios in base case condition

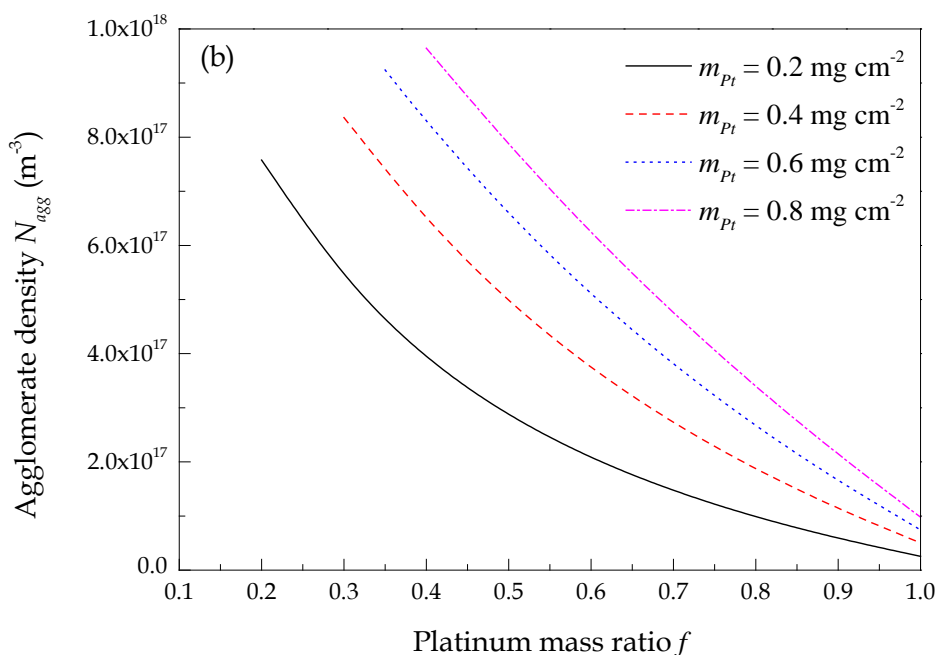


Figure 4-5 Agglomerate densities with different platinum mass ratios in base case condition

### Ionomer film thickness

Figure 4-6 shows the variation of the ionomer film thicknesses with the platinum loading from 0.2 to 0.8 mg cm<sup>-2</sup> and platinum mass ratio from 0.2 to 0.9, respectively. The ionomer film thickness increases as the platinum loading decreases and the platinum mass ratio increases. For example, the increase in platinum mass ratio from 0.2 to 0.8 increases the ionomer film thickness from 0.1 to 0.5 μm when the platinum loading and the catalyst layer thickness are fixed at 0.4 mg cm<sup>-2</sup> and 15 μm, respectively. On the other hand, the increase in the platinum loading from 0.2 to 0.8 mg cm<sup>-2</sup> decreases the ionomer film thickness from 0.7 μm to 0.3 μm when the platinum mass ratio and the catalyst layer thickness are fixed at 0.8 and 15 μm, respectively. As mentioned above, the increase in platinum mass ratio and the decrease in platinum loading result in an increase in porosity then a decrease in the volume fraction of the solid phase of the catalyst layer. It is assumed that, the ionomer firstly fills part of the primary pores of the agglomerate then the remainder covers the agglomerate forming a thin film surrounding the agglomerates. The decrease in the volume of solid phase means a decrease in the volume of primary pore. Consequently, more ionomer will occupy the secondary pores, resulting in an increase in the ionomer film thickness. Moreover, according to Eq. (4-28), the ionomer film thickness varies linearly with the agglomerate radius. The value of agglomerate radius therefore has an important influence on the ionomer film thickness and the oxygen transport resistance.

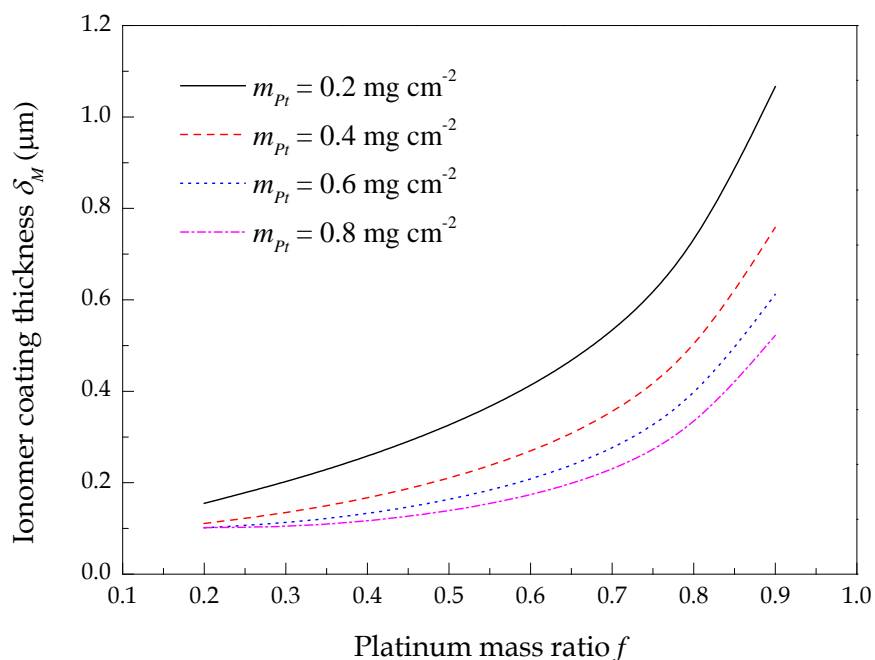


Figure 4-6 Ionomer film thicknesses with different platinum mass ratios in base case condition

### 4.3.3 Reactant gas distribution

The distribution of the concentration of oxygen, hydrogen and water vapour are given in the following sections. Note that the concentrations of all reactant gases are corrected by dividing by their inlet concentration.

#### *Distribution of dimensionless oxygen concentration*

The dimensionless oxygen concentration profiles in the gas diffusion layer and catalyst layer are shown in [Figure 4-7](#). In [Figure 4-7\(a\)](#), the boundaries of  $X = 0$  and  $X = 1$  refer to the distances from CL-GDL interface ( $F-F'$ ) to GDL-channel interface ( $G-G'$ ), while in [Figure 4-7\(b\)](#), the boundaries of  $X = 0$  and  $X = 1$  refer to the distances from membrane-CL interface ( $E-E'$ ) to CL-GDL interface ( $F-F'$ ), respectively. In both [Figure 4-7\(a\)](#) and [Figure 4-7\(b\)](#), the boundaries of  $Y = 0$  and  $Y = 1$  refer to the outlet and inlet of the cathode, respectively.

Oxygen remains at a very high concentration (close to the inlet concentration) in the flow channel in the full range of cell voltages from 0.3 V to 0.9 V due to the fact that oxygen in the feed air is supplied above stoichiometric requirements. It is clear in [Figure 4-7\(a\)](#) that along the diffusion direction ( $X$  coordinate) through the gas diffusion layer, the dimensionless concentration of oxygen decreases from 1.0 to 0.6 as the cell voltage decreases from 0.9 V to 0.3 V. Along the flow direction ( $Y$  coordinate) through the gas diffusion layer, although the decrease of dimensionless concentration of oxygen can be neglected at higher cell voltages, it decreases from 0.6 to 0.4 at the cell voltage of 0.3 V. The decrease in oxygen concentration along both the diffusion and flow directions, especially at lower cell voltages, can be explained by the increase in oxygen consumption due to the accelerated oxygen reduction reaction (ORR) as the cell voltage decreases and the presence of oxygen transport resistance through the gas diffusion layer. Oxygen transport resistance is determined by the micro structure of the porous media only, and therefore can be considered as constant during a full range of cell voltages. As described in [Section 3.1.2](#), the overall rate of an electrochemical reaction is determined by the rate of the slowest process involved in the coupled diffusion-reaction processes. At higher cell voltage, the rate of oxygen consumption is lower. In this condition, the oxygen transport resistance almost has no effect on the overall rate. However, at lower cell voltages, the rate of oxygen consumption becomes faster. In this condition, the oxygen transport from the flow channel to the active surface of the

catalyst particles is constrained due to the transport resistance. The overall rate of the ORR is determined by oxygen diffusion rate rather than the oxygen reaction rate in this condition.

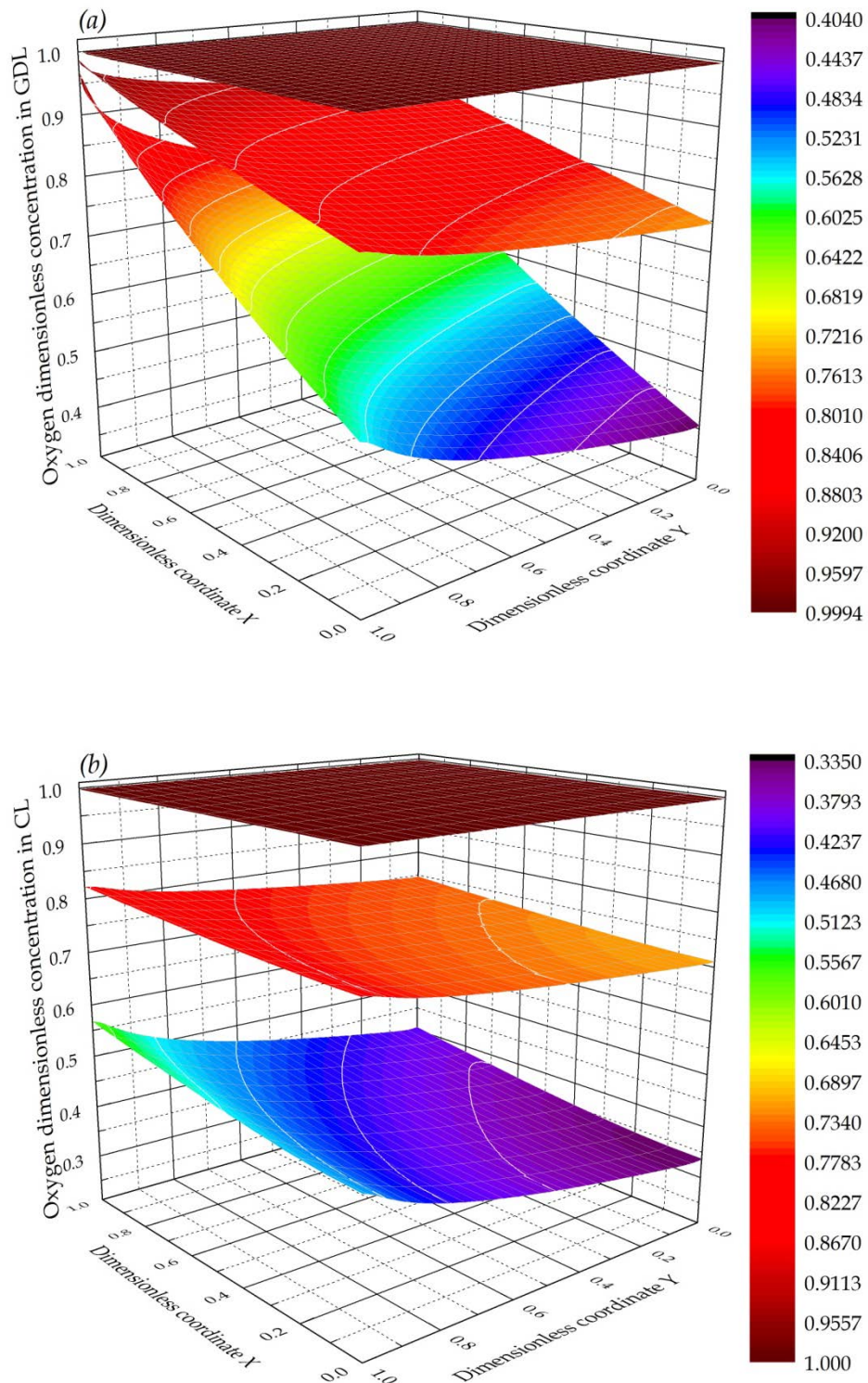


Figure 4-7 Dimensionless concentration of oxygen in gas diffusion layer (a) and catalyst layer (b) in base case condition ( $E^{\text{cell}} = 0.3, 0.6$  and  $0.9$  from down up)

Figure 4-7(b) shows that oxygen concentration decreases along the diffusion direction from the boundary of GDL-CL (F-F') to CL-membrane (E-E') resulting in a lower utilisation of the active sites in the catalyst layer located near the membrane (away from the gas diffusion layer). The lower oxygen concentration near the membrane is due to two reasons: firstly, oxygen consumption by electrochemical reaction, and secondly, the oxygen diffusion resistance. At higher cell voltages, e.g. larger than 0.6 V, the oxygen concentration is mainly determined by the electrochemical reaction rate, which is lower at higher cell voltages, leading to a relative higher concentration (approximate 70%) near the membrane. However, the oxygen concentration is determined by the diffusion rate instead of the reaction rate at lower cell voltage, e.g. lower than 0.4 V. When the cell voltage decreases to 0.3 V, only 30% of the oxygen could reach the active sites located near the membrane.

#### *Distribution of dimensionless hydrogen concentration*

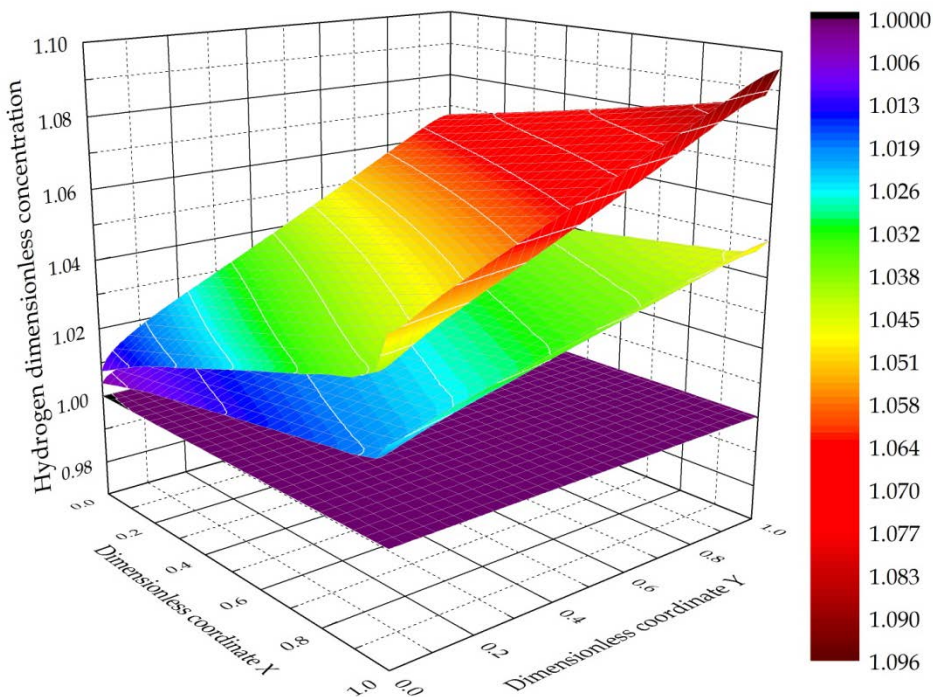


Figure 4-8 Dimensionless concentration of hydrogen in anode gas diffusion layer and catalyst layer in base case condition ( $E^{\text{cell}} = 0.3, 0.6 \text{ and } 0.9$  from up down)

The dimensionless hydrogen concentration profile in gas diffusion layer and catalyst layer are shown in Figure 4-8, in which  $X = 0$  and  $X = 1$  refer to the distances from channel-GDL interface (B-B') to CL-membrane interface (D-D') while  $Y = 0$  and  $Y = 1$  refer to the inlet and outlet of cathode, respectively. Surprisingly, rather than decreases

in concentration, the hydrogen concentration remains almost at the inlet concentration at the cell voltage of 0.9 V, and increases approximately 10% at the cell voltage of 0.3 V along the flow direction. This is because water transport through the membrane from anode to cathode increases the hydrogen fraction of the anode reactant. Especially near the anode outlet ( $Y=1$ ) the greater current density takes more water molecules from anode to cathode. Although hydrogen is consumed along the flow direction by the hydrogen oxidation reaction (HOR), the decrease in hydrogen concentration is compensated by the decrease in water concentration which results in a slight increase in hydrogen concentration along the flow direction.

### ***Distribution of dimensionless water vapour concentration***

Figure 4-9 shows the dimensionless water vapour concentration profiles in the gas diffusion layer and catalyst layer of anode and cathode. The dimensionless coordinate  $X$  and  $Y$  in Figure 4-9(a) refers to the same geometry as shown in Figure 4-8. In Figure 4-9(b), coordinate  $Y$  refers to the same geometry as shown in Figure 4-7 and the boundary  $X=0$  and  $X=1$  refer to the distance from membrane-CL interface (E-E') to GDL-channel interface (G-G'). It is clear in Figure 4-9(a) that, as expected, the anode water vapour concentration decreases along the flow and diffusion directions as the cell voltage decreases, which dehydrates the membrane at the anode side and increases the proton transport resistance.

However, as shown in Figure 4-9(b), the water vapour concentration is higher than the inlet value in full range of cell voltages, and the maximum concentration is observed in the cathode catalyst layer near the membrane. This can be explained by two reasons. Firstly, water is produced by the oxygen reduction reaction inside the cathode catalyst layer. Secondly, water is carried by protons from anode to cathode due to the effect of electro-osmotic drag. It is important to note that water vapour will condense when it reaches the saturation level. However, water phase transfer is not included in this single-phase flow model, which will be taken into account in the two-phase flow model in Chapter 5.

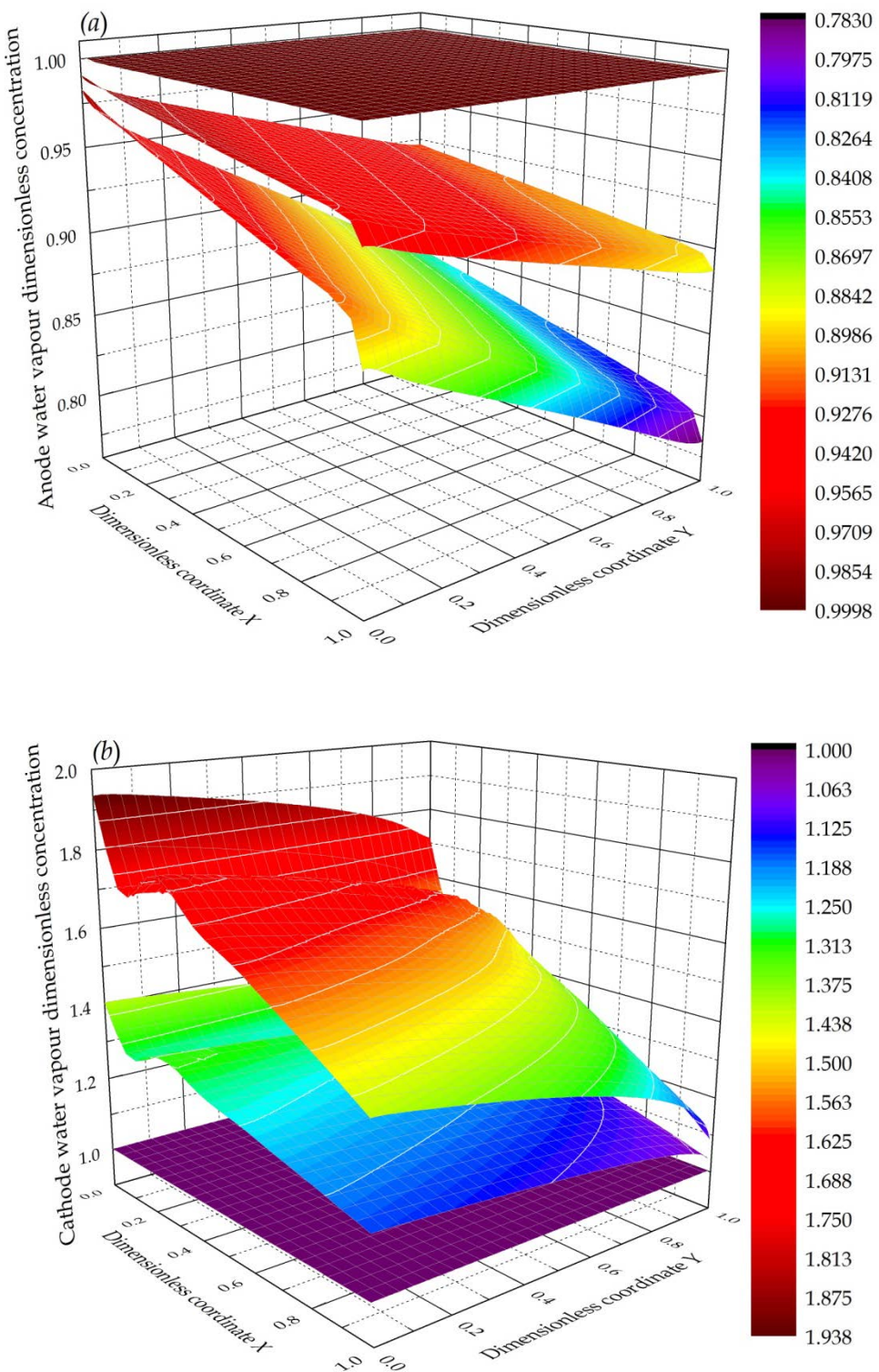


Figure 4-9 Dimensionless concentration of water vapour in the gas diffusion layer and catalyst layer of anode (a) and cathode (b) in base case condition ( $E^{\text{cell}} = 0.3, 0.6$  and  $0.9$  from down up for case (a) and from up down for case (b))

#### 4.3.4 Effectiveness factor

The distribution of the effectiveness factor of the cathode catalyst layer ( $E_r$ ) at different cell voltages is presented in Figure 4-10. The coordinates  $X$  and  $Y$  refer to the

same geometry as shown in Figure 4-7(b). The highest effectiveness factor (approximately equal to 1.0) is observed at 0.7 V, and it decreases with the decrease of cell voltage from 0.7 to 0.3 V. The decrease in effectiveness factor is due to the higher reaction rate at lower cell voltages. At the cell voltage of 0.7 V, the overall rate of oxygen reduction reaction is determined by the rate of electrochemical reaction rather than the rate of oxygen diffusion. The platinum catalyst is therefore almost fully utilised leading to a very high effectiveness factor.

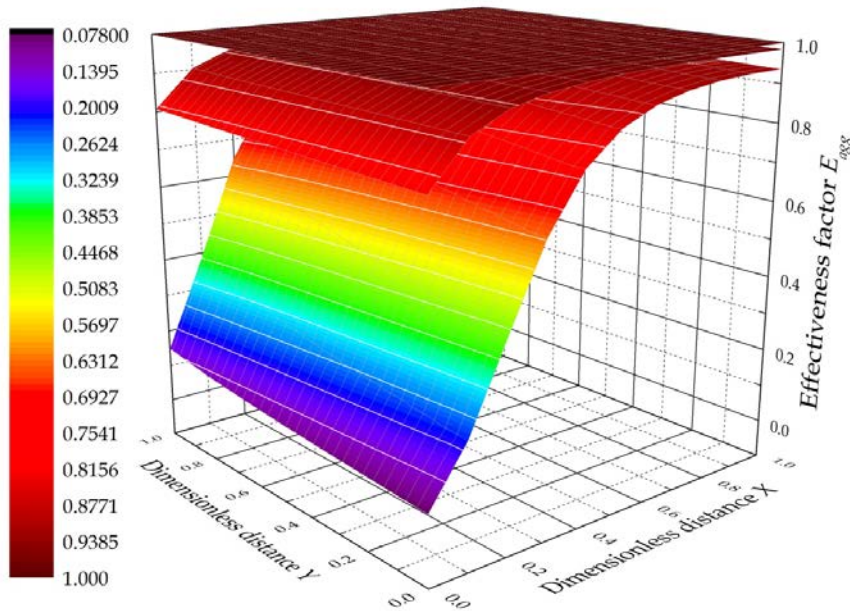


Figure 4-10 Effectiveness factor of cathode catalyst layer at three cell voltages in base case condition ( $E_{\text{cell}}^{\text{cell}} = 0.3, 0.6 \text{ and } 0.9 \text{ V}$  from down up)

As the cell voltage decreases, the increase in electrochemical reaction rate leads to faster oxygen consumption relative to the oxygen diffusion rate to the catalyst surface. The rate determining process therefore changes from electrochemical reaction to oxygen diffusion. Consequently, along the oxygen diffusion direction through catalyst layer, the catalyst utilisation is higher near the GDL-CL boundary ( $X=1$ ) than that of the CL-membrane boundary ( $X=0$ ). For a cell voltage of 0.3 V, corresponding to a current density of approximate  $1.4 \text{ A cm}^{-2}$ , the dimensionless effectiveness factor decreases from 0.9 at the GDL-CL boundary to 0.08 at the CL-membrane boundary. It is important to note that the change of the effectiveness factor is not pronounced along the reactant flow direction ( $Y$  direction). At 0.3 V, it only decreases from 0.15 to 0.08 along the CL-membrane boundary. This is because the geometric effect, i.e. the land and channel effect, is omitted in this the along channel model. In other words, oxygen is

considered to be distributed uniformly everywhere within the cathode catalyst layer along the flow direction in this along-the-channel model. In order to simplify the figure, the two-dimensional effectiveness factor ( $E_r$ ) can be replaced by the one-dimensional average effectiveness factor ( $\bar{E}_r$ ).

#### 4.3.5 Distribution of membrane water content

The distribution of water content at different cell voltages is presented in Figure 4-11. At a higher cell voltage, e.g. 0.9 V, the water content distribution is almost uniform. The water content within the membrane at both the anode and cathode side is equal to their initial values, which are determined by the relative humidity of the gas inlet according to Eq. (3-209). With the decrease in cell voltage, the current density increases and leads to a water transport through the membrane from anode to cathode. As shown in Figure 4-11, the decrease in cell voltage from 0.9 to 0.6 V results in a slight water content distribution along the reactant flow direction ( $Y$  direction). However, the cell voltage decreases from 0.6 to 0.3 V leads to a non-uniform water content distribution along both the diffusion and flow directions. This indicates more water transport through the membrane from anode ( $X = 0$ ) to cathode ( $X = 1$ ) and more water movement from cathode inlet ( $Y = 1$ ) to the cathode outlet ( $Y = 0$ ) along the air flow direction as the cell voltage decreases from 0.6 V to 0.3 V. The increase in water flux through the membrane can be explained by the increase in current density within the membrane.

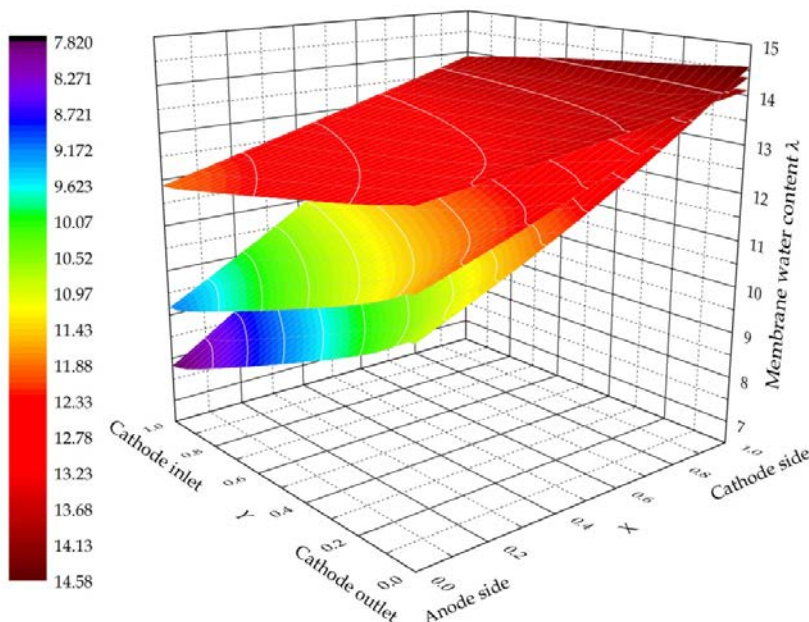


Figure 4-11 Water content distribution within the membrane at three cell voltages in base case condition ( $E^{cell} = 0.3, 0.6$  and  $0.9V$  from down up)

The current density within the membrane is uniform when the cell voltage is higher, e.g. at 0.8 V. However, as shown in Figure 4-12, it becomes higher at the cathode outlet ( $Y = 0$ ) than that at the cathode inlet ( $Y = 1$ ) when the voltage decreases, e.g. from 0.6 V to 0.3 V. This is because water back diffusion from cathode to anode cannot compensate for the electro-osmotic drag at the cathode inlet ( $Y = 1$ ), resulting in dehydration of the membrane on the anode side, which leads to an increase in the membrane resistance. The electro-osmotic drag flux is therefore reduced by the decreased current density within the membrane near the cathode inlet.

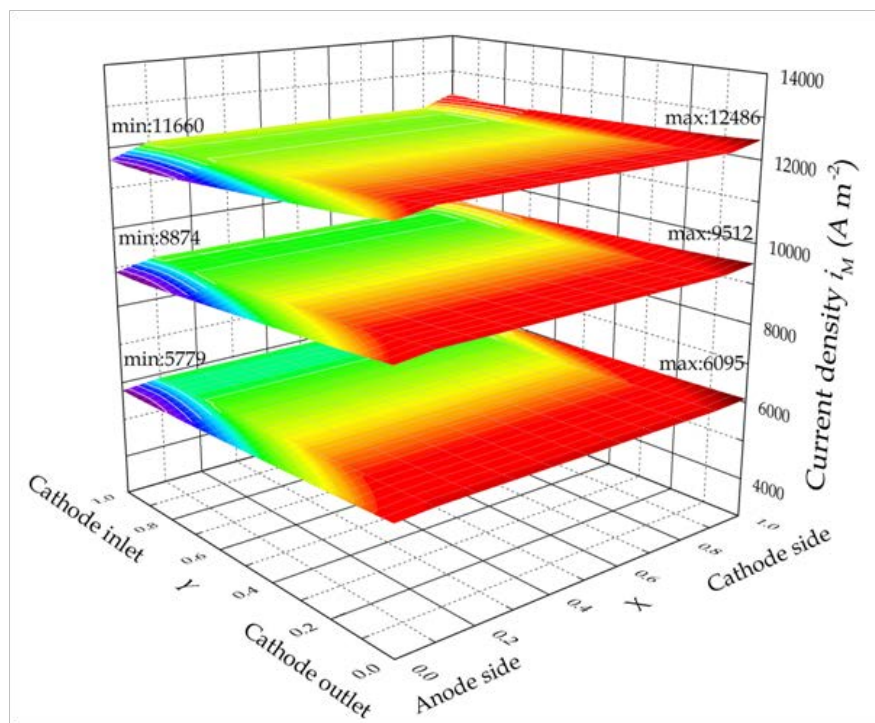


Figure 4-12 Current density distribution within the membrane with different cell voltages in base case condition ( $E^{\text{cell}} = 0.4, 0.5$  and  $0.6$  V from up down)

#### 4.3.6 Distribution of current density

Figure 4-13 shows the current density distributions with the catalyst layers of anode and cathode with the cell voltage varying from 0.7 to 0.3 V. These figures illustrate where the current density generated inside the catalyst layers. It is clear that the current densities in both catalyst layers of the anode and cathode increase, in other words, more current is extracted from the cell, as the cell voltage decreases. Moreover, both the current densities of the anode and cathode decrease along the reactant diffusion direction, leading to an insufficient utilisation of the catalyst near the CL-membrane boundary ( $X = 0$  for cathode and  $X = 1$  for anode). On the contrary, the current densities

almost maintain constants along the reactant flow direction. It is apparent that the current density distribution in the anode catalyst layer is more uniform than that in the cathode catalyst layer. In the region near the CL-membrane boundary, the anode current density is higher than the cathode current density at a fixed cell voltage. This can be explained by the relative slow oxygen reduction reaction (ORR) in the cathode. Due to the slower ORR in the cathode, the interior of the cathode catalyst layer is not fully utilised, especially in case of higher current densities are produced.

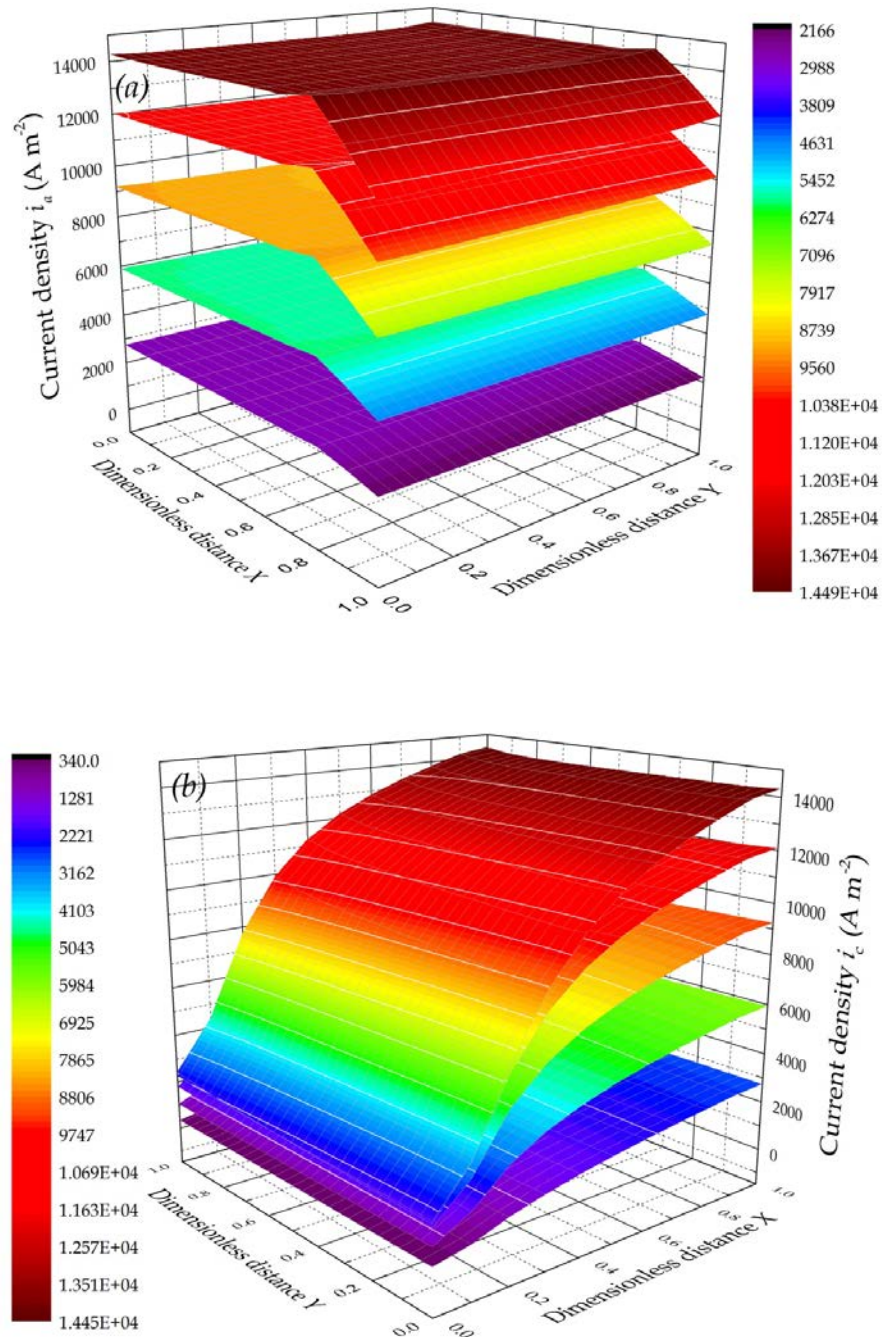


Figure 4-13 Current density distributions with the catalyst layers of anode and cathode in base case condition ( $E^{\text{cell}} = 0.3, 0.4, 0.5, 0.6, 0.7$  from up down)

### 4.3.7 Effect of platinum and carbon loading

As shown in Figure 4-14, the cell performance is improved by increasing the cathode platinum loading. This improvement can be explained by the increase in reaction rate and the increase in effective specific area of the catalyst layer which can be calculated according to Eq. (3-31) and Eq. (4-27), respectively. However, this improvement is limited because, according to Eq. (3-23) and Eq. (3-24), the effectiveness factor decreases dramatically as the reaction rate increases. In other words, the increase in reaction rate leads to faster reactant consumption near the GDL-CL boundary (F-F') inside the catalyst layer, which results in insufficient utilisation of the catalyst layer near the CL-membrane boundary (E-E').

Simultaneously, the increase in platinum loading leads to a decrease in catalyst layer porosity, which is showed in Figure 4-4. The effective oxygen diffusion coefficient decreases due to the loss of void space, resulting in an increase in the mass transport resistance. As shown in Figure 4-14, the fuel cell performance improves very slightly when the platinum loading is doubled, especially at higher current densities. It is apparent that the increase in platinum loading from 0.4 to 0.8 mg cm<sup>-2</sup> makes a slight contribution to the current density improvement.

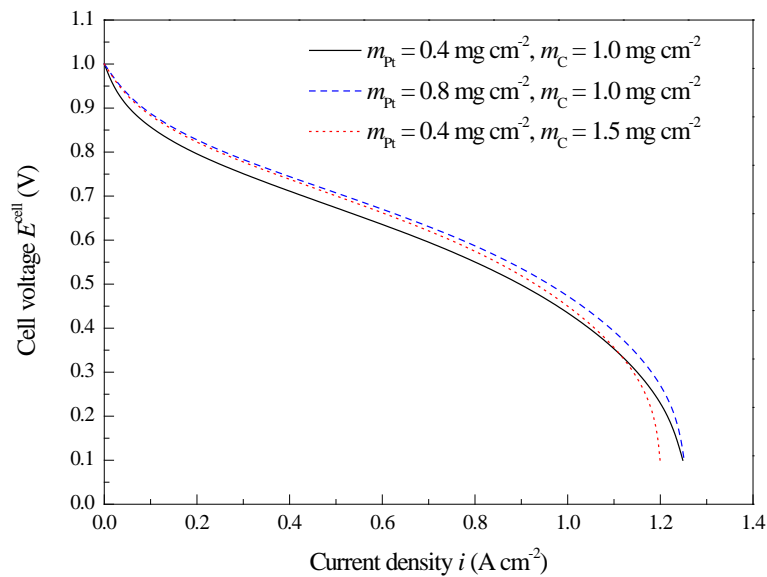


Figure 4-14 Polarisation curves for different platinum and carbon loadings in base case condition

Figure 4-15 shows the average effectiveness factors of the cathode catalyst layer with different platinum loadings. It is clear that, due to the slower transport rate of oxygen to

the platinum surface, the catalysts in the interior of the catalyst layer cannot be fully utilised, which results in a decrease in effectiveness factor and thus a waste of platinum.

The effect of cathode carbon loading can be also seen in Figure 4-14. Similar to the effect of platinum loading, the increase in effective specific area and decrease in catalyst layer porosity are observed as the carbon loading increases according to Eq. (4-29) and Figure 4-4. Unlike the effect of the platinum loading, the increase in carbon loading increases the specific area rather than the reaction rate. As shown in Figure 4-14, the fuel cell performance is improved at lower current densities as the carbon loading increases from  $1.0$  to  $1.5 \text{ mg cm}^{-2}$ . However, it is also clear in Figure 4-4 that the increase in carbon loading decreases the catalyst layer porosity, which leads to a decrease in effective oxygen diffusion coefficient. Consequently, the cell performance is decreased at higher current densities, e.g. larger than  $1.1 \text{ A cm}^{-2}$ . In this condition, the improved fuel cell performance resulting from the increased catalyst layer specific area is offset by the decreased oxygen diffusion coefficient.

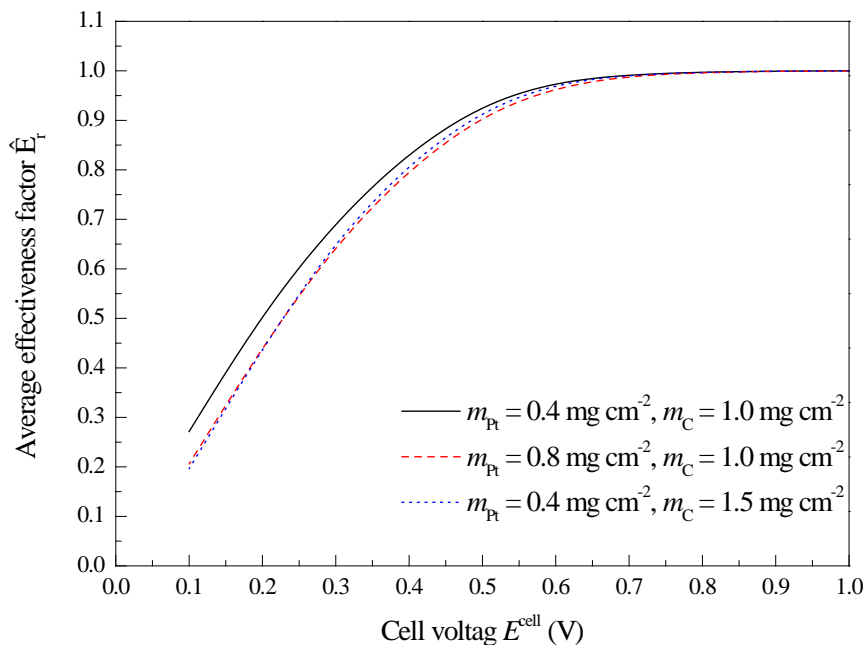


Figure 4-15 Average effectiveness factors for different platinum and carbon loadings in base case condition

In addition, the simulation results (not plotted here) show that the polarisation curves change slightly (< 5.0%) with different platinum and carbon loadings in the anode catalyst layer. It can be concluded, the oxygen reduction reaction at the cathode plays a more important role in determining the overall performance of the fuel cell.

### 4.3.8 Effect of agglomerate radius

The effect of agglomerate radius on the cell performance is shown in Figure 4-16. At lower current densities, the effect of agglomerate radius is not significant because of the slower reaction rate. However, it is clear that the cell performance improves with smaller agglomerates at higher current densities. This improvement is due to two reasons. Firstly, as shown in Eq. (4-28), the ionomer film is thinner with a smaller agglomerate radius. Smaller agglomerates lead to a decrease in the ionomer film thickness, which decreases the oxygen transport resistance through the ionomer film. Secondly, smaller agglomerates increase the effectiveness factor (see Figure 4-17) which is caused by the decreased Thiele's modulus according to Eq. (3-24). Therefore, the oxygen diffusion resistance inside the agglomerate is reduced, which leads to a higher oxygen concentration on the platinum surface.

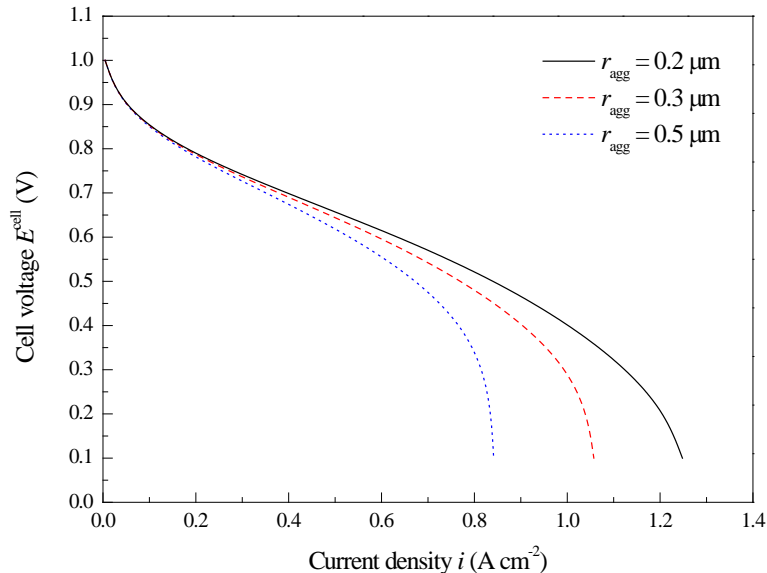


Figure 4-16 Polarisation curves for different agglomerate radius in base case condition

In Figure 4-16, the rapid decrease in current density at lower cell voltage is due to the oxygen diffusion resistance through the ionomer film surrounding the agglomerate. The larger agglomerate radius adopted, a thicker ionomer film is formed and higher oxygen diffusion resistance is obtained. If no ionomer film is generated, the expressions of current density would changes from Eq. (4-16) and Eq. (4-17) to Eq. (4-18) and Eq. (4-19), in which only the effectiveness factor is used to correct the intrinsic Buter-Volmer kinetic. As shown in Figure 4-3, this overestimates the current density at lower cell voltages. This indicates that the oxygen transport limitation through the ionomer film is

the main obstacle for improving the cell performance. Therefore, an optimal ionomer volume fraction is important. Moreover, regardless of the negative effect, such as increased oxygen transport resistance through the smaller pores inside the smaller agglomerate, a smaller agglomerate radius is of great benefit to the cell performance.

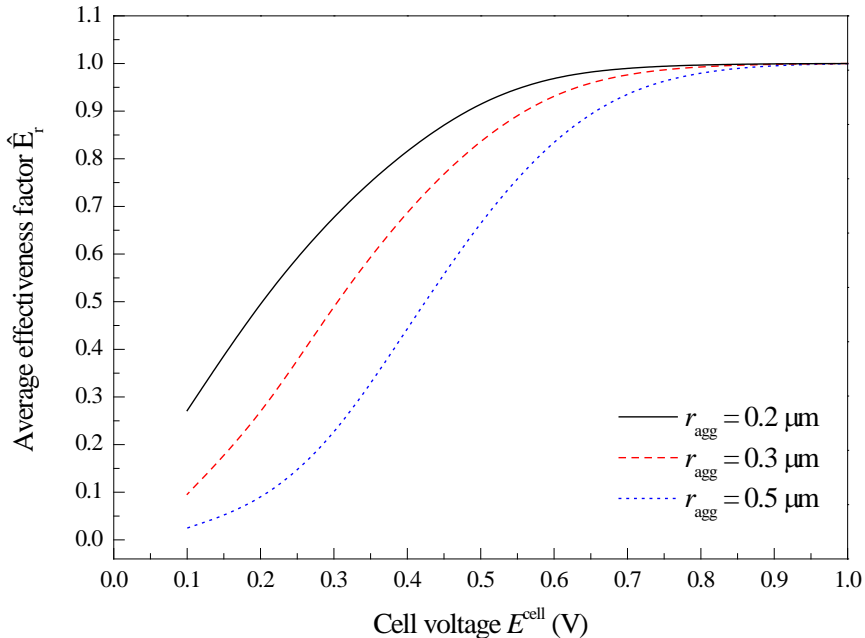


Figure 4-17 Average effectiveness factors for different agglomerate radius in base case condition

#### 4.3.9 Effect of gas inlet pressure

The effect of gas inlet pressures on the cell performance is shown in Figure 4-18. The fuel cell is as expected performs better with higher inlet pressures, for both the anode and cathode. However, the increase in anode inlet pressure leads to a limited improvement of the cell performance, although hydrogen concentration is increased. This is due to the low polarisation losses at the anode.

On the contrary, higher cathode inlet pressure makes a significant improvement in the fuel cell performance. This is because the overall reaction rate is determined by the relative sluggish oxygen reduction reaction at the cathode. The higher oxygen partial pressure increases the dissolved oxygen into the agglomerate, resulting in a greater current density. Moreover, the higher cathode pressure to some extent prevents water migration from the anode, which results in a higher membrane conductivity.

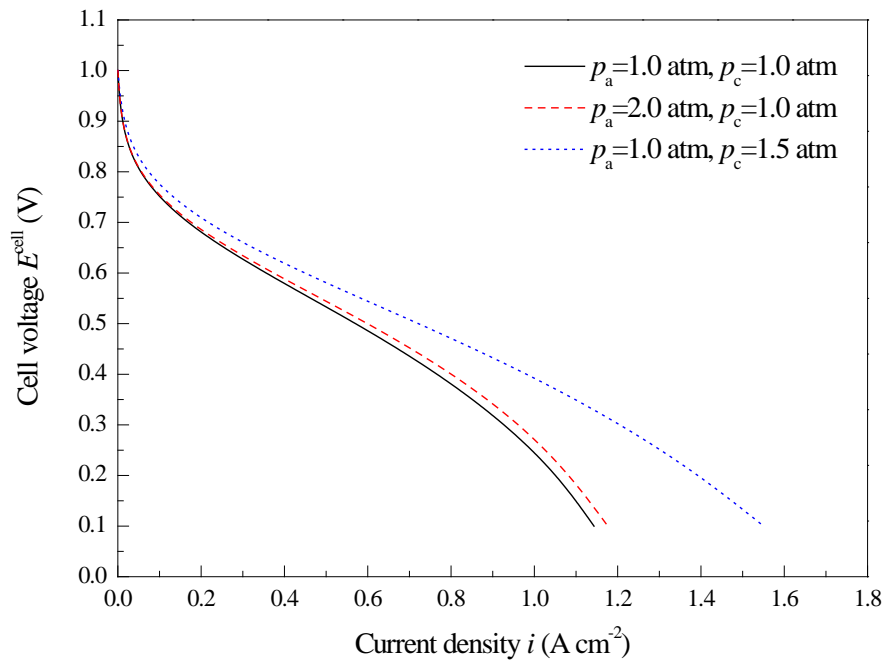


Figure 4-18 Polarisation curves for different inlet pressures compared to base case condition

#### 4.4 Conclusions

A two-dimensional, along-the-channel, steady-state, isothermal, single-phase flow model based on an agglomerate catalyst layer structure is developed. Catalyst layer property, including porosity, agglomerate density, ionomer film thickness, and specific area, are quantitatively represented by a mathematical simulation. The presence of the ionomer film surrounding the agglomerate is the main reason for the rapid drop in the current density at lower cell voltages due to the increase in oxygen transport resistance. Higher cathode inlet pressure and platinum loading are of benefit to the cell performance. However, too much carbon loading decreases the current density at lower cell voltages. Both higher platinum and carbon loading decrease the effectiveness factor of the catalyst layer, which leads to a poor utilisation of the catalyst layer. This model gives a theoretical guidance on the effect of operating condition and catalyst layer composition to enhance the fuel cell performance and reduce the cost.

#### 4.5 References

1. Djilali, N, *Computational modeling of polymer electrolyte membrane (PEM) fuel cells: Challenges and opportunities*. Energy, 2007. **32**: p. 269-280.
2. Carton, J.G. and A.G. Olabi, *Wind/hydrogen hybrid systems: Opportunity for Ireland's wind resource to provide consistent sustainable energy supply*. Energy,

2010. **35**: p.4536-4544.
3. Weber, A.Z., S. Balasubramanian and P.K. Das. *Proton Exchange Membrane Fuel Cells*. in K. Sundmacher (editor), *Advances in Chemical Engineering Fuel Cell Engineering*, USA: Elsevier Inc; 2012. **40**: p. 66-143.
  4. Springer, T.E., T.A. Zawodzinski and S. Gottesfeld, *Polymer Electrolyte Fuel Cell Model*, Journal of Electrochemistry Society, 1991. **138**: p. 2234-2342.
  5. Bernardi, D.M. and M.W. Verbrugge. *A mathematical model of the solid-polymer-electrolyte fuel cell*. Journal of Electrochemistry Society, 1992. **139**: p. 2477-2491.
  6. Broka, K. and P. Ekdunge, *Modelling the PEM fuel cell cathode*. Journal of Applied Electrochemistry, 1997. **27**: p. 281-289.
  7. Marr, C. and X. Li, *Composition and performance modelling of catalyst layer in a proton exchange membrane fuel cell*. Journal of Power Sources, 1999. **77**: p. 17-27.
  8. Berning, T., D.M. Lu and N. Djilali, *Three-dimensional computational analysis of transport phenomena in a PEM fuel cell*. Journal of Power Sources, 2002. **106**: p. 284-294.
  9. Sun, W., B.A. Peppley and K. Karan, *An improved two-dimensional agglomerate cathode model to study the influence of catalyst layer structural paramets*. *Electrochimica Acta*, 2005. **50**: p. 3359-3374.
  10. Thepkaew, J., A. Therdthianwong and S. Therdthianwong, *Key parameters of active layers affecting proton exchange membrane fuel cell performance*. Energy, 2008. **33**: p. 794-1800.
  11. N. Khajeh-Hosseini-Dalasm, M.J. Kermani, D.G. Moghaddam and J.M. Stockie, *A parametric study of cathode catalyst layer structural parameters on the performance of a PEM fuel cell*. International Journal of Hydrogen Energy, 2010. **35**: p. 2417-2427.
  12. Nguyen, T.V. and R.E. White, *A water and heat management model for proton-exchange-membrane fuel cells*. Journal of Electrochemistry Society, 1993. **140**: p. 2178-2186.
  13. Ge, S.H. and B.L. Yi, *A mathematical model for PEMFC in different flow modes*. Journal of Power Sources, 2003. **124**: p. 1-11.

14. Yi, J.S. and T.V. Nguyen, *An along-the-channel model for proton exchange membrane fuel cells*. Journal of Electrochemistry Society, 1998. **145**: p. 1149-1159.
15. Basu, S., J. Li and C.Y. Wang, *Two-phase flow and maldistribution in gas channels of a polymer electrolyte fuel cell*. Journal of Power Sources, 2009. **187**: p. 431-443.
16. Murgia, G., L. Pisani, M. Valentini and B.D. Aguanno, *Electrochemistry and Mass Transport in Polymer Electrolyte Membrane Fuel Cells. I. Model*. J. Journal of Electrochemistry Society, 2002. **149**: p. A31-A38.
17. Costamagna, P., *Transport phenomena in polymeric membrane fuel cells*. Chemical Engineering Science, 2001. **56**: p. 323-332.
18. Hertwig, K., L. Martens and R. Karwoth, *Mathematical modelling and simulation of polymer electrolyte membrane fuel cells. Part I: Model structures and solving an isothermal one-cell model*. Fuel Cells, 2002. **2**: 61-77.
19. Yan, Q., H. Toghiani and H. Causey, *Steady-state and dynamic performance of proton exchange membrane fuel cells (PEMFCs) under various operating conditions and load changes*. Journal of Power Sources, 2006. **161**: p. 492-502.
20. Suzuki, A., U. Sen, T. Hattori, R. Miura, R. Nagumo, H. Tsuboi, N. Hatakeyama, A. Endou, H. Takaba, M.C. Willims and A. Miyamoto, *Ionomer content in the catalyst layer of polymer electrolyte membrane fuel cell (PEMFC): Effect on diffusion and performance*. International Journal of Hydrogen Energy, 2011. **36**: 2221-2229.
21. Sousa, T., M. Mamlouk, K. Scott, *A non-isothermal model of a laboratory intermediate temperature fuel cell using PBI doped phosphoric acid membranes*. Fuel Cells, 2010. **10**: p. 993-1012.
22. Ismail, M.S., K.J. Hughes, D.B. Ingham, L. Ma and M. Pourkashanian, *Effect of anisotropic permeability and electrical conductivity of gas diffusion layers on the performance of proton exchange membrane fuel cells*. Applied Energy, 2012. **95**: p. 50-63.
23. Xing, L., X.G. Song, K. Scott, V. Pickert and W.P. Cao, *Multi-variable optimisation of PEMFC cathodes based on surrogate modelling*. International Journal of Hydrogen Energy, 2013. **38**: p. 14295-14313.
24. Liu, Z., Z. Mao and C. Wang, *A two-dimensional partial flooding model for PEMFC*. Journal of Power Sources, 2006. **158**: p. 1229-1239.

## Chapter 5. Two-phase flow isothermal model

This chapter describes a two-dimensional, across-the-channel, two-phase flow, isothermal, steady-state model based on a spherical-agglomerate catalyst structure combined with a comprehensive water phase-transfer and transport mechanism. This is used to investigate the effect of catalyst layer parameters and operating conditions on membrane and ionomer swelling and then the performance of the cell. The model provides guidance for optimisation of the dry ionomer volume fraction in the cathode catalyst layer and the relative humidity of the cathode reactant gas.

### 5.1 Introduction

The performance of PEMFCs is particularly affected by the performance of the cathode catalyst layer, in which the relatively slow oxygen reduction reaction (ORR) occurs [1-5]. In order to understand the coupled kinetics and mass transport processes in the cathode catalyst layer, numerous researchers have proposed a spherical-agglomerate model as the structure of the catalyst layer of the cathode and concluded that this gives a superior representation of the porous catalyst layer compared with the ultra-thin layer model or pseudo-homogeneous film model [4-6].

Adequate hydration of the perfluorinated membrane, such as Nafion<sup>®</sup>, is critical to successful fuel cell operation. During fuel cell operation, the ionic conductivity and the structure of the membrane strongly depend on the membrane water content [1, 7-9]. The polymeric matrix of the membrane expands leading to an increase in the membrane volume when membrane water absorption (water uptake) occurs. Normally a dry Nafion<sup>®</sup> membrane swells approximately 20% when fully hydrated by water vapour [7, 9]. The membrane penetrates into the gas diffusion layer, combined with the platinum catalyst and ionomer to construct the catalyst layer. Membrane/ionomer swelling has two effects on fuel cell performance. For the membrane, higher swelling increases the membrane ionic conductivity and the water diffusion coefficient, while for the ionomer higher swelling increases the thickness of the ionomer film surrounding the agglomerate and decreases the void space within the catalyst layer, leading to an increase in species transport resistance, specifically the oxygen diffusion [7]. Numerous experimental and numerical studies [10-12] have investigated the membrane swelling

and its effect on the fuel cell performance. However, very few studies account for ionomer swelling.

Water exists as three different phases [10-12]: dissolved water in the membrane/ionomer (membrane/ionomer absorbed water), water vapour and liquid water in the porous media. The main phase transfer mechanisms include: phase transfer between liquid water and water vapour (condensation/evaporation), phase transfer between dissolved water and water vapour (membrane/ionomer absorption or water uptake), and phase transfer between liquid water and dissolved water (membrane/ionomer desorption). Water transport in the membrane plays an important role in determining the water content in the membrane/ionomer [1, 7, 10-12]. During fuel cell operation, water transport through the membrane occurs via three mechanisms: electro-osmotic drag of water molecules carried by protons migrating from anode to cathode, back diffusion driven by the concentration gradient of water, and convection generated by the pressure gradient. By entirely considering the three water transport mechanisms mentioned above, Ge and Yi [13] developed a two-dimensional steady-state model to describe water transport through the membrane with fuel and oxidant gases in co-flow and counter-flow modes. This so-called combinational water transport model was successfully applied in the literature [14-16].

The properties of the membrane, gas diffusion layer and catalyst layer play a vital role in water control. The porous electrode must have sufficient porosity to allow oxygen transport and must have sufficient hydrophobic properties to avoid liquid water build-up. Wang *et al.* [15, 17-19] described the liquid water transport by combining the so-called multi-phase mixture ( $M^2$ ) approach with the volume of fluid (VOF) method. Nam and Kaviany [20] studied the distribution of water saturation in the porous media and highlighted its tendency in reducing the effective mass diffusivity. Nguyen *et al* [21] introduced the agglomerate structure of the catalyst layer into the two-phase flow model and showed that liquid water flooding in the catalyst layer was more severe than that in gas diffusion layer. Consequently, catalyst layer must be considered as an individual domain rather than a segment of gas diffusion layer. The combination of agglomerate structure with the two-phase flow model was improved by Shah *et al.* [7]. In their model, liquid water was assumed to be a thin film surrounding the agglomerate. Wu *et al.* [10] and Yang *et al.* [12] developed a three-dimensional water transport model by considering the phase transfer processes between water vapour, dissolved water and

liquid water. However, despite the numerous two-phase flow models available, very few have considered ionomer swelling and its effect on the PEMFC performance.

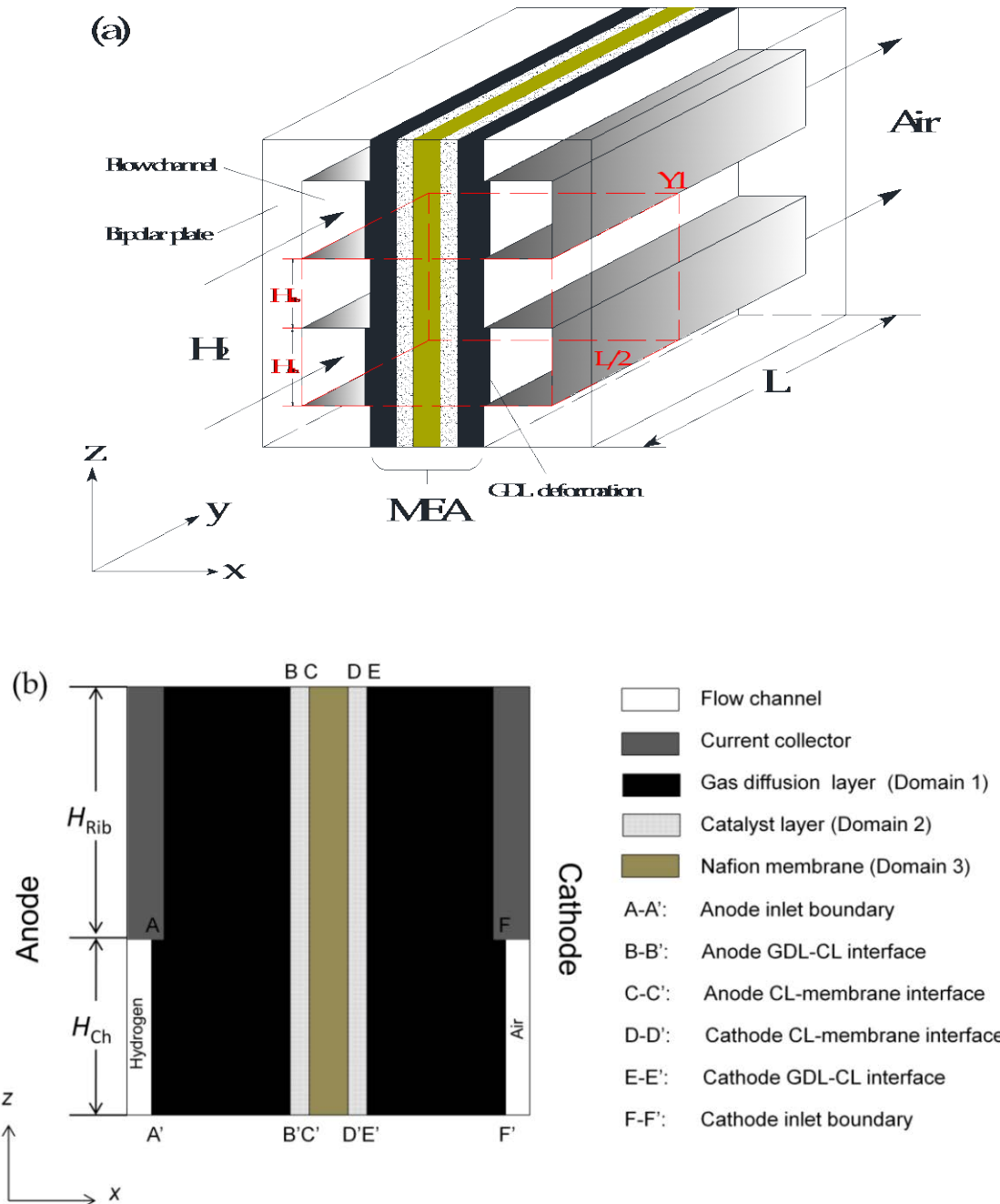
## 5.2 Model description

### 5.2.1 Computational domain and assumption

The three-dimensional representation of the PEMFC has been presented in detail in Chapter 4. Different from the along-the-channel model shown in Figure 4-1(b), a two-dimensional across-the-channel computational domain, plane Y1 in Figure 5-1(a), is selected. This plane is located in the middle of the cell along reactant flow direction, which is shown in detail in Figure 5-1(b). In addition to the geometric parameters in Chapter 4, the shoulder width ( $H_{Rib}$ ) and the channel width ( $H_{Ch}$ ) are defined as 0.75 mm and 0.5 mm, respectively. The rest of the geometric parameters and material properties in this model are same as that of the along-the-channel model in Chapter 4.

In the two-phase flow model, particular model features and assumptions are added as follow:

1. Ideal gas mixture.
2. Reactant crossover is omitted.
3. Spherical agglomerate structure of the catalyst layer.
4. Agglomerates are in turn surrounded by ionomer and liquid water films.
5. The shape of both the swelled membrane and the bulged GDL are half ellipses.
6. Ionomer swelling increases the thickness of the ionomer film rather than the catalyst layer.
7. Liquid water only exists in the secondary pores within cathode, which is generated by water vapour condensation and membrane/ionomer desorption.
8. Water absorbed in membrane/ionomer is in the dissolved phase, which enters the membrane/ionomer from the vapour phase during water uptake and leaves the membrane in the liquid phase when the water content reaches complete saturation. The product water in the cathode catalyst layer is generated in the dissolved phase.

Figure 5-1 Sketch of a typical PEMFC (a) 3D representation (b) 2D computational domain  $Y_1$ 

### 5.2.2 Governing equations

Having accounted for all assumptions, the governing equations described in Chapter 3 can be specified in Table 5-1 to account for the particular processes occurred in the selected domains. Note that flow channels (Domain 1) are not included in the computational domain.

Table 5-1 Governing equations used in the two-phase flow and isothermal model

Gas diffusion layers (Domain 2)	
Conservation of mass	$-\frac{\rho^g k_p}{\mu^g} \nabla \cdot (\nabla p) = 0 \quad (5-1)$
Conservation of species	$\rho^g \mathbf{u}^g \cdot \nabla w_i^g - \nabla \cdot [-\rho^g \sum_{j=1}^N (1-s^j) D_{ij} (\nabla x_j^g - w_j^g) \frac{\nabla p}{p}] = 0 \quad (5-2)$
Conservation of charge	$\nabla (-\sigma_s^{eff} \nabla \phi_s) = \nabla (-\sigma_M^{eff} \nabla \phi_M) = 0 \quad (5-3)$
Catalyst layers (Domain 3)	
Conservation of mass	$-\frac{\rho^g k_p}{\mu^g} \nabla \cdot (\nabla p) = S_m \quad (5-4)$
Conservation of species	$\rho^g \mathbf{u}^g \cdot \nabla w_i^g - \nabla \cdot [-\rho^g \sum_{j=1}^N (1-s^j) D_{ij} (\nabla x_j^g - w_j^g) \frac{\nabla p}{p}] = M_i S_i^g \quad (5-5)$
Conservation of charge	$\nabla (-\sigma_s^{eff} \nabla \phi_s) = Q_s \quad (5-6)$
Conservation of charge	$\nabla (-\sigma_M^{eff} \nabla \phi_M) = Q_M \quad (5-7)$
Membrane (Domain 4)	
Conservation of charge	$\nabla (-\sigma_M^{eff} \nabla \phi_M) = 0 \quad (5-8)$

### 5.2.3 Electrochemical reactions kinetics

Due to the presence of liquid water film surrounding the agglomerate, the oxygen transport resistance is increased. In order to account for the oxygen diffusion resistance through the ionomer and liquid water films, the cathode volumetric current density based on the agglomerate model is modified as follow:

$$i_{c,agg} = 4F \frac{p_{O_2}}{H_{O_2}} \left[ \frac{1}{E_{agg,c} k_{agg,c}} + \frac{(r_{agg} + \delta)}{\gamma_{agg}} \right]^{-1} \quad (5-9)$$

where  $\gamma$  ( $s^{-1}$ ) is the oxygen diffusion rate through the ionomer/liquid water film to the agglomerate interface and  $\delta$  (m) is the total thickness of the ionomer and liquid water film. The rest of the parameters used in Eq. (5-9) are those used in Eq. (4-17).

$$\gamma = \frac{\gamma_M \gamma_w}{\gamma_M + \gamma_w}, \quad \gamma_M = \frac{a_{agg} D_{O_2-M}}{\delta_M}, \quad \gamma_w = \frac{a_{agg} D_{O_2-w}}{\delta_w}, \quad \delta = \delta_M + \delta_w \quad (5-10)$$

in which  $\delta_M$  (m) and  $\delta_w$  (m) are the thicknesses of the ionomer film and liquid water film, respectively.  $D_{O_2-M}$  ( $\text{m}^2 \text{ s}^{-1}$ ) and  $D_{O_2-w}$  ( $\text{m}^2 \text{ s}^{-1}$ ) are the diffusion coefficient of oxygen through ionomer and liquid water, respectively.  $a_{agg}$  ( $\text{m}^{-1}$ ) is the specific area of the agglomerate without the ionomer film and  $a'_{agg}$  ( $\text{m}^{-1}$ ) is the agglomerate with the ionomer film.

#### 5.2.4 Gas transport within catalyst layers

Hydrogen transport in a porous anode is described as the same way by Eq. (4-20) in Section 4.2.4. However, due to the fact that the secondary pores are partially occupied by the liquid water, the effective diffusion coefficient of oxygen diffusing in the secondary pores is corrected as follow:

$$D_{O_2,s}^{eff} = [\varepsilon_s(1-s')]^{1.5} D_{O_2-P} \quad (5-11)$$

where  $s'$  is the corrected liquid water saturation, defined as the volume fraction of the secondary pores occupied by the liquid water, and relates to  $s$  via:

$$s' = s \frac{\varepsilon_{CL}}{\varepsilon_s} \quad (5-12)$$

where  $s$  is the liquid water saturation, defined as the volume fraction of the entire pores occupied by the liquid water.

According to the assumption, no liquid water exist in the primary pores, oxygen diffusion inside agglomerates is therefore described by Eq. (4-21).

#### 5.2.5 Thickness of the liquid water film

The properties of the catalyst layer in the single-phase flow model were described in Section 4.2.5. In the two-phase flow model, the thickness of the liquid water film is included, which can be calculated by Eq. (3-65) in Chapter 3.

$$\delta_w = \sqrt[3]{(r_{agg} + \delta_M)^3 + \frac{s' \varepsilon_{CL} (1 - \varepsilon_{CL}) r_{agg}^3}{L_{Pt/C}} - (r_{agg} + \delta_M)} \quad (5-13)$$

### 5.2.6 Liquid water transport

By applying the volume average approach to the continuity equation and then utilising Darcy's law for both the liquid and gas phases [10, 12, 18, 22], the governing equation for the liquid water transport is obtained as shown in Eq. (3-94). At steady-state, it can be simplified as follow:

$$\nabla \cdot (\rho_w^l D_c \nabla S - \frac{\rho_w^l k_r^l \mu_w^g}{k_r^g \mu_w^l} \mathbf{u}^g) = M_w S_w^l \quad (5-14)$$

where  $\rho$  (kg m<sup>-3</sup>) is the density,  $\mu$  (Pa s) is the viscosity,  $k$  is the relative permeability,  $\mathbf{u}$  (m s<sup>-1</sup>) is the velocity vector,  $M$  (kg mol<sup>-1</sup>) is the molecular weight, and  $S$  (mol m<sup>-3</sup> s<sup>-1</sup>) is the source term, respectively. The subscript  $w$  is liquid water, and the superscript  $g$  and  $l$  are gas phase and liquid water, respectively.  $D_c$  (m<sup>2</sup> s<sup>-1</sup>) is the capillary diffusion coefficient, which is calculated using the following equation:

$$D_c = -\frac{k_r^l}{\mu_w^l} \sigma \cos(\theta_c) (\varepsilon k_p)^{1/2} \frac{dJ(s)}{ds} \quad (5-15)$$

in which the surface tension ( $\sigma$ ), contact angel ( $\theta_c$ ), electrode porosity ( $\varepsilon$ ) and permeability ( $k_p$ ) were either described in Table 4-1 in Chapter 4 or in Table 5-2 in this chapter. The rest of the parameters were described in detail in Section 3.3.2.

### 5.2.7 Dissolved water transport

By accounting for the water phase change and membrane/ionomer swelling, the dissolved water transport at steady-state condition can be described by the following equation:

$$\nabla \cdot (n_d \frac{i_M}{F}) - \nabla \cdot (D_{w-M} \nabla c_w^d) - \nabla \cdot \left( \frac{k_{p,M} c_w^d}{\mu_w} \nabla p \right) = S_w^d \quad (5-16)$$

in which the electro-osmotic drag coefficient  $n_d$ , membrane permeability  $k_{p,M}$  (m<sup>2</sup>) and water diffusion coefficient through the membrane  $D_{w-M}$  (m<sup>2</sup> s<sup>-1</sup>), which are shown in Table 5-2, are water content dependent parameters. Nafion® membrane/ionomer swells when absorbing water until reaching the saturation level, the concentration of dissolved water depends on the water content of the membrane as follow [7]:

$$c_w^d = \frac{\rho_M}{EW} \frac{\lambda}{1+k_s\lambda} \quad (5-17)$$

when ionomer swelling, the volume fraction of the ionomer in the cathode catalyst layer increases to:

$$L_M = (1+k_s\lambda)L_M^{dry} \quad (5-18)$$

Table 5-2 Transport parameters

Parameters	Value	Reference
Membrane swelling coefficient, $k_s$	0.0126	[7]
Molar volume of water, $V_W$ ( $\text{m}^3 \text{ mol}^{-1}$ )	$1.8 \times 10^{-5}$	[14]
Molar volume of dry membrane, $V_M$ ( $\text{m}^3 \text{ mol}^{-1}$ )	$5.5 \times 10^{-4}$	[14]
Liquid water density, $\rho_w^l$ ( $\text{kg m}^{-3}$ )	988	[12]
Surface tension, $\sigma$ ( $\text{N m}^{-1}$ )	0.0625	[12, 17-19]
Contact angle, $\theta_c$ ( $^\circ$ )	120	[12]
Condensation rate, $k_{con}$ ( $\text{s}^{-1}$ )	100	[22]
Evaporation rate, $k_{eva}$ ( $\text{atm}^{-1} \text{ s}^{-1}$ )	100	[22]
Electro-osmotic drag coefficient, $n_d$	$(2.5/22)\lambda$	[1, 12]
Membrane permeability, $k_{p,M}$ ( $\text{m}^2$ )	$2.86 \times 10^{-20} \lambda$	[3]

### 5.2.8 Source terms

The conservation of water in different phases, including water vapour, dissolved water and liquid water, is shown in Table 5-3.

Table 5-3 Conservation of water in different phases

	Anode GDL	Anode CL	Cathode CL	Cathode GDL
Water vapour	$S_w^v = 0$	$S_w^v = -S_{vd}$	$S_w^v = S_w^g - S_{vd} - S_{vl}$	$S_w^v = -S_{vl}$
Liquid water	$S_w^l = 0$	$S_w^l = 0$	$S_w^l = S_{dl} + S_{vl}$	$S_w^l = S_{vl}$
Dissolved water	$S_w^d = 0$	$S_w^d = S_{vd}$	$S_w^d = S_{vd} - S_{dl}$	$S_w^d = 0$

Note: The unit for every source term is ( $\text{mol m}^{-3} \text{ s}^{-1}$ )

The source terms for reactant gas  $S_m$  in Eq. (5-4) and  $S_i^g$  in Eq. (5-5), for liquid water  $S_w^l$  in Eq. (5-14) and for dissolved water  $S_w^d$  in Eq. (5-16) are given in Table 5-4.

Table 5-4 Source terms

<i>Source terms</i>	<i>Unit</i>	<i>Domain</i>
$S_m = M_{H_2} S_{H_2}^g + M_{O_2} S_{O_2}^g + M_w S_w^v$	$\text{kg m}^{-3} \text{ s}^{-1}$	All domain
$S_{H_2}^g = \frac{i_a}{2F}$	$\text{mol m}^{-3} \text{ s}^{-1}$	Anode CL
$S_{O_2}^g = \frac{i_c}{4F}$	$\text{mol m}^{-3} \text{ s}^{-1}$	Cathode CL
$S_w^{rc} = \frac{i_c}{2F}$	$\text{mol m}^{-3} \text{ s}^{-1}$	Cathode CL
$S_w^{vd} = k_{ads}(c_w^{eq} - c_w^d) \quad c_w^d < c_w^{eq}$	$\text{mol m}^{-3} \text{ s}^{-1}$	Anode and cathode CLs
$S_w^{dl} = k_{des}(c_w^d - c_w^{eq}) \quad c_w^d \geq c_w^{eq}$	$\text{mol m}^{-3} \text{ s}^{-1}$	Anode and cathode CLs
$S_w^{vl} = \begin{cases} k_{con} \frac{\varepsilon(1-s)x_w^g}{R_g T} (x_w^g p^g - p_{sat}) & x_w^g p^g \geq p_{sat} \\ k_{eva} \frac{\varepsilon s \rho_w^l}{M_w} (p_{sat} - x_w^g p^g) & x_w^g p^g < p_{sat} \end{cases}$	$\text{mol m}^{-3} \text{ s}^{-1}$	Cathode CL and GDL

### 5.2.9 Boundary conditions

The pressures at the GDL-flow channel interfaces of anode (A-A') and cathode (F-F') are defined as  $p_a$  (Pa) and  $p_c$  (Pa), respectively. The liquid water saturation  $s$ , at the cathode GDL-flow channel interface (F-F') is also defined as the Dirichlet boundary with the value of zero, which means no liquid water in the flow channel. The water content on the CL-membrane interfaces of anode (C-C') and cathode (D-D') are defined as the Dirichlet boundaries with their values given by Eq. (3-209). The fraction of the species at the inlets of anode and cathode are calculated by the equations in Table 4-4 of Chapter 4.

### 5.2.10 Numerical solution

The numerical solution in this study is based on the same principle described in Section 4.2.7 in Chapter 4. The computational geometry in this across-the-channel model is simpler in comparison with the along-the-channel model. Therefore, it consists of 8040 elements, less than half of that in the along-the-channel model. However, by accounting for the effect of liquid water, a self developed two-phase flow module is introduced, which makes the computational process more difficult. The used equations

accounting for the different phenomena are fully coupled and are solved following the schematic shown in Figure 5-2.

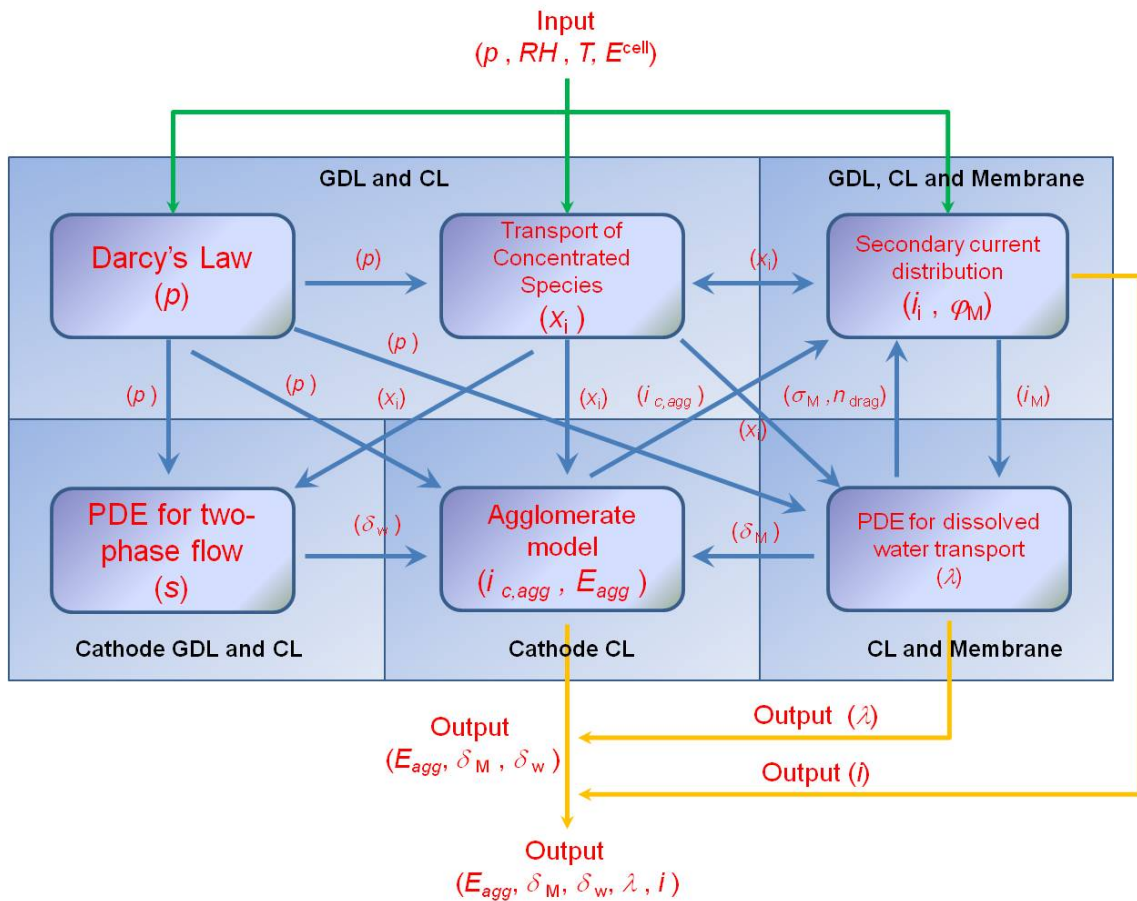


Figure 5-2 Schematic of the computational process

### 5.3 Results and discussion

#### 5.3.1 Model validation

Figure 5-3 compares experimental data with the results simulated by the single-phase flow model and two-phase flow mode, respectively. In the single-phase flow model, all species are assumed to exist in the gaseous phase. However, in the two-phase flow model, the liquid water generation and transport are taken into account. The experimental data used in this chapter at 60 °C is the same as those in Chapter 4, which is obtained using a single PEM fuel cell with an active area of  $1 \times 1 \text{ cm}^2$ . The catalyst layers are prepared with the platinum loadings of 0.1 and  $0.4 \text{ mg cm}^{-2}$  for anode and cathode, respectively. Both the mass ratios of platinum and ionomer are 20% in the catalyst layers of the anode and cathode. The operating condition is temperature at 60 °C, pressure of 1.0 atm, gas humidity of 100%. Based on the same condition, the other

group of experimental data is obtained at 80 °C. The detailed parameters of the cell and operating conditions are listed in **Table 5-5**.

Table 5-5 Parameters for model validation and base case condition

Symbol	Description (unit)	Validation	Base case
$l_{GDL}$	GDL thickness (m)	$3.0 \times 10^{-4}$	$3.8 \times 10^{-4}$
$l_{CL}$	CL thickness (m)	$1.5 \times 10^{-5}$	$1.5 \times 10^{-5}$
$l_M$	Membrane thickness (m)	$5.5 \times 10^{-5}$	$8.0 \times 10^{-5}$
$\varepsilon_{GDL}$	GDL porosity	40%	40%
$m_{Pt}$	Platinum loading ( $\text{mg cm}^{-2}$ )	0.40	0.40
$f$	Platinum mass ratio	20%	40%
$L_M^{dry}$	Volume fraction of dry membrane	13.3%	30%
$T$	Operating temperature (°C)	60, 80	70
$p$	Operating pressure (atm)	1.0	1.0
$\alpha_c$	Cathode transfer coefficient	0.85 (60°C) 0.95 (80°C)	$0.495 + 2.3 \times 10^{-3}(T - 300)$
$r_{agg}$	Agglomerate radius ( $\mu\text{m}$ )	1.0	0.5
$RH$	Relative humidity (%)	100%	100%

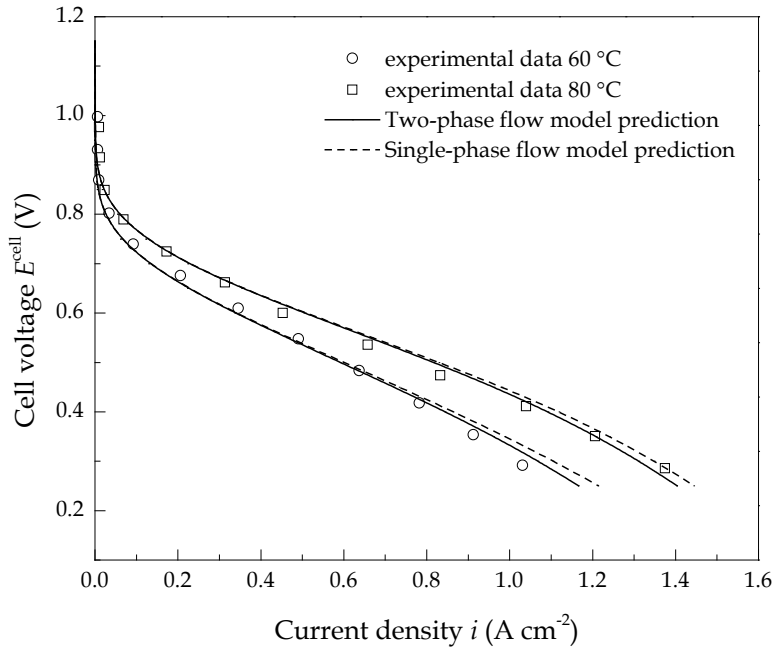


Figure 5-3 Validation of the modelling results to the experimental data at 60 °C and 80 °C

( $m_{Pt,a} = 0.1 \text{ mg cm}^{-2}$ ,  $m_{Pt,c} = 0.4 \text{ mg cm}^{-2}$ ,  $f_a = 20\%$ ,  $f_c = 20\%$ ,  $L_S = 6\%$ ,  $l_{CL} = 15 \mu\text{m}$ ,

$\varepsilon_{GDL} = 40\%$ ,  $L_M = 13.3\%$ ,  $T = 60^\circ\text{C}$ ,  $p = 1.0 \text{ atm}$ ,  $RH = 100\%$ )

It is apparent from Figure 5-3 that, due to the weak mass transport impact at higher cell voltages (i.e. lower current densities), the two models give very close simulation results in agreement with the experimental data. With increasing current density there is the typical decrease in cell voltage. At higher current densities there is a rapid fall in cell voltage caused by mass transport restrictions. By accounting for the increase in mass transport resistance resulting from membrane and ionomer swelling and considering the void space loss due to liquid water occupation (flooding), the two-phase flow model gives reasonable predictions of the polarisation curve.

Normally, membrane swelling has a significant impact on the species transport as the gas diffusion layer bulges into the channel while ionomer swelling leads to an increase in the volume of ionomer and a decrease in the porosity of the cathode catalyst layer. Considering the membrane and ionomer swelling into the two-phase flow model gives an accurate simulation of the current densities. Similar results can be found in a semi-empirical model developed by Choi and Bae [24].

### 5.3.2 Liquid water film thickness

In addition to the properties of the catalyst layer discussed in Section 4.3.2 of Chapter 4, the variation in liquid water film thicknesses with the liquid water saturation from zero to 1.0 and the platinum mass ratio from 0.3 to 0.8 are shown in Figure 5-4.

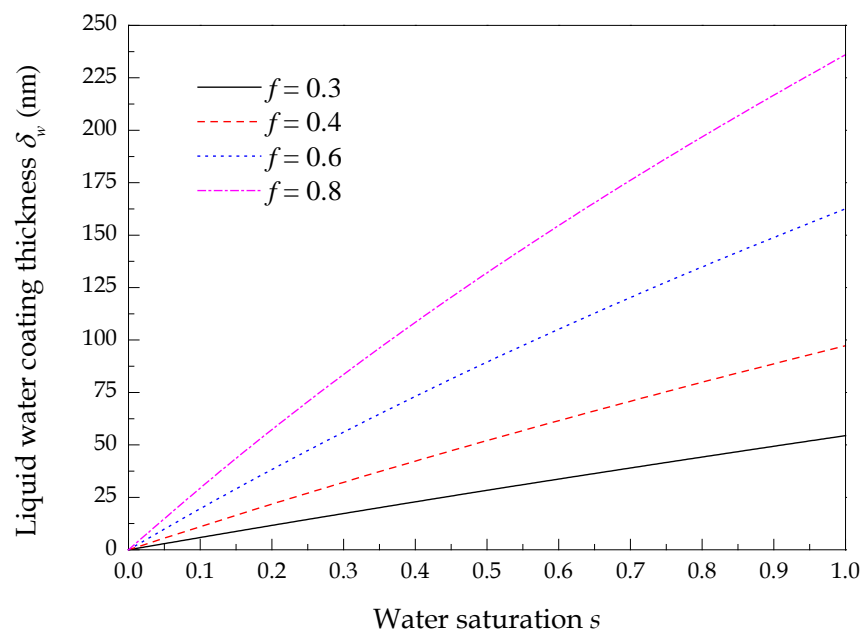


Figure 5-4 Liquid water film thicknesses with different platinum mass ratios in base case condition

The simulation results show that the liquid water film thickness increases as the liquid water saturation and the platinum mass ratio increases. The change in liquid water film thickness can be explained by Eq. (5-13), in which the liquid water film thickness is directly proportional to the liquid water saturation and the porosity of the catalyst layer and is inversely proportional to the agglomerate density. As expected, the increase in the liquid water saturation increases the liquid water film thickness since larger water saturation results in larger portion of the produced water in the liquid phase. For example, the increase in the liquid water saturation from 0.2 to 0.8 increases the liquid water film thickness from 60 nm to 200 nm when the platinum loading and platinum mass ratio are fixed at 0.4 mg cm<sup>-2</sup> and 0.8, respectively.

As assumed in Section 5.2.1, the liquid water only exists as the liquid water film surrounding the agglomerate. When the agglomerate density decreases, the numbers of agglomerates decrease. Consequently, thicker liquid water films are formed surrounding each individual agglomerates. Due to the fact that oxygen diffusion is faster in liquid water than that in Nafion® ionomer [5, 25], the liquid water has less effect on the overall oxygen diffusion resistance through the liquid water film in comparison with the ionomer film when both of them have the same thickness.

### 5.3.3 Comparison of the membrane and ionomer swelling

Figure 5-5 shows the effect of membrane and ionomer swelling on the fuel cell performance. The polarisation curves are obtained in four conditions: considering the membrane swelling only, considering the ionomer swelling only, considering both the swellings and neglecting both the swellings. The membrane/ionomer swelling coefficient in Eq. (5-17) is set to zero in the case of the model neglecting the membrane and ionomer swelling.

It is apparent that, at lower current densities, the four polarisation curves almost overlap each other due to the weak mass transport influence. At higher current densities, by ignoring the membrane and ionomer swellings, the two-phase flow model over estimates the current density at higher current densities where mass transport effect is significant. The relatively higher simulated current densities can be explained by two reasons: firstly, the unchanged porosity of the cathode catalyst layer when the ionomer swelling is not considered; secondly, the constant reactant gas transport resistance when the MEA bulge is not included. It is also clear in Figure 5-5 that the polarisation curve

obtained by considering the membrane swelling only is very close to that considering the ionomer swelling only. This indicates that the effects of ionomer swelling and membrane swelling are of equal importance.

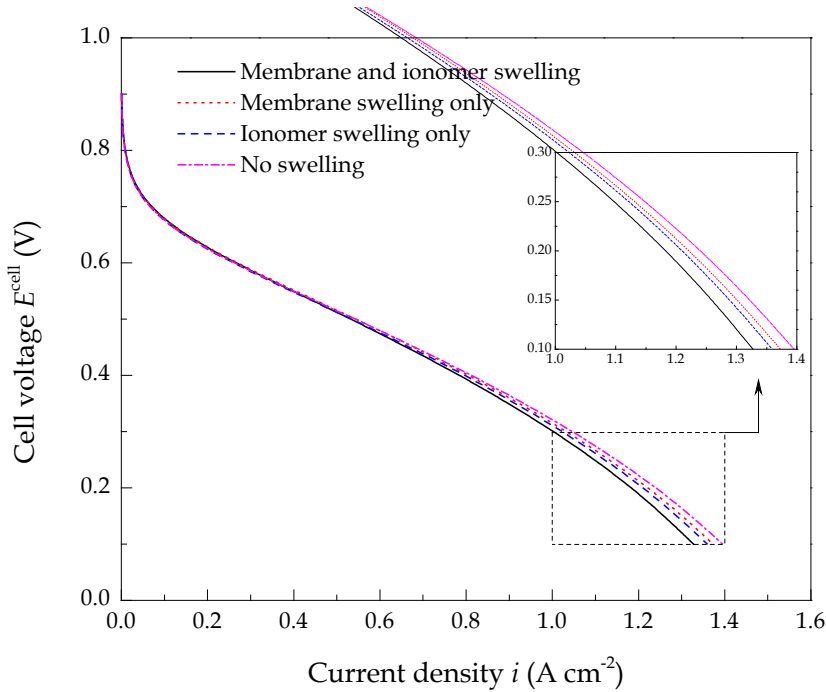


Figure 5-5 Comparison of the effect of membrane and ionomer swelling on fuel cell performance

### 5.3.4 Membrane and ionomer water content

Figure 5-6 shows the profiles of membrane and ionomer water content as a function of the local current density and position. The influence of electro-osmotic drag is apparent from these results. At lower current density, there is a slight change in water content due to the relatively low amount of drag water and to the fact that the vapour activities at the GDL-CL interfaces of both the anode ( $B-B'$ ) and cathode ( $E-E'$ ) are nearly identical according to Eq. (3-209). As the current density increases, the membrane/ionomer water content becomes more non-uniform since the anode dehydrates and the cathode water content increases. It is apparent in Figure 5-6 that the lowest water content with the value of 3.94 is observed at anode GDL-CL interface ( $B-B'$ ) while the water content at cathode GDL-CL interface ( $E-E'$ ) reaches to saturation at the current density of  $0.86 \text{ A cm}^{-2}$ , in agreement with the experimental data of Buchi and Scherer [26] and the simulation results of Kulikovsky [27]. In addition, as shown in Figure 5-6, the anode dehydration is more severe and the cathode ionomer water content is higher under the land than under the channel. This is explained by the higher water migration flux driven by the force of electro-osmotic drag under the land.

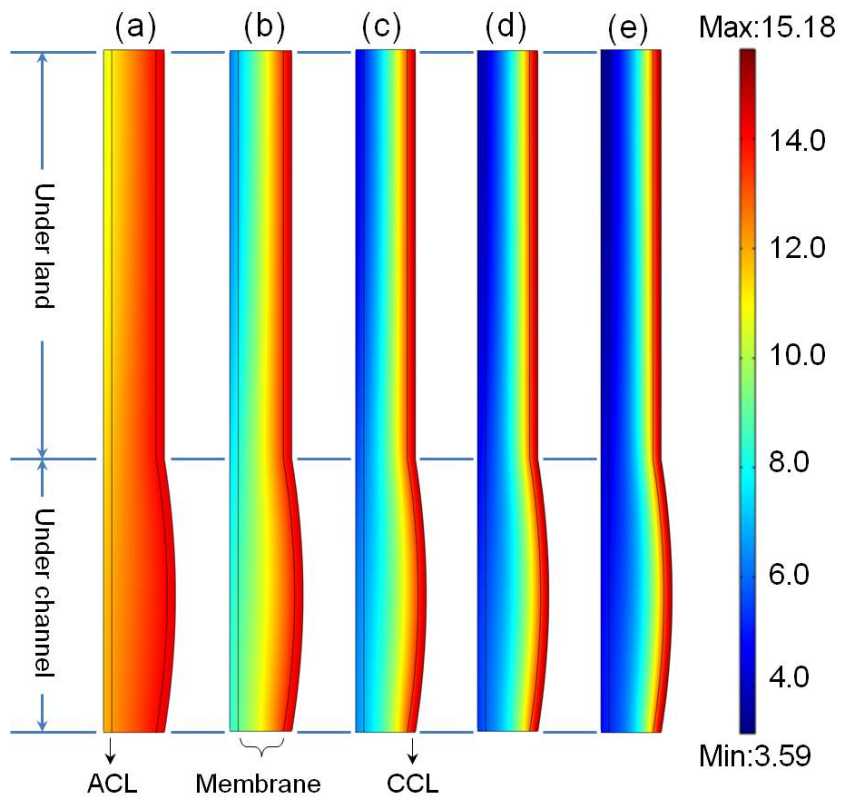


Figure 5-6 Membrane and ionomer water contents at different current densities (a)  $0.06 \text{ A cm}^{-2}$ ; (b)  $0.26 \text{ A cm}^{-2}$ ; (c)  $0.53 \text{ A cm}^{-2}$ ; (d)  $0.79 \text{ A cm}^{-2}$ ; (e)  $1.00 \text{ A cm}^{-2}$  in base case condition

### 5.3.5 Ionomer volume fraction in cathode catalyst layer

Figure 5-7 shows the profiles of the ionomer volume fraction within the cathode catalyst layer for the dry ionomer volume fraction of 0.3. The boundaries of  $X = 0$  and  $X = 1$  refer to the interfaces of CL-membrane (D-D') and CL-GDL (E-E'). The boundaries of  $Y = 0$  and  $Y = 1$  refer to the lower boundary of the flow channel (D'-E') and the upper boundary of the current collector (D-E) as shown in Figure 5-1(b), respectively. At a cell voltage of 0.3 V, the corresponding current density is  $1.0 \text{ A cm}^{-2}$ . Similar to the distribution of the ionomer water content, it is shown in Figure 5-7 that the highest ionomer volume fraction (swelling) is observed at the cathode CL-GDL interface (E-E') under the land. The observed higher ionomer volume fraction near the cathode CL-GDL interface in comparison to that of the CL-membrane interface indicates that ionomer water absorption (water uptake) is the main process in determining the ionomer water content rather than electro-osmotic drag (EOD). This is because the EOD effect is pronounced closer to the membrane at the studied current density. However, the higher ionomer swelling gradient from membrane-CL to CL-GDL under the land in

comparison to that under the channel signifies the importance of the EOD on ionomer swelling.

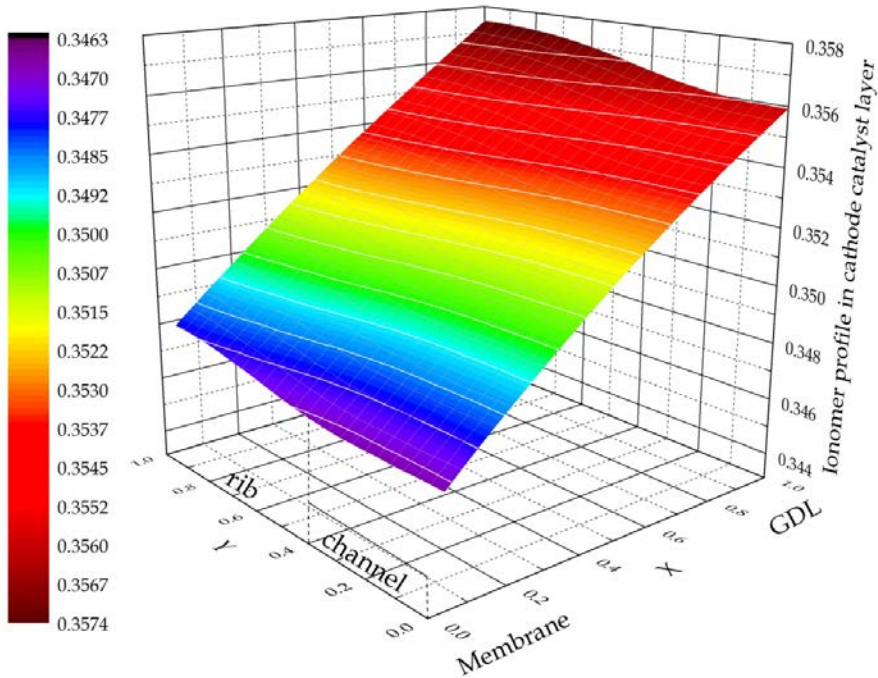


Figure 5-7 Ionomer volume fraction within cathode catalyst layer with dry ionomer volume fraction of 30% in base case condition at the cell voltage of 0.3 V

### 5.3.6 Liquid water saturation in cathode porous electrode

Figure 5-8 shows the profiles of the liquid water saturation within the cathode porous electrode with two dry ionomer volume fractions. The liquid water, generated via water vapour condensation and ionomer desorption, is prone to occur under the land and close to the cathode CL-membrane interface. The distribution of liquid water in the cathode catalyst layer is consistent with the numerical prediction and neutron radiography data of Wang and Chen [28]. The dry ionomer volume fraction has a small effect on the distribution of liquid water. However, the liquid water saturation increases as the dry ionomer volume fraction decreases. This is explained by the fact that the ionomer in cathode catalyst layer is the carrier of dissolved water. The decrease in the dry ionomer volume fraction reduces the amount of dissolved water, resulting in more liquid water surrounding the agglomerate.

Figure 5-9 shows the average liquid water saturation and the liquid water film thickness within the cathode porous electrode as a function of the local current density and relative humidity. As expected, both the average water saturation and the average

liquid water film thickness increase as the current density increases. As expected, when the cathode gas inlet is fully humidified, liquid water saturation occurs at all current densities.

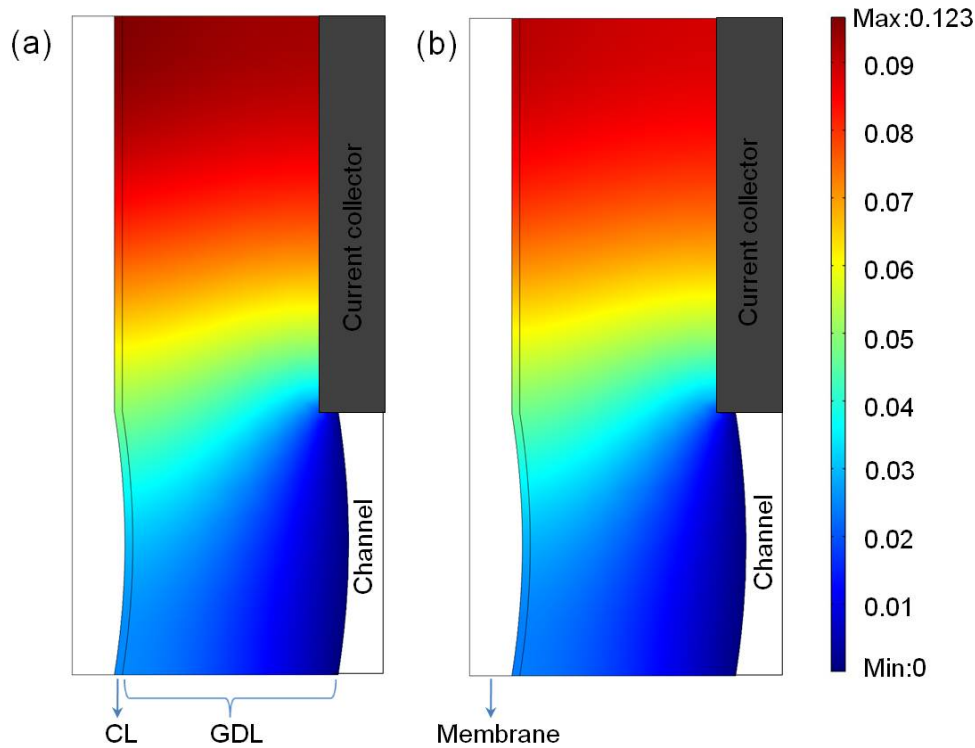


Figure 5-8 Liquid water saturation with dry ionomer volume fraction of 0.2 (a) and 0.4 (b) in base case condition at the cell voltage of 0.3 V

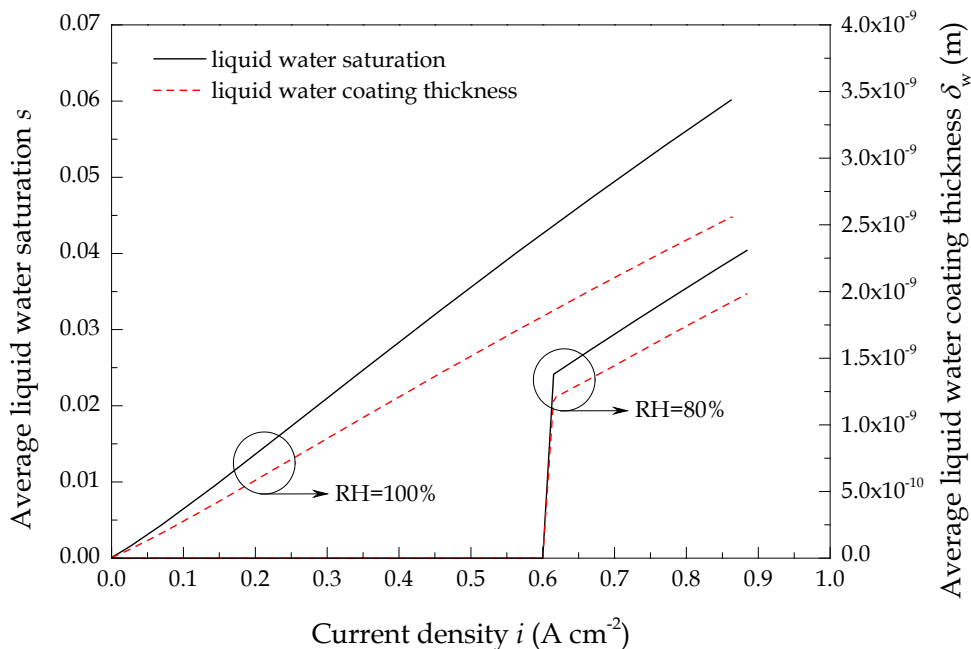


Figure 5-9 Average liquid water saturations and liquid water film thicknesses at different current densities and relative humidity in base case condition

On the contrary, liquid water saturation as shown in Figure 5-9 is only observed at higher current density when the relative humidity of the cathode gas inlet is lower than 100%. In the later case, both the liquid water saturation and the liquid water film thickness are smaller than that of the former case.

### 5.3.7 Optimal ionomer water content

According to the agglomerate assumption of the catalyst layer, oxygen needs to diffuse through the ionomer and liquid water film before reaching the platinum particle surface (see Figure 5-10).

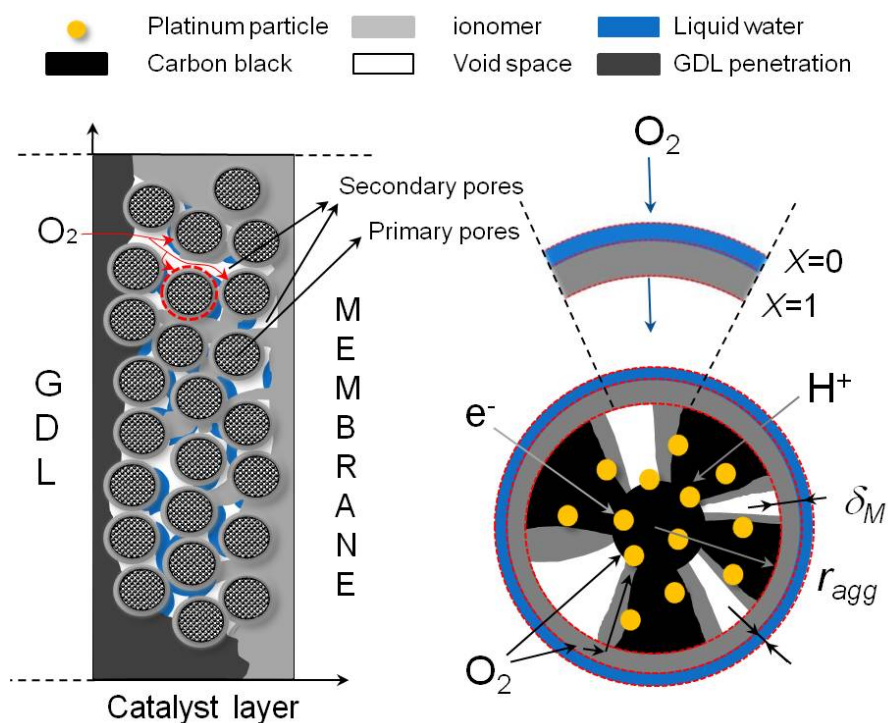


Figure 5-10 Sketch of oxygen diffusion through the ionomer and liquid water film

As shown in Figure 3-7 in Chapter 3, the diffusion coefficient of oxygen through the liquid water is more than ten times bigger than that through the ionomer (above 70 °C), the ionomer film therefore has a more significant effect on the oxygen transport. If no liquid water is generated, the oxygen diffusion flux can be described by the dimensionless Fick's law shown as follow.

$$\vec{N}_{O_2-M} = -\nu c_{O_2}^0 \nabla C_{O_2} \quad (5-18)$$

where the parameter  $\nu$ , is the quotient of oxygen diffusion coefficient and the ionomer film thickness, which represents to the oxygen diffusion rate through the ionomer film.

$$\nu = \frac{D_{O_2-M}}{\delta_M} (m/s) \quad (5-19)$$

The boundary condition for Eq. (5-18) is:

$$\begin{cases} X = 0, & C_{O_2} = 1 \\ X = 1, & \nabla C_{O_2} = 0 \end{cases} \quad (5-20)$$

As shown in Eq. (3-175) and Eq. (3-60), the increase in ionomer water content results in increases in both the oxygen diffusion coefficient and ionomer film thickness. In the following section, the effect of the ionomer water content on parameter  $\nu$  is investigated to obtain the optimal ionomer water content.

The effect of ionomer water content on parameter  $\nu$  with different platinum loading, platinum mass ratio and dry ionomer volume fraction is shown in Figure 5-11, in which Figure 5-11(a) shows the effect of ionomer water content on parameter  $\nu$  with two platinum loadings of 0.2 and 0.4 mg cm<sup>-2</sup> at fixed platinum mass ratio of 0.6 and dry ionomer volume fraction of 0.3; Figure 5-11(b) shows the effect of ionomer water content on parameter  $\nu$  with two platinum mass ratios of 0.3 and 0.7 at fixed platinum loading of 0.4 mg cm<sup>-2</sup> and dry ionomer volume fraction of 0.3; and Figure 5-11(c) shows the effect of ionomer water content on parameter  $\nu$  with two dry ionomer volume fractions of 0.3 and 0.4 at fixed platinum loading of 0.4 mg cm<sup>-2</sup> and platinum mass ratio of 0.4, respectively.

For the three conditions above, the thickness of the cathode catalyst layer is fixed at 15 μm. The results in Figure 5-11 show that the optimal water content is higher for smaller platinum loading, larger platinum mass ratio and larger dry ionomer volume fraction. This can be explained by the ionomer film thickness at different platinum loadings, platinum mass ratios and dry ionomer volume fractions. As discussed in Chapter 4, the ionomer film is thicker when smaller platinum loading and larger platinum mass ratio and dry ionomer volume fraction are adopted. The increase in thickness of the thicker ionomer film is smaller than that of the thinner film. For example, the dry ionomer films are  $2.31 \times 10^{-7}$  m and  $1.40 \times 10^{-7}$  m for the platinum loadings of 0.2 and 0.4 mg cm<sup>-2</sup>, respectively. At the water content of 14, the ionomer film thicknesses increase 74.2% and 89.5%, respectively. In short, the optimal water

content is lower than the fully saturated level of the ionomer. The optimal water content is strongly dependent on the properties of the cathode catalyst layer.

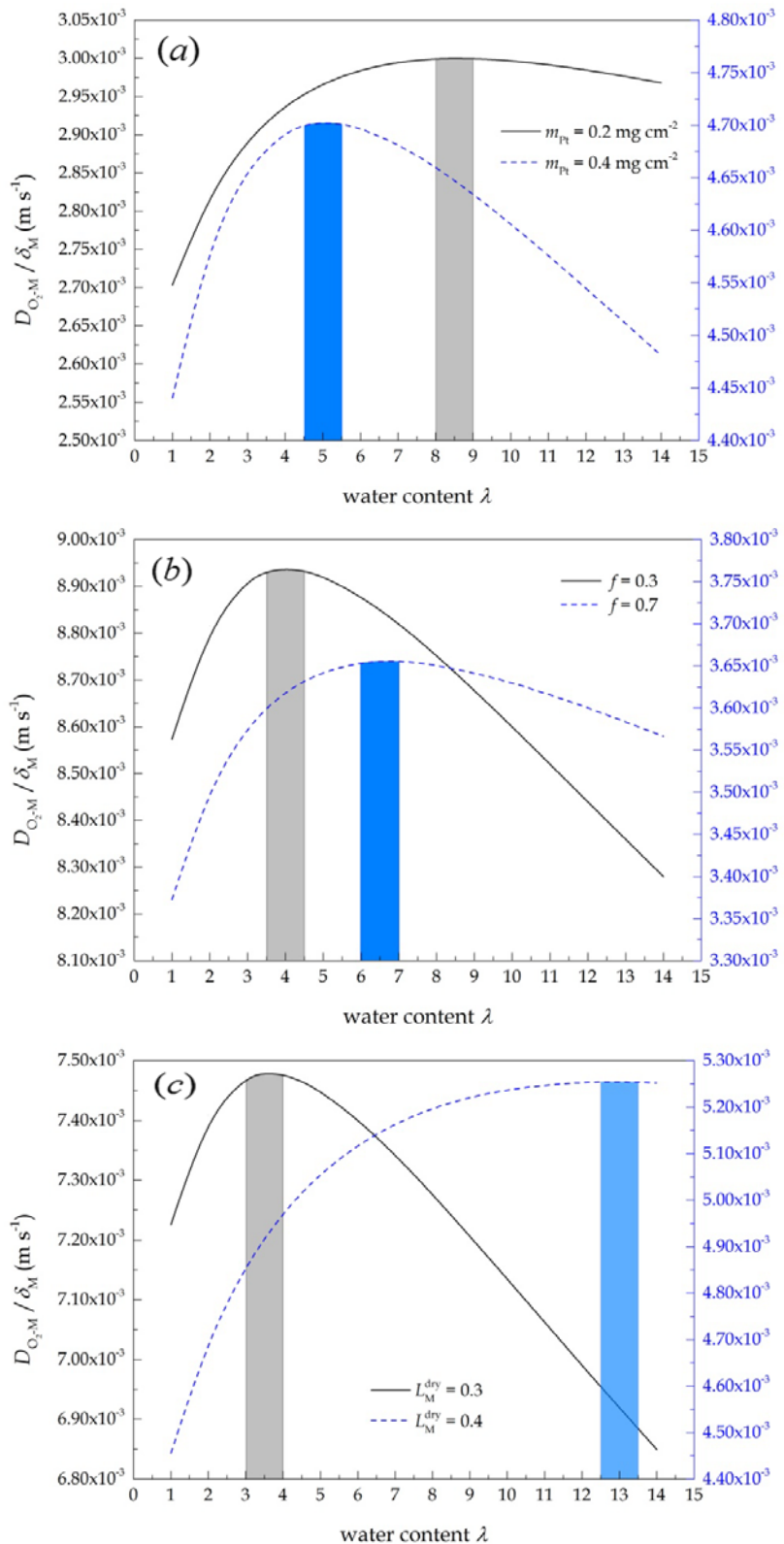


Figure 5-11 Effect of ionomer water content on parameter  $v$  with different platinum loading (a), platinum mass ratio (b) and dry ionomer volume fraction (c)

### 5.3.8 Orthogonal array testing

The orthogonal array testing is a systematic and statistical way of testing that enables the design of a reasonably small set of test cases that provide maximum test coverage. It is used when the number of design possibilities to the system is relatively small, but too large to allow for exhaustive testing of every possibility to the systems. It is particularly effective in testing the combinations and integrations by considering the interactions between the possibilities. The orthogonal array in this study is applied in fuel cell performance testing, which consists of four design parameters with three levels of each. Platinum loading, platinum mass ratio, dry ionomer volume fraction and catalyst layer thickness are the four parameters and nice testing is carried out. The orthogonal array and testing results are shown in [Table 5-6](#) and [Table 5-7](#), respectively.

Table 5-6 Orthogonal array  $L_9(3^4)$ 

Test case	$m_{Pt}$ (mg cm <sup>-2</sup> )	$f$	$L_M^{dry}$	$l_{CL}$ (μm)
1	0.2	0.4	0.2	10
2	0.2	0.6	0.3	15
3	0.2	0.8	0.4	20
4	0.4	0.4	0.3	20
5	0.4	0.6	0.4	10
6	0.4	0.8	0.2	15
7	0.6	0.4	0.4	15
8	0.6	0.6	0.2	20
9	0.6	0.8	0.3	10

Table 5-7 Orthogonal array testing result

Cases	$a_{agg} \times 10^{-7}$ (m <sup>-1</sup> )	$\delta_M \times 10^7$ (m)	$\varepsilon_s$	$\sigma^{eff}$ (S m <sup>-1</sup> )	$v \times 10^3$ (m s <sup>-1</sup> )	0.9V		0.5V		0.3V	
						$i \times 10^4$ (A cm <sup>-2</sup> )	$\delta_w \times 10^{13}$ (m)	$i \times 10^4$ (A cm <sup>-2</sup> )	$\delta_w \times 10^{11}$ (m)	$i \times 10^4$ (A cm <sup>-2</sup> )	$\delta_w \times 10^{10}$ (m)
1	4.519	1.559	0.373	4.342	7.681	4.712	171.1	4.509	614.0	8.928	117.1
2	4.351	3.99	0.393	5.77	2.982	5.708	286.5	4.565	762.6	8.551	137.9
3	4.713	8.776	0.344	7.063	1.351	8.322	358.6	4.547	815.9	7.439	129.6
4	5.481	1.988	0.262	5.579	5.926	9.618	153.5	5.226	385.9	9.492	68.4
5	5.715	2.998	0.207	6.84	3.987	5.972	83.3	4.458	296.2	8.473	54.5
6	3.507	3.178	0.493	4.581	3.739	4.602	385.0	4.368	1029.8	8.521	193.9
7	7.643	1.882	0.011	6.864	6.325	9.828	4.8	2.052	4.9	4.844	1.2
8	4.104	1.694	0.401	4.372	6.921	7.211	257.2	4.979	673.5	9.392	123.7
9	7.562	1.348	0.019	5.661	8.87	7.89	9.1	2.561	12.5	6.147	2.9

In [Table 5-7](#), the specific area, ionomer film thickness, porosity of the secondary pores, proton conductivity, parameter  $\nu$ , and the obtained current densities and liquid water film thickness at different cell voltages are investigated. It is clear that the highest current density at the cell voltages of 0.9 V, 0.5 V and 0.3 V are observed in case 7, case 4 and case 4, respectively. The proton conductivity and the specific area of case 7 are the biggest and the second biggest among the nice cases. This indicates that the oxygen reduction kinetic and the proton conductivity are the most important two factors in determining the fuel cell performance at high cell voltages. Both the highest current densities at the cell voltage of 0.5 and 0.3 V are observed in case 4. However, no studied parameters in case 4 are the highest or lowest. The values of all the parameters are in between of the highest and lowest. Case 8 also leads to very high current densities at 0.5 and 0.3 V, which are quite close to the current densities obtained from case 4. All parameters in case 8, except the specific area, are more optimal compared to that in case 4. This indicates that the oxygen reduction kinetics is also very important at low cell voltages. Similarly, all parameters in case 9, except the porosity, are more optimal than that in case 4. However, the obtained current densities are much lower, especially at lower cell voltages. This indicates the importance of the porosity. Therefore, the gas transport is another factor in determining the cell performance at low cell voltages. In medium cell voltages, the fuel cell performance is under a mixed control where the effects of proton conductivity, kinetics and gas transport are of equal importance.

### 5.3.9 Optimal platinum loading

The polarisation curves and the effectiveness factors of the catalyst layer with various platinum loadings from 0.1 to 0.6 mg cm<sup>-2</sup> are shown in [Figure 5-12](#) and [Figure 5-13](#), respectively. The platinum mass fraction, dry ionomer volume fraction and catalyst layer thickness are set to 0.6, 0.3 and 15 µm, respectively. It is clear in [Figure 5-12](#) that the increase in platinum loading from 0.1 to 0.4 mg cm<sup>-2</sup> improves the cell performance. This improvement can be explained by the increase in the specific area and the decrease in the ionomer film thickness. However, the current density increases very slightly when the platinum loading increases from 0.4 to 0.6 mg cm<sup>-2</sup> due to the decrease in catalyst layer porosity. Consequently, too much platinum loading rather than improves the cell performance can waste expensive platinum.

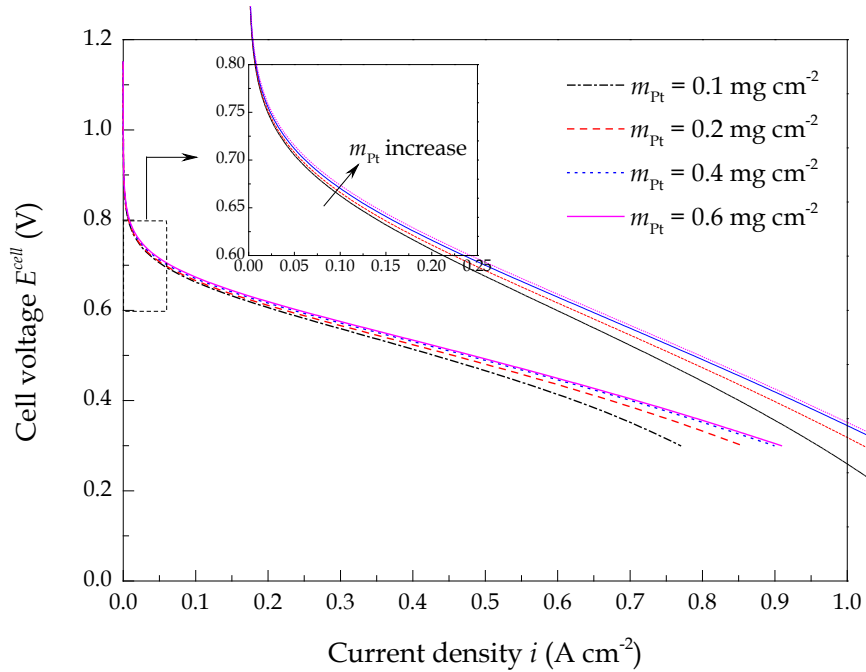


Figure 5-12 Effect of platinum loading on fuel cell performance

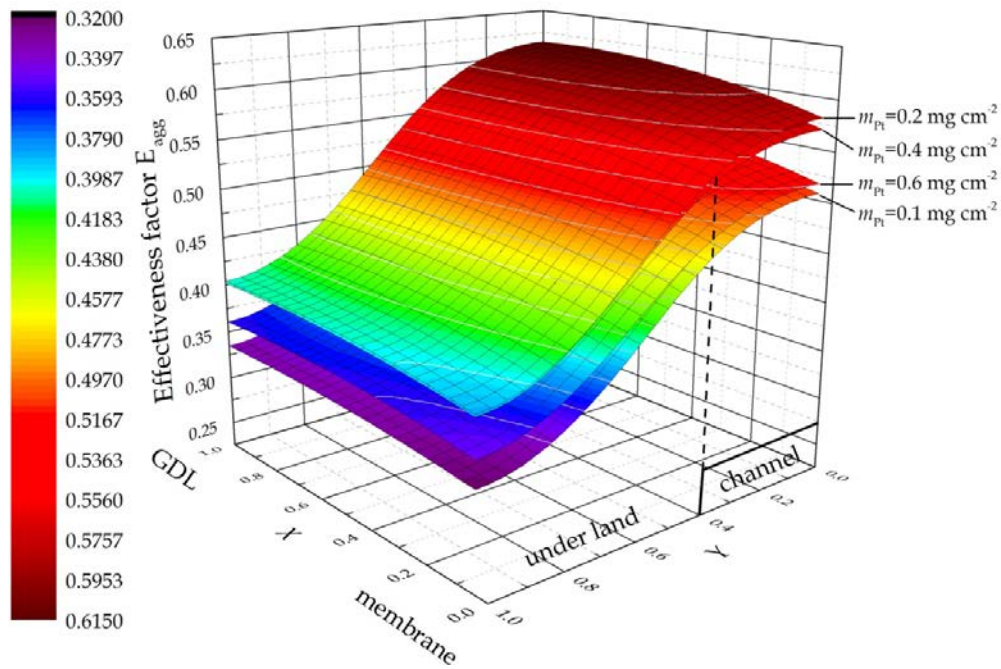


Figure 5-13 Effect of platinum loading on effectiveness factor of cathode catalyst layer

The effectiveness factors of the catalyst layer with various platinum loadings are shown in Figure 5-13. The effectiveness is higher under the channel than that under the land due to the relative high oxygen concentration under the channel. It is clear, the platinum loading of  $0.2 \text{ mg cm}^{-2}$  leads to the highest effectiveness. The effectiveness factor with the platinum loading of  $0.4 \text{ mg cm}^{-2}$  almost overlaps that of  $0.2 \text{ mg cm}^{-2}$ .

The effectiveness decreases as the platinum loading further increases. The effectiveness of platinum loading of  $0.1 \text{ mg cm}^{-2}$  is the lowest. Consequently,  $0.2 - 0.4 \text{ mg cm}^{-2}$  are the optimal platinum loading.

### 5.3.10 Optimal platinum mass ratio

The polarisation curves and the effectiveness factors of the catalyst layer with varying the platinum mass ratio from 0.3 to 0.7 are shown in Figure 5-14 and Figure 5-15, respectively. The platinum loading, dry ionomer volume fraction and catalyst layer thickness are set to  $0.4 \text{ mg cm}^{-2}$ , 0.3 and  $15 \mu\text{m}$ , respectively. It is apparent in Figure 5-14 that at higher cell voltages, e.g. higher than  $0.7 \text{ V}$ , lower platinum mass ratio improves the fuel cell performance. However, at medium and lower cell voltages, the cell performance initially increases as the platinum mass ratio increases from 0.3 to 0.5 and decreases as the platinum mass ratio further increases from 0.5 to 0.7.

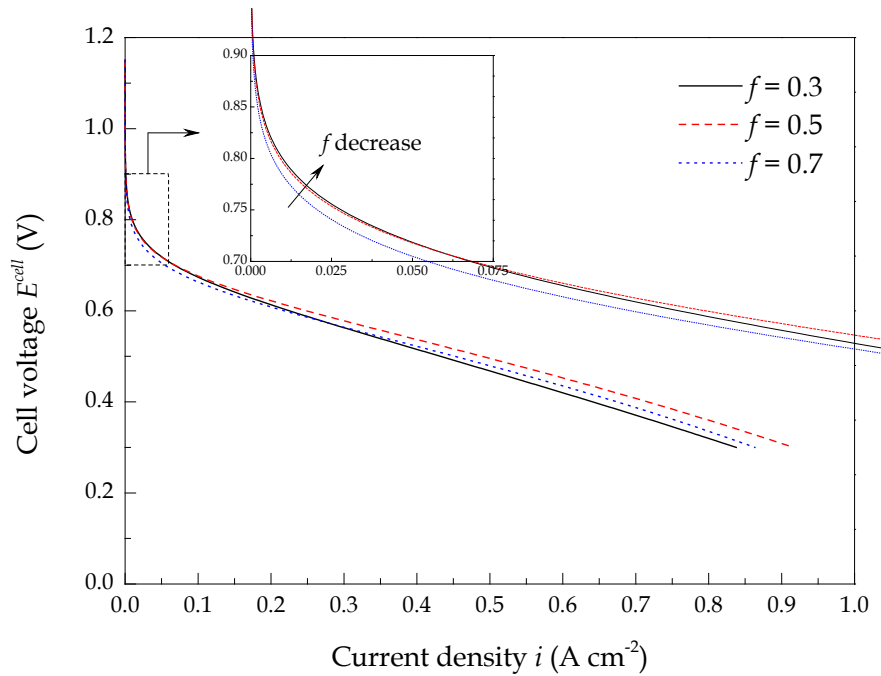
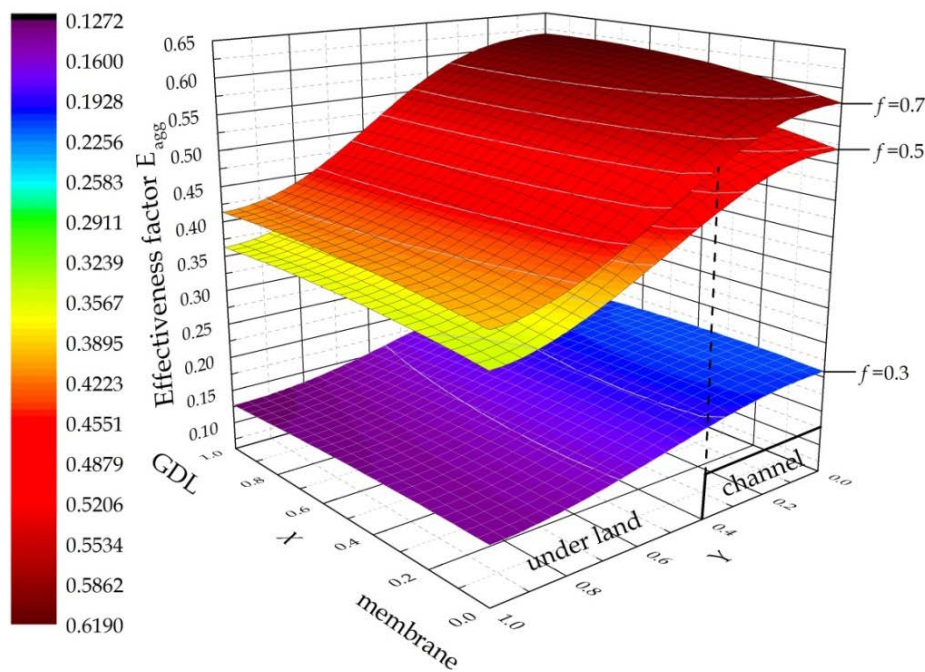


Figure 5-14 Effect of platinum mass ratio on fuel cell performance

As shown in Figure 4-4 and Figure 4-5, the increase in platinum mass ratio increases the porosity and ionomer film thickness. The initial increase in the cell performance resulting from the platinum mass ratio from 0.3 to 0.5 is possibly due to the increase in porosity. As analysed by the orthogonal array testing, catalyst layer porosity is vitally important to the fuel cell performance at higher current densities. However, as the platinum mass ratio further increases from 0.5 to 0.7, the increase in ionomer film

thickness plays a more important role in determining the fuel cell performance. In this condition, the fuel cell performance decreases due to the increased oxygen transport resistance through the thicker ionomer film. Consequently, the optimal platinum mass ratio is around 0.5 in this study. The effectiveness factors of the catalyst layer with various platinum mass ratios are shown in [Figure 5-15](#). It is obvious that the increase in platinum mass ratio increases the effectiveness factor.



[Figure 5-15](#) Effect of platinum mass ratio on effectiveness factor of cathode catalyst layer

### 5.3.11 Optimal dry ionomer loading

The polarisation curves and the agglomerate effectiveness factors for various dry ionomer loadings are shown in the [Figure 5-16](#) and [Figure 5-17](#) as follow. Similarly, the platinum loading, platinum mass fraction, and catalyst layer thickness are set to constants with the values of  $0.4 \text{ mg cm}^{-2}$ , 0.4 and  $15\mu\text{m}$ , respectively. As shown in [Figure 5-14](#), the increase in dry ionomer loading increases the current densities at higher cell voltages whereas it decreases the current densities at lower cell voltages. The improved fuel cell performance at higher cell voltages is because higher ionomer loading increases the proton conductivity and ionomer film thickness. Due to the fact that the electrochemical reaction rate is relative slow at higher cell voltages, the overall rate is therefore mainly control by the proton transport rate. As a result, the increase in ionomer loading is of benefit to the cell performance. However, at medium and low cell voltages, the impact of mass transport becomes significant. The increase in ionmomer

loading decreases the porosity and increases the mass transport resistance. It is clear that the current densities at medium and low cell voltages drop rapidly as the ionomer loading increases to  $1.65 \text{ mg cm}^{-2}$ . The optimal dry ionomer loading is between 0.2 to  $0.3 \text{ mg cm}^{-2}$ , which agrees well with the experimental results of Passalacqua *et al.* [29] and Kim *et al.* [30]. Figure 5-17 shows that the agglomerate effectiveness decreases as the ionomer loading increases.

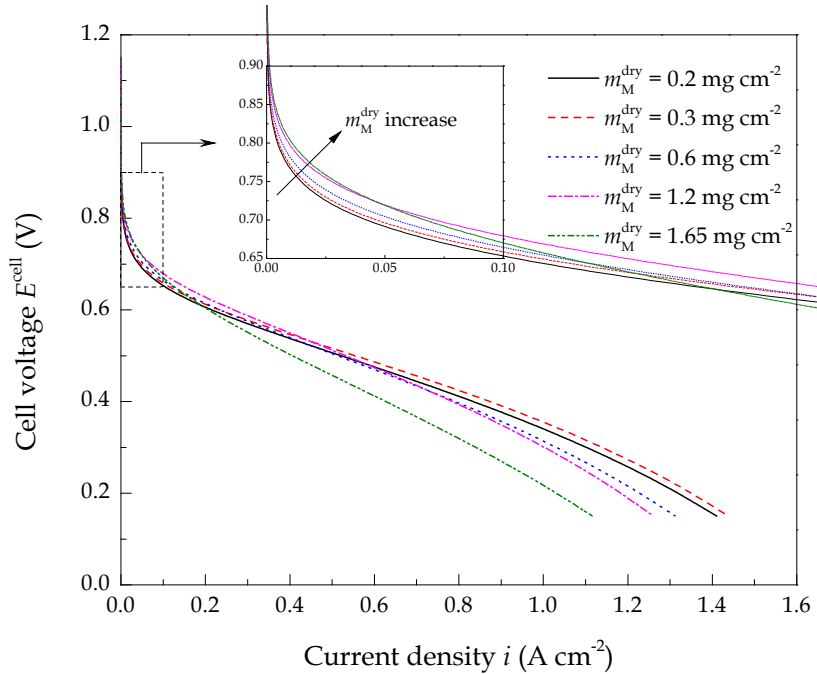


Figure 5-16 Effect of dry ionomer loadings on fuel cell performance

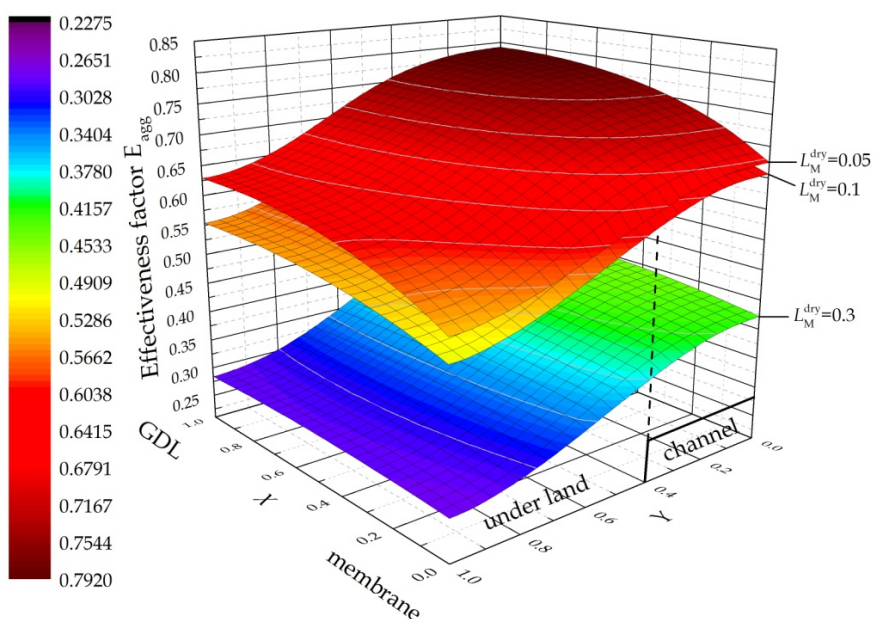


Figure 5-17 Effect of dry ionomer loading on effectiveness factor of cathode catalyst layer

### 5.3.12 Optimal relative humidity

The polarisation curves for different operating cathode relative humidity are shown in Figure 5-18. It is clear that the effect of the cathode relative humidity on the cell performance can be divided into three segments. With the initial increase in relative humidity, the cell performance decreases at lower current densities and improves at medium current densities and decreases again at higher current densities.

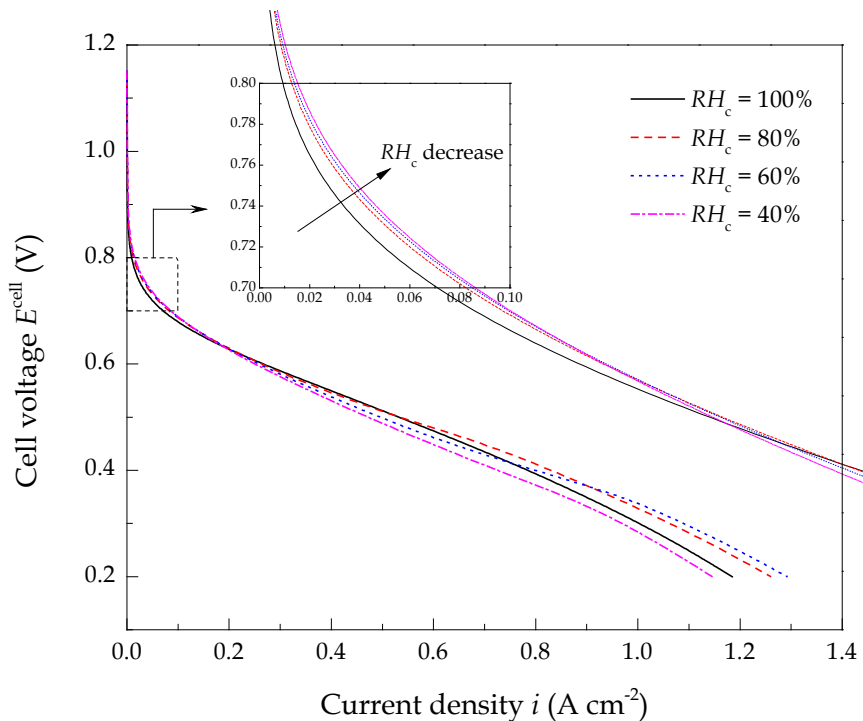


Figure 5-18 Effect of cathode relative humidity on fuel cell performance

At lower current densities, the lower relative humidity benefits the cell performance because a lower relative humidity increases the oxygen fraction of cathode gas inlet and increases the catalyst layer porosity by reducing the ionomer swelling. Even though the oxygen diffusion coefficient through the ionomer is reduced by the lower relative humidity, the negative effect is less remarkable because the mass transport impact is not significant at lower current densities. At medium current densities, the electrode is under mixed control of both the kinetics and mass transport. In this situation, the increase in cathode relative humidity increases the oxygen diffusion rate through the ionomer film and results in an increase in oxygen reduction rate until liquid water is generated at higher current densities. However, the thickness of the ionomer film increases significantly at higher cathode relative humidity. As shown in Table 5-8, the ionomer film thickness increases 26% at the current density of  $1.0 \text{ A cm}^{-2}$  with the

relative humidity of 60% and 80%, which increases the oxygen mass transport resistance.

Table 5-8 Average ionomer film thicknesses at different current densities and relative humidity in base case condition

RH <sub>c</sub>	Dry ionomer	Swelled ionomer at various current densities			
		0.2 A cm <sup>-2</sup>	0.6 A cm <sup>-2</sup>	1.0 A cm <sup>-2</sup>	1.4 A cm <sup>-2</sup>
80%		142.9 nm	156.9 nm	168.2 nm	168.2 nm
60%	133.2 nm	141.6 nm	144.4 nm	167.8 nm	167.8 nm
40%		139.9 nm	141.8 nm	143.9 nm	----- nm

It is apparent in Figure 5-18 that when the cathode is fed with fully humidified air, the higher cathode relative humidity offsets the improved fuel cell performance at higher current densities due to the increase in oxygen diffusion resistance resulting from the increased thickness of the liquid water film (flooding). This observation is consistent with the experimental results of Yan *et al.* [31] and the simulation results of Nguyen and White [32]. For example, at cathode relative humidity of 80%, the average water saturation is 4.0% and the average thickness of the liquid water film is 2.0 nm at 0.88 A cm<sup>-2</sup>. Theoretically, the best fuel cell performance is achieved when the ionomer is properly saturated by water with minimum liquid water generation. In this study, the best performance is achieved at a cathode relative humidity between 40% and 60% at the current density of 1.2 A cm<sup>-2</sup>.

## 5.4 Conclusions

A two-dimensional, across-the-channel, steady-state, isothermal, two-phase flow model based on an agglomerate catalyst layer structure is presented. The water phase transfer between vapour, dissolved and liquid water is addressed in this two-phase flow model leading to a greater accuracy in validating the experimental data compared to the single-phase flow model. The dissolved water transport through the membrane/ionomer is modelled by a combined mechanism in which electro-osmotic drag (EOD), back diffusion and hydraulic permeation are all included. The modelling results show that the non-uniform distribution of the membrane/ionomer water content is caused by the EOD and ionomer water absorption (water uptake). At higher relative humidity and lower current density, ionomer water absorption plays a more important role than EOD. However, at lower relative humidity and higher current density, EOD also plays an

important role in determining the profile of the membrane/ionomer water content. At higher current density, higher membrane/ionomer water contents are observed near the cathode CL-GDL and under the land.

Membrane and ionomer swelling occurs in contact with water, the volume of membrane and ionomer therefore strongly depends on the water content. The modelling results show that the ionomer volume fraction in the cathode catalyst layer approximately increases by 25% when completely saturated. The membrane swelling increases the portion of GDL bulged into flow channel, while the ionomer swelling decreases the catalyst layer porosity and increases the ionomer film thickness. Both the membrane and ionomer swelling lead to an increase in oxygen transport resistance.

The optimal dry ionomer loading (initial ionomer content) is from 0.2 to 0.3 mg cm<sup>-2</sup> and the optimal cathode relative humidity is around 60% for the best performance of the fuel cell. This model could give a theoretical prediction of how changing the operating conditions and the catalyst layer composition can be used to enhance the fuel cell performance and reduce cost.

## 5.5 References

1. Springer, T.E., T.A. Zawodzinski and S. Gottesfeld, *Polymer Electrolyte Fuel Cell Model*. Journal of Electrochemistry Society, 1991. **138**: p. 2234-2242.
2. Bernardi, D.M. and M.W. Verbrugge, *Mathematical model of a gas diffusion electrode bonded to a polymer electrolyte*. AIChE Journal, 1991. **37**: p. 1151-1163.
3. Bernardi, D.M. and M.W. Verbrugge, *A mathematical model of the solid-polymer-electrolyte fuel cell*. Journal of Electrochemistry Society, 1992. **139**: p.2477-2491.
4. Broka, K. and P. Ekdunge, *Modelling the PEM fuel cell cathode*. Journal of Applied Electrochemistry, 1997. **27**: p. 281-289.
5. Marr, C. and X. Li, *Composition and performance modelling of catalyst layer in a proton exchange membrane fuel cell*. Journal of Power Sources 1999. **77**: p. 17-27.
6. Sun, W., B.A. Peppley and K. Karan, *An improved two-dimensional agglomerate cathode model to study the influence of catalyst layer structural parameters*. Electrochimica Acta, 2005. **50**: p. 3359-3374.
7. Shah, A.A., G.S. Kim, P.C. Sui and D. Harvey, *Transient non-isothermal model of a polymer electrolyte fuel cell*. Journal of Power Sources, 2007. **163**: p. 793-806.

8. Weber, A.Z. and J. Newman, *Transport in polymer-electrolyte membranes I. Physical model*. Journal of Electrochemistry Society, 2003. **150**: p. A1008-A1015.
9. Weber, A.Z. and J. Newman, *Transport in polymer-electrolyte membranes II. Mathematical model*. Journal of Electrochemistry Society, 2004. **151**: p. A311-A325.
10. Wu, H., P. Berg and X. Li, *Modelling of PEMFC Transients with Finite-Rate Phase-Transfer Processes*. Journal of Electrochemistry Society, 2010. **157**: B1-B12.
11. Wu, H., P. Berg and X. Li, *Steady and unsteady 3D non-isothermal modelling of PEM fuel cells with the effect of non-equilibrium phase transfer*. Applied Energy, 2010. **87**: p. 2778-2784.
12. Yang, X.G., Q. Ye and P. Cheng, *Matching of water and temperature fields in proton exchange membrane fuel cells with non-uniform distributions*. International Journal of Hydrogen Energy, 2011. **36**: p. 12524-12537.
13. Ge, S. and B. Yi, *A mathematical model for PEMFC in different flow modes*. Journal of Power Sources, 2003. **124**: p. 1-11.
14. Ge, S., X. Li, B. Yi and I.M. Hsing, *Absorption, Desorption, and Transport of Water in Polymer Electrolyte Membrane for Fuel Cells*. Journal of Electrochemistry Society, 2005. **152**: p. A1149-A1157.
15. Basu, S., J. Li, C.Y. Wang, *Two-phase flow and maldistribution in gas channels of a polymer electrolyte fuel cell*. Journal of Power Sources, 2009. **187**: p. 431-443.
16. Hertwig, K, L. Martens and R. Karwoth, *Mathematical modelling and simulation of polymer electrolyte membrane fuel cells. Part I: Model structures and solving an isothermal one-cell model*. Fuel Cells, 2002. **2**: p. 61-77.
17. Wang, Z.H., C.Y. Wang and K.S. Chen, *Two-phase flow and transport in the air cathode of proton exchange membrane fuel cells*. Journal of Power Sources, 2001. **64**: p. 40-50.
18. Pasaogullari, U. and C.Y. Wang, *Two-phase transport and the role of micro-porous layer in polymer electrolyte fuel cells*. Electrochimica Acta, 2004. **49**: p. 4359-4369.
19. Pasaogullari, U. and C.Y. Wang, *Two-phase modelling and flooding prediction of polymer electrolyte fuel cells*. Journal of Electrochemistry Society, 2005. **152**: p. A380-A390.

20. Nam, J.H. and M. Kaviany, *Effective diffusivity and water-saturation distribution in single- and two-layer PEMFC diffusion medium*. International Journal of Heat and Mass Transfer, 2003. **46**: p. 4595-4611.
21. Lin, G.Y., W.S. He and T.V. Nguyen, *Modeling liquid water effects in the gas diffusion and catalyst layers of the cathode of a PEM fuel cell*. Journal of Electrochemistry Society, 2004. **151**: p. A1999-A2006.
22. He, W.S., J.S. Yi and T.V. Nguyen, *Two-phase flow model of the cathode of PEM fuel cells using interdigitated flow fields*. AIChE Journal, 2000. **46**: p. 2053-64.
23. Wang, L., A. Husar, T. Zhou and H.T. Liu, *A parameter study of PEM fuel cell performances*. International Journal of Hydrogen Energy, 2003. **28**: p. 1263-72.
24. Choi, J.E. and Y.C. Bae, *Swelling effect of a polymer electrolyte membrane on the development of a semi-empirical cell voltage model*. Journal of Applied Electrochemistry, 2009. **39**: p. 1419-1425.
25. Xing L., M. Mamlouk and K. Scott, *A two-dimensional agglomerate model for a proton exchange membrane fuel cell*. Energy, 2013. **61**: p. 196-210.
26. Buchi, F.N. and G.G. Scherer, *Investigation of the transversal water profile in Nafion membranes in polymer electrolyte fuel cells*. Journal of Electrochemistry Society, 2001. **148**: p. A183-A188.
27. Kulikovsky, A.A., *Quasi-3D modelling of water transport in polymer electrolyte fuel cells*. Journal of Electrochemistry Society, 2003. **150**: p. A1432-A1439.
28. Wang, Y. and K.S. Chen, *Through-plane water distribution in a polymer electrolyte fuel cell: comparison of numerical prediction with neutron radiography data*. Journal of Electrochemistry Society, 2010. **157**: p. B1878-B1886.
29. Passalacqua, E., F. Lufrano, G. Squadrito, A. Patti and L. Giorgi, *Nafion content in the catalyst layer of polymer electrolyte fuel cells: effects on structure and performance*. Electrochimica Acta, 2001. **46**: p. 799-805.
30. Kim, K.H., K.Y. Lee, H.J. Kim, E. Cho, S.Y. Lee, T.H. Lim, S.P. Yoon, I.C. Hwang, J.H. Jang, *The effects of Nafion® ionomer content in PEMFC MEAs prepared by a catalyst-coated membrane (CCM) spraying method*. International Journal of Hydrogen Energy, 2010. **35**: p. 2119-2126.

31. Yan, Q., H. Toghiani and H. Causey, *Steady-state and dynamic performance of proton exchange membrane fuel cells (PEMFCs) under various operating conditions and load changes*. Journal of Power Sources, 2006. 161: p. 492-502.
32. Nguyen, T.V. and R.E. White, *A water and heat management model for proton-exchange-membrane fuel cells*. Journal of Electrochemistry Society, 1993. 140: p. 2178-86.

## Chapter 6. Two-phase flow Non-isothermal model

This chapter describes a two-dimensional, across-the-channel, steady-state, two-phase flow, and non-isothermal model based on a spherical agglomerate catalyst structure combined with a comprehensive water phase transfer and transport, namely (1) water vapour condensation and liquid water evaporation, (2) membrane and ionomer water absorption or water uptake, (3) membrane and ionomer desorption, (4) water transport through membrane via electro-osmotic drag, back diffusion and hydraulic permeation. The distribution of water content of membrane and ionomer, temperature and liquid water saturation in the fuel cell and their effects on the performance of the cell under various operating temperatures are investigated. Ionomer swelling is associated with the non-uniform distribution of water in the ionomer. Two approaches, namely (1) applying different operating temperatures on anode and cathode and (2) enlarging the width ratio of the channel/current collector rib, are adopted to improve the fuel cell performance.

### 6.1 Introduction

As heat is released during the operation of the fuel cells, thermal management is important due to the effect of temperature on various transport, kinetic and phase-transfer parameters [1, 2]. Therefore, numerous mathematical models were developed with the aim of fully understanding the species, momentum and thermal transport by coupling water and thermal transport [3-9, 13-17].

The earliest water and thermal interrelated models were developed by Nguyen and White [3] and Fuller and Newman [4], in which the heat transfer between water evaporation and condensation were coupled with the species transport. Yi and Nguyen [5] improved the previous model [3] by including the convective water transport across the membrane and the temperature distribution in the solid phase, and stated that the counter-flow mode is most effective for heat removal. Djilali and Lu [6] investigated the influence of heat transfer on gas and water transport in fuel cells and concluded that the non-uniform distribution of temperature and pressure have a large impact on the liquid water and vapour fluxes in the porous medias. Ju *et al.* [7] analysed the energy balance in anode catalyst layer, membrane and cathode catalyst layer with the aid of a developed single-phase, non-isothermal model, and confirmed the necessity for non-isothermal modelling of the PEMFCs.

As a new mechanism of heat and water transport, the so-called “heat-pipe effect” in which water evaporates at the hotter catalyst layer, diffuses through the gas diffusion layer, and condenses on the colder plates was first presented by Wang and Wang [8]. The “heat-pipe effect” was emphasised in the one-dimensional model developed by Weber and Newman [9], in which the maximum temperature was observed within the cathode catalyst layer and the heat released by the oxygen reduction reaction occupies approximate 80% of the total heat generated. However, due to the simplified treatment of the catalyst layer as an ultra-thin interface between the gas diffusion layer and membrane, these models [3-9] show limitation in modelling the catalyst layer. Thus, numerous models adopted a spherical agglomerate structure as the catalyst layer and concluded that the agglomerate model was superior in representing the real porous catalyst layer than the ultra-thin layer model and pseudo-homogeneous film model [10-12].

Water exists as three different phases: dissolved water in membrane/ionomer, water vapour and liquid water in porous electrodes. In recent years, researchers began to focus on the thermal transport during the water phase transfer between vapour, dissolved water and liquid water [13-17]. As stated by Yang *et al.* [17], the absorption or release of heat associated with the water phase transfer, corresponds to approximate 20% of the total heat generated within the whole cell and therefore cannot be neglected. Typically, the membrane/ionomer swells when water uptake occurs, which results in an increase in the ionic conductivity of the membrane/ionomer and a decrease in porosity of the electrode [15]. Consequently, water management is another crucial issue in balancing the operation of the fuel cell to achieve optimum performance.

## 6.2 Model description

### 6.2.1 Computational domain and assumption

The computational domain is that for the isothermal two-phase flow model represented in Chapter 5. In addition to the assumptions given in Chapter 5, the thickness of the membrane is assumed as a constant in order to simplify the model. It is also assumed that the ionomer film thickness changes with its water content.

### 6.2.2 Governing equations

The governing equations for the non-isothermal and two-phase flow model in this chapter are summarised in [Table 6-1](#) as follow:

Table 6-1 Governing equations used in the two-phase flow and non-isothermal model

Gas diffusion layers (Domain 2)	
Conservation of mass	$-\frac{\rho^g k_p}{\mu^g} \nabla \cdot (\nabla p) = 0 \quad (6-1)$
Conservation of species	$\rho^g \mathbf{u}^g \cdot \nabla w_i^g - \nabla \cdot [-\rho^g \sum_{j=1}^N (1-s^j) D_{ij} (\nabla x_j^g - w_j^g) \frac{\nabla p}{p}] = 0 \quad (6-2)$
Conservation of charge	$\nabla (-\sigma_s^{eff} \nabla \phi_s) = \nabla (-\sigma_M^{eff} \nabla \phi_M) = 0 \quad (6-3)$
Conservation of energy	$\nabla \cdot [\sum_{i=g,l} (\varepsilon \rho_i c_{p,i} \mathbf{u}_i) T] - \nabla \cdot (\sum_{i=g,l,s} k_i \nabla T) = S_T \quad (6-4)$
Catalyst layers (Domain 3)	
Conservation of mass	$-\frac{\rho^g k_p}{\mu^g} \nabla \cdot (\nabla p) = S_m \quad (6-5)$
Conservation of species	$\rho^g \mathbf{u}^g \cdot \nabla w_i^g - \nabla \cdot [-\rho^g \sum_{j=1}^N (1-s^j) D_{ij} (\nabla x_j^g - w_j^g) \frac{\nabla p}{p}] = M_i S_i^g \quad (6-6)$
Conservation of charge	$\nabla (-\sigma_s^{eff} \nabla \phi_s) = Q_s \quad (6-7)$
	$\nabla (-\sigma_M^{eff} \nabla \phi_M) = Q_M \quad (6-8)$
Conservation of energy	$\nabla \cdot [\sum_{i=g,l} (\varepsilon \rho_i c_{p,i} \mathbf{u}_i) T] - \nabla \cdot (\sum_{i=g,l,s} k_i \nabla T) = S_T \quad (6-9)$
Membrane (Domain 4)	
Conservation of charge	$\nabla (-\sigma_M^{eff} \nabla \phi_M) = 0 \quad (6-10)$
Conservation of energy	$\nabla \cdot [\sum_{i=g,l} (\varepsilon \rho_i c_{p,i} \mathbf{u}_i) T] - \nabla \cdot (\sum_{i=g,l,s} k_i \nabla T) = S_T \quad (6-11)$

In this non-isothermal model, heat generation originating from reaction, Joule heating (ohmic heating) and water phase transfers are all considered in the source term,  $S_T$ . It is worth noting that the hydrogen oxidation reaction in the anode is endothermic whereas the oxygen reduction reaction in the cathode is exothermic. In the equations of conservation of energy shown in [Table 6-1](#), the subscript  $i$  refers to gas mixture, liquid water and solid phase of the electrode. In addition to the source terms which have been

given in [Chapter 5](#), the conservation of heat and heat source terms are listed in [Table 6-2](#) and [Table 6-3](#), respectively.

Table 6-2 Conservation of heat in different computational domains

Anode GDL	Anode CL	Membrane	Cathode CL	Cathode GDL
$S_T^{sa}$	$S_T^{vd} + S_T^{ra} + S_T^{sa} + S_T^M$	$S_T^M$	$S_T^{dl} + S_T^{vl} + S_T^{vd} + S_T^{rc} + S_T^{sc} + S_T^M$	$S_T^{vl} + S_T^{sc}$

Note: The unit for each source term is ( $\text{W m}^{-3}$ )

Table 6-3 Source terms of heat

Source terms	Unit	Domain
$S_T^{sa} = \frac{i_a^2}{\sigma_{GDL,a}^{eff}}$	$\text{W m}^{-3}$	Anode GDL
$S_T^{sc} = \frac{i_c^2}{\sigma_{GDL,c}^{eff}}$	$\text{W m}^{-3}$	Cathode GDL
$S_T^M = \frac{i_M^2}{\sigma_M^{eff}}$	$\text{W m}^{-3}$	Membrane, Anode and cathode CLs
$S_T^{ra} = - i_a  \left[ \frac{\nabla S_a}{2F} \right]$	$\text{W m}^{-3}$	Anode CL
$S_T^{rc} =  i_c  \left[  \eta_c  - \frac{\nabla S_c}{4F} \right]$	$\text{W m}^{-3}$	Cathode CL
$S_T^{vd} = M_w S_w^{vd} \nabla h_w^{vd}$	$\text{W m}^{-3}$	Anode and cathode CLs
$S_T^{dl} = M_w S_w^{dl} \nabla h_w^{dl}$	$\text{W m}^{-3}$	Cathode CL
$S_T^{vl} = M_w S_w^{vl} \nabla h_w^{vl}$	$\text{W m}^{-3}$	Cathode GDL and CL

### 6.2.3 Thermal parameters

The effective thermal conductivity and specific heat capacity depend on the volume fractions of the species within a chosen domain. Without a doubt, the cathode catalyst layer is the most complicated domain in which gas mixture, liquid water, ionomer, *Pt/C* catalyst, penetrated GDL are all involved. The detailed expressions for the effective thermal conductivity, specific heat capacity of GDL, CL and membrane/ionomer are listed in [Table 6-4](#). The thermal parameters and temperature dependent heat capacity and thermal conductivity used in this model are given in [Table 6-5](#) and [Table 6-6](#).

Table 6-4 Effective specific heat capacity and thermal conductivity of GDL, CL and membrane

GDL	CL	Membrane
$c_p^{eff}$	$\varepsilon_{GDL} c_{p,C} + (L_C + L_s) c_{p,C} + L_M c_{p,M} + s \varepsilon_{CL} c_{p,w}^l + (1-s) \varepsilon_{CL} c_p^g$	$c_{p,M}$
$k^{eff}$	$\varepsilon_{GDL} k_C + (L_C + L_s) k_C + L_M k_M$	$k_M$

Table 6-5 Thermal parameters

Parameters	Value	Reference
Platinum specific heat capacity, $c_{p,pt}$ ( $J \text{ kg}^{-1} \text{ K}^{-1}$ )	$1.3 \times 10^2$	[15]
Carbon specific heat capacity, $c_{p,C}$ ( $J \text{ kg}^{-1} \text{ K}^{-1}$ )	894.4	[15]
Membrane specific heat capacity, $c_{p,M}$ ( $J \text{ kg}^{-1} \text{ K}^{-1}$ )	1090.0	[15]
Liquid water specific heat capacity, $c_{p,w}^l$ ( $J \text{ kg}^{-1} \text{ K}^{-1}$ )	4187.0	[15]
Membrane thermal conductivity, $k_M$ ( $\text{W m}^{-1} \text{ K}^{-1}$ )	0.25	[9]
Entropy of hydrogen oxidation, $\nabla S_a$ ( $J \text{ mol}^{-1} \text{ K}^{-1}$ )	161.2	[27]
Entropy of oxygen reduction, $\nabla S_c$ ( $J \text{ mol}^{-1} \text{ K}^{-1}$ )	-324.0	[27]
Latent heat of membrane adsorption, $\nabla h_w^{ad}$ ( $J \text{ kg}^{-1}$ )	$3.462 \times 10^6$	[21]
Latent heat of membrane desorption, $\nabla h_w^{dd}$ ( $J \text{ kg}^{-1}$ )	$3.462 \times 10^6$	[21]
Latent heat of condensation/evaporation, $\nabla h_w^v$ ( $J \text{ kg}^{-1}$ )	$2.308 \times 10^6$	[21]

Table 6-6 Temperature dependent heat capacity and thermal conductivity

Parameters	Expressions	Reference
Hydrogen heat capacity, $c_{p,H_2}^g$	$1.914 \times 10^{-6} T^2 - 8.314 \times 10^{-4} T + 28.890$	fitted [28]
Oxygen heat capacity, $c_{p,O_2}^g$	$-4.281 \times 10^{-6} T^2 + 1.371 \times 10^{-2} T + 25.431$	fitted [28]
Nitrogen heat capacity, $c_{p,N_2}^g$	$1.788 \times 10^{-5} T^2 + 2.924 \times 10^{-3} T + 27.848$	fitted [28]
Water vapour heat capacity, $c_{p,w}^g$	$1.180 \times 10^{-6} T^2 + 9.621 \times 10^{-3} T + 30.326$	fitted [28]
Platinum thermal conductivity, $k_{pt}$	$-5.037 \times 10^{-9} T^3 + 2.483 \times 10^{-5} T^2 - 2.282 \times 10^{-2} T + 77.80$	[29]
Carbon thermal conductivity, $k_C$	$1.048 \times 10^{-6} T^2 - 2.869 \times 10^{-3} T + 2.979$	[29]
Liquid water thermal conductivity, $k_w^l$	$-1.118 \times 10^{-5} T^2 + 8.388 \times 10^{-3} T - 0.9004$	fitted [28]
Hydrogen thermal conductivity, $k_{H_2}$	$3.777 \times 10^{-4} T + 7.444 \times 10^{-2}$	fitted [28]
Oxygen thermal conductivity, $k_{O_2}$	$6.204 \times 10^{-5} T + 8.83 \times 10^{-3}$	fitted [28]
Nitrogen thermal conductivity, $k_{N_2}$	$5.453 \times 10^{-5} T + 1.088 \times 10^{-2}$	fitted [28]
Water vapour thermal conductivity, $k_{H_2O}$	$1.188 \times 10^{-4} T - 2.404 \times 10^{-2}$	fitted [28]

Note: the unit for heat capacity is ( $J \text{ mol K}^{-1}$ ) and for thermal conductivity is ( $\text{W m}^{-1} \text{ K}^{-1}$ )

### 6.2.4 Boundary conditions

In addition to the boundary conditions shown in Chapter 5, the temperatures at the inlets of anode and cathode are defined as  $T_a^0$  and  $T_c^0$  (K), respectively. Note that the temperatures of the anode and cathode gas inlets are the same as the operating temperatures of the current collectors of anode and cathode, respectively. At a given temperature, the mole fraction of reactants at anode and cathode can be calculated by the following equations:

$$x_{H_2O,a}^0 = \frac{p_{sat}RH_a}{p_a}, \quad x_{H_2,a}^0 = 1 - x_{H_2O,a,in} \quad (6-12)$$

$$x_{H_2O,c}^0 = \frac{p_{sat}RH_c}{p_c}, \quad x_{O_2,c}^0 = 0.21(1 - x_{H_2O,c,in}), \quad x_{N_2,c}^0 = 0.21(1 - x_{H_2O,c,in}) \quad (6-13)$$

### 6.2.5 Numerical solution

The numerical solution in this study is based on the same principle described in Chapter 5. By accounting for the temperature distribution, the fully coupled equations are solved according to the computational process shown schematically in Figure 6-1 as follow:

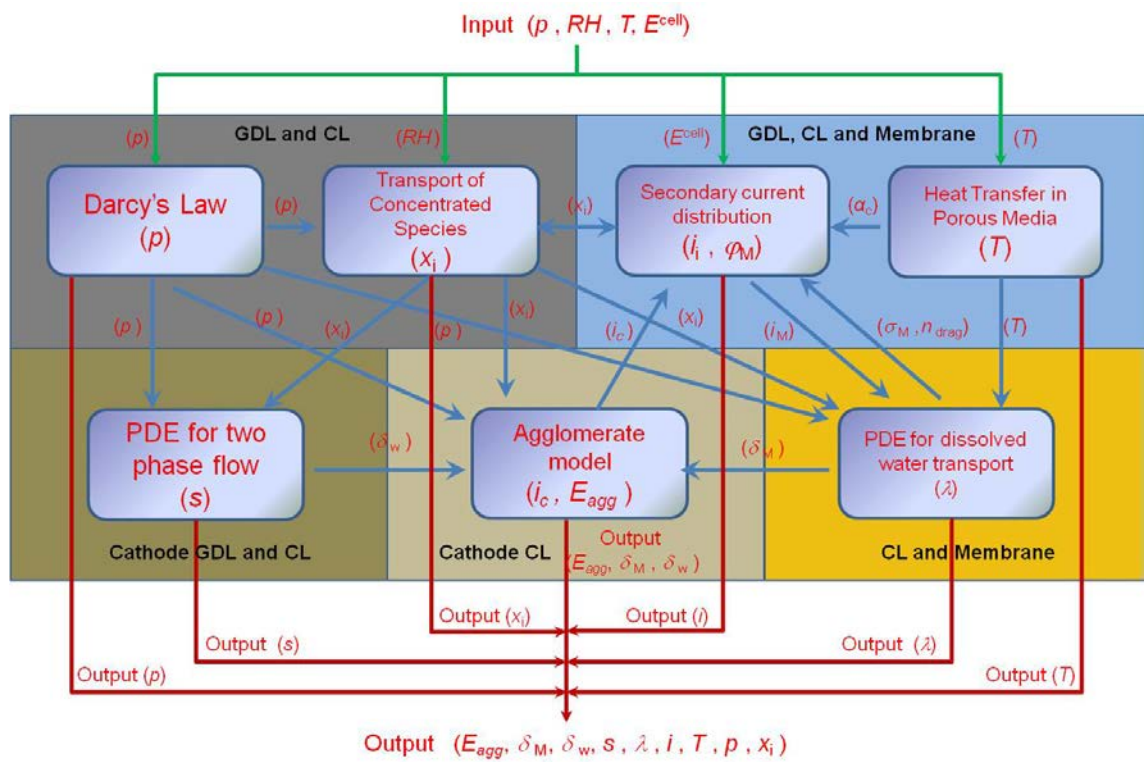


Figure 6-1 Schematic of the computational process

## 6.3 Results and discussion

### 6.3.1 Temperature distribution

Though not shown here, the temperature profiles are very similar at three different operating temperatures (60, 70 and 80 °C) at a fixed current density, i.e. at 0.7 A cm<sup>-2</sup>, the highest temperatures are observed in the cathode catalyst layer under the channel which are approximately 2.3 °C higher than the temperatures at the inlet boundary, which is in agreement of the simulation results of Jung *et al.* [18]. This is because, at a fixed current density, the released heat is almost equivalent at various temperatures as the oxygen reduction reaction (ORR) at the cathode is the main heat source. However, as shown in Figure 6-2, the temperature profiles vary with cell voltages. When the cell voltage is fixed to 0.3 V, the current densities at 60, 70 and 80 °C are 0.73, 0.87 and 0.95 A cm<sup>-2</sup>, respectively. With increasing operating temperature, the temperature distribution within the cathode catalyst layer becomes more non-uniform. As shown in Figure 6-2, the heat accumulation occurs within the cathode catalyst layer on the region under the channel. The temperature gradients are observed in two directions: one from CL to GDL, and the other from the region under the channel to that under the land. In the two directions, the temperature gradients increase as the operating temperature increases. This is because the ORR in the cathode catalyst layer is exothermic, and the heat released by ORR is the main heat source compared to others. As shown in Table 6-7, the heat released by ORR occupies at least 67% of the total heat at 0.7 A cm<sup>-2</sup>. According to Eq. (3-31), the reaction rate is accelerated by increasing the temperature. It is worth noting that, more heat is generated in the region under the channel where ORR first occurs. Among the heat sources, the total Joule heat ( $S_s^T + S_M^T$ ) only corresponds to approximately 2% of the total heat due to the high conductivities of the electrode and membrane, therefore it can be neglected. The water phase transfer heat ( $S_{vd}^T + S_{dl}^T + S_{vl}^T$ ) account for approximate 5% of the total heat in which the membrane and ionomer desorption is the main heat source during the phase transfer process.

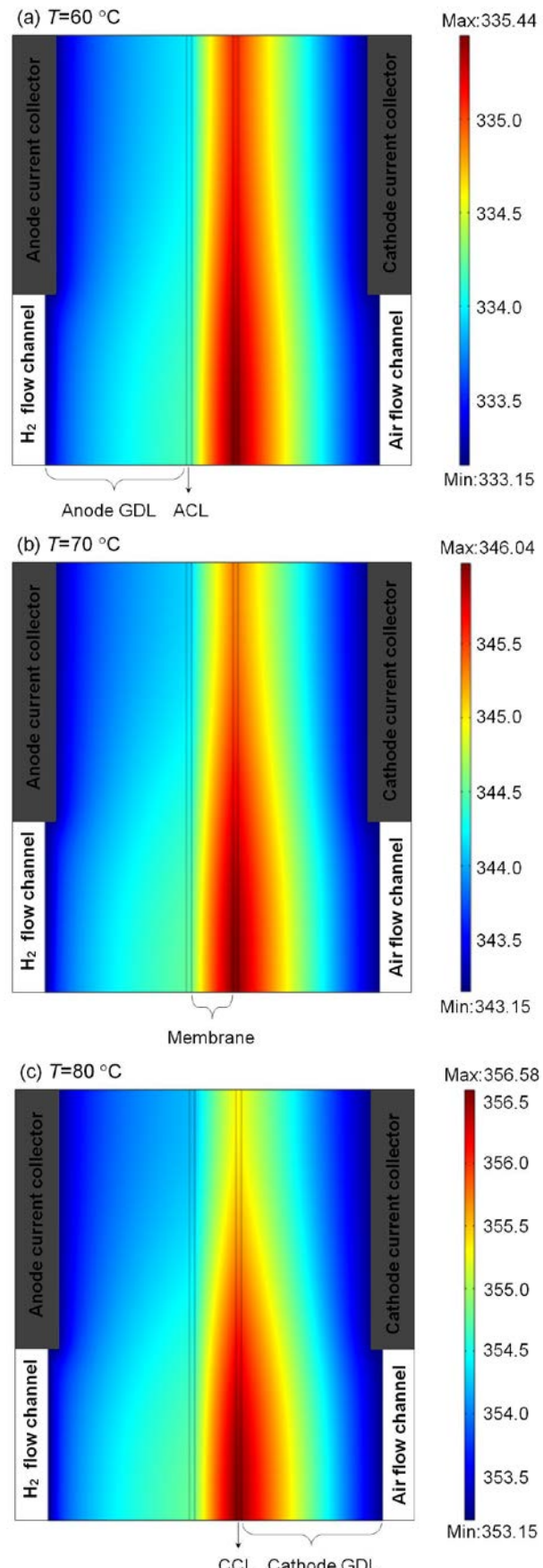


Figure 6-2 Temperature profiles at the cell voltage of 0.3 V and at (a)  $60\text{ }^{\circ}\text{C}$  ( $0.73\text{ A cm}^{-2}$ ), (b)  $70\text{ }^{\circ}\text{C}$  ( $0.87\text{ A cm}^{-2}$ ) and (c)  $80\text{ }^{\circ}\text{C}$  ( $0.95\text{ A cm}^{-2}$ )

### 6.3.2 Effect of temperature on liquid water saturation

The liquid water saturation profiles at  $0.7 \text{ A cm}^{-2}$  at different temperatures are shown in Figure 6-3. From the liquid water saturation contours, it can be seen that flooding is more severe and the two-phase flow region is enlarged as the temperature decreases when inlet gases are humidified at a fixed relative humidity, which is consistent with the neutron radiographs tested by Owejan *et al.* [19]. This can be explained by the decrease in the water saturation pressure, which strongly depends on temperature. And this can be also explained with the aid of Table 6-7 in which the total sources for liquid water ( $S_{dl}^w + S_{vl}^w$ ) increase as the temperature decreases.

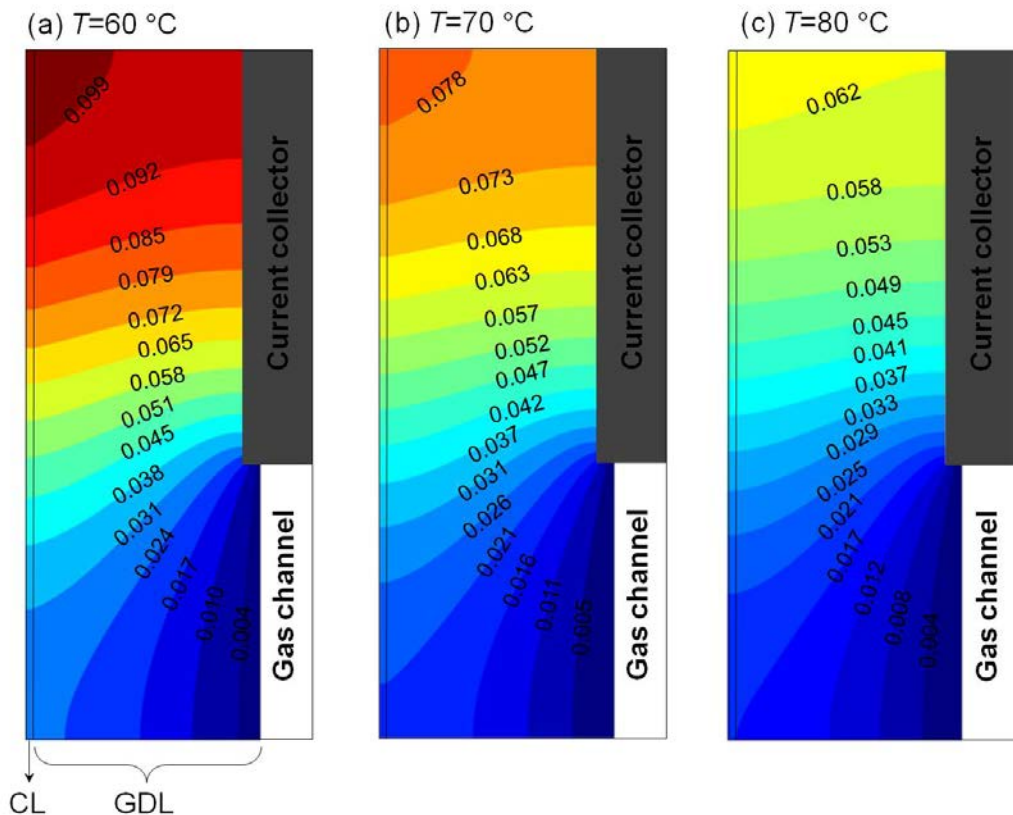


Figure 6-3 Liquid water saturation profiles at  $0.7 \text{ A cm}^{-2}$  with fully humidified inlet gases at (a)  $60 \text{ }^\circ\text{C}$  ( $0.32 \text{ V}$ ), (b)  $70 \text{ }^\circ\text{C}$  ( $0.39 \text{ V}$ ) and (c)  $80 \text{ }^\circ\text{C}$  ( $0.42 \text{ V}$ )

In addition, it is evident from Figure 6-3 that the local saturation is higher in the region close to the CL-membrane interface and under the land, which is consistent with the numerical prediction and neutron radiography data and simulation results of Wang and Chen [20]. As discussed in Chapter 5 and shown in Table 6-7, the liquid water is generated via water vapour condensation and membrane/ionomer desorption, and the membrane/ionomer desorption plays a more important role compared to the water

vapour condensation. The dissolved water under the land firstly reaches to saturation level due to the stronger effect of electro-osmotic drag (EOD) under the land. Consequently, more liquid water is generated under the land than under the channel. In fact, the source term of the liquid water strongly depends on the water production mechanisms: the water generated by ORR exists as vapour, dissolved water or liquid water [21]. In this study, the dissolved water production mechanism is used.

Table 6-7 Dissolved water transport flux, water phase-change and thermal source terms at 0.7 A cm<sup>-2</sup>

	60 °C (0.32 V)		70 °C (0.39 V)		80 °C (0.42 V)	
<b>Dissolved water transport flux</b>						
$F_{EOD}$ (mol m <sup>-2</sup> s <sup>-1</sup> )	$4.3 \times 10^{-2}$	(50.58%)	$5.1 \times 10^{-2}$	(56.65%)	$6.2 \times 10^{-2}$	(65.92%)
$F_{BD}$ (mol m <sup>-2</sup> s <sup>-1</sup> )	$4.2 \times 10^{-2}$	(49.40%)	$3.9 \times 10^{-2}$	(43.32%)	$3.2 \times 10^{-2}$	(34.02%)
$F_{HP}$ (mol m <sup>-2</sup> s <sup>-1</sup> )	$2.1 \times 10^{-5}$	(0.02%)	$3.0 \times 10^{-5}$	(0.03%)	$4.9 \times 10^{-5}$	(0.05%)
Total flux	$8.5 \times 10^{-2}$		$9.0 \times 10^{-2}$		$9.4 \times 10^{-2}$	
<b>Water phase change sources</b>						
$S_{vd}^w$ (mol m <sup>-3</sup> s <sup>-1</sup> )	$2.2 \times 10^2$	(1.10%)	$2.3 \times 10^2$	(1.17%)	$2.4 \times 10^2$	(1.2%)
$S_{dl}^w$ (mol m <sup>-3</sup> s <sup>-1</sup> )	$7.9 \times 10^2$	(3.94%)	$3.8 \times 10^2$	(1.93%)	$1.9 \times 10^2$	(1.23%)
$S_{vl}^w$ (mol m <sup>-3</sup> s <sup>-1</sup> )	54.2	(0.27%)	52.9	(0.27%)	50.97	(0.98%)
$S_{ORR}^w$ (mol m <sup>-3</sup> s <sup>-1</sup> )	$1.9 \times 10^4$	(94.70%)	$1.9 \times 10^4$	(96.63%)	$1.9 \times 10^4$	(97.53%)
Total phase-change sources	$2.01 \times 10^4$		$1.97 \times 10^4$		$1.95 \times 10^4$	
<b>Thermal sources</b>						
$S_{vd}^T$ (W m <sup>-3</sup> )	$1.3 \times 10^7$	(1.67%)	$1.4 \times 10^7$	(1.95%)	$1.5 \times 10^7$	(2.15%)
$S_{dl}^T$ (W m <sup>-3</sup> )	$4.9 \times 10^7$	(6.30%)	$2.4 \times 10^7$	(3.34%)	$1.2 \times 10^7$	(1.72%)
$S_{vl}^T$ (W m <sup>-3</sup> )	$2.3 \times 10^6$	(0.33%)	$2.2 \times 10^6$	(0.31%)	$2.1 \times 10^6$	(0.30%)
$S_{HOR}^T$ (W m <sup>-3</sup> )	$-1.8 \times 10^8$	(23.15%)	$-1.5 \times 10^8$	(20.85%)	$-1.4 \times 10^8$	(20.10%)
$S_{ORR}^T$ (W m <sup>-3</sup> )	$5.2 \times 10^8$	(66.89%)	$5.2 \times 10^8$	(72.27%)	$5.2 \times 10^8$	(74.66%)
$S_s^T$ (W m <sup>-3</sup> )	$7.7 \times 10^5$	(0.10%)	$7.8 \times 10^5$	(0.11%)	$7.9 \times 10^5$	(0.11%)
$S_M^T$ (W m <sup>-3</sup> )	$1.2 \times 10^7$	(1.54%)	$8.5 \times 10^6$	(1.18%)	$6.6 \times 10^6$	(0.95%)
Total thermal source	$7.77 \times 10^8$		$7.19 \times 10^8$		$6.96 \times 10^8$	

Note: the values in brackets are the percentage each item corresponded to the total

### 6.3.3 Effect of temperature on membrane/ionomer water content

Figure 6-4(a) to Figure 6-4(c) show the profiles of membrane/ionomer water content at a fixed current density of 0.7 A cm<sup>-2</sup> while varying the operating temperature from 60 °C to 80 °C, while Figure 6-4(d) is added to compare the membrane/ionomer water content profiles at a fixed temperature of 80 °C with the current densities of 0.2 A cm<sup>-2</sup>.

It is clear that due to the effect of electro-osmotic drag (EOD), the water content of the membrane and ionomer is lower at the anode and higher at the cathode. Thus, the membrane is prone to dry out at the anode and to be saturated at the cathode. As shown in [Figure 6-4\(a\)](#) to [Figure 6-4\(c\)](#), the influence of temperature on the water content is apparent. The relatively higher water content is observed at higher temperature. This can be explained by the increase in the water carrying capacity (WCC) of the reactant gases according to [Eq. \(6-12\)](#) and [Eq. \(6-13\)](#) as the temperature increases. Moreover, as shown in [Table 6-7](#), the net water diffusion flux ( $F_{EOD} - F_{BD} - F_{HP}$ ) increases as the temperature increases at a fixed current density, which means more water migrates to cathode. However, the increase in temperature enhances the amount of water carried by the anode gases. Calculated by [Eq. \(6-12\)](#), when the inlet gases are fully humidified, the molar fractions of water are 0.196 at 60 °C and 0.468 at 80 °C. Although the increase in temperature reinforces the net water diffusion flux through the membrane, the increase in WCC of the anode gas compensates for the loss of water at the anode side of the membrane leading to a relatively higher membrane water content. In addition, as shown in [Table 6-7](#), the water diffusion flux driven by the hydraulic permeation can be neglected as it is three orders of magnitude less than the water diffusion fluxes driven by the EOD and back diffusion.

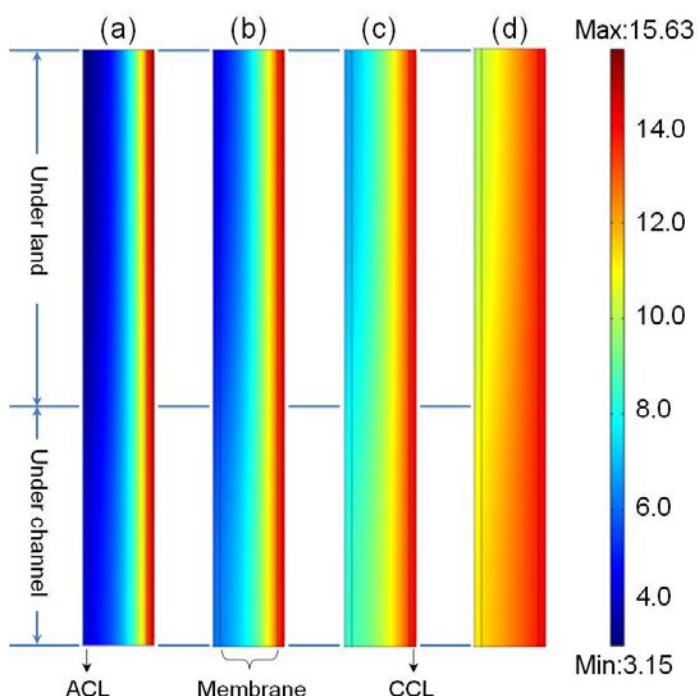


[Figure 6-4](#) Membrane/ionomer water content profiles at (a) 60 °C, 0.7 A cm<sup>-2</sup> (0.32 V), (b) 70 °C, 0.7 A cm<sup>-2</sup> (0.39 V), (c) 80 °C, 0.7 A cm<sup>-2</sup> (0.42 V) and (d) 80 °C, 0.2 A cm<sup>-2</sup> (0.61 V) with fully humidified inlet gases

The water contents at a fixed temperature with various current densities are shown in [Figure 6-4\(c\)](#) and [Figure 6-4\(d\)](#). At lower current density, a relative small change in water content is observed due to the lower amount of drag. When the current density increases, the water content becomes more non-uniform since the anode dehydrates and the cathode water content increases. It is clear in [Figure 6-4](#) that the minimum water content, with the value of 3.15, is observed at the anode side of the membrane (ionomer in the anode CL) while the water content reaches the equilibrium level at the cathode side of the membrane, which agrees with the experimental data of Buchi and Scherer [\[22\]](#). Moreover, anode dehydration is more severe under the land than that under the channel, which can be explained by the higher water migration flux driven by the EOD.

#### ***6.3.4 Effect of temperature on fuel cell performance***

The predicted polarisation curves obtained using the isothermal and non-isothermal models for the operating temperature from 60 to 80 °C are shown in [Figure 6-5](#). At 60 and 70 °C, the cell performance is expected to improve as the operating temperature increases and the predicted current densities are higher obtained using the non-isothermal model than that of the isothermal model. This can be explained by the increase in the cathode exchange current density ([Eq. 3-158](#)) and transfer coefficient ([Eq. 3-156](#)) and the decrease in liquid water saturation resulting from the temperature increase in the MEA, the cathode catalyst layer in particular. However, at 80 °C, the current density predicted using the non-isothermal model is lower than that of the isothermal model. This can be explained by the decrease in the oxygen mole fraction as the temperature increases. Without considering the temperature increase in the MEA, the oxygen mole fraction is 11.2% at 80 °C with fully humidified gas. Then it decreases to 9.7% when approximate 3.4 °C increase in temperature is taken into account. The insufficient oxygen limits the cell performance at higher current densities when the relative humidity is 100%. It can be concluded that lower cathode relative humidity is required when fuel cells are operated at higher temperatures, e.g. higher than 80 °C.

It is also clear that the increase in temperature from 60 to 70 °C leads to a greater improvement on the cell performance than that from 70 to 80 °C. At a fixed cell voltage of 0.3V, as the temperature increases from 60 to 70 and 80 °C, the ionic conductivity of the membrane increases from 4.88 to 6.08 and 8.14 S m<sup>-1</sup>, and the liquid water saturation decreases from 0.057 to 0.054 and 0.047, respectively. Compared with the

increase in temperature from 60 to 70 °C, the temperature change from 70 to 80 °C makes a greater contribution towards increasing membrane conductivity and reducing oxygen transport resistance. However, the oxygen fraction of the cathode inlet gases decreases from 16.9% at 60°C to 14.5% at 70°C, and to 11.2% at 80°C. The depletion of oxygen results in a limitation of the cathode performance since the cathode volumetric current density increases from  $377.5 \text{ A cm}^{-3}$  at 60°C to  $450.7 \text{ A cm}^{-3}$  at 70°C, and to  $490.8 \text{ A cm}^{-3}$  at 80°C. It is clear the increase in cathode volumetric current density is much smaller as the temperature changes from 70 to 80 °C than that change from 60 to 70 °C. Consequently, only increasing the operating temperature is prone to lead to the oxygen starvation on the cathode, which is a limitation to the improvement of the cell performance, unless the relative humidity of the cathode inlet gas is reduced simultaneously.

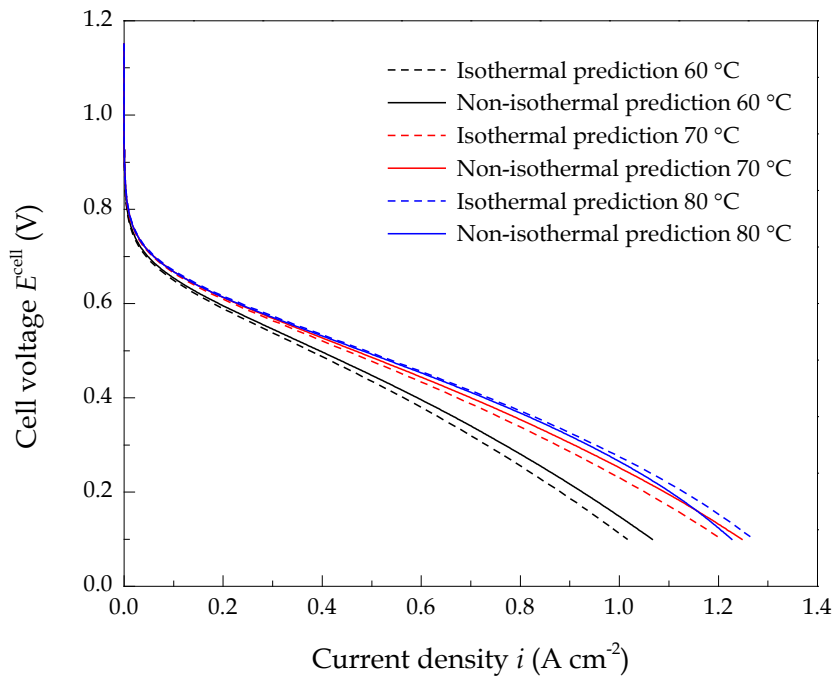


Figure 6-5 Polarisation curves at three operating temperatures with fully humidified inlet gases

#### 6.4 Optimise the temperature distribution and improve the cell performance

Although numerous researchers studied the effect of temperature on fuel cell performance [5, 9, 15, 17], few of them applied different temperatures on the anode and cathode, respectively. The effects of channel geometry and the widths of channel and shoulder were studied by Ahmed and Sung [24, 25] and Wang *et al.* [26]. Based on the analysis above, two parameters were varied to optimise the temperature distribution and

improve the fuel cell performance in this section. This entailed increasing the operating temperature on the anode and the width ratio of the channel/rib, respectively.

#### 6.4.1 Increasing the operating temperature on the anode

Due to the fact that higher inlet temperature increases the water carrying capacity (WCC) of the inlet gases, three anode temperatures and two cathode temperatures are applied to the current model to investigate the temperature effect on the polarisation curves. Note that heat conduction through the bipolar plates is not allowed as the single cell is assumed to be perfectly insulated. Figure 6-6 shows the polarisation curves with varying temperature on anode and cathode from 70°C to 90°C. It is clear that the increase in anode temperature increases the cell performance at higher current densities whereas it decreases the cell performance at lower current densities. However, the increase in cathode temperature is of benefit to the cell performance at lower current densities and makes a very slight change on the cell performance at higher current densities. When the inlet gases are fully humidified, the water mole fraction of the inlet gases increases from 19.6% at 60°C to 30.8% at 70°C, and to 46.8% at 80°C. According to Eq. (3-209), Eq. (3-210), Eq. (6-12) and Eq. (6-13), the membrane/ionomer water content is finally determined by the relative humidity of the reactant gas on the boundary of CL-GDL.

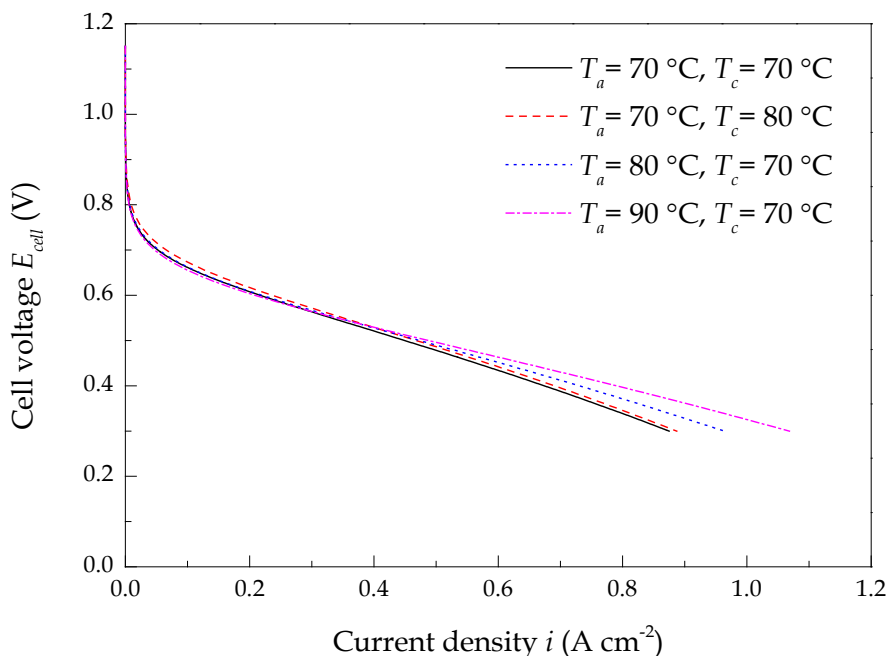


Figure 6-6 Polarisation curves at different anode and cathode temperatures with fully humidified inlet gases

As shown in [Figure 6-4](#), the minimum membrane/ionomer water content is observed on the anode side of the membrane (ionomer in the anode CL). By increasing the anode temperature from 70°C to 90°C, the minimum membrane/ionomer water content increases from 3.9 to 5.8 at the cell voltage of 0.3 V, which results in an increase in the average ionic conductivity of the membrane from  $6.1 \text{ S m}^{-1}$  to  $7.3 \text{ S m}^{-1}$ . The increase in the ionic conductivity of the membrane is the main reason for the improvement of the cell performance at higher current densities. At lower current densities, the ionic conductivities of the membrane are almost the same for different temperatures on anode and cathode, i.e. at 0.8 V, when the cathode temperature is fixed at 70°C, the ionic conductivities of the membrane are  $11.1 \text{ S m}^{-1}$  at the anode temperature of 70°C and  $11.2 \text{ S m}^{-1}$  at the anode temperature of 90°C, respectively. In this situation, the membrane conductivity is not the most important factor in determining the cell performance. The decrease in fuel cell performance at lower current densities can be explained by the decrease in hydrogen mole fraction resulting from the increase in the water carrying capacity (WCC) as the anode temperature increases. As shown in [Figure 6-6](#), only increasing the cathode temperature makes very limited improvement in the current density at lower cell voltage because the average oxygen mole fraction in cathode catalyst layer decreases from 6.6% to 4.3% as the cathode temperature increases from 70°C to 80°C. Even when the ORR rate is increased, the lack of oxygen remains a barrier to improving the performance of the cell. However, the increase in the cathode temperature improves the cell performance at higher cell voltage which can be explained by the increased ORR rate as the cathode temperature increases.

The temperature profiles at two different anode and cathode temperatures are shown in [Figure 6-7](#). In the first condition, the anode and cathode temperatures are set to 70, 80 °C, respectively. In the second condition, the anode and cathode temperatures are set to 80, 70 °C, respectively. It is clear that the temperature profiles of the two conditions are not the same even with the same temperature difference of 10 °C. The heat accumulation is observed at cathode when the higher temperature (80 °C) is applied at the cathode, which is due to the exothermic ORR occurring within the cathode catalyst layer. In this condition, heat transport from the cathode to anode results in an average membrane temperature increase of 9.2 °C. For the other condition, when the lower temperature (70 °C) is applied at the cathode, no heat accumulation occurs at the anode, which is because of the endothermic HOR within the anode catalyst layer as shown in

**Table 6-5.** It is believed that a certain amount of heat is absorbed by the HOR during the transport process from the anode to cathode, which leads to a decrease in temperature within the anode catalyst layer. Therefore, the average increase in temperature of the membrane is 4.9 °C, which is much smaller than that of the first condition.

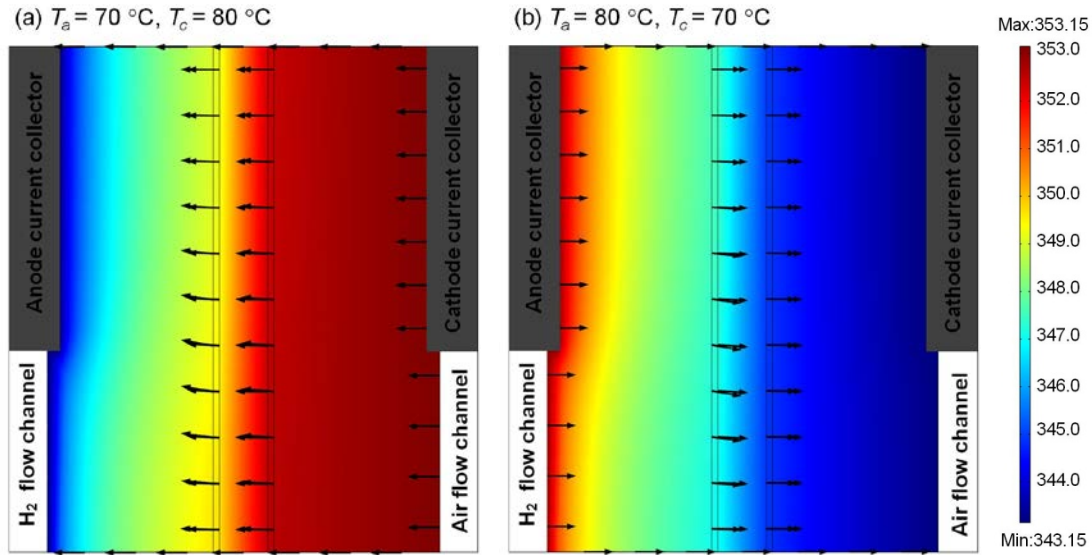


Figure 6-7 Temperature profiles at two conditions: (a)  $T_a = 70 \text{ } ^\circ\text{C}$ ,  $T_c = 80 \text{ } ^\circ\text{C}$ , (b)  $T_a = 80 \text{ } ^\circ\text{C}$ ,  $T_c = 70 \text{ } ^\circ\text{C}$  with fully humidified inlet gases

#### 6.4.2 Increasing the width ratio of the channel/rib

The polarisation curves corresponding with different width ratios of the channel/rib from 0.4 to 0.8 are shown in Figure 6-8. It is clear that the increase in the width ratio of the channel/rib improves the cell performance during the full range of cell voltages, which can be explained by the increase in the reaction area of the oxygen with the cathode catalyst layer and the increase in the amount of water at both the anode and cathode.

By increasing the width ratio of the channel/rib from 0.4 to 0.6 and 0.8, the average membrane/ionomer water content increases from 6.1 to 6.4 and 6.7 at 0.3 V, respectively. However, the cell performance is improved slightly when the width ratio of the channel/rib increases from 0.6 to 0.8, which is due to the limitation of the ORR rate. Under this condition, although the oxygen mole fraction within the cathode catalyst layer increases from 6.6% to 8.3% and 9.5%, the average cathode volumetric current density increases from 450.74 to 494.84 and 506.44 A cm<sup>-3</sup> as the width ratio of the channel/rib increases from 0.4 to 0.6 and 0.8, respectively. It is clear that the

increase in the cathode volumetric current density varies slightly as the width ratio of the channel/rib increases from 0.6 to 0.8. Consequently, it is believed that the sluggish ORR at the cathode is the main obstacle to the improvement of the cell performance. The temperature profiles of two different width ratios of channel/rib at 0.3 V are shown in Figure 6-9. By comparing with Figure 6-2, it is clear that the temperature gradient from the region under the channel to that under the land is reduced by increasing the width ratio of channel/rib, which is beneficial to preventing hot spots within the cathode catalyst layer and membrane.

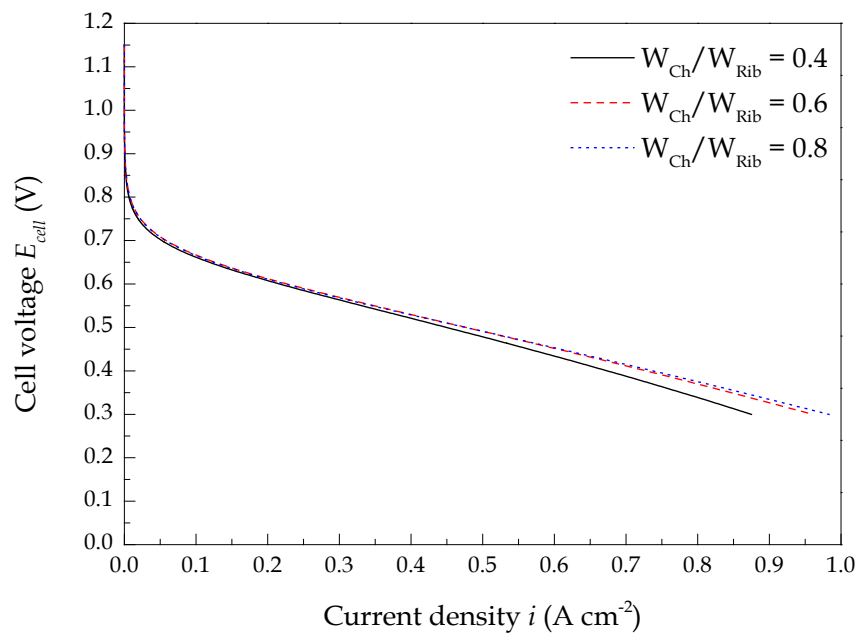


Figure 6-8 Polarisation curves with different width ratios of channel/rib and fully humidified inlet gases

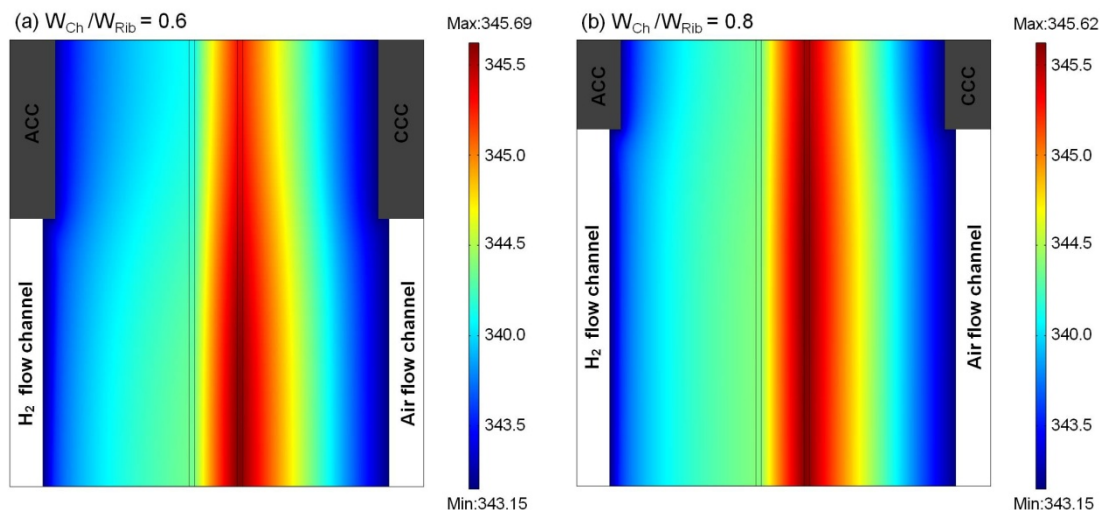


Figure 6-9 Temperature profiles with two different width ratios of channel/rib and fully humidified inlet gases

## 6.5 Conclusions

A two-dimensional, across-the-channel, steady-state model for a proton exchange membrane fuel cell is developed in which the non-isothermal model for temperature distribution, the two-phase flow model for liquid water saturation and the agglomerate model for oxygen reduction reaction are fully coupled. Several insights given by the modelling results are as follows:

1. At a fixed current density, the increase in operating temperature increases the membrane/ionomer water content and reduces the liquid water saturation which improves the cell performance.
2. At a fixed current density of  $0.7 \text{ A cm}^{-2}$ , the amount of water and heat generated by the ORR correspond to at least 94% of the total amount of water phase transfer and 67% of the total heat, respectively.
3. In accounting for the factors influencing water transport through the membrane, the hydraulic permeation can be neglected as it is three orders of magnitude less than the EOD and back diffusion.
4. Applying higher temperatures on the anode increases the water carrying capacity (WCC) of the anode gas which improves the cell performance at higher current densities.
5. Applying higher temperatures on the cathode increases the ORR kinetics, thus improving the cell performance at lower current density. However, higher temperatures on the cathode also decrease the oxygen mole fraction when the cathode gases are fed at fully humidity which probably leads to an oxygen starvation that then limits the cell performance.
6. Heat accumulates within the cathode catalyst layer on the region under the channel. Applying higher temperatures on the anode and lower temperatures on the cathode optimises the temperature distribution within the fuel cell.
7. Enlarging the width ratio of channel/rib improves the cell performance. However, the improvement is limited by the sluggish ORR.

## 6.6 References

1. Wang, Y., K.S. Chen, J. Mishler, S.C. Cho and X.C. Adroher, *A review of polymer electrolyte membrane fuel cells: Technology, applications and needs on fundamental research*. Applied Energy, 2011. **88**: p. 981-1007.
2. Weber, A.Z., S. Balasubramanian and P.K. Das. *Proton Exchange Membrane Fuel Cells*. in K. Sundmacher (editor), *Advances in Chemical Engineering Fuel Cell Engineering*, USA: Elsevier Inc; 2012. p. 66-143.
3. Nguyen, T.V. and R.E. White, *A Water and Heat Management Model for Proton-Exchange-Membrane fuel cells*. Journal of Electrochemistry Society, 1993. **140**: p. 2178-2186.
4. Fuller, T.F. and J. Newman, *Water and Thermal Management in Solid-Polymer-Electrolyte Fuel Cells*. Journal of Electrochemistry Society, 1993. **140**: p. 1218-1225.
5. Yi, J.S. and T.V. Nguyen, *An Along-the-Channel Model for Proton Exchange Membrane Fuel Cells*. Journal of Electrochemistry Society, 1998. **145**: p. 1149-1159.
6. Djilali, N. and D. Lu, *Influence of heat transfer on gas and water transport*. Internation Journal of Thermal Science, 2002. **41**: p. 29-40.
7. Ju, H., H. Meng, C.Y. Wang, *A single-phase, non-isothermal model for PEM fuel cells*. International Journal of Heat and Mass Transfer, 2005. **48**: p. 1303-1315.
8. Wang, Y. and C.Y. Wang, *A non-isothermal, Two-Phase Model for Polymer Electrolyte Fuel Cells*. Journal of Electrochemistry Society, 2006. **153**: p. A1193-A1200.
9. Weber, A.Z. and J. Newman, *Coupled Thermal and Water Management in Polymer Electrolyte Fuel Cells*. Journal of Electrochemistry Society, 2006. **153**: p. A2205-A2214.
10. Sun, W., B.A. Peppley and K. Karan, *An improved two-dimensional agglomerate cathode model to study the influence of catalyst layer structural parameters*. Electrochimica Acta, 2005. **50**: p. 3359-3374.
11. Kamarajugadda, S. and S. Mazumder, *Numerical investigation of the effect of cathode catalyst layer structure and composition on polymer electrolyte membrane fuel cell performance*. Journal of Power Sources, 2008. **183**: p. 629-642.

12. Khajeh-Hosseini-Dalasm, N., M. Fesanghary, K. Fushinobu and K. Okazaki, *A study of the agglomerate catalyst layer for the cathode side of a proton exchange membrane fuel cell: Modeling and optimization.* Electrochimica Acta, 2012. **60**: p. 55-65.
13. Khajeh-Hosseini-Dalasm, N., K. Fushinobu and K. Okazaki, *Phase change in the cathode side of a proton exchange membrane fuel cell.* Journal of Power Sources. 2010. **195**: p. 7003-7010.
14. Ge, S., X. Li, B. Yi, I.M. Hsing, *Absorption, Desorption, and Transport of Water in Polymer Electrolyte Membranes for Fuel Cells.* Journal of Electrochemistry Society, 2005. **152**: A1149-A1157.
15. Shah, A.A., G.S. Kim, P.C. Sui, and D. Harvey, *Transient non-isothermal model of a polymer electrolyte fuel cell.* Journal of Power Sources, 2007. **163**: p.793-806.
16. Wu, H., P. Berg and X. Li, *Modeling of PEMFC Transients with Finite-Rate Phase-Transfer Processes.* Journal of Electrochemistry Society, 2010. **157**: p. B1-B12.
17. Yang, X.G., Q. Ye and P. Cheng, *Matching of water and temperature fields in proton exchange membrane fuel cells with non-uniform distributions.* International Journal of Hydrogen Energy, 2011. **36**: p. 12524-12537.
18. Jung, C.Y., H.S. Shim, S.M. Koo, S.H. Lee, and S.C. Yi, *Investigations of the temperature distribution in proton exchange membrane fuel cells.* Applied Energy, 2012. **93**: p. 733-741.
19. Owejan, J.P., J.J. Gagliardo, J.M. Sergi, S.G. Kandlikar and T.A. Trabold, *Water management studies in PEM fuel cells, Part I: Fuel cell design and in situ water distributions.* International Journal of Hydrogen Energy, 2009. **34**: 3436-3444.
20. Wang, Y. and K.S. Chen, *Through-Plane Water Distribution in a Polymer Electrolyte Fuel Cell: Comparison of Numerical Prediction with Neutron Radiography Data.* Journal of Electrochemistry Society, 2010. **157**: p. B1878-B1886.
21. Wu, H., P. Berg and X. Li, *Steady and unsteady 3D non-isothermal modelling of PEM fuel cells with the effect of non-equilibrium phase transfer.* Applied Energy, 2010. **87**: 2778-2784.

22. Buchi, F.N. and G.G. Scherer, *Investigation of the transversal water profile in Nafion membranes in polymer electrolyte fuel cells*. Journal of Electrochemistry Society, 2001. **148**: p. A183-A188.
23. Yan, Q., H. Toghiani and H. Causey, *Steady-state and dynamic performance of proton exchange membrane fuel cells (PEMFCs) under various operating conditions and load changes*. Journal of Power Sources, 2006. **161**: p. 492-502.
24. Ahmed, D.H. and H.J. Sung, *Effects of channel geometrical configuration and shoulder width on PEMFC performance at high current density*. Journal of Power Sources, 2006. **162**: p. 327-339.
25. Ahmed, D.H. and H.J. Sung, *Design of a deflected membrane electrode assembly for PEMFCs*. International Journal of Heat and Mass Transfer, 2008. **51**: p. 5443-5453.
26. Wang, X.D., G. Lu, Y.Y. Duan and D.J. Lee, *Numerical analysis on performance of polymer electrolyte membrane fuel cells with various cathode flow channel geometries*. International Journal of Hydrogen Energy, 2012. **37**: p. 15778-15786.
27. Lampinen, M.J. and M. Fomino, *Analysis of Free Energy and Entropy Change for Half-Cell Reactions*. Journal of Electrochemistry Society, 1993. **140**: p. 3537-3546.
28. R.C. Reid, J.M. Prausnitz, B.E. Poling BE, *The properties of gases and liquids*, 4th ed., McGraw-Hill, New York, 1987.
29. Sousa, T., M. Mamlouk and K. Scott, *A Non-isothermal Model of a Laboratory Intermediate Temperature Fuel Cell Using PBI Doped Phosphoric Acid Membrane*. Fuel Cells, 2010. **10**: p. 993-1012.

## Chapter 7. Anode partial flooding model

This chapter describes a two-phase flow, along-the-channel, two-dimensional, steady-state and non-isothermal model by considering liquid water formation and transport at the anode during PEMFCs operation. Based on the anode partial flooding model developed, the properties of gas diffusion layer and channel geometries are numerically studied and optimised. The interactive effects of operation conditions, including relative humidity, stoichiometric flow ratio and channel length are numerically investigated. Optimal operating conditions at various current densities are suggested and novel channel design is proposed to mitigate the mass transport resistance initiated by liquid water flooding.

### 7.1 Introduction

Water is unavoidable in PEMFCs due to the oxygen reduction reaction (ORR) at the cathode and the use of humidified reactant gases at both cathode and anode. An adequate amount of water is essential to a successful fuel cell operation, because a hydrated membrane and ionomer in the catalyst layers is required to maintain high conductivity. However, excess water may cause flooding inside the porous electrode and channel, resulting in a pronounced decrease in mass transport rate and thus reduction in the overall fuel cell performance.

Water transport through the membrane, in terms of three mechanisms: electroosmotic drag (EOD), back diffusion and hydraulic permeation, determines the membrane/ionomer water content, which then significantly affects the membrane/ionomer conductivity. The liquid water formed in the porous electrode is mainly attributed to membrane/ionomer desorption (the membrane/ionomer water content reaches equilibrium) and water vapour condensation (partial pressure of water vapour exceeds the saturation pressure). At the anode side, hydrogen consumption could result in the humidified anode reactant gas becoming supersaturated with water vapour, which transfers to liquid water by condensation. Experimental studies have detected liquid water in the anode; more liquid water was observed at a high anode relative humidity [1]. However, anode flooding has not been considered in the majority of previous modelling research.

The amount of liquid water in the porous electrode is a consequence of the interaction

between many parameters, such as contact angle, electrode porosity and microstructure, flow patterns, flow field design, and operating conditions. Intensive experimental studies have been focused on novel gas diffusion layer (GDL) and catalyst layer (CL) materials [2, 3], optimal PTFE content [4, 5] and optimised operating conditions [6, 7]. For a CL with a fixed thickness, the increase in platinum loading and Pt/C ratio could increase the CL porosity and the electrochemical active surface area (ECSA). The increased CL porosity facilitates gas transport and increases the CL ability to remove water due to the increased capillary diffusion coefficient [8 -10]. In the meanwhile, the increased ECSA accelerates formation of liquid water due to the faster ORR process. The role of the GDL is to facilitate the transport of reactant and product gases, liquid water and heat between the channel and CL. Reactant gases can be uniformly dispersed when diffusing through GDL before reaching catalyst sites, which can then avoid local hot spots at electrodes near the inlet, created by the non-uniform distributed reactant concentration along its flow direction. A certain thickness of GDL is required for well dispersed reactant gases but it is at the expense of higher diffusion resistance, which could limit the fuel cell performance at high current densities. For liquid water transport through the GDL, the use of higher amount of hydrophobic materials could lead to the lower level of flooding [11]. Application of micro-porous layers (MPL) has been an effective approach to mitigate liquid water flooding in the porous electrodes in many commercial cells. Cho and Mench [12] directly visualised the liquid water profiles within a cell using hydrogen-deuterium contrast neutron radiography (NR), the MPL has proved to mitigate flooding in the cathode side through enhanced transport of water to the anode side. Despite many advanced understandings made by the studies, a complete investigation is still required to fully understand the role of all the factors that affect the anode performance and flooding. For example, up to now, the GDL thickness on temperature rise and strategies to mitigate flooding using novel flow field designs are still not well investigated in the literature.

The operating conditions interactively affect the water balance in the fuel cell and ultimately the cell performance [13]. During PEM fuel cells operation, temperature, pressure, stoichiometric flow ratio and humidification condition are the most common parameters that can affect performance and thus need to be carefully considered when applying specific membrane electrode assembly (MEA) and flow field design.

Without considering the durability of fuel cell component materials, higher operating temperature is desirable due to the positive impact of temperature on various transport, kinetic and phase-transfer processes [14, 15]. However, high temperature condition is a significant challenge for practical fuel cells as it can lead to the mechanical and chemical failure of Nafion® membrane [16]. In addition, the increased water carrying capacity (WCC) of gas at high operating temperature may lead to reactant gas starvation, especially in the case of fully humidified inlet gas at the cathode [17].

High operating pressure is capable of increasing the fuel cell open circuit potential (Nernst equation), exchange current density and gas-pair diffusivity due to the increased partial pressure of the reactant gases at both the anode and cathode [18, 19]. Therefore, improved fuel cell performance is normally achieved when operating at higher pressure, especially at higher cathode pressure [20]. High cell performance is obtainable at high operating pressures but the net system efficiency may be lower on account of the power needed for air compression. Moreover, high back pressure is a challenge of the mechanical strength and safety issues of fuel cell unit.

To facilitate the transportation of gases to the reactive sites within fuel cells, it may be plausible to operate the cell under less wet conditions to avoid liquid water flooding. On the other hand, it is desirable to maintain certain level of wet condition to ensure high membrane/ionomer proton conductivity. One way to mitigate the dilemma is by controlling the access of external water to the cell through the control of relative humidity (RH) of the inlet reactant flow. The effects of RH on reaction kinetics [21, 22], catalyst utilisation [23], water accumulation [24], and membrane and ionomer swelling [25, 26] have been intensively studied. These studies indicated that the decrease in RH depresses the electrode kinetics but mitigates the degree of flooding of the Nafion® based fuel cells. An optimal RH needs to be found, in order to maximise the fuel cell performance under steady-state load condition. RH also significantly affects the electrode degradations. Specifically, Pt particle growth [27], effective Pt surface area loss [28], carbon corrosion rate [29], are generally accelerated under increased RH. On the contrary, the effect of humidification conditions on membrane degradation is complex. Increasing RH can increase the membrane gas crossover, which then accelerates electrode degradation due to partial fuel starvation [30, 31]. However, inadequate moisture membrane content at low RH also results in detrimental impacts on membrane degradation [32]. Thus, an optimal RH is required to prolong the dynamic lifetime of fuel cells.

Generally, relative high stoichiometric flow ratio is required to avoid reactant gas dilution/starvation and to guarantee the uniform distribution of the reactant gas at the GDL-channel boundary along-the-channel. Low cathode stoichiometric flow ratio may lead to oxygen starvation on the reaction zone, resulting in the cell voltage undershoot during load change which accelerates the electrode degradation [33]. Higher cathode stoichiometric flow ratio is also of benefit to improving the liquid water removal rate inside the channel [34]. The cell performance is therefore improved due to the increased volume fraction of reactant gas and reduced mass transport resistance.

Due to the water transport through the membrane under the combinational force of electro-osmotic drag (EOD), back diffusion and hydraulic permeation, the optimal RH at anode and cathode inlets were not identical. Such optimal anode and cathode RH have been rarely studied in most of available literatures. In the majority of previous work, liquid water formation and the two-phase flow process at the anode were omitted. In addition, the interactive impact of RH, stoichiometric flow ratio and channel length on liquid water and heat removal through the porous electrode have not been clearly investigated.

## 7.2 Model description

### 7.2.1 Computational domain and assumption

Based on the sketch of PEMFC unit developed in Figure 4-1 in Chapter 4, the 2D computational domain and mesh of PEM fuel cell in this chapter is shown in Figure 7-1, which includes channels, gas diffusion layers (GDLs), anode catalyst layer (ACL), cathode catalyst layer (CCL) and membrane. The geometric and structural parameters as well as material properties are listed in Table 7-1. The following assumptions were adopted:

- (1). Feed gases at both the anode and cathode were treated as ideal gases and the gas flow in the channels is laminar flow.
- (2). Water absorbed in the membrane/ionomer was in the dissolved phase, which enters the ionomer from the vapour phase during water uptake and leave the ionomer in the liquid phase when the water content reaches complete saturation.
- (3). The product water in CCL due to oxygen reduction reaction (ORR) is in dissolved phase.

- (4). Liquid water can exist in both the anode and cathode, including CLs, GDLs and channels.
- (5). Nafion® membrane is only permeable to proton and dissolved water.
- (6). Catalyst layers of both the anode and cathode are modelled using agglomerate model.
- (7). Ionomer swelling due to water uptake is taken into account.
- (8). Counter flow mode is applied.

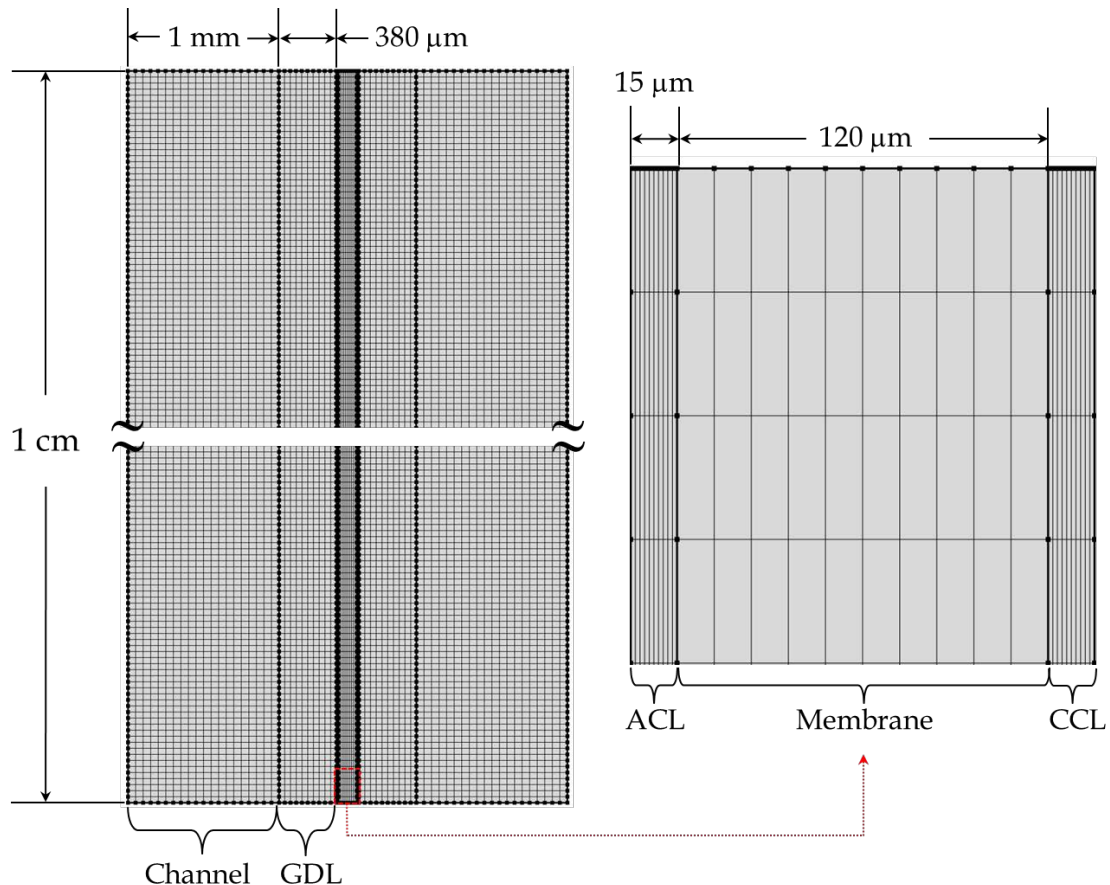


Figure 7-1 Computational domain and mesh of the studied PEM fuel cell

### 7.2.2 Governing equations

By taking all assumptions above into consideration, the governing equations for selected computational domains in this chapter can be specified by combining [Table 4-2](#), [Table 5-1](#) and [Table 6-1](#) in previous chapters, which can be summarized as follow:

First of all, a general convection-diffusion equation was given to describe the conservation of mass, momentum, species, charge and energy at a steady-state.

$$\nabla \cdot (\rho \mathbf{u}^s \phi) = \nabla \cdot (\Gamma_\phi \nabla \phi) + S_\phi \quad (7-1)$$

where  $\phi$  is the general variable to be solved,  $\tilde{\rho}$  is the nominal density,  $\mathbf{u}^g$  is the average velocity of gas,  $\Gamma_\phi$  is the generalized diffusion coefficient of  $\phi$ . The expressions of  $\phi$ ,  $\tilde{\rho}$  and  $\Gamma_\phi$  for different equations were listed in [Table 7-2](#).  $S_\phi$  is the source term of  $\phi$  in different modelling domain, which was given in detail in [Tables 7-3](#) to [Table 7-5](#).

Table 7-1 Structural parameters and material properties of the PEM fuel cells

Parameters	Symbol	Unit	Value	Reference
<b>Gas diffusion layer (GDL)</b>				
Thickness	$\delta_{GDL}$	$\mu\text{m}$	380	[11, 23, 24]
Porosity	$\varepsilon_{GDL}$		0.4	[11, 23, 24]
Conductivity	$\sigma_{GDL}$	$\text{S m}^{-1}$	1250	[11, 23, 24]
Permeability	$k_{p,GDL}$	$\text{m}^2$	$4.97 \times 10^{-3}$	[11, 23, 24]
<b>Catalyst layer (CL)</b>				
Thickness	$\delta_{CL}$	$\mu\text{m}$	15	[11, 23, 24]
Permeability	$k_{p,CL}$	$\text{m}^2$	$4.97 \times 10^{-3} \varepsilon_{CL} / \varepsilon_{GDL}^{1.5}$	[11, 14, 23, 24]
Platinum density	$\rho_{Pt}$	$\text{kg m}^{-3}$	$2.145 \times 10^4$	[11, 45]
Carbon density	$\rho_C$	$\text{kg m}^{-3}$	$1.8 \times 10^3$	[11, 45]
<b>Membrane and ionomer</b>				
Thickness	$\delta_M$	$\mu\text{m}$	120	[14, 46]
Dry membrane density	$\rho_M$	$\text{kg m}^{-3}$	$2.0 \times 10^3$	[14, 46, 47]
Ionomer equivalent weight	$EW$	$\text{g mol}^{-1}$	$1.1 \times 10^3$	[14, 46, 47]
Permeability	$k_{p,M}$	$\text{m}^2$	$1.8 \times 10^{-18}$	[11, 14, 23, 24]
<b>Channel</b>				
Depth	$\delta_{Ch}$	$\text{mm}$	1.0	Assume
Length	$L$	$\text{cm}$	1.0	Assume

Table 7-2 Specific expressions in the general convection-diffusion equation

Computational domain	Mass	Momentum	Species	Energy	Charges
Computational domain	Channels, GDLs and CLs			All domains	CLs and membrane
$\phi$	1	$\mathbf{u}^g$	$x_i$	$T$	$\varphi_s, \varphi_M$
$\tilde{\rho}$	$\rho^g$	$\rho^g / \varepsilon^2$	$\rho^g$	$\rho^g$	0
$\Gamma_\phi$	0	$\mu^g / \varepsilon$	$\rho^g D_i^{eff}$	$k^{eff} / c_p^{eff}$	$\sigma_s, \sigma_M$

Table 7-3 Conservation of water in different phases and heat within different computational domain

	Channels	GDLs	CLs
Water vapour $S_w^v$	$-S_w^{vl}$	$-S_w^{vl}$	$-S_w^{vd} - S_w^{vl}$
Liquid water $S_w^l$	$S_w^{vl}$	$S_w^{vl}$	$S_w^{dl} + S_w^{vl}$
Dissolved water $S_w^d$	0	0	$S_w^{r,i} + S_w^{vd} - S_w^{dl}$

Note: superscript  $i$  represents the anode or cathode, the unit for each water source term is  $(\text{mol m}^{-3} \text{ s}^{-1})$ .

Table 7-4 Conservation of heat

Membrane	CLs	GDLs	Channels
$S_T^M$	$S_T^{dl} + S_T^{vl} + S_T^{vd} + S_T^{r,i} + S_T^{s,i} + S_T^M$	$S_T^{vl} + S_T^{s,i}$	$S_T^{vl}$

Note: superscript  $i$  represents the anode or cathode, the unit for each heat source is  $(\text{W m}^{-3})$ .

Note that Eq. (7-1) is applied on reactant gas only and the gas velocity in porous electrodes could be related to pressure according to Darcy's law, which can be found in Chapter 3. For the purpose of describing dissolved and liquid water transport, Eq. 3-71 and Eq. 3-94 in Chapter 3 are used. Note that liquid water can be existed at the anode because hydrogen consumption at the anode may lead to the humidified anode gas becoming supersaturated with water vapour, which can transfer to liquid water after condensation. The membrane/ionomer water content is proposed as a function of water activity as shown in Eq. 3-79. The equilibrium membrane/ionomer water content, determined based on water uptake measurement, was given in Eq. 3-78. Similar to the liquid water transport in porous electrode described using capillary theory, same equation is used to simulate the liquid water transport in gas channels, for both the anode and cathode, respectively. The permeability of gas channels in Eq. 3-95 is calculated by Hagen-Poiseuille equation [35].

$$k_{p,ch} = \frac{c_{sf} d_h^2}{32} \quad (7-2)$$

where  $c_{sf}$  is the flow shape factor (1.127 for a square cross-section) and  $d_h$  is the hydraulic diameter of a channel, which can be calculated by the relation of the cross-sectional area and wetted perimeter.

In the conservation equation of charge, the electrochemical reactions inside the catalyst layers according to agglomerate assumption can be described using Eq. 5-9 and Eq. 5-10 developed in Chapter 5. Note that the agglomerate kinetics are applied for both the hydrogen oxidation reaction at the anode and oxygen reduction reaction at the

cathode, respectively. The properties of the catalyst layer (porosity, specific area, ionomer and water film thickness), gas transport through the porous electrode (species diffusion in gas mixture and Knudsen diffusion), numerous key parameters and fundamental equations can be found in [Chapter 3](#).

In order to study the ratio of the rate of advection by flow to the rate of diffusion driven by gradients with respect to liquid water and heat transport, the dimensionless Peclet number ( $P_e$ ) was used and defined as the following form:

$$P_e \text{ for liquid water: } P_e = \frac{\delta \mathbf{u}_w^l}{D_c} \quad (7-3)$$

$$P_e \text{ for heat: } P_e = \frac{\rho^{eff} c_p^{eff} \mathbf{u}^g}{k^{eff}} \quad (7-4)$$

where  $\delta$  (m) is the thickness of the electrode,  $D_c$  ( $m^2 s^{-1}$ ) is the capillary diffusion coefficient of liquid water,  $\rho^{eff}$  ( $kg m^{-3}$ ),  $c_p^{eff}$  ( $J mol^{-1} K^{-1}$ ) and  $k^{eff}$  ( $W m^{-1} K^{-1}$ ) are the effective density, specific heat capacity and thermal conductivity of the electrode, the detailed expressions were given in [Table 7-6](#).  $\mathbf{u}^g$  ( $m s^{-1}$ ) is the velocity of gas mixture,  $\mathbf{u}_w^l$  ( $m s^{-1}$ ) is the velocity of liquid water, which can be expressed by reorganizing equations in [Chapter 3](#).

$$\mathbf{u}_w^l = D_c \nabla s + \frac{k_r^l k_p}{\mu_w^l} \nabla p \quad (7-5)$$

where  $s$  is the liquid water saturation, defining as the volume fraction of void space occupied by the liquid water,  $k_r^l$  ( $= s^3$ ) is the relative permeability of liquid water,  $\mu_w^l$  ( $Pa s$ ) is the liquid water viscosity,  $k_p$  ( $m^2$ ) is the permeability of the porous media,  $p$  ( $Pa$ ) is the pressure of gas mixture, which can be obtained by Darcy's equation.

The specific heat capacity and thermal conductivity of the gas mixture were obtained by an empirical equation developed by Wilke [36] as follow:

$$c_p^g = \sum_i x_i c_{p,i}^g, \quad k^g = \sum_i \frac{x_i k_i}{\sum_j x_j \Phi_{ij}} \quad (7-6)$$

Table 7-5 Source terms for mass and heat

Source terms	Unit	Domain
$S_m = M_{H_2}S_{H_2}^g + M_{O_2}S_{O_2}^g + M_wS_w^v$	$\text{kg m}^{-3} \text{s}^{-1}$	GDLs, CLs and channels
$S_{H_2}^g = \frac{i_a}{2F}$	$\text{mol m}^{-3} \text{s}^{-1}$	Anode CL
$S_{O_2}^g = \frac{i_c}{4F}$	$\text{mol m}^{-3} \text{s}^{-1}$	Cathode CL
$S_w^{rc} = \frac{i_c}{2F}$	$\text{mol m}^{-3} \text{s}^{-1}$	Cathode CL
$S_w^{vd} = k_{ads}(c_w^{eq} - c_w^d) \quad c_w^d < c_w^{eq}$	$\text{mol m}^{-3} \text{s}^{-1}$	CLs
$S_w^{dl} = k_{des}(c_w^d - c_w^{eq}) \quad c_w^d \geq c_w^{eq}$	$\text{mol m}^{-3} \text{s}^{-1}$	CLs
$S_T^{sa} = \frac{i_a^2}{\sigma_{GDL,a}^{eff}}$	$\text{W m}^{-3}$	Anode GDL
$S_T^{sc} = \frac{i_c^2}{\sigma_{GDL,c}^{eff}}$	$\text{W m}^{-3}$	Cathode GDL
$S_T^M = \frac{i_M^2}{\sigma_M^{eff}}$	$\text{W m}^{-3}$	Membrane, CLs
$S_T^{ra} = - i_a  \left[ \frac{T \nabla S_a}{2F} \right]$	$\text{W m}^{-3}$	Anode CL
$S_T^{rc} =  i_c  \left[  \eta_c  - \frac{T \nabla S_c}{4F} \right]$	$\text{W m}^{-3}$	Cathode CL
$S_T^{vd} = M_w S_w^{vd} \nabla h_w^{vd}$	$\text{W m}^{-3}$	CLs
$S_T^{dl} = M_w S_w^{dl} \nabla h_w^{dl}$	$\text{W m}^{-3}$	CLs
$S_T^{vl} = M_w S_w^{vl} \nabla h_w^{vl}$	$\text{W m}^{-3}$	CLs, GDLs and channels
$S_w^{vl} = \begin{cases} k_{con} \frac{\varepsilon(1-s)x_w^g}{RT} (x_w^g p^g - p_{sat}) & x_w^g p^g \geq p_{sat} \\ k_{eva} \frac{\varepsilon \rho_w^l}{M_w} (p_{sat} - x_w^g p^g) & x_w^g p^g < p_{sat} \end{cases}$	$\text{mol m}^{-3} \text{s}^{-1}$	CLs, GDLs and channels

Table 7-6 Effective specific heat capacity and thermal conductivity of GDL, CL and channel

	GDLs	CLs	Channels	Membrane
$c_p^{eff}$	$\varepsilon_{GDL} c_{p,C} + s \varepsilon_{GDL} c_{p,w}^l + (1-s) \varepsilon_{GDL} c_p^g$ $+ s \varepsilon_{CL} c_{p,w}^l + (1-s) \varepsilon_{CL} c_p^g$	$L_{p_t} c_{p,p_t} + (L_C + L_S) c_{p,C} + L_M c_{p,M}$ $+ s \varepsilon_{CL} c_{p,w}^l + (1-s) \varepsilon_{CL} c_p^g$	$s c_{p,w}^l + (1-s) c_p^g$	$c_{p,M}$
$k^{eff}$	$\varepsilon_{GDL} k_C + s \varepsilon_{GDL} k_w^l + (1-s) \varepsilon_{GDL} k^g$	$L_{p_t} k_{p_t} + (L_C + L_S) k_C + L_M k_M$ $+ s \varepsilon_{CL} k_w^l + (1-s) \varepsilon_{CL} k^g$	$s k_w^l + (1-s) k^g$	$k_M$

### 7.2.3 Boundary conditions

At the inlets of anode and cathode, the temperature, mole fractions of reactant gases in gas mixture, and liquid water saturation were given as below:

$$T = T_a^0, x_{w,a}^0 = \frac{p_{sat} R H_a}{p_a}, \quad x_{H_2}^0 = 1 - x_{w,a}^0, \quad s_a = 0 \quad (7-7)$$

$$T = T_c^0, x_{w,c}^0 = \frac{p_{sat} R H_c}{p_c}, \quad x_{O_2}^0 = 0.21(1 - x_{w,c}^0), \quad x_{N_2}^0 = 0.79(1 - x_{w,c}^0), \quad s_c = 0 \quad (7-8)$$

The gas velocities at the inlets of both electrodes were related to their stoichiometric flow ratios shown as follows:

$$\mathbf{u}_a^{g,0} = \frac{\xi_a R T i^{ref} A_M}{2 F p_a x_{H_2} A_{ch}}, \quad \mathbf{u}_c^{g,0} = \frac{\xi_c R T i^{ref} A_M}{4 F p_c x_{O_2} A_{ch}} \quad (7-9)$$

where  $i^{ref}$  is the reference current density (defined as 1.0 A cm<sup>-2</sup> here),  $\xi_a$  and  $\xi_c$  are the stoichiometry of the anode and cathode, respectively.  $A_M$  (m<sup>2</sup>) and  $A_{ch}$ (m<sup>2</sup>) are the effective area of electrode and the cross-sectional area of channel, respectively.

At the outlets of both the anode and cathode, the pressure is given as a boundary condition.

$$p_a = p_a^0, \quad p_c = p_c^0 \quad (7-10)$$

The water content on the CL-membrane interfaces of anode and cathode were defined as Dirichlet boundaries with the values according to Eq. 3-79, in which the water activity can be expressed as [22, 23]:

$$\alpha_w = x_w \frac{p}{p_{sat}} + 2s \quad (7-11)$$

#### 7.2.4 Numerical solution

The numerical solution of the fully coupled governing equations is based on the finite element method (FEM). First of all, a mesh is developed over the computational domain by dividing it into numerous elements. The distance between each element is known as the step. At each step, the equations accounting for different phenomena are fully coupled and computed with the boundary conditions following the schematic as shown in Figure 7-2. Initial value is given to each parameter at the first attempt then followed by an iterative process until the calculation error is smaller than 10<sup>-5</sup>.

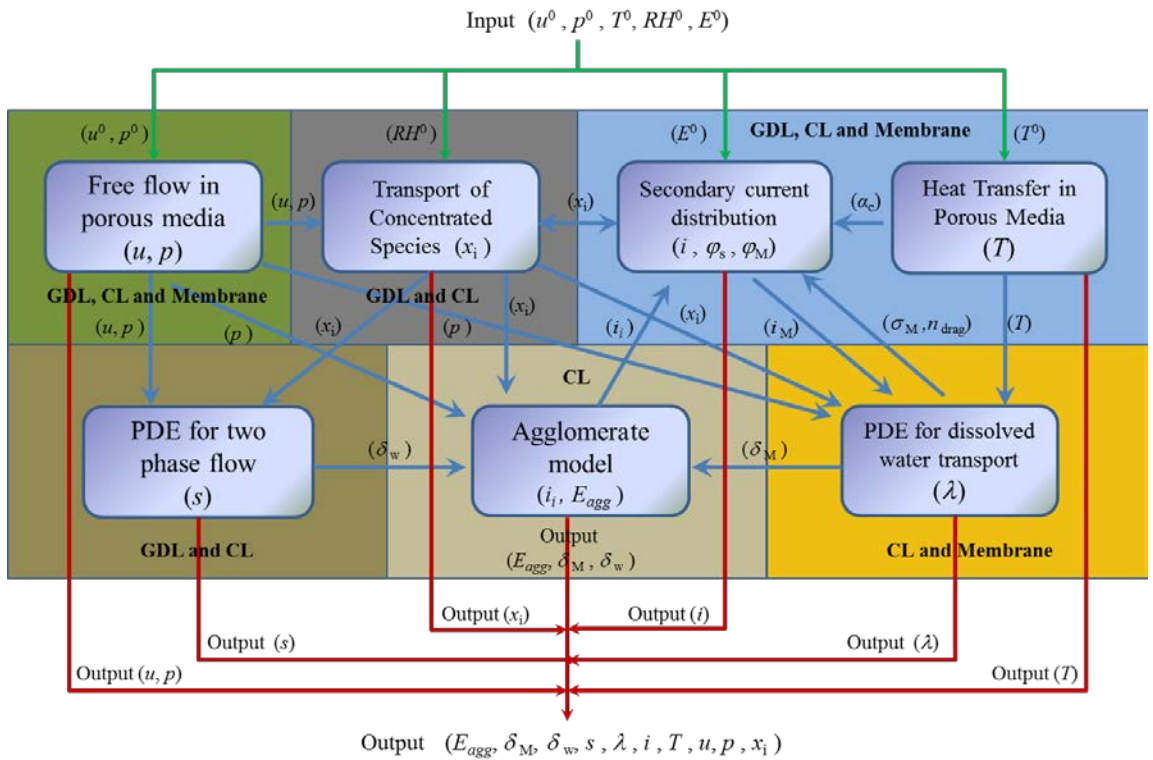


Figure 7-2 Schematic of the computational process

(Green lines - parameters input; blue lines - model interaction; red lines - model output)

### 7.3 Model verification and validation

#### 7.3.1 Mesh independence

The computation error in the solution related to the mesh grid disappears for an increasingly fine mesh. Considering that the impact of mesh characters on the modelling results is increased at high current density, a suitable mesh grid for the model is found by comparing the limiting current densities (predicted at the cell voltage of 0.05 V) at various mesh grids. Nine groups of mesh grids as shown in Table 7-7 are evaluated. Note that the number of elements is fixed at 300 along-the-channel length and vary along the depth/thickness of different domains, including channels, GDLs, CLs and membrane. Three levels of element number on each domain are investigated and the increase in total number of elements of  $1.2 \times 10^4$  is guaranteed of each modelling process. The current density at 0.05V as shown in Table 7-7 reaches an asymptotic value as the consequence of the increased number of the mesh elements. Using any mesh finer than Grid 6 results in a constant current density but increases computational duration. To balance both the computational accuracy and the duration, Grid 6 is selected considering a sufficient reliability to ensure mesh independence with acceptable computing time.

Table 7-7 Predicted current densities and computing time with various mesh characters

Channels	GDLs	CLs	Membrane	Total elements	$i$ at 0.05V (A cm <sup>-2</sup> )	Computing time (s)
Grid 1	10	10	10	10	$2.1 \times 10^4$	2.02324
Grid 2	30	10	10	10	$3.3 \times 10^4$	2.02063
Grid 3	50	10	10	10	$4.5 \times 10^4$	2.01766
Grid 4	50	30	10	10	$5.7 \times 10^4$	2.01765
Grid 5	50	50	10	10	$6.9 \times 10^4$	2.01764
Grid 6	50	50	30	10	$8.1 \times 10^4$	2.01652
Grid 7	50	50	50	10	$9.3 \times 10^4$	2.01641
Grid 8	50	50	50	50	$1.05 \times 10^5$	2.01639
Grid 9	50	50	50	90	$1.17 \times 10^5$	2.01639
Note: The number of elements along-the-channel is fixed at 300.						

### 7.3.2 Model validation

The modelling results are validated by the experimental data for two cases, in-house and selected from the work of Wang et al. [18], as shown in Figure 7-3. Details of MEA preparation and fuel cell testing can be found elsewhere [37]. Parameters used for model validation are listed in Table 7-8. For the in-house case, parameters are measured experimentally while for the case of Wang et al. [18] parameters are selected from their paper. Note that the cathode transfer coefficient ( $\alpha_c$ ) is obtained by fitting the experimental polarisation curves in the kinetics control zone (cell voltage higher than 0.8 V).

Figure 7-3 shows a good consistency between the modelling results and the experimental data. The agreement is very good, especially at high cell voltages ( $> 0.5$  V), due to the relatively slow electrochemical reaction and weak impact of mass transport in this region. Due to various losses such as activation loss, Ohmic loss and concentration polarisation loss, the cell voltage typically falls with the increase in current density, which is also captured by the model. The model-predicted cell voltage is almost identical with experimental results in a wide range of current densities up to  $1.0 \text{ A cm}^{-2}$  for the in-house case and  $0.9 \text{ A cm}^{-2}$  for the data taken from Wang et al. [18]. The results in Figure 7-3 clearly demonstrate that our model is able to predict the cell voltage very well in the normal range of operating current densities ( $0\text{-}1.0 \text{ A cm}^{-2}$ ) and also the trend at higher current densities where a more rapid drop in cell voltage is observed with experimental results at higher current densities. The discrepancy between the modelling and experimental cell voltage at very high current densities is small,

especially for the in-house case ( $\sim 10\%$  at  $1.4 \text{ A cm}^{-2}$ ). This small discrepancy is caused by the increased mass transport resistance. At high current densities, more water is formed due to the accelerated electrochemical reaction.

Table 7-8 Parameters used for model validation and base case condition in the study

<i>Symbol</i>	<i>Description (unit)</i>	<i>In-house</i>	<i>Wang et al. [18]</i>	<i>Base case</i>
$\delta_{GDL}$	GDL thickness (m)	$3.0 \times 10^{-4}$	$3.0 \times 10^{-4}$	$3.8 \times 10^{-4}$
$\delta_{CL}$	CL thickness (m)	$1.5 \times 10^{-5}$	$1.29 \times 10^{-5}$	$1.5 \times 10^{-5}$
$\delta_M$	Membrane thickness (m)	$5.5 \times 10^{-5}$	$1.08 \times 10^{-4}$	$1.2 \times 10^{-4}$
$\delta_{Ch}$	Flow channel depth (m)	$1.0 \times 10^{-3}$	$1.0 \times 10^{-3}$	$1.0 \times 10^{-3}$
$L$	Channel length (m)	$1.0 \times 10^{-2}$	$7.2 \times 10^{-2}$	$1.0 \times 10^{-2}$
$\varepsilon_{GDL}$	GDL porosity	0.40	0.40	0.40
$m_{Pt}$	Platinum loading ( $\text{mg cm}^{-2}$ )	0.10 (anode) 0.40 (cathode)	0.40	0.40
$f$	Pt/C mass ratio	20%	40%	40%
$L_M$	Volume fraction of ionomer	13.3%	32.5%	40%
$\theta$	Contact angel	$120^\circ$	$120^\circ$	$120^\circ$
$T$	Operating temperature ( $^\circ\text{C}$ )	80.0	70.0	70.0
$p$	Operating pressure (atm)	1.0	1.0	1.0
$RH$	Relative humidity	100%	100%	100%
$\alpha_c$	Cathode transfer coefficient	0.6	2.0	0.7
$r_{agg}$	Agglomerate radius (m)	$1.0 \times 10^{-6}$	$1.0 \times 10^{-6}$	$1.0 \times 10^{-6}$
$\xi_a$	Anode stoichiometric flow ratio	11.8 <sup>a</sup>	1.8 <sup>b</sup>	1.2
$\xi_c$	Cathode stoichiometric flow ratio	12.4 <sup>a</sup>	1.4 <sup>b</sup>	2.0

a: calculated at the volumetric flow ratio of 200 and 500 sccm using Eq. 7-9 for anode and cathode, respectively, at in-house operation conditions; b: calculated at the volumetric flow ratio of 1200 and 2200 sccm using Eq. 7-9 for anode and cathode, respectively, at given operation conditions in Wang et al. [18].

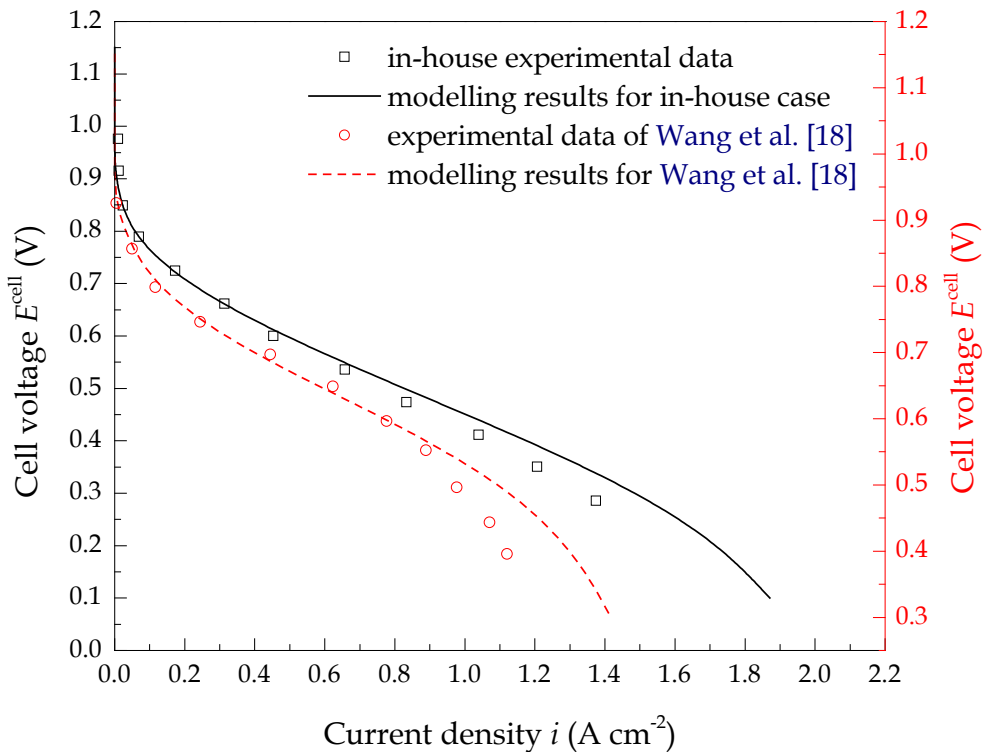


Figure 7-3 Comparison of modelling results with experimental data for two cases

In-house: 80 °C, 20% Pt/C,  $m_{\text{Pt,a}} = 0.1 \text{ mg cm}^{-2}$ ,  $m_{\text{Pt,c}} = 0.4 \text{ mg cm}^{-2}$ , Nafion 112 membrane, effective area: 1.0 cm × 1.0 cm, channel width and depth: 1 mm; Wang et al. [18]: 70 °C, 40% Pt/C,  $m_{\text{Pt,a}} = m_{\text{Pt,c}} = 0.4 \text{ mg cm}^{-2}$ , effective area: 7.2 cm × 7.2 cm, channel width and depth: 1 mm. For both cases: RH = 100%, pressure: 1.0 atm.

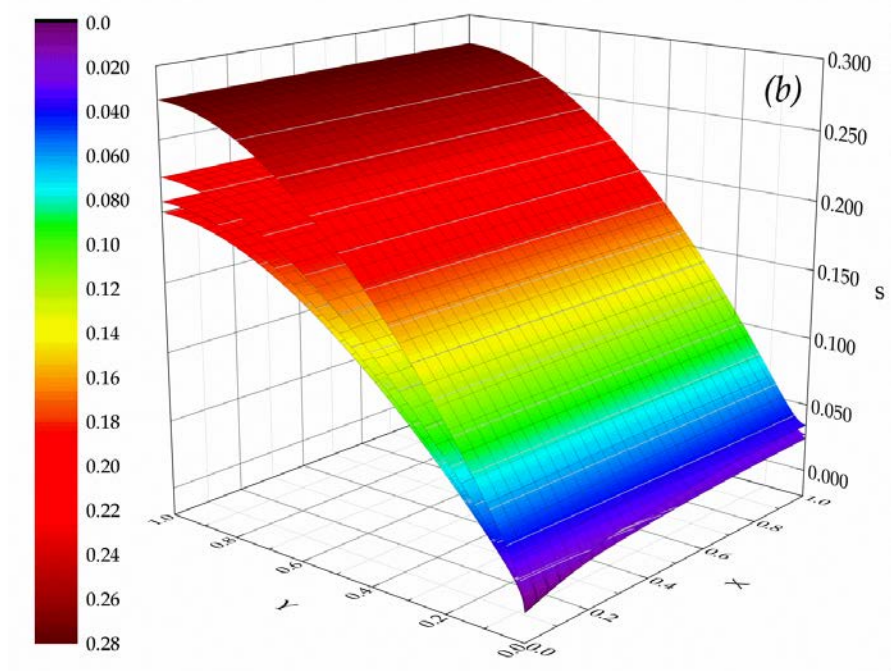
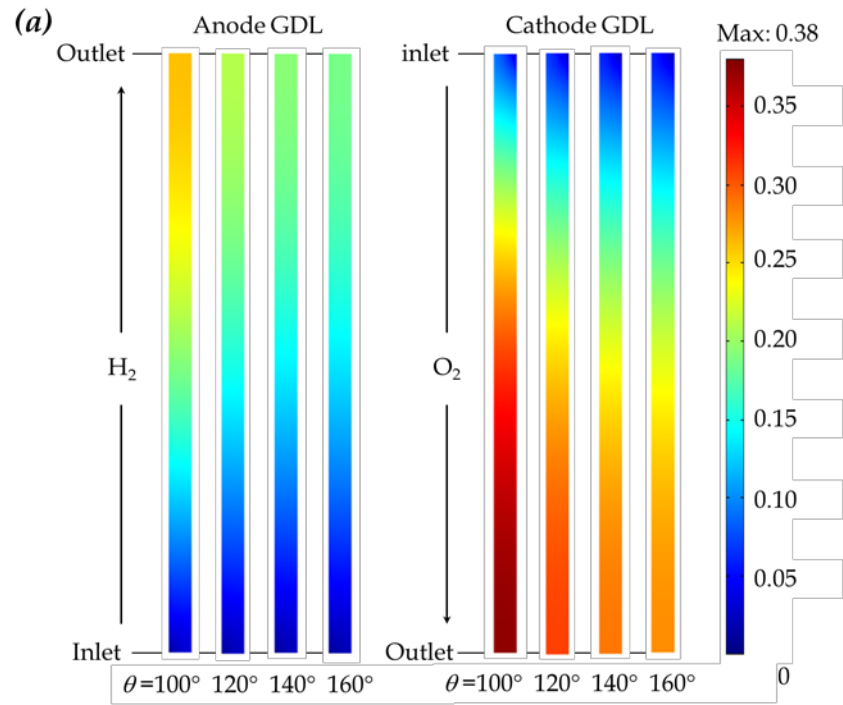
The formation of liquid water within the void space of the electrode may limit the oxygen diffusion, especially near the channel outlets where liquid water is prone to accumulation. As a result, it is expected that the oxygen transport resistance through the porous electrode, which is determined by both the electrode structure and reactant gas provided (e.g. the porosity of the electrode and the mole fraction of oxygen against nitrogen and vapour in the cathode channel), is increased. The 2D model used in this paper does not take into account the heterogeneity of the electrode structure in the third dimension. This leads to an under-estimation of the oxygen transport resistance and therefore an over-estimation of the current densities in comparison with the experimental data. The discrepancy is more apparent for large size cells at high current densities as large size cells have more heterogeneity in the electrode structure. This is a disadvantage of the 2D models, which indicates that future development should pay attention to 3D models.

## 7.4 Results and discussions

### 7.4.1 The effect of contact angle in GDL on liquid water saturation

Liquid water saturation is an indicator of the degree of flooding inside the porous electrodes and channels, which is defined as the volume fraction of void space occupied by liquid water. Liquid water saturation is a dimensionless parameter, which equals to unity when the void space of the porous media is fully filled with water. The effect of contact angle on liquid water saturation in the GDLs of the anode and cathode is shown in [Figure 7-4](#).  $X$  and  $Y$  are the dimensionless through-plane and in-plane directions. Boundaries  $X=0$  is the anode channel-GDL interface in [Figure 7-4\(b\)](#) and cathode GDL-CL interface in [Figure 7-4\(c\)](#),  $X=1$  is the anode GDL-CL interface in [Figure 7-4\(b\)](#) and cathode channel-GDL interface in [Figure 7-4\(c\)](#),  $Y=0$  is the anode gas inlet in [Figure 7-4\(b\)](#) and cathode gas outlet in [Figure 7-4\(c\)](#),  $Y=1$  is the anode gas outlet in [Figure 7-4\(b\)](#) and cathode gas inlet in [Figure 7-4\(c\)](#).

Liquid water on hydrophobic electrode surface exhibits a contact angel larger than  $90^\circ$ . Thus, capillary diffusion coefficient of liquid water through the porous electrode is proportional to the contact angel. It can be seen from [Figure 7-4\(a\)](#) that the liquid water saturations in both the GDLs of the anode and cathode increase as the contact angle decreases. This can be explained by the improved hydrophobic property of the GDL. Due to the fact that the diffusion media are composite structures with hydrophobic and hydrophilic component, the composite contact angle is determined by the volume fractions of the hydrophobic and hydrophilic component. The increase in contact angle means more hydrophobic component is used. This is capable of increasing the capillary diffusion coefficient of the water through the diffusion media. It is shown in both [Figure 7-4\(b\)](#) and [Figure 7-4\(c\)](#) that, more apparent non-uniform distribution of liquid water is observed along the gas flow than that through the electrode thickness, especially near the outlets of both the anode and cathode. Comparing the gradients of liquid water saturations in [Figure 7-4\(b\)](#) and [Figure 7-4\(c\)](#) indicates that liquid water formation in the cathode GDL is more significant. Moreover, the distribution of liquid water in the cathode GDL is more non-uniform, both in-plane and through-plane, in comparison with that in the anode GDL. The porous electrodes are likely filled with liquid water in the over-humidified environment. It is expected that more hydrophobic electrodes would suffer from water starvation and thus a higher mass transport limiting current density occurs.



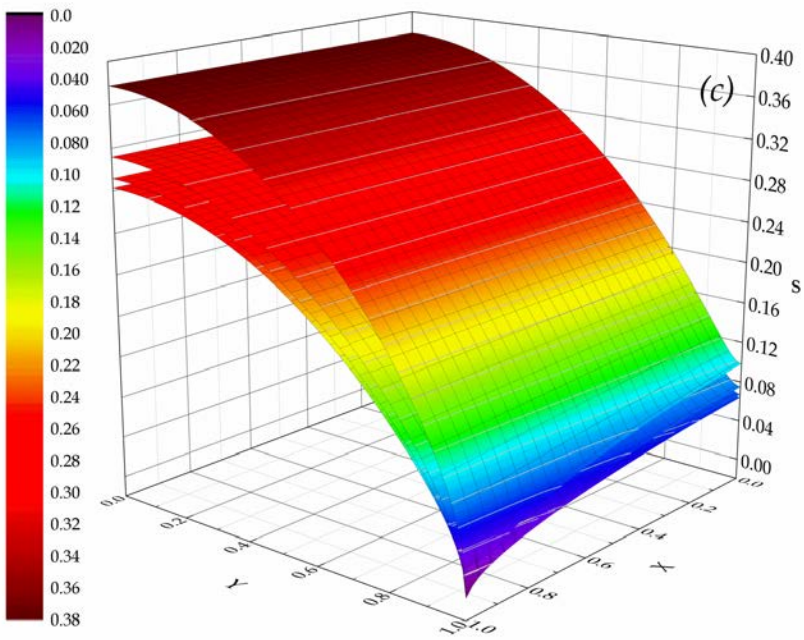


Figure 7-4 Dimensional liquid water saturation in (a) anode and cathode GDLs and dimensionless liquid water saturation in (b) anode GDL and (c) cathode GDL with various contact angles at 0.3 V in base-case condition:  $\theta = 100^\circ, 120^\circ, 140^\circ$  and  $160^\circ$  from up down.

#### 7.4.2 The effect of GDL porosity on liquid water saturation

The liquid water saturation in the GDLs of the anode and cathode with various GDL porosities are shown in Figure 7-5. Coordinate X and Y indicate the same geometry as it was in Figure 7-4. It is shown in both Fig. 7-5(a) and Fig. 7-5(b) that the increase in GDL porosity increases the liquid water saturation inside the GDLs of the anode and cathode. This can be attributed to the increased void space for water vapour condensation when the GDL porosity is increased. At 0.3 V, the increase in GDL porosity from 20% to 80% increases the liquid water sources term ( $S_w^l$ ) (which is a direct indicator of the level of water vapour condensation) from 3.72 to 16.41 ( $\text{mol m}^{-3} \text{s}^{-1}$ ) in the anode GDL and from 27.55 to 46.81 ( $\text{mol m}^{-3} \text{s}^{-1}$ ) in the cathode GDL, respectively, according to the source terms in Table 7-3 and Table 7-4. For the anode GDL at 0.3 V, the average liquid water saturation is 12% and 17% at the porosity of 20% and 80%, respectively. Due to the fact that the liquid water saturation is defined as the volume fraction of void space occupied by liquid water, the volume fraction of the remaining void space without liquid water occupation is 17.6% and 66.4% at the porosity of 20% and 80%, respectively. For the cathode GDL, there are still an average of 16% and 60% of the void space unoccupied by liquid water with GDL porosities of

20% and 80% respectively. The current density predicted at 0.3 V is increased from 0.821 to 1.593 A cm<sup>-2</sup> as the GDL porosity is increased from 20% to 80%.

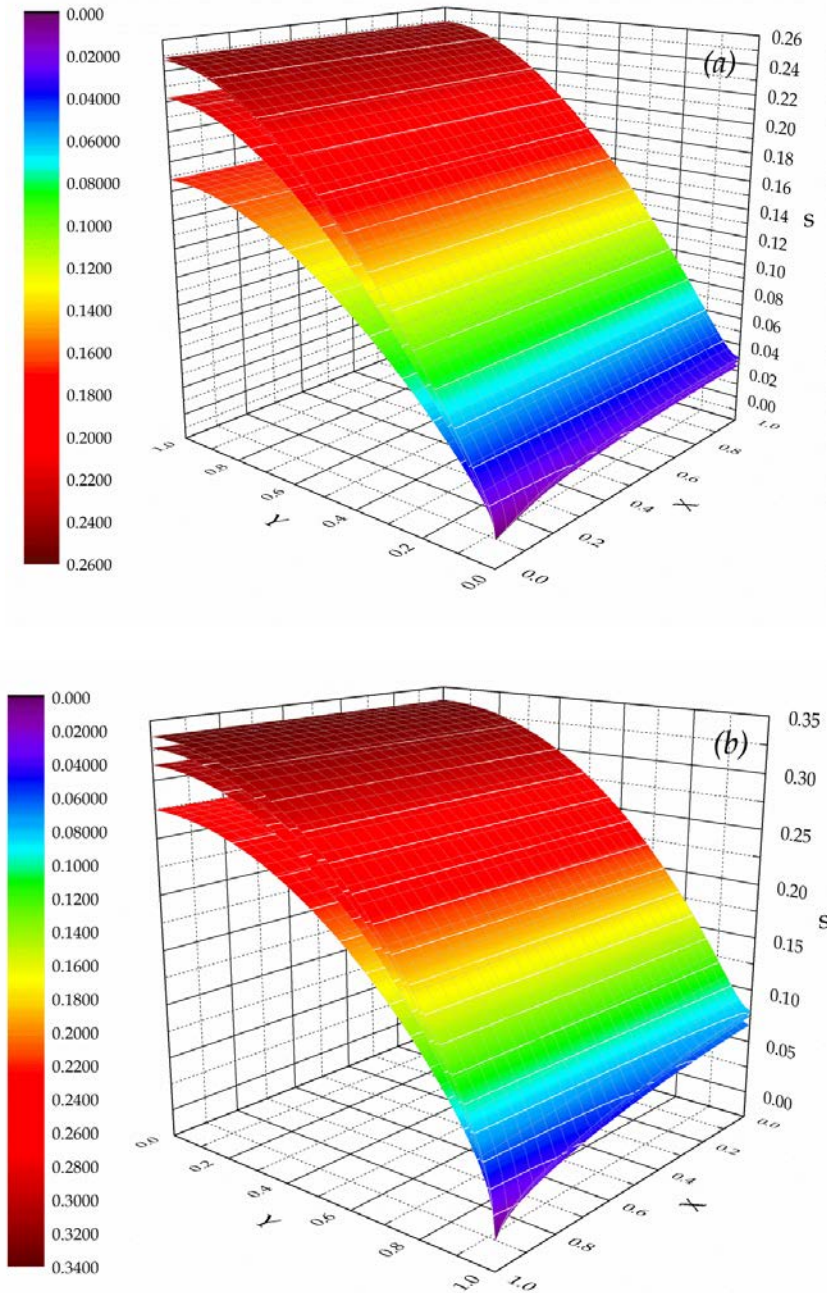


Figure 7-5 Liquid water saturation in (a) anode GDL and (b) cathode GDL with various GDL porosities at 0.3 V in base-case condition:  $\varepsilon_{GDL} = 80\%, 60\%, 40\%$  and  $20\%$  from up down.

It is also clear that the effect of GDL porosity on liquid water saturation is more significant when it increases from 20% to 40%. The further increase of the porosity from 60% to 80% results in a small contribution to the liquid water saturation, in particular at the anode. Fig. 7-5(a) clearly indicates that, with the GDL porosities increased from 60% to 80%, the liquid water saturation levels in the anode GDL remain

almost constant. This can be explained by the fact that the increase in porosity also increases the possibility of liquid water evaporation. The equilibrium between water vapour condensation and liquid water evaporation is achieved at a particular GDL porosity. High GDL porosity is of benefit to the cell performance but it will be a challenge to the mechanical issues of the GDL. The clamping force between the bipolar plates may lead to structure failure of the GDL [38], and carbon corrosion may result in a more significant impact on the performance degradation. Based on the above results, we can conclude that the optimal GDL porosity is 40%.

#### ***7.4.3 The effect of platinum loading on liquid water saturation and CCL effectiveness factor***

Figure 7-6 shows the liquid water saturation in the CCL with various platinum loadings. The effectiveness factor, which accounts for the interaction between diffusion and reactions in porous media and indicates how sufficient the catalyst in the CCL is utilised, is shown in Figure 7-7 with various platinum loadings. In both the figures, boundaries X=0 is the cathode membrane-CL interface, X=1 is the cathode GDL-CL interface, Y=0 is the cathode gas outlet and Y=1 is the cathode gas inlet, respectively.

It is seen that the increase in platinum loading increases the liquid water saturation in the CCL. However, the increase in the liquid water saturation is not proportional to the increase in platinum loading. This can be explained by the fact that, at fixed Pt/C ratio and catalyst layer thickness, the increase in platinum loading simultaneously increases the specific area and decreases the catalyst layer porosity [39]. The decrease in porosity offsets the improved cell performance resulting from the increased reaction rate. In this condition, the reactant gas transport becomes the dominant process, resulting in an insufficient utilization of the platinum catalyst near the membrane.

As the platinum loading increases, the CCL effectiveness factor decreases along two directions: reactant flowing along-the-channel and diffusion through the catalyst layer. The maximum effectiveness factor is observed at the CCL-GDL boundary near the cathode inlet, where the reactant gas firstly contacts the catalyst layer.

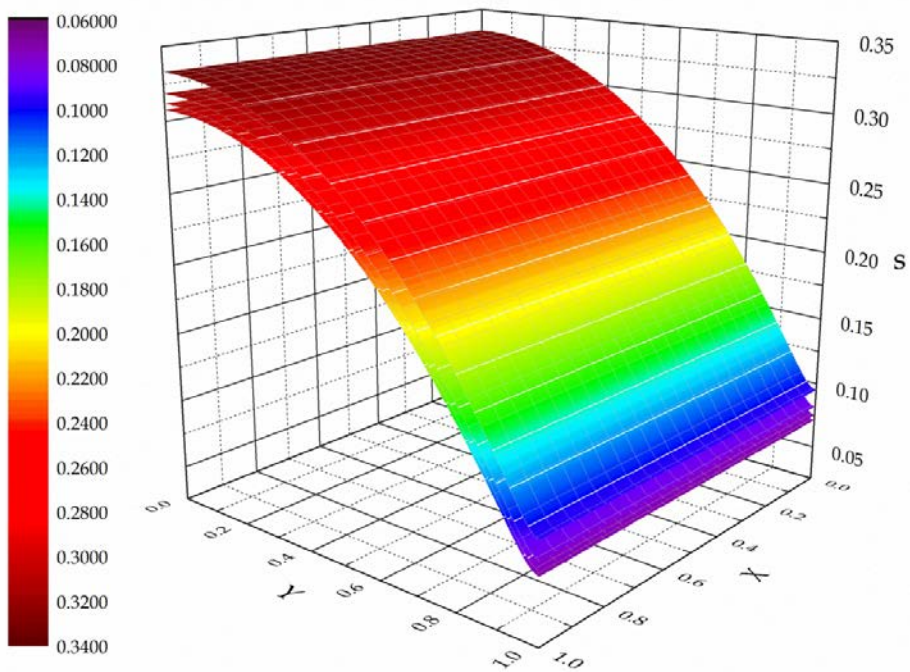


Figure 7-6 Liquid water saturation in CCL with various platinum loadings at 0.3 V in base-case condition:  $m_{Pt} = 0.8, 0.6, 0.4$  and  $0.2 \text{ mg cm}^{-2}$  from up down.

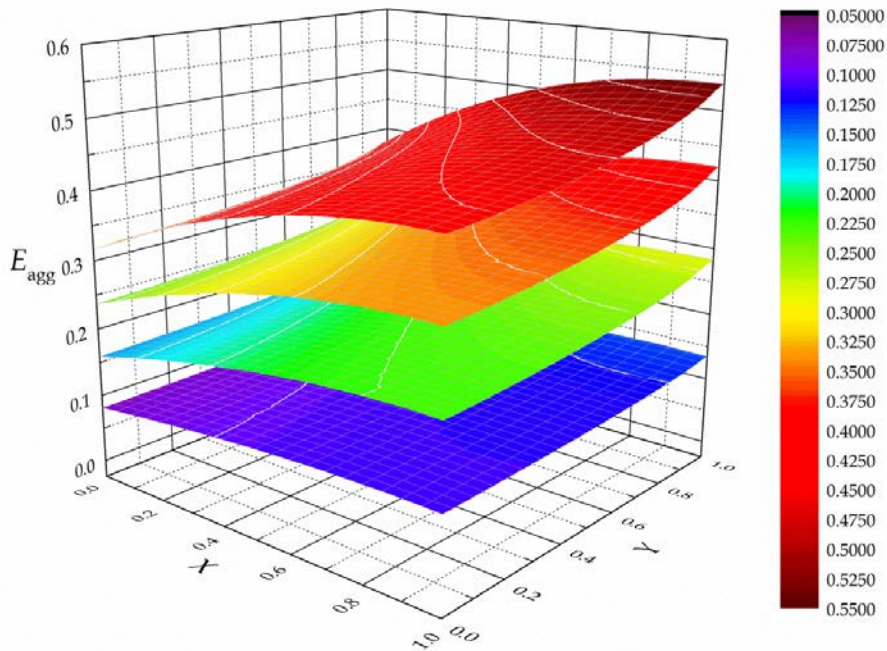


Figure 7-7 CCL effectiveness factor with various platinum loadings at 0.3 V in base-case condition:  $m_{Pt} = 0.2, 0.4, 0.6$  and  $0.8 \text{ mg cm}^{-2}$  from up down.

#### 7.4.4 The effect of the GDL thickness on temperature profiles and CCL effectiveness factor

The temperature profiles along the cathode CCL-GDL interface with various GDL thicknesses at the cell voltage of 0.4 - 0.1 V are shown in Figure 7-8. It is shown that the temperature rises (from the initial temperature of 343 K) sharply near the cathode inlet and increases slowly along the direction of air flowing to the outlet. The sharp rise in temperature can be explained by the exothermic ORR inside the CCL and the relative high temperature near the outlet due to the heat released by water phase-transfer. More liquid water is generated and accumulated in the downstream channel; its phase-transfer contributes roughly 10% of total heat at the cathode at  $1.0 \text{ A cm}^{-2}$ . Theoretically, greater fuel cell performance can be achieved with thinner GDL due to the reduced reactant diffusion resistance. However, this is at a cost of more significant temperature rise. In Figure 7-8, six GDL thicknesses, 10, 20, 60, 100, 200 and 260  $\mu\text{m}$  are compared, in reference to the case of no GDL. It is found that the local temperature along the cathode CL-GDL interface is higher for thinner GDLs and the temperature distribution is more non-uniform for thinner GDL at low cell voltages (corresponding to high current densities). The reason for the higher temperature rise when use thinner GDL is due to the reduced heat transfer resistance and non-uniform distribution of reactant gases. The use of a GDL of 260  $\mu\text{m}$  decreases the local temperatures near the cathode outlet by 1.3  $^{\circ}\text{C}$  at 0.4 V and 5.8  $^{\circ}\text{C}$  at 0.1 V, as shown in Figure 7-8(a) and Figure 7-8(b) respectively, compared to the case of no GDL. It is important to note that a further increase in GDL thickness larger than 200  $\mu\text{m}$  leads to only a slight change in temperature; for example, the increase in GDL thickness from 200 to 260  $\mu\text{m}$  has very little effect on the temperature rise.

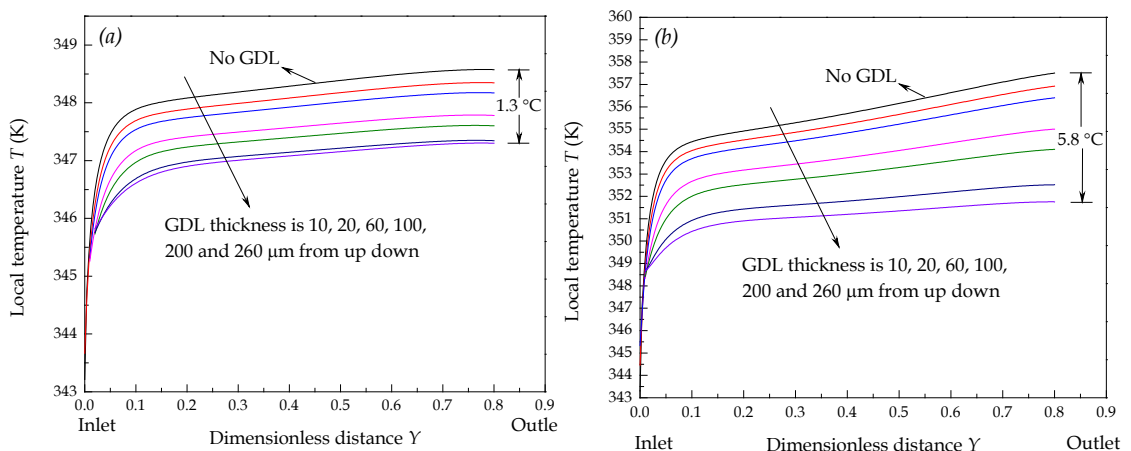


Figure 7-8 Temperature profile at cathode CL-GDL interface at the cell voltages of (a) 0.4 V (b) 0.1 V with various GDL thickness in base-case condition:  $\delta_{\text{GDL}} = 10, 20, 60, 100, 200$  and  $260 \mu\text{m}$  from up down.

The increase in GDL thickness also decreases the effectiveness factor of the cathode catalyst layer. The effectiveness factors of the CCL with various GDL thicknesses are shown in Figure 7-9, in which the boundaries are as same as shown in Figure 7-6 and Figure 7-7. The CCL effectiveness factor decreases along two directions, along the reactant gas flowing direction and through the CCL, and the gradient of CCL effectiveness factor is more significant through the CCL than that along-the-channel. The decrease in CCL effectiveness factor with a thicker GDL can be explained by the increase in reactant gas diffusion resistance, which may become the rate control process at high current density. In other words, the reactant consumption rate may be faster than the reactant diffusion rate through the GDL at high current density. In this condition, the relatively slow gas transport process controls the overall rate of the diffusion-reaction process instead of the electrochemical reaction. For example, the increase in GDL thickness from 60 to 380  $\mu\text{m}$  leads to an average 28% decrease in the CCL effectiveness factor, which then reduces the current density from 1.68 to 1.37  $\text{A cm}^{-2}$ , approximately 19.0% decrease, at 0.3 V.

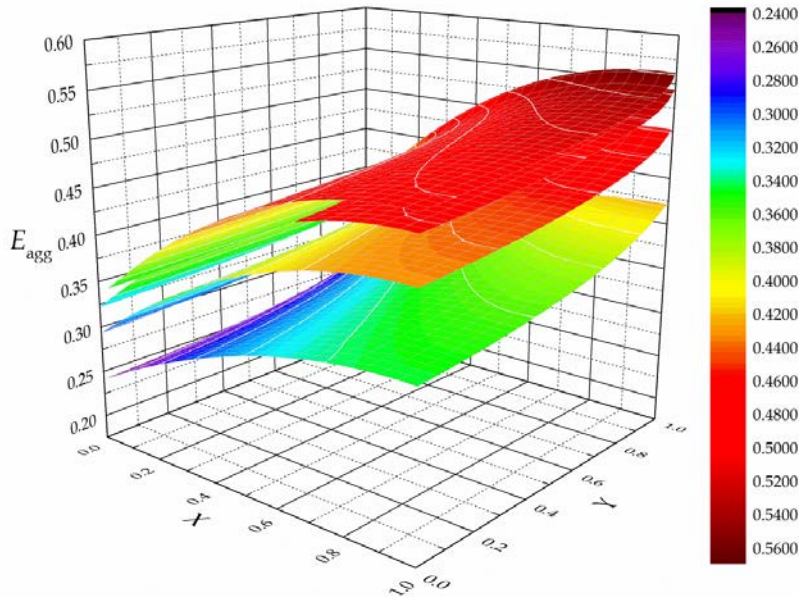


Figure 7-9 CCL effectiveness factor with various GDL thicknesses at 0.3 V in base-case condition:  $\delta_{\text{GDL}} = 60, 100, 200 \text{ and } 380 \mu\text{m}$  from up down.

#### 7.4.5 The effect of flow channel length and depth on liquid water saturation

Figure 7-10 shows the liquid water saturation, in both the anode and the cathode channels, with various channel lengths in the range of 0.5 - 4.0 cm. Boundaries  $X=0$  is the anode channel outer boundary in Figure 7-10(a) and cathode GDL-channel interface

in Figure 7-10(b),  $X=1$  is anode channel-GDL interface in Figure 7-10(a) and cathode channel outer boundary in Figure 7-10(b),  $Y=0$  is the anode gas inlet in Figure 7-10(a) and cathode gas outlet in Figure 7-10(b),  $Y=1$  is the anode gas outlet in Figure 7-10(a) and cathode gas inlet in Figure 7-10(b). At the cell voltage of 0.3 V, the water generation rate is significantly fast, leading to a rapid accumulation of liquid water in the channel. It is shown in Figure 7-10 that the liquid water distribution along-the-channel is non-uniform. The downstream regions are more easily affected by more severe water flooding. The longer the channel is, the more severe water flooding is observed in the downstream regions. At the anode outlets ( $Y=1$ ) in Figure 7-10(a), the increase of channel length from 1.0 to 4.0 cm increased the liquid water saturation from 11% to 19%. Similarly, the liquid water saturation is increased from 22% to 41% at the cathode outlet, as shown in Figure 7-10(b).

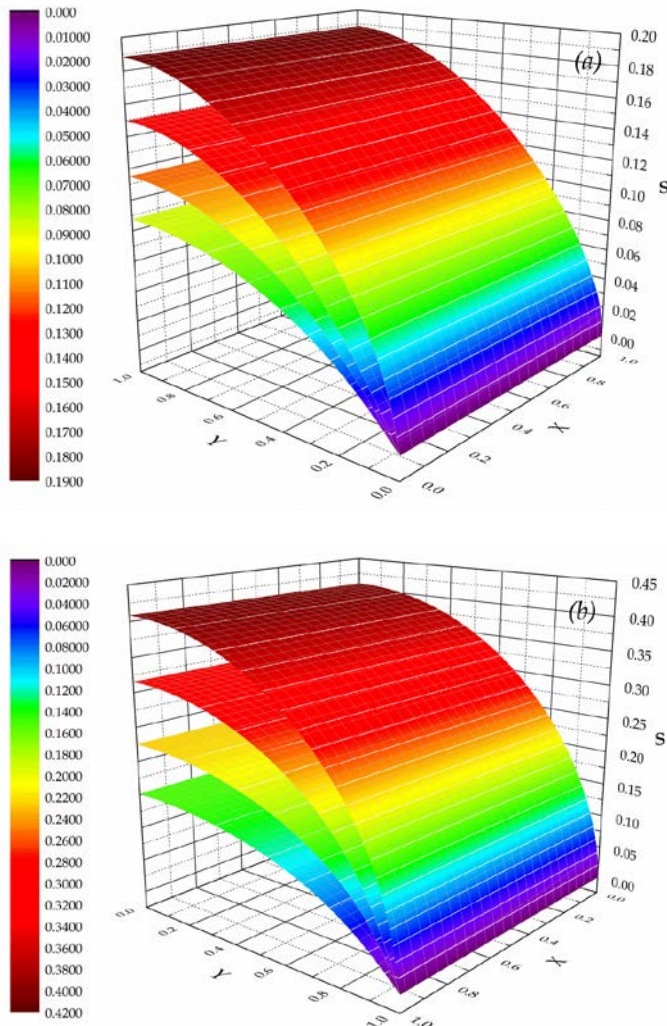


Figure 7-10 Liquid water saturation in (a) anode channel and (b) cathode channel with various channel lengths at 0.3 V in base-case condition:  $L = 4.0, 2.0, 1.0$  and  $0.5$  cm from up down.

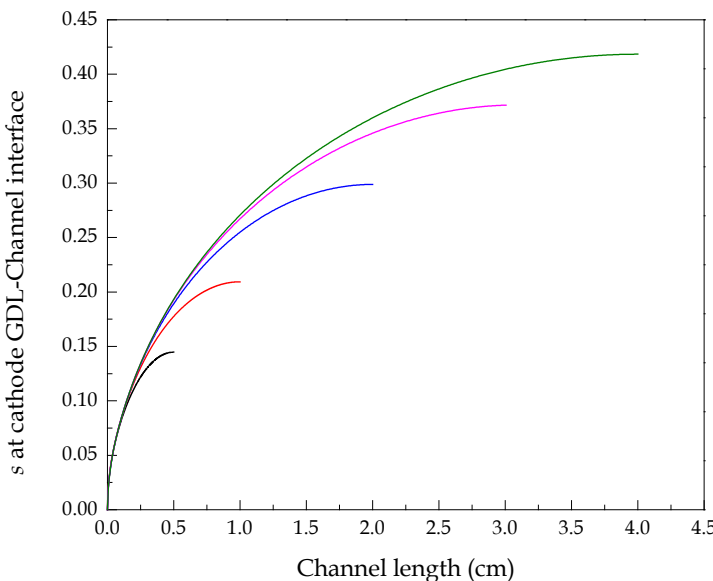


Figure 7-11 Liquid water saturation at cathode GDL-channel interface at 0.3 V:  $X = 0$  is the cathode channel inlet,  $X = 0.5, 1.0, 2.0, 3.0$  and  $4.0$  is the outlet, respectively.

It is important to note that the distribution of liquid water saturation over the channel depth (coordinate  $X$ ) is almost uniform. In addition, liquid water is not observed in particular regions near the inlet. This is in good agreement with Yang et al.'s work [10], which showed that the first 2 cm of a 20 cm cathode channel did not suffer from liquid water flooding. As indicated in Figure 7-11, it is found that the length of such particular region is almost independent on the channel length applied. The length of the no liquid water saturation region, e.g. liquid water saturation less than 10%, is identical for various channel lengths.

The liquid water saturations, in both the anode and the cathode channels, with various channel depths in the range of 0.5 - 2.0 mm at the cell voltage of 0.3 V, are shown in Figure 7-12. At a fixed stoichiometric flow ratio and a channel width, the velocity of the reactant gas varies inversely with the channel depth. The reactant gas flow is faster in a shallow channel, which could homogenise the spatial distribution of reactant gases along-the-channel and improve the water removal ability. In Figure 13a, as the anode channel depth increases from 0.5 to 2.0 mm, the maximum water saturation is decreased from 13% to 10%. On the contrary, the maximum water saturation in the cathode channel is decreased from 0.25 to 0.19 as the cathode depth increases from 0.5 to 2.0 mm. The effect of the cathode channel depth on water saturation is larger than that of the anode channel depth. As indicated in Table 10, an increase in channel depth from 0.5 to 2.0 mm leads to a decrease in current density from  $1.37$  to  $1.32 \text{ A cm}^{-2}$  at 0.3 V. Moreover, the differential pressure between adjoining channels is increased for the

shallow channel, thus the oxygen transfer rate to an electrode is increased by the gas flow through the GDL [40].

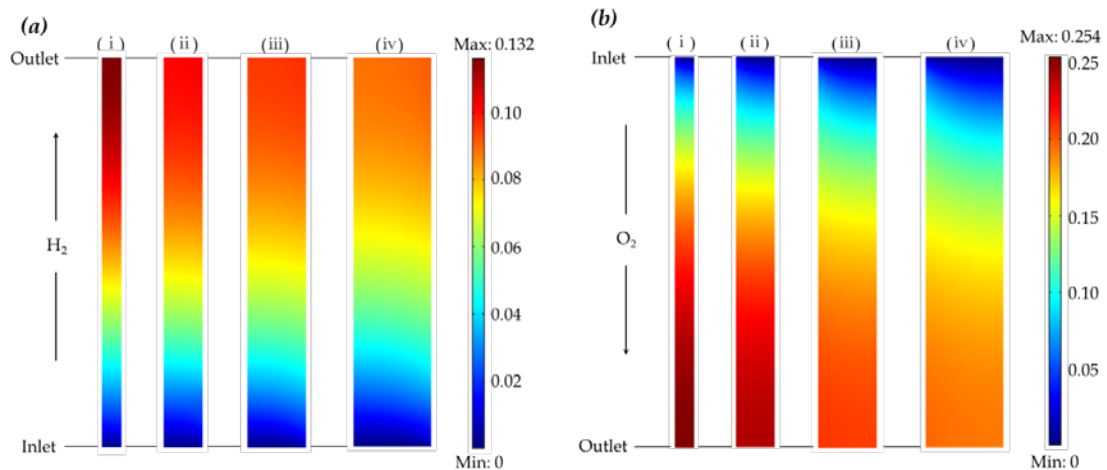


Figure 7-12 Liquid water saturation in (a) anode channel and (b) cathode channel with various channel depth at 0.3 V in base-case condition:  $\delta_{\text{Ch}} = 0.5, 1.0, 1.5$  and  $2.0$  mm from left to right.

#### 7.4.6 Parametric study

A parametric study is carried out to study the effect of six parameters on the current densities at four levels. The parameters are listed in Table 7-9. The predicted current densities corresponding to the four levels at three cell voltages are presented in Table 7-10. These studied parameters are related to the properties of the electrodes and channels, including platinum loading ( $m_{\text{Pt}}$ ), GDL porosity ( $\varepsilon_{\text{GDL}}$ ), GDL thickness ( $\delta_{\text{GDL}}$ ), contact angle ( $\theta$ ), channel length ( $L$ ) and channel depth ( $\delta_{\text{Ch}}$ ). The results indicate that the increase in GDL thickness and channel depth lead to a monotonically decrease in cell performance in the range of cell voltages from 0.7 to 0.3 V. This can be explained by the increased mass transport resistance and decreased velocity of reactant gases at a fixed stoichiometry. On the contrary, the current densities predicted at various cell voltages are almost proportional to the GDL porosity. Ideally, the mass transport of reactant gases can be reinforced when a high porosity is used. However, it is a challenge to the GDL mechanical strength and stability. Contact angle and channel length almost have no effect on the cell performance at high cell voltages (low current densities) due to the insignificant amounts of liquid water formed. As the cell voltages decreases, the corresponding current densities gradually increase, resulting in a significant formation of liquid water inside the electrodes and channels. In this condition, the effect of contact angle and channel length become more important due to the increased impact on the capillary coefficient of liquid water transport and the degree of liquid water flooding in the channel. The effect of platinum loading on current density is complicated. At high

cell voltage, the current density is mainly determined by kinetics of electrochemical reactions rather than mass transport. Thus, the increase in platinum loading increases the current density due to the increased specific area of the catalyst layer [39].

Table 7-9 Details of levels of various study parameters and the predicted current densities at 0.05 V

	Level 1	Level 2	Level 3	Level 4
$m_{\text{Pt}}$ (mg cm <sup>-2</sup> )	0.2	0.4	0.6	0.8
$\varepsilon_{\text{GDL}}$ (%)	20	40	60	80
$\delta_{\text{GDL}}$ ( $\mu\text{m}$ )	60	200	260	380
$\theta$ (°)	100	120	140	160
$L$ (cm)	0.5	1.0	2.0	4.0
$\delta_{\text{Ch}}$ (mm)	0.5	1.0	1.5	2.0

Table 7-10 Predicted current densities with various levels of study parameters at different cell voltages

Study parameters	Cell voltage (V)	Current densities (A cm <sup>-2</sup> ) with different levels of study parameters			
		Level 1	Level 2	Level 3	Level 4
$m_{\text{Pt}}$	0.7	0.0492	0.0547	0.0585	0.0585
	0.5	0.592	0.598	0.575	0.487
	0.3	1.382	1.357	1.294	1.123
$\varepsilon_{\text{GDL}}$	0.7	0.0538	0.0547	0.0542	0.0535
	0.5	0.488	0.598	0.627	0.639
	0.3	0.821	1.357	1.523	1.593
$\delta_{\text{GDL}}$	0.7	0.0557	0.0553	0.0551	0.0547
	0.5	0.664	0.635	0.623	0.598
	0.3	1.686	1.554	1.497	1.357
$\theta$	0.7	0.0546	0.0547	0.0547	0.0547
	0.5	0.596	0.598	0.599	0.599
	0.3	1.334	1.357	1.364	1.367
$L$	0.7	0.0546	0.0547	0.0547	0.0547
	0.5	0.595	0.598	0.598	0.597
	0.3	1.349	1.357	1.337	1.301
$\delta_{\text{Ch}}$	0.7	0.0547	0.0547	0.0546	0.0545
	0.5	0.601	0.598	0.594	0.590
	0.3	1.371	1.357	1.337	1.318

Note: when investigating the study parameter, others are fixed at constants in base-case condition in Table 7-8.

At low cell voltages, electrode porosity plays a vital important role in determining the current density as the rate control process turns to mass transport, especially the oxygen transport through the electrode. As a consequence, the increase in platinum loading decreases the current density at low cell voltages. At medium cell voltages, the cell performance is under a mixed control where both reaction kinetics and reactant transport approximately equally contribute to the current density. As a result, the current density is initially increased as the platinum loading increases, and then decreased with a further increase in platinum loading beyond the optimal value.

#### **7.4.7 Effect of relative humidity**

Figure 7-13 shows the effect of both anode relative humidity ( $RH_a$ ) and cathode relative humidity ( $RH_c$ ) on the current densities predicted at 0.8, 0.5 and 0.2 V, corresponding to high, medium and low cell voltages. At high cell voltages, e.g. 0.8 V, the current densities increase as the relative humidity decreases. This increase in current density with the decrease of the relative humidity is observed for both anode and cathode. However, the cathode relative humidity ( $RH_c$ ) has a larger impact on current density, which is in consistence with the finding of Iranzo et al. [41]. For example, when  $RH_c$  decreases from 100% to 50% at a fully humidified anode gas, the increase in current density is  $3.56 \times 10^{-3} \text{ A cm}^{-2}$ ; whilst when  $RH_a$  decrease from 100% to 50% at a fully humidified cathode gas, the increase in current density is  $4.4 \times 10^{-4} \text{ A cm}^{-2}$ . This can be explained by the increased mole fraction of reactant gases, oxygen at the cathode in particular. At high cell voltages, corresponding to low current densities, the rate control process is intrinsic ORR kinetics rather than the mass transport [39]. Increasing the mole fraction of reactant gases by reducing the relative humidity is therefore of benefit to the cell performance at high cell voltages. At medium cell voltages, e.g. 0.5 V, as the cathode relative humidity ( $RH_c$ ) decreases, the current densities firstly increases and then undergo a decrease. The optimal  $RH_c$  is between 80-90% when  $RH_a$  is in the range of 50-100% and the optimal  $RH_a$  is kept as 100% in full range of  $RH_c$ . The relatively high  $RH_a$  and  $RH_c$  required to maintain the optimal cell performance at medium cell voltage is due to the insufficient oxygen reduction reaction (ORR) and thus insufficient water generation at such cell voltages. A large amount of extra water is needed to maintain the membrane hydration. At low cell voltages, e. g. 0.2 V, we observe a different phenomenon. It is found that the optimal  $RH_c$  increases as the  $RH_a$  decreases. When  $RH_a$  is in the range of 80-100%, the optimal  $RH_c$  can be lower than 50%. However, as the  $RH_a$  decreases to the range of 50-70%, the optimal  $RH_c$  increases to

around 60-70%. It is particularly worth noting that the  $\text{RH}_a$  is of vital importance to the cell performance at low cell voltages. Due to the high current densities at low cell voltages, sufficient water is generated by ORR at low relative humidity, which is capable of maintaining the membrane hydration at the cathode side. High relative humidity is prone to increase the liquid water saturation inside the porous electrode and deteriorate the mass transport. High current densities also lead to considerable water migration through the membrane from the anode to the cathode and result in severe membrane dehydration on the anode side.

To further verify this, the influence of the anode relative humidity on the anode ionomer water content is investigated and shown in [Figure 7-14](#). It is demonstrated that, at low cell voltages, the minimum ionomer water content within the anode catalyst layer is almost proportional to the anode relative humidity. The minimum ionomer water content at the anode is compared with its average value along the anode CL-GDL interface. It is also clear that at low  $\text{RH}_a$  these two curves almost overlap each other, which indicates that the ionomer is dehydrated along-the-channel resulting in very similar ionomer water content at both the anode inlet and outlet. As the  $\text{RH}_a$  increases, the ionomer water content increases. The increasing departure between the minimum ionomer water content with the anode CL and the average ionomer water content at the anode CL-GDL interface can be explained by the relative high ionomer water content near the anode outlet. As the  $\text{RH}_a$  increases to 100%, the anode ionomer water content reaches saturation level ( $\lambda \approx 14.1$ ) and four curves almost overlap each other, which indicates a fully saturated ionomer in the anode CL at a fully humidified anode gas. Note that the increase in  $\text{RH}_c$  from 50% to 100% leads to a slight change of anode ionomer water content. It can be confirmed that the anode ionomer water content is mainly determined by the anode relative humidity. Using the fully humidified anode gas is therefore essential to the optimal cell performance at full range of cathode relative humidity.

As indicated in [Figure 7-13](#), at medium and low cell voltages, 100%  $\text{RH}_a$  leads to the maximum current densities at various  $\text{RH}_c$ . However, the optimal  $\text{RH}_c$  values at the medium and low cell voltages can not be clearly seen in [Figure 7-3](#). Therefore, the optimal  $\text{RH}_c$  values at the medium and low cell voltages are further presented in [Figure 7-15](#), with  $\text{RH}_a$  being varied from 100% to 50% for the case of short channel of 1.0 cm.

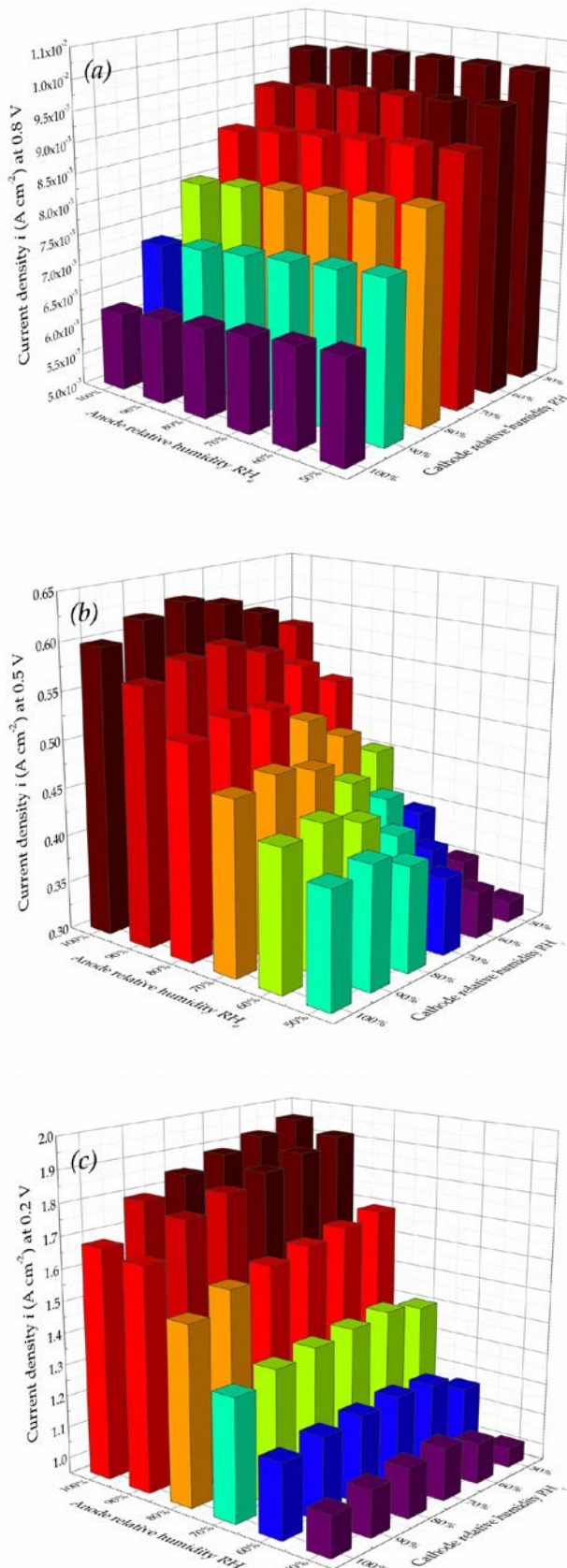


Figure 7-13 Current densities at various anode and cathode relative humidity at (a) 0.8 V (b) 0.5 V and (c) 0.2 V,  $L = 1 \text{ cm}$ ,  $\xi_a = 1.2$ ,  $\xi_c = 2.0$ .

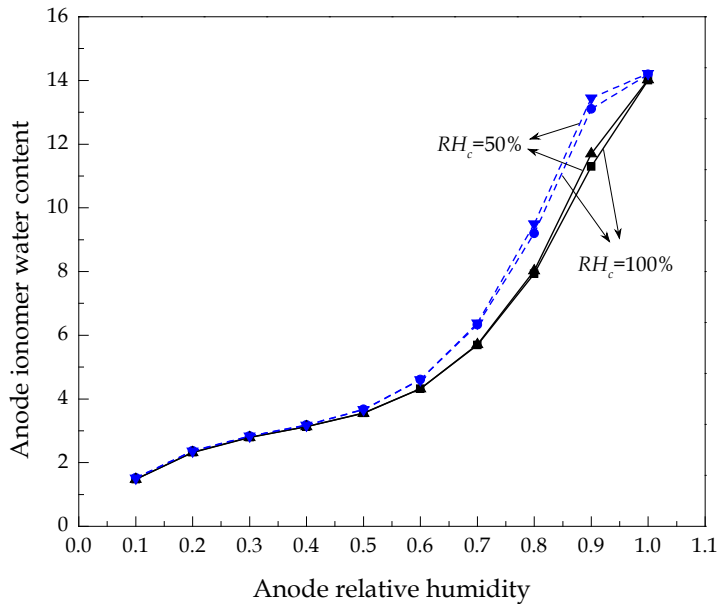


Figure 7-14 Ionomer water content in the anode catalyst layer at various anode relative humidity at 0.2 V:  $L = 1$  cm,  $\xi_a = 1.2$ ,  $\xi_c = 2.0$ . Solid line - the minimum ionomer water content within the anode catalyst layer; Dash line - average ionomer water content along the anode CL-GDL interface.

As shown in Figure 7-15, the optimal  $RH_c$  is different at various  $RH_a$ : a higher value is found with a lower  $RH_a$ . For example, at 0.2 V, the optimum  $RH_c$  is 30% at the  $RH_a$  of 100% and it increases to 70% at the  $RH_a$  of 50%. The situation is similar at 0.5 V, the optimal  $RH_c$  increases from 80% to 90% as the  $RH_a$  decreases from 100% to 50%. The relative low optimal  $RH_c$  at low cell voltages in comparison with that at medium cell voltages can be explained by the more water generated at higher current densities. Too much extra water introduced by the cathode reactant gas is prone to water flooding in the electrode, which could limit the mass transport and decline the cell performance.

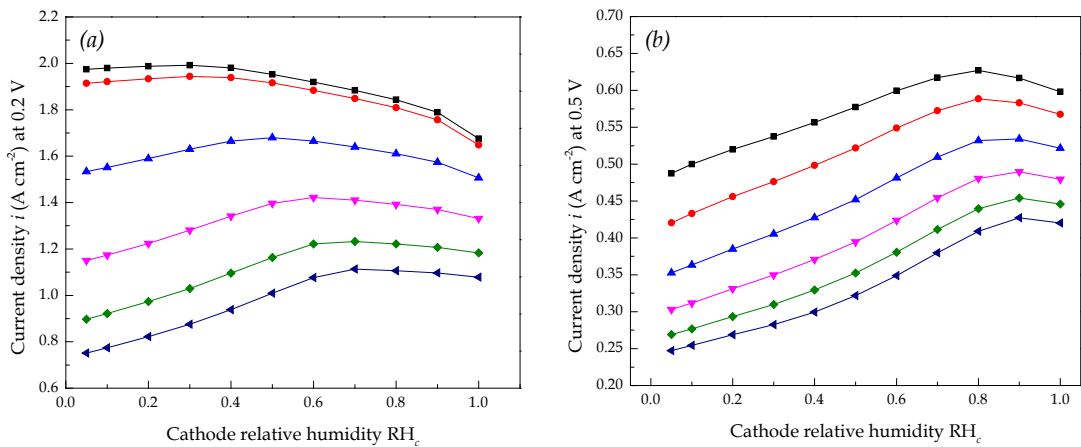


Figure 7-15 Optimal cathode relative humidity ( $RH_c$ ) of a short channel at (a) low and (b) medium cell voltages:  $RH_a = 100\%$  to  $50\%$  with the step of  $10\%$  from up down,  $L = 1\text{ cm}$ ,  $\xi_a = 1.2$ ,  $\xi_c = 2.0$ .

The optimal  $RH_c$  for fuel cells applying  $10\text{ cm}$  long flow channels at low and medium cell voltages is shown in Figure 7-16. At medium cell voltage of  $0.5\text{ V}$ , the profiles using long flow channels are very similar to the profiles at the same conditions using short channels. However, at low cell voltage of  $0.2\text{ V}$ , the effects of both  $RH_a$  and  $RH_c$  are more significant for long flow channels, than for short channels. As the  $RH_a$  decreases from  $100\%$  to  $50\%$ , the optimal  $RH_c$  increases from  $40\%$  to  $70\%$  at  $0.2\text{ V}$  and increases from  $80\%$  to  $90\%$  at  $0.5\text{ V}$ , respectively. Comparing Figure 7-15 and Figure 7-16 is clear that, at low cell voltage of  $0.2\text{ V}$ , the optimal  $RH_c$  at  $100\% RH_a$  is  $30\%$  and  $40\%$  respectively when using short and long flow channels.

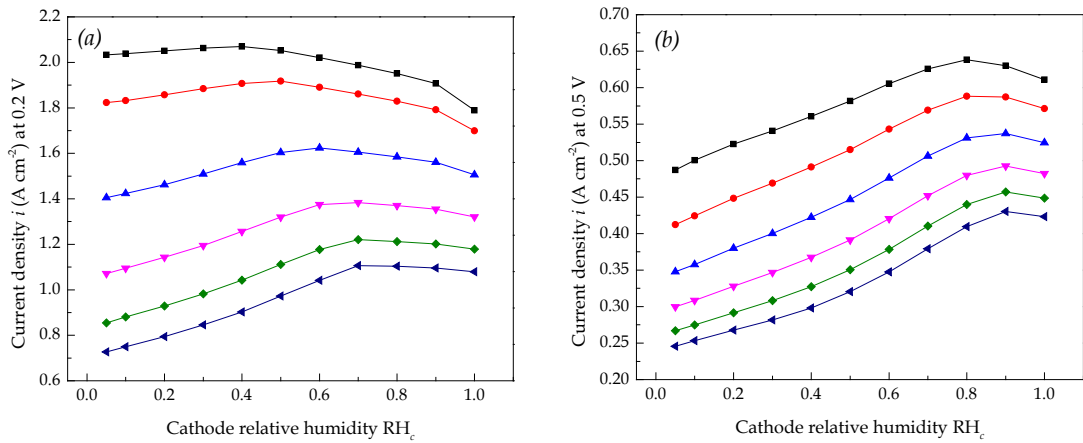


Figure 7-16 Optimal cathode relative humidity ( $RH_c$ ) of a long channel at (a) low and (b) medium cell voltages:  $RH_a = 100\%$  to  $50\%$  with the step of  $10\%$  from up down,  $L = 10\text{ cm}$ ,  $\xi_a = 1.2$ ,  $\xi_c = 2.0$ .

This can be explained by linking to the membrane/ionomer water content at the cathode side for different flow channel lengths, which is shown in Figure 7-17. In this figure,  $X = 0$  is the anode GDL-CL interface,  $X = 1$  is the cathode GDL-CL interface,  $Y = 0$  is the cathode outlet and  $Y = 1$  is the cathode inlet, respectively. The maximum membrane/ionomer water content at the cathode decreases from  $12.1$  to  $9.65$  as the channel length increases from  $1\text{ cm}$  to  $10\text{ cm}$ , showing a lower membrane/ionomer water content for a longer flow channel. Therefore, when using long flow channels, a higher relative humidity is required to maintain the hydration of the membrane, which is of benefit to the cell performance.

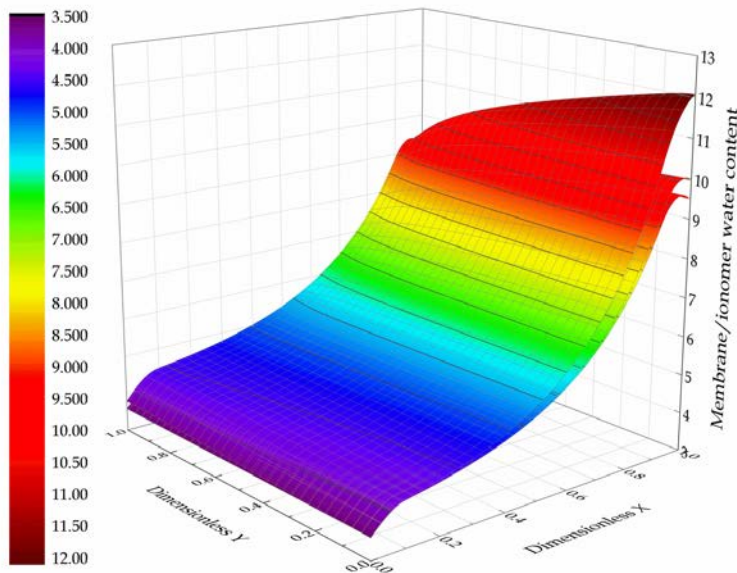


Figure 7-17 Membrane/ionomer water content with various length of channel at 0.2 V with  $RH_a = 50\%$  and  $RH_c = 60\%$ : upper layer – 1 cm channel; middle layer – 5 cm channel; lower layer – 10 cm channel.

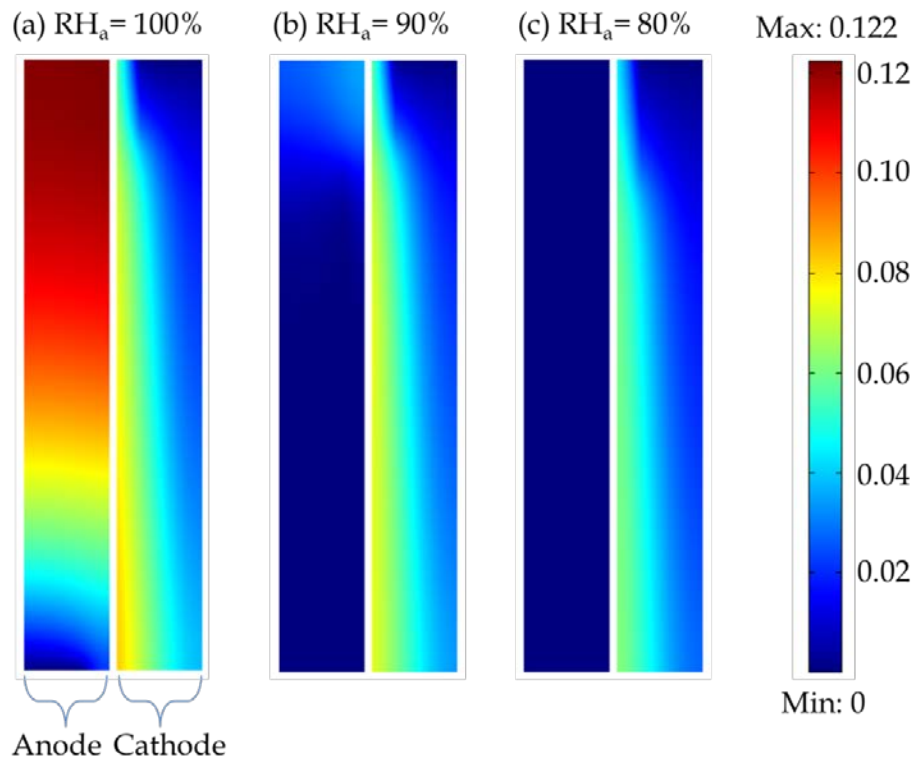


Figure 7-18 Effect of anode relative humidity ( $RH_a$ ) on liquid water saturation with  $RH_c = 90\%$  at 0.2 V: the current density predicted at each case is (a) 1.790, (b) 1.758 and (c)  $1.576 \text{ A cm}^{-2}$ .

Figure 7-18 shows the effect of  $RH_a$  on the liquid water saturation at both the anode and cathode with a fixed  $RH_c$  of 90% at 0.2 V. For the investigated  $RH_a$  values (which is in the range of 80-100%), liquid water is accumulated along the reactant gas flow

direction, for both the anode and the cathode. The decrease in the  $\text{RH}_a$  not only reduces the liquid water at the anode, but also mitigates the degree of water flooding at the cathode. When the  $\text{RH}_c$  is fixed at 90%, almost no liquid water exists at the anode if the  $\text{RH}_a$  is smaller than 90%. Although the liquid water saturation at the cathode is reduced as the  $\text{RH}_a$  decreases, the current density predicted at 0.2 V decreases from 1.790 to 1.576 A cm<sup>-2</sup> as the  $\text{RH}_a$  decreases from 100% to 80%. To explain this, the membrane/ionomer water content at various  $\text{RH}_a$  with  $\text{RH}_c$  of 90% at 0.2 V is investigated and reported in Figure 7-19. In this figure,  $X = 0$  is the anode GDL-CL interface,  $X = 1$  is the cathode GDL-CL interface,  $Y = 0$  is the anode inlet and  $Y = 1$  is the anode outlet, respectively. As shown in Figure 7-19, at fixed  $\text{RH}_c$  of 90%, the ionomer in the cathode catalyst layer can be fully saturated by water, while the ionomer in the anode catalyst layer is dehydrated as the  $\text{RH}_a$  decreases. For example, the decrease of  $\text{RH}_a$  from 100% to 60% leads to the ionomer water content in the anode catalyst layer decreasing from around 14 to 5. The decrease in ionomer water content decreases the proton conductivity, therefore reduces the current density predicted at low  $\text{RH}_a$ . It is also clear in Figure 7-19 that, the membrane/ionomer water content near the anode outlet is higher than that near the inlet. This can be explained by the more liquid water accumulated near the downstream channel as shown in Figure 7-18.

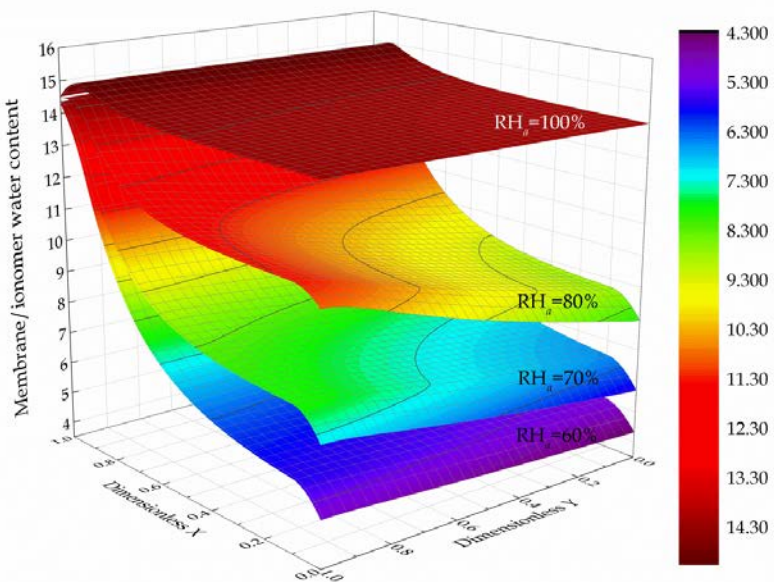


Figure 7-19 Membrane/ionomer water content at various  $\text{RH}_a$  with  $\text{RH}_c = 90\%$  at 0.2 V.

Although the dissolved water in the anode ionomer migrates to the cathode under the driving force of EOD, the dry ionomer can absorb water via ionomer water uptake, especially near the anode outlet where the mole fraction of water vapour is relative high.

However, when the  $\text{RH}_a$  becomes extremely low, e.g. lower than 60%, the water uptake is hard to compensate the decrease of ionomer water content, resulting in a constant ionomer water content along-the-channel.

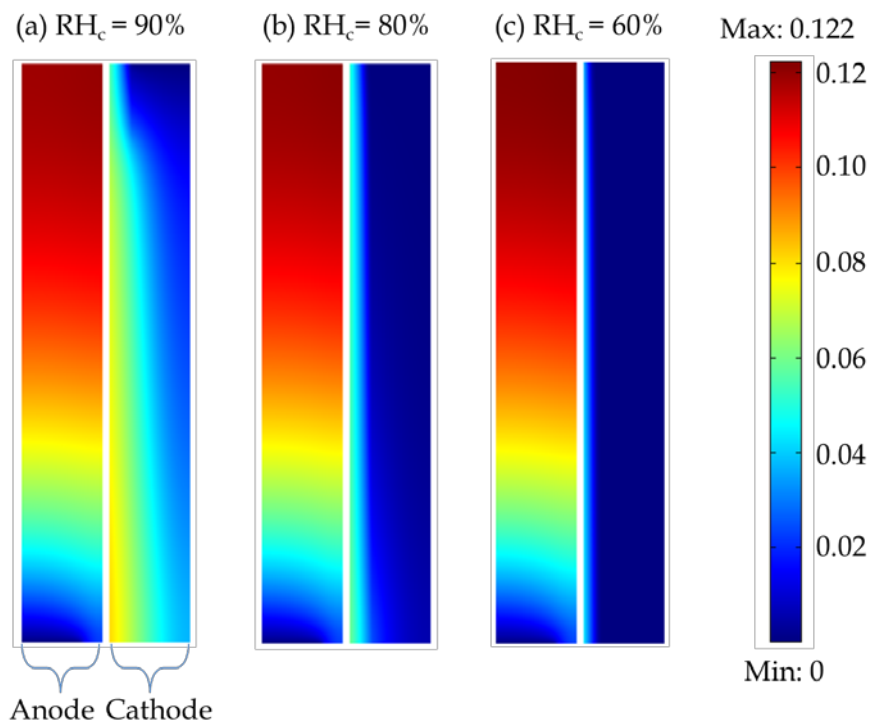


Figure 7-20 Effect of cathode relative humidity ( $\text{RH}_c$ ) on liquid water saturation with  $\text{RH}_a = 100\%$  at 0.2 V: the current density predicted at each case is (a) 1.790, (b) 1.844 and (c)  $1.920 \text{ A cm}^{-2}$

Figure 7-20 shows the effect of  $\text{RH}_c$  on the liquid water saturation at both the anode and cathode with a fixed  $\text{RH}_a$  of 100% at 0.2 V. Due to the fully humidified reactant gas introduced at the anode and electrochemical reaction converting hydrogen to water, liquid water is accumulated along the anode channel and reaches to the maximum level at the anode outlet. On the contrary, the liquid water saturation at the cathode is less significant when the reactant gas is not fully humidified. Especially when low  $\text{RH}_c$  is applied, the liquid water generated by ORR and EOD only leads to liquid water formation in the cathode electrode near the membrane. For example, as the  $\text{RH}_c$  decreases from 90% to 60%, the average liquid water saturation decreases from 0.034 to  $10^{-5}$  in the cathode channel, and it decreases from 0.064 to 0.012 in the cathode gas diffusion layer. Using low  $\text{RH}_c$  improves the cell performance by reducing the liquid water generation and increasing the mole fraction of oxygen. For example, oxygen mole fraction increases from 15.2% to 17.1% as  $\text{RH}_c$  from 90% to 60%. As a consequence of the decrease in  $\text{RH}_c$ , the obtained current density increases from 1.790 to  $1.920 \text{ A cm}^{-2}$ . Theoretically, the optimal  $\text{RH}_c$  is to maintain the membrane/ionomer hydration while

minimising the negative effect of liquid water generation. It is clear in Figure 7-20(c) that even the 60%  $\text{RH}_c$  can maintain hydrated membrane/ionomer.

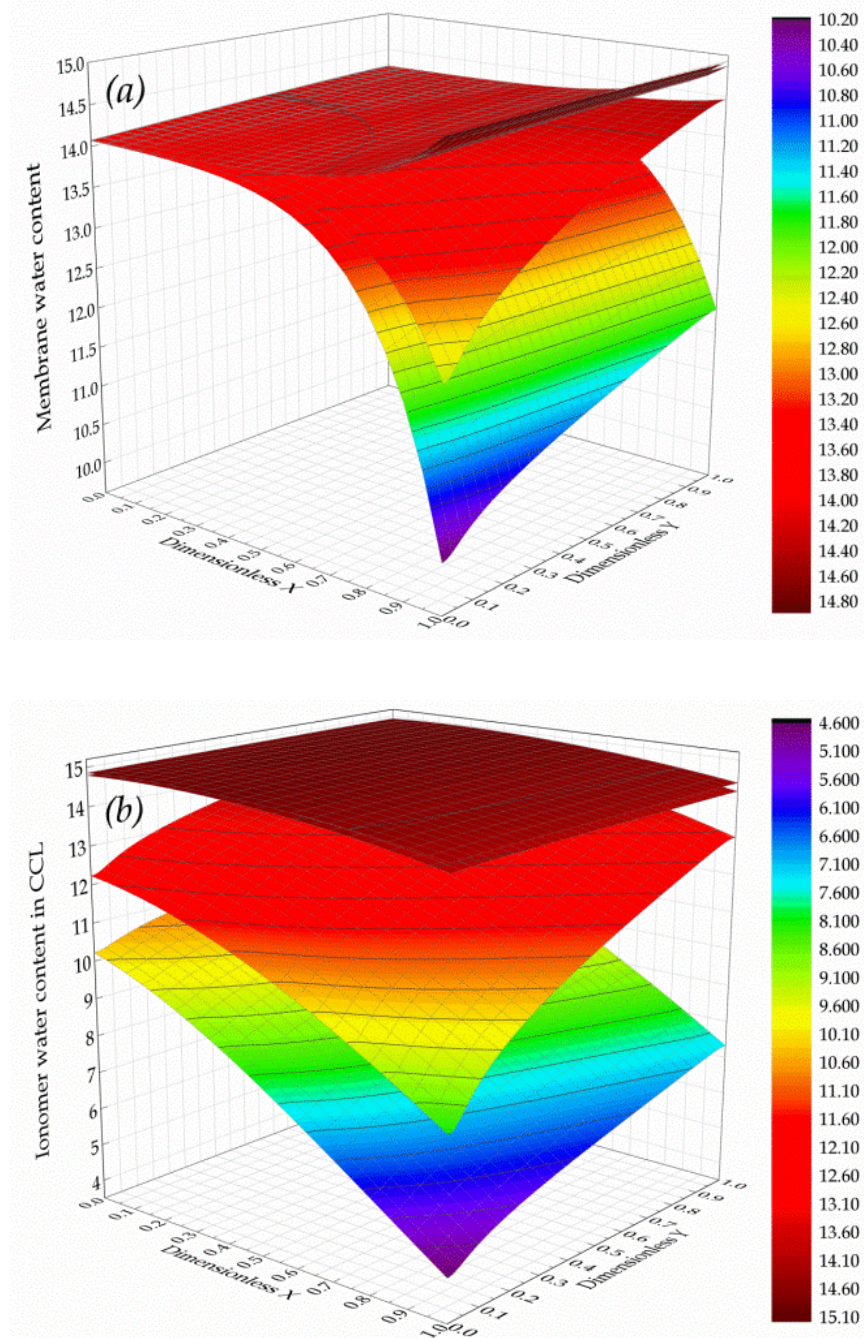


Figure 7-21 Membrane/ionomer water content in (a) membrane and (b) cathode catalyst layer at various  $\text{RH}_c$  with  $\text{RH}_a = 100\%$  at 0.2 V:  $\text{RH}_c = 70\%, 50\%, 30\%$  and 10% from up down.

The profiles of membrane and cathode ionomer water content at various  $\text{RH}_c$  at 0.2 V is shown in Figure 7-21. In Figure 7-21(a),  $X = 0$  is the anode CL-membrane interface,  $X = 1$  is the cathode CL-membrane interface; in Figure 7-21(b),  $X = 0$  is the cathode CL-membrane interface and  $X = 1$  is the cathode CL-GLD interface. In both figures,  $Y = 0$  is the cathode inlet and  $Y = 1$  is the cathode outlet, respectively. It is shown that the

membrane/ionomer water content decreases as the  $\text{RH}_c$  decrease.  $\text{RH}_c$  of 50% and 70% result in very similar membrane/ionomer water content profiles, which indicates that the membrane and ionomer can be fully saturated with  $\text{RH}_c$  higher than 50% and fully humidified anode gas. When the  $\text{RH}_c$  is lower than 50%, the ionomer in the cathode catalyst layer is hard to be saturated by EOD even fully humidified anode gas is applied. Figure 7-21(b) clearly shows that the ionomer water content is relatively low at the CL-GDL interface near the cathode inlet, especially when  $\text{RH}_c$  is lower than 50%. It indicates that the EOD is the main mechanism of determining the ionomer water content at the cathode at low  $\text{RH}_c$  [26]. The water migration under the driving force of EOD fails to compensate the ionomer dehydration away from the membrane-CL interface, resulting in the part of ionomer near the CL-GDL interface dehydrated. The polarisation curves in Figure 7-15 and Figure 7-16 show that the maximum current density is achieved at the  $\text{RH}_c$  between 30-40% and  $\text{RH}_a$  of 100% at 0.2 V. The further decrease in  $\text{RH}_c$  leads to sever dehydration of membrane and ionomer, which decreases the membrane/ionomer conductivity then decrease the cell performance. On the contrary, the optimal  $\text{RH}_c$  and  $\text{RH}_a$  is 80% and 100% at 0.5 V, respectively. The experimental work of Kim [42] found that the optimal  $\text{RH}_c$  is around 70% at an ionomer content of 30% at  $0.4 \text{ A cm}^{-2}$ , which supports the reliability of the modelling in this work in medium current densities range.

#### 7.4.8 Effect of stoichiometric flow ratio

At a fixed channel cross-sectional area, higher stoichiometric flow ratio only results in higher gas flow rate along-the-channel. Higher gas velocity is of benefit to the improved cell performance due to the accelerated removal rate of liquid water and heat.

Table 7-11 Limiting current densities predicted at various anode stoichiometric flow ratios with fully humidified gases

	$\xi_a = 0.4$	$\xi_a = 0.8$	$\xi_a = 1.2$	$\xi_a = 2.0$	$\xi_a = 3.0$
$\xi_c = 2.0$	1.9824	1.9807	1.9802	1.9797	1.9793
$\xi_c = 3.0$	2.0276	2.0257	2.0250	2.0245	2.0241

Note: the unit of current density is ( $\text{A cm}^{-2}$ )

Table 7-11 shows the effect of anode stoichiometric flow ratio on the limiting current density (current density at the cell voltage of 0.05 V) at two different cathode stoichiometric flow ratios, 2.0 and 3.0, respectively. It is clear the current densities change very slightly as the anode stoichiometric flow ratio increases. For example, as the anode stoichiometric flow ratio increases from 0.4 to 3.0, the limiting current

density only changes 0.157% and 0.172% for two levels of cathode stoichiometric flow ratios, respectively. The insignificant effect of anode stoichiometric flow ratio on limiting current density can be explained by the relative low degree of flooding and its weak effect on the HOR at the anode. Our previous study indicated that, by taking the anode flooding into account, the effectiveness of the ACL can be higher than 80% at  $1.2 \text{ A cm}^{-2}$  [43]. Consequently, the overall cell performance is dominated by the chemical and physical processes at the cathode side.

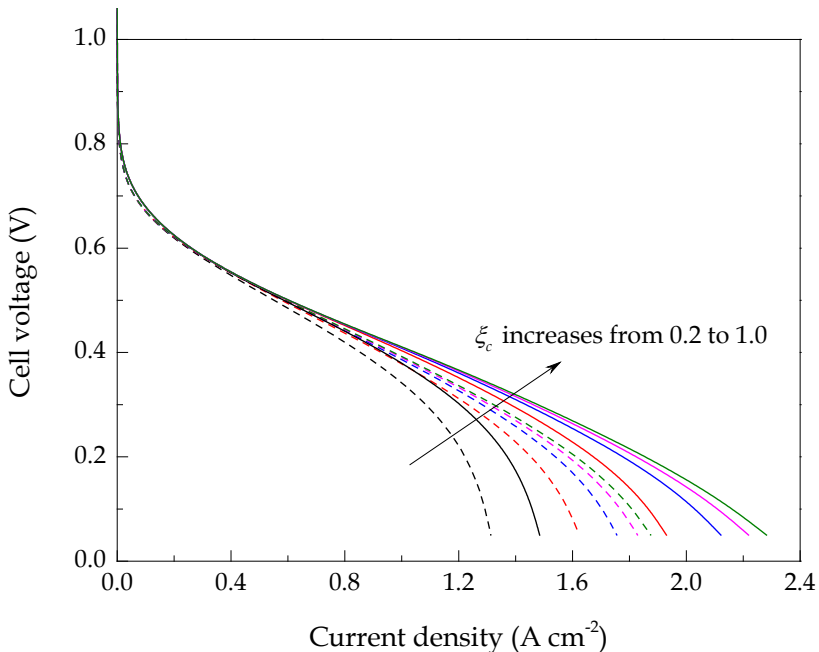


Figure 7-22 Effect of cathode stoichiometric flow ratio on cell performance at low cathode stoichiometric flow ratio at two levels of  $\text{RH}_c$ : solid line -  $\text{RH}_c = 60\%$ , dash line -  $\text{RH}_c = 100\%$ . Operating condition:  $\text{RH}_a = 100\%$ ,  $\xi_a = 2.0$ ,  $\xi_c = 0.2, 0.4, 0.6, 0.8, 1.0$ .

At a fixed anode stoichiometric flow ratio, the impact of cathode stoichiometric flow ratio on cell performance demonstrates different behavior in two  $\text{RH}_c$  ranges: 0.2 - 1.0 and 2.0 - 5.0. Figure 7-22 shows the effect of cathode stoichiometric flow ratio, increased from 0.2 to 1.0, on the polarisation curves with fully humidified anode gas and two levels of  $\text{RH}_c$ . The anode stoichiometric flow ratio was fixed at 2.0. The initial increase in cathode stoichiometric flow ratio (from 0.2 to 0.6) significantly improves the cell performance for two  $\text{RH}_c$  levels at low cell voltages because the current density is limited by oxygen transport at low oxygen concentration downstream the channel [44]. However, the further increases in cathode stoichiometry results in only small changes of current densities. This tendency is in consistence with the simulation results of Kulikovsky [45], which stated that the oxygen concentration is constant along-the-channel at a large cathode stoichiometric flow ratio. In this case, the limiting current

density became independent of the stoichiometric flow ratio. It is because stoichiometric flow ratio only changes the flow rate of reactant gases in the channels. The mole fraction of gas component is not changed at various stoichiometric flow ratios. At low cathode stoichiometric flow ratios, the supply of reactant gases may become insufficient because oxygen is rapidly consumed near the cathode inlet. As the cathode stoichiometric flow ratio increases, oxygen can be sufficiently and uniformly distributed along-the-channel. In this situation, oxygen transport in the porous electrode becomes the rate control process instead of ORR kinetics. Without doubt, the increase in stoichiometric flow ratio increases the water removal ability inside the channel. However, such effect becomes insignificant when only small amount of liquid water is generated at low cell voltages.

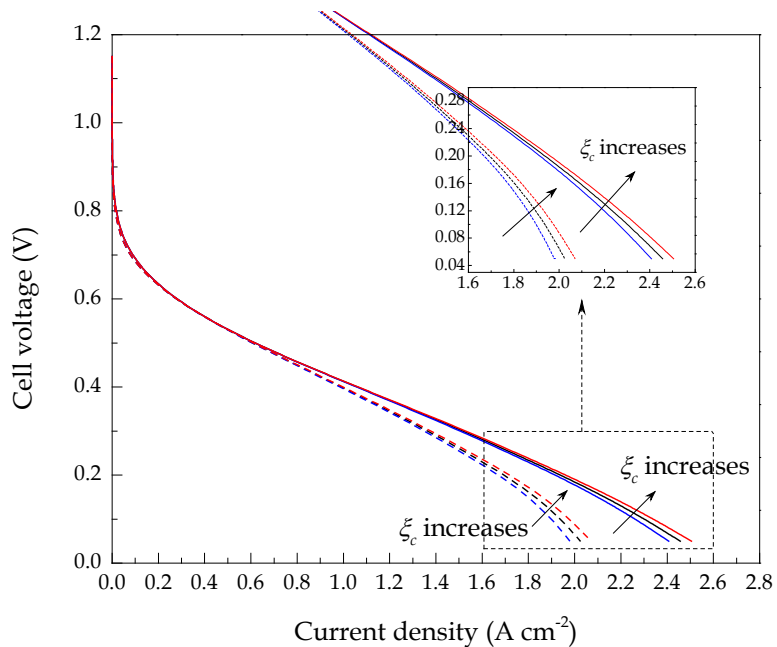


Figure 7-23 Effect of cathode stoichiometric flow ratio on cell performance at two levels of  $RH_c$ : solid line -  $RH_c = 60\%$ , dash line -  $RH_c = 100\%$ . Operating condition:  $RH_a = 100\%$ ,  $\xi_a = 2.0$ ,  $\xi_c = 2.0, 3.0$  and  $5.0$ .

Figure 7-23 shows the effect of cathode stoichiometric flow ratio, in the range of 2.0 to 5.0, on the polarisation curves at two levels of relative humidity. The RH and stoichiometric flow ratio at the anode were fixed at 100% and 2.0, respectively. At various cathode stoichiometric flow ratios, the cell performance at high and medium cell voltages almost overlap each other, indicating the weak influence of stoichiometric flow ratio at relatively low current densities. This is due to the less liquid water formation at low current densities. At large current densities, corresponding to low cell voltages, the effect of stoichiometric flow ratio on cell performance becomes significant.

However, beyond a value of 2.0 the gain in current density is relatively small in comparison with the gain in the range of 0.2 to 2.0. This tendency is very similar to the parametric study in the model developed by Berning and Djilali [19]. The increase in the stoichiometric flow ratio only leads to an approximate 4% of the improvement of the cell performance near the limiting current densities. The improvement of cell performance at various cathode relative humidity is similar using higher cathode stoichiometric flow ratio, indicating the independent water removal ability to relative humidity.

It is observed from Figure 7-22 and Figure 7-23 that the impact of stoichiometric flow ratio on cell performance becomes more pronounced as the current density increases. When the cell voltages decrease to a very low value, 0.05 V in this study, the limiting current densities are achieved. Such effect on the limiting current density at various cathode relative humidity is shown in Figure 7-24.

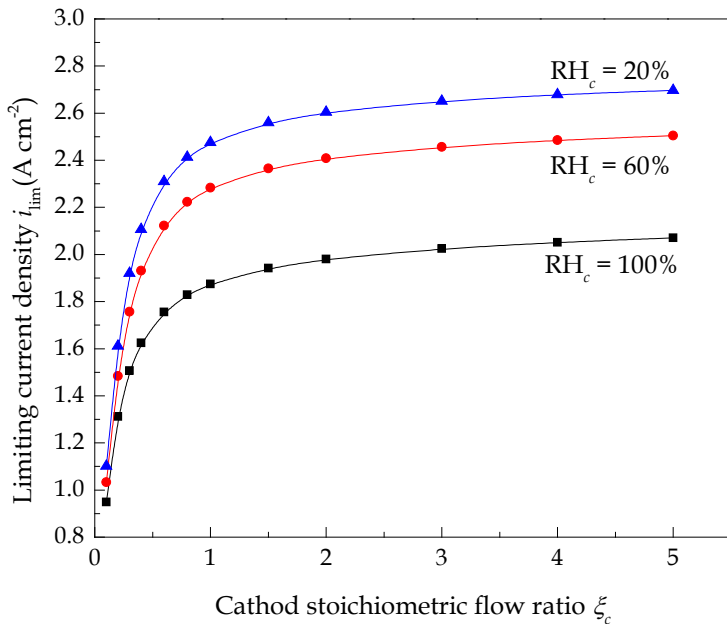


Figure 7-24 Effect of cathode stoichiometric flow ratio on limiting current density at various cathode relative humidity of a short channel:  $\xi_a = 1.2$ ,  $\text{RH}_a = 100\%$ ,  $L=1 \text{ cm}$

It is clear that the limiting current density at various  $\text{RH}_c$  is very close to each other at cathode stoichiometric flow ratio lower than 0.5. As the cathode stoichiometric flow ratio increases from 0.1 to 1.0, the limiting current density apparently increases from 1.0 to  $1.9 \text{ A cm}^{-2}$  at  $\text{RH}_c$  of 100%, to  $2.3 \text{ A cm}^{-2}$  at  $\text{RH}_c$  of 60%, and to  $2.5 \text{ A cm}^{-2}$  at  $\text{RH}_c$  of 20%. The further increase in the cathode stoichiometric flow ratio from 1.0 leads to only small increase in the limiting current density for all humidification conditions. The increased limiting current density at low cathode stoichiometric flow ratio can be

explained by the increased supplement of oxygen at the cathode. When the stoichiometric flow ratio is low, the supplied oxygen is insufficient along-the-channel. Due to the consumption of oxygen along the gas flow, the fuel cell near the cathode outlet may suffer from oxygen starvation, which can be avoided when high cathode stoichiometric flow ratio is applied. However, too high stoichiometric flow ratio rather leads to significant improvement of limiting current density than waste of energy that required for the reactant flow in the channel. It is also clear that more significant improvement of limiting current density is achieved as the  $\text{RH}_c$  decrease from 100% to 60% than when it decreases from 60% to 20%. Moreover, the limiting current densities obtained at the anode stoichiometric flow ratio of 2.0 in [Figure 7-22](#), [Figure 7-23](#) are almost identical to the limiting current densities with the anode stoichiometric flow ratio of 1.2 in [Figure 7-24](#), which reveals the insignificance of anode stoichiometric flow ratio on cell performance.

[Figure 7-25](#) shows the liquid water saturations in 4 cm and 10 cm cathode channels at various cathode stoichiometric flow ratios of 1.0, 2.0 and 4.0 with fully humidified gases. In this figure,  $X$  represents the distance along-the-channel depth from the channel-GDL interface to the outer boundary,  $Y = 0$  is the cathode inlet and  $Y = 1$  is the cathode outlet, respectively. As shown in [Figure 7-25](#), liquid water accumulates in the cathode channel along the gas flow direction after a short distance from the inlet and the amount of liquid water decreases as the stoichiometric ratio increase. The impact of stoichiometric flow ratio on liquid water saturation in longer channel is more significant in comparison with the short one. Due to the more pronounced liquid water accumulation near the downstream channel, it is believed that high stoichiometric flow ratio is required to maintain a high cell performance with long channels.

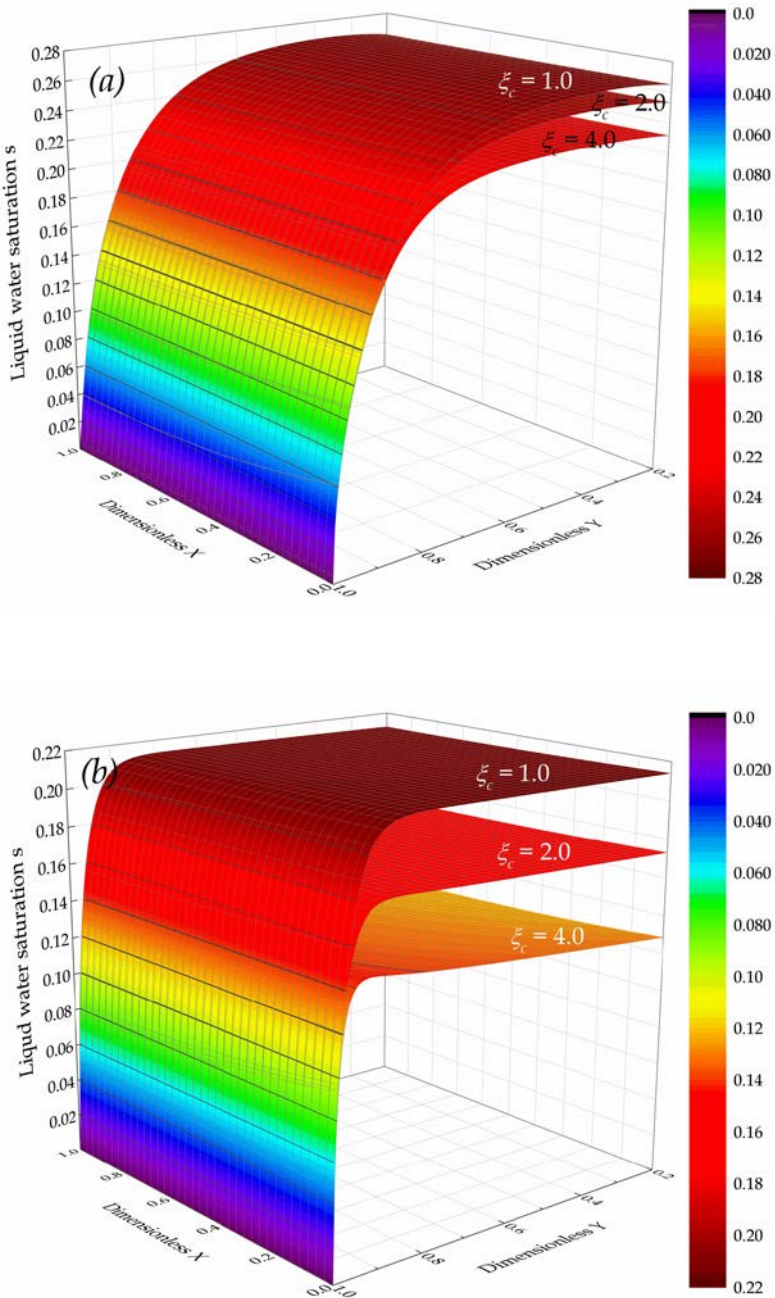


Figure 7-25 Liquid water saturation in cathode channel of (a) 4 cm and (b) 10 cm at various cathode stoichiometric flow ratios with fully humidified gases:  $\xi_a = 1.2$ .

In order to demonstrate the cell performance at various stoichiometric flow ratios for a longer channel, Figure 2-26 is used to reveal the effect of cathode stoichiometric flow ratio on the limiting current density with fully humidified anode and cathode conditions for various channel length from 0.5 to 10 cm. The cathode stoichiometric flow ratio varies from 1.0 to 4.0 with an anode stoichiometric flow ratio fixed at 1.2. It is found that the limiting current density is increased as the cathode stoichiometric flow ratio increases, and the increase is more significant for fuel cells using longer channels. For

example, the increase in stoichiometric flow ratio leads to approximate 2.8% and 11.6% improvements in the limiting current densities, respectively, for the channel length of 0.5 and 10 cm. The reduced impact of stoichiometric flow ratio for short channel is due to the less amount of liquid water accumulated.

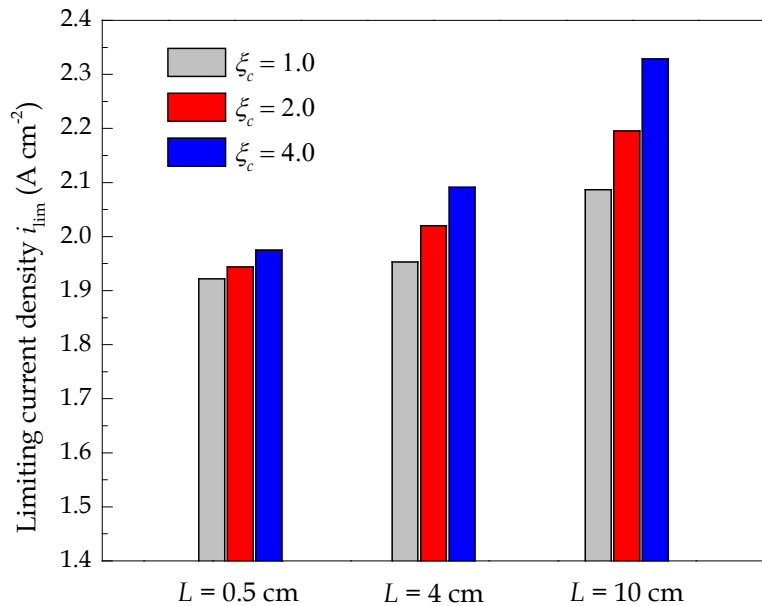


Figure 7-26 Effect of cathode stoichiometric flow ratio on limiting current density at various channel length with fully humidified gases:  $\xi_a = 1.2$

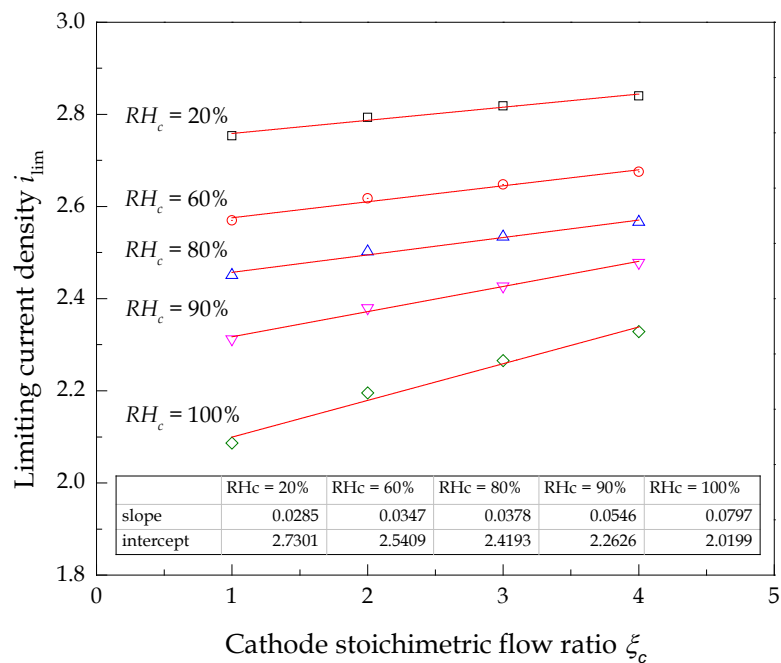


Figure 7-27 Effect of cathode stoichiometric flow ratio on limiting current density at various cathode relative humidity of a long channel:  $\xi_a = 1.2$ ,  $RH_a = 100\%$ ,  $L = 10\text{cm}$ .

Figure 2-27 shows the limiting current densities at various cathode relative humidity and stoichiometric flow ratios of a long channel of 10 cm. The anode relative humidity and stoichiometric flow ratio are fixed at 100% and 1.2, respectively. It is clear that the limiting current density is almost linear to the stoichiometric flow ratio at various  $\text{RH}_c$ . The slopes indicate the sensitivity of predicted limiting current density to the cathode stoichiometric flow ratio. The slope decreases as a consequence of the decreased  $\text{RH}_c$ , indicating the less significant effect of stoichiometric flow ratio when less liquid water is accumulated.

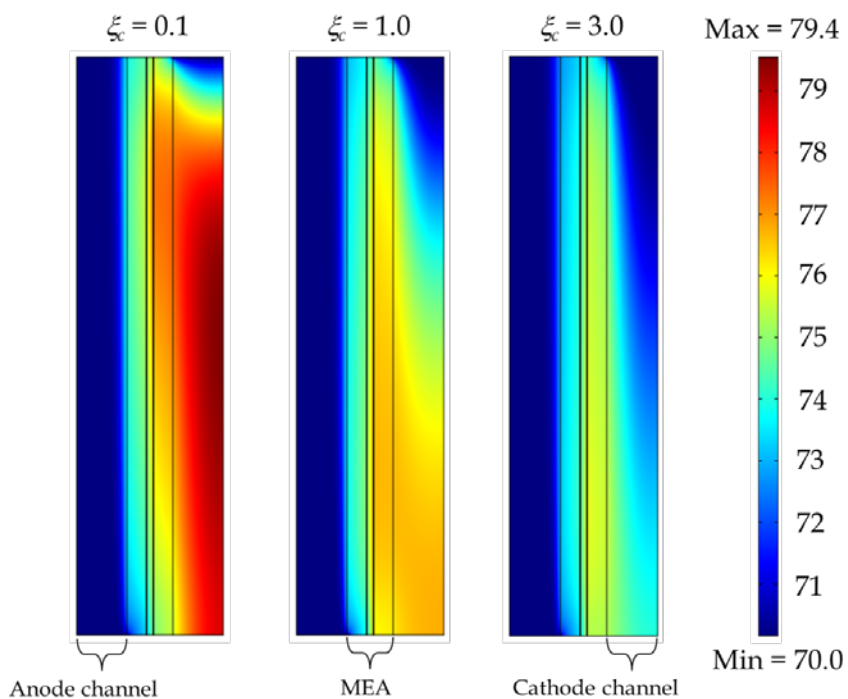


Figure 7-28 Effect of cathode stoichiometric flow ratio on temperature profiles with fully humidified gases:  $\xi_a = 2.0$

The effect of stoichiometric flow ratios on the temperature profiles is also investigated. Figure 2-28 shows the temperature profiles inside the MEA and channels with fully humidified gases at various cathode stoichiometric flow ratios. The anode stoichiometric flow ratio is fixed at 2.0. The temperature profiles indicate the heat removal ability of the cathode gas at various stoichiometric flow ratios. It is clear that the temperature distribution is non-uniform: the temperature increases along the air flow in the cathode channel and from the anode to the cathode, with the highest rise near the cathode outlet. The temperature rise is mainly attributed to the exothermic ORR and water phase-transfer. For the same fuel cell operated at fixed temperature and humidification conditions, the effect of stoichiometric flow ratio on heat removal is apparent. At low cathode stoichiometric flow ratios, the oxygen is hard to be uniformly

distributed along-the-channel, resulting in a local heat hotspot near the cathode inlet. In addition, the heat generated via ORR is hard to be pushed downstream to the channel exit by the cathode reactant at low cathode stoichiometric flow ratios, which deteriorates the heat removal and promotes the temperature rise.

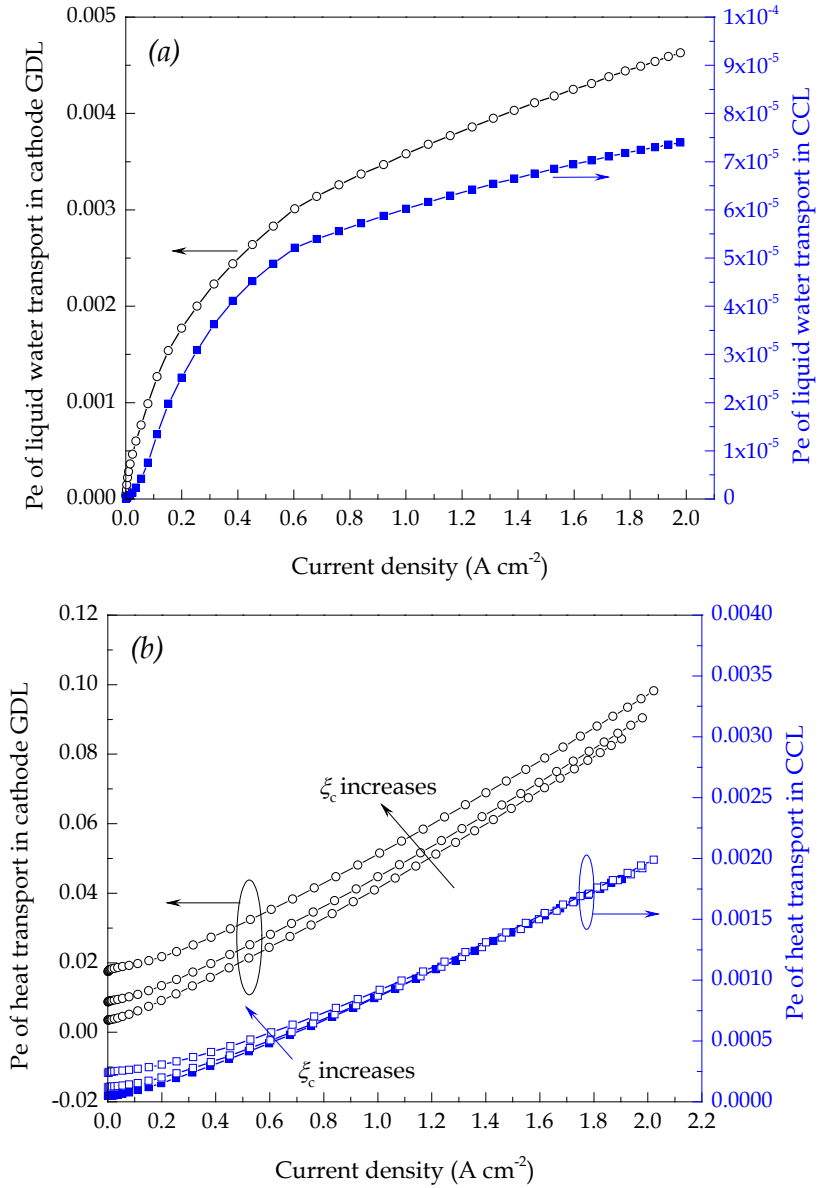


Figure 7-29 Average Paclet number ( $Pe$ ) of (a) liquid water transport and (b) heat transport within the GDL and CL of the cathode at various current densities with fully humidified gases

Paclet number ( $Pe$ ) is used to investigate the contributions of the rate of advection and diffusion for liquid water and heat transport, respectively. The average  $Pe$  of the liquid water transport and heat transport is shown in Figure 2-29. It is clear that both the  $Pe$  for liquid water and heat transport increases as the current density increases. It is also found that the  $Pe$  in GDL is larger than that in CL. This is contributed by the fact that GDL is located close to the channel, where the effect of convective mass transport is

more significant, especially near the GDL-channel boundary. Even not shown here, the curves obtained at various cathode stoichiometries almost overlap each other, indicating the slight effect of stoichiometry on liquid water transport. Thus, capillary diffusion is the main mechanism of liquid water transport through the electrode, leading to the neglectable advective effect. On the contrary, the effect of stoichiometry on the  $Pe$  of heat transport is relatively significant. In [Figure 2-29](#), the cathode stoichiometric flow ratios of 2.0, 5.0 and 10.0 are studied. The increase in cathode stoichiometric flow ratio leads to the increase in  $Pe$ . Moreover, the  $Pe$  is almost linearly dependent to the current density in the range of high current density. Comparing the  $Pe$  in the GDL and CL of the cathode shows that, heat in the catalyst layer is mainly removed by heat conduction. However, in the GDL, convective heat transfer corresponds to maximum 10% of total heat transport. It is because near the GDL-channel boundary the air flow velocity within the GDL is relative high in comparison with the area away from this boundary.

#### ***7.4.9 The novel flow channel design***

Due to the accumulation of liquid water downstream the channel, a long channel is prone to suffering from reactant gas mass transport problems. On the contrary, short channel may have the problem of insufficient electrochemical reactions. In other words, the reactant gases in short channels are not completely electrochemically reacted. As indicated in [Table 7-10](#), when other parameters are fixed constantly in base-case condition shown in [Table 7-8](#), 1 cm is the optimal channel length among the four channel lengths of 0.5, 1.0, 2.0 and 4.0 cm. In order to mitigate the impact of liquid water along-the-channel, a novel channel design which features multi- outlets and inlets grooved along the cathode channel is proposed as shown in [Figure 7-30](#) and [Figure 7-31](#). Two mitigation strategies are compared, depending on the numbers of inlet and outlet added.

[Figure 7-30](#) shows the velocity magnitude inside the electrodes and channels of three channel designs. Due to the relatively high stoichiometry at the cathode, the air flow velocity inside the cathode channel is faster than that of hydrogen at the anode. It is clear that the gas velocity downstream of the new grooved outlets is relatively low. This is mainly explained by the counter flow behavior between the pre-existent and newly introduced gases. Moreover, the newly introduced gases do not affect the overall gas flow direction.

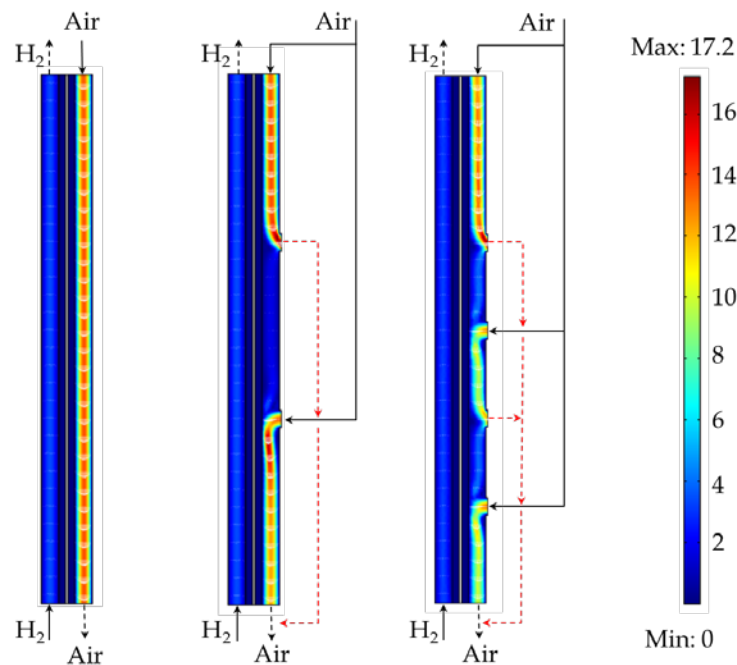


Figure 7-30 Velocity magnitudes of reactant gases at 0.3 V of three channel designs in base-case condition

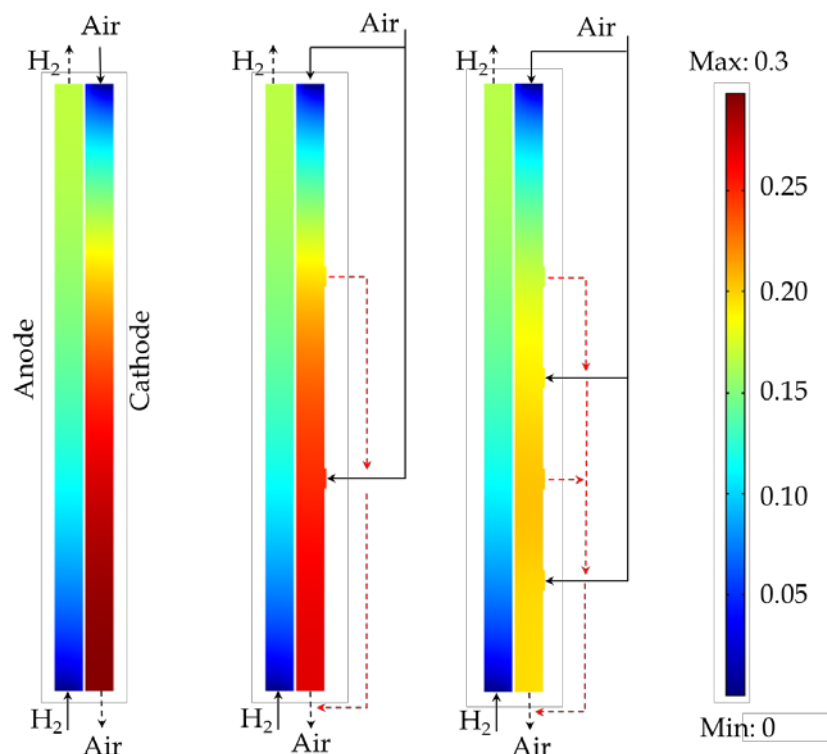


Figure 7-31 Profiles of liquid water saturation of three channel designs at  $1.2 \text{ A cm}^{-2}$  in base-case condition

The profiles of liquid water saturation inside the channels of three channel designs at  $1.2 \text{ A cm}^{-2}$  are shown in Figure 7-31. The liquid water saturation at both electrodes is reduced when a multi- inlets and outlets design is applied, which drain the liquid water

from the channel and avoid the accumulation of liquid water downstream the channel. The practical multi- air inlets and outlets channel is schematically showed in Figure 7-32. As demonstrated, air flows through the central channel (black one) and the generated liquid water can be diverted through the channel on the right (blue one) after a certain distance, while consumed oxygen in air flow will be replenished using the channel on the left (red one). More inlets and outlets can be added based on the conception indicated in Figure 7-32.

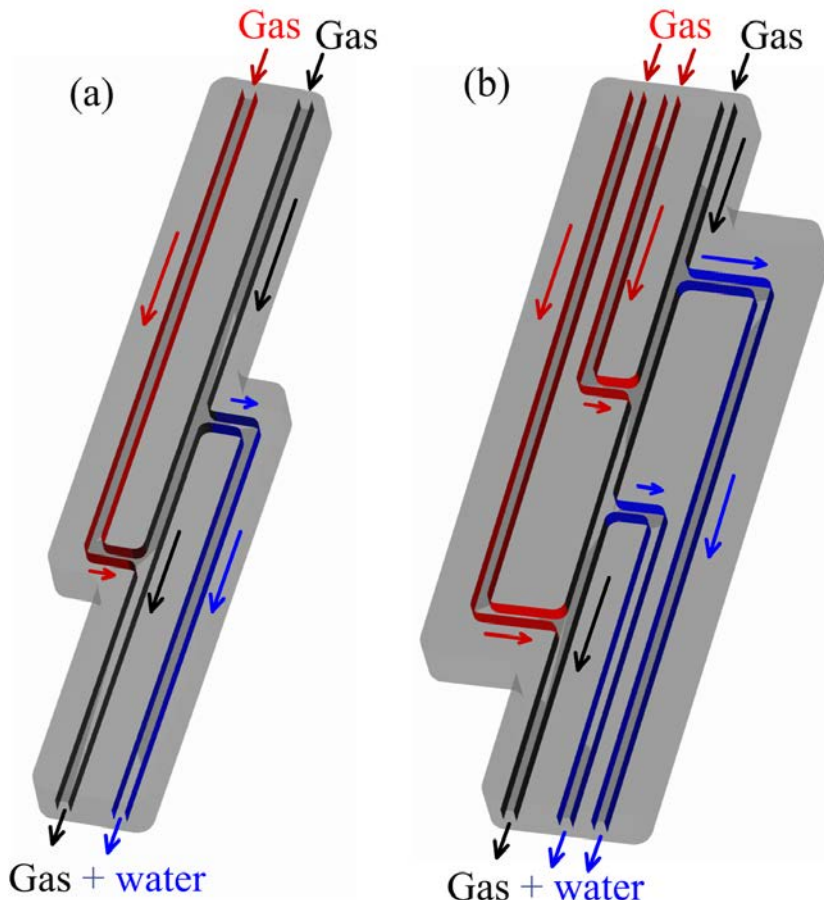


Figure 7-32 Sketch of gas channel using multi- inlets and outlets design (a) double (b) triple

## 7.5 Conclusions

A two-dimensional, along-the-channel, two-phase flow, non-isothermal, CFD model based on agglomerate catalyst layer structure is developed to study the distributions of liquid water and heat and catalyst layer effectiveness factors within the MEA and channels for a low temperature PEMFC. Liquid water flooding at the anode side is taken into account. The model developed is used to study the effects of electrode properties, e.g. contact angle, GDL porosity and thickness, and platinum loading, as well as channel geometries including channel length and depth, on the liquid water

distributions inside the MEA and channels. In addition, the interactive effects of relative humidity, stoichiometric flow ratio and channel length on the non-uniform distribution of liquid water, membrane/ionomer water content and heat, as well as cell performance are numerically studied.

The modelling results reveal that the increase in GDL thickness and channel depth lead to a monotonically decrease in cell performance in a large range of current densities while contact angle and channel length almost had no effect on the cell performance at low current densities. At high current densities, liquid water flooding can be mitigated when electrodes with larger contact angle, lower porosity and low platinum loading are used. In the meanwhile, liquid water saturations (volume fraction of liquid water in void space) can be reduced by shorter and deeper flow channels. Simulation results indicate a current density dependent optimal relative humidity. At low current densities, low relative humidity is of benefit to the cell performance. At medium and high current densities, the optimal cathode relative humidity increases as the anode relative humidity decreases. It is found that anode relative humidity is vital important to a high performance fuel cell due to the proportional relationship between anode relative humidity and the membrane/ionomer water content at the anode side. Therefore, fully humidified anode gas is required of maintaining the membrane/ionomer hydration. The optimal cathode relative humidity depends on anode relative humidity, channel length and current density. At medium current densities, as the anode relative humidity decreases from 100% to 50%, the optimal cathode relative humidity increases from 80% to 90% for channel length varies from 1.0 cm to 10 cm. On the contrary, at high current densities, the optimal cathode relative humidity increases from 30% to 70% for a 1.0 cm channel and increases from 40% to 70% for a 10 cm channel. Liquid water flooding cannot be avoided at the cathode using fully humidified gas, resulting in high cathode relative humidity an undesirable operating condition in full range of current densities. However, too low cathode relative humidity is hard to maintain the hydrated membrane/ionomer at the cathode side, resulting in a decrease in cell performance at medium and high current densities. At medium current densities, with fully humidified anode gas, the optimal cathode relative humidity is 80% for different lengths of channel of 1.0 and 10 cm. At high current densities, the optimal cathode relative humidity is 30% and 40% for 1.0 cm and 10 cm channel, respectively.

The increase in stoichiometric flow ratios at both the anode and cathode almost has no effect on the cell performance at low current densities. At medium and high current

densities, the initial increase in the cathode stoichiometric flow ratio improves the cell performance, e.g. the limiting current densities at various relative humidity. However, the further increase larger than 2.0 leads to limited contributions. The increase in stoichiometric flow ratio shortens the water flooding region and mitigates the degree of flooding in the channel, resulting in a more significant improvement of limiting current density for longer channel. The effect of anode stoichiometric flow ratio on cell performance can be omitted.

The Peclet number indicates that advection almost has no effect on the liquid water transport in the porous electrode, which is mainly governed by the capillary diffusion mechanism. On the contrary, advection contributes approximate 10% of heat transport inside the gas diffusion layer at limiting current densities. In flow channels, the heat removal ability of cathode gas is reduced as the stoichiometric flow ratio decreases.

It is also found that the temperature rise is sharp near the cathode inlet and the temperature slowly increases along the air flow to the outlet. The increase in GDL thickness could mitigate the temperature rise within the MEA but it is at an expense of the effectiveness factor of the catalyst layers due to the increased mass transport resistance. The flow channel of 1 cm is found to be the optimal length to the cell performance at high current densities. A new channel design featured with multi- outlets and inlets along-the-channel is capable of mitigating the water flooding and improving the cell performance.

## 7.6 Reference

1. Wong, K.H., K.H. Loo, Y. M. Lai, S.C. Tan and C.K. Tse, *A theoretical study of inlet relative humidity control in PEM fuel cell*. International Journal of Hydrogen Energy, 2011. **36**: p. 11871-11885.
2. Park, S., J.-W. Lee and B.N. Popov, *A review of gas diffusion layer in PEM fuel cells: Materials and designs*. International Journal of Hydrogen Energy, 2012. **37**: p. 5850-5865.
3. Holdcroft, S., *Fuel cell catalyst layer: A polymer science perspective*. Chemistry of Materials, 2014, **26**: p. 381-393.
4. Shimpalee, S., U. Beuscher and J.W. Van Zee, *Analysis of GDL flooding effects on PEMFC performance*. Electrochimica Acta, 2007. **52**: P. 6748-6754.

5. Park, S., J.-W. Lee and Popov, B.N., *Effect of PTFE content in microporous layer on water management in PEM fuel cells*. Journal of Power Sources, 2008. **177**: p. 457-463.
6. Ge, S. and C.-Y. Wang, *Liquid water formation and transport in the PEFC anode*. Journal of Electrochemistry Society, 2007. **154**: p. B998-B1005.
7. Barelli, L., G. Bidini, F. Gallorini and A. Ottaviano, *Analysis of the operating conditions influence on PEM fuel cell performance by means of a novel semi-empirical model*. International Journal of Hydrogen Energy, 2011. **36**: p. 10434-10442.
8. Wu, H., P. Berg and X. Li, *Modelling of PEMFC transients with finite-rate phase transfer processes*. Journal of Electrochemistry Society, 2010. **157**: p. B1-B12.
9. Wu, H., P. Berg and X. Li, *Steady and unsteady 3D non-isothermal modelling of PEM fuel cells with the effect of non-equilibrium phase transfer*. Applied Energy, 2010. **87**: 2778-2784.
10. Yang, X.G., Q. Ye and P. Cheng, *Matching of water and temperature fields in proton exchange membrane fuel cells with non-uniform distributions*. International Journal of Hydrogen Energy, 2011. **36**: p. 12524-12537.
11. Pasaogullari, U. and C.-Y. Wang, *Liquid water transport in gas diffusion layer of polymer electrolyte fuel cells*. Journal of Electrochemistry Society, 2004. **151**: p. A399-A406.
12. Cho, K.T. and M.M. Mench, *Investigation of the role of the micro-porous layer in polymer electrolyte fuel cells with hydrogen deuterium contrast neutron radiography*. Physical Chemistry Chemical Physics, 2012. **14**: p. 4296-4302.
13. Li, H., Y. Tang, Z. Wang, Z. Shi, S. Wu, D. Song et al., *A review of water flooding issues in the proton exchange membrane fuel cell*. Journal of Power Sources, 2008. **178**: p. 103-117.
14. Djilali, N., *Computational modelling of polymer electrolyte membrane (PEM) fuel cells: challenges and opportunities*. Energy, 2007. **32**: p. 269-280.
15. Siegel, C., *Review of computational heat and mass transfer modelling in polymer-electrolyte-membrane (PEM) fuel cells*. Energy, 2008. **33**: p. 1331-1352.
16. Shao, Y., G. Yin, Z. Wang and Y. Gao, *Proton exchange membrane fuel cell from low temperature to high temperature: Material challenges*. Journal of Power Sources, 2007. **167**: p. 235-242.

17. Xing, L., X. Liu, T. Alaje, R. Kumma, M. Mamlouk and K. Scott, *A two-phase flow and non-isothermal agglomerate model for a proton exchange membrane (PEM) fuel cell*. Energy, 2014. **73**: p. 618-634.
18. Wang, L., A. Husar, T. Zhou and H. Liu, *A parametric study of PEM fuel cell performances*. International Journal of Hydrogen Energy, 2003. **28**: p. 1263-1272.
19. Berning, T. and N. Djilali, *Three-dimensional computational analysis of transport phenomena in a PEM fuel cell – a parametric study*. Journal of Power Sources, 2003. **124**: p. 440-452.
20. Xing, L., M. Mamlouk and K. Scott, *A two-dimensional agglomerate model for a proton exchange membrane fuel cell*. Energy, 2013. **61**: p. 196-210.
21. Zhang, J., Y. Tang, C. Song, Z. Xia, H. Li, H. Wang and J. Zhang, *PEM fuel cell relative humidity (RH) and its effect on performance at high temperature*. Electrochimica Acta. 2008. **53**: p. 5315-5321.
22. Neyerlin, K.C., H. A. Gasteiger, C.K. Mittelsteadt, J. Jorne and W. Gu, *Effect of relative humidity on oxygen reduction kinetics in a PEMFC*. Journal of Electrochemistry Society, 2005. **152**: p. A1073-A1080.
23. Shinozaki, K., H. Yamada and Y. Morimoto, *Relative Humidity Dependence of Pt Utilization in Polymer Electrolyte Fuel Cell Electrodes: Effects of Electrode Thickness, Ionomer-to-Carbon Ratio, Ionomer Equivalent Weight, and Carbon Support*. Journal of Electrochemistry Society, 2011. **158**: p. B467-B475.
24. Turhan, A., K. Heller, J.S. Brenizer and M.M. Mench, *Quantification of liquid water accumulation and distribution in a polymer electrolyte fuel cell using neutron imaging*. Journal of Power Sources, 2006. **160**: p. 1195-203.
25. Xing, L., M. Mamlouk, R. Kumar and K. Scott, *Numerical investigation of the optimal Nafion ionomer content in cathode catalyst layer: An agglomerate two-phase flow modelling*. International Journal of Hydrogen Energy, 2014. **39**: 9087-9104.
26. Xing, L., P.K. Das, X. Song, M. Mamlouk and K. Scott, *Numerical analysis of the optimum membrane/ionomer water content of PEMFCs: The interaction of Nafion ionomer content and cathode relative humidity*. Applied Energy, 2015. **138**: p. 440.
27. Borup, R.L., J.R. Davey, F.H. Garzon, D.L. Wood and M.A. Inbody, *PEM fuel cell electrocatalyst durability measurements*. Journal of Power Sources, 2006. **163**: p. 76-81.

28. Bi, W., Q. Sun, Y. Deng and T.F. Fuller, *The effect of humidity and oxygen partial pressure on degradation of Pt/C catalyst in PEM fuel cell*. *Electrochimica Acta*, 2009. **54**: p. 1826-1833.
29. Lim, K.H., H.S. Oh, S.E. Jang, Y.J. Ko, H.J. Kim and H. Kim, *Effect of operating conditions on carbon corrosion in polymer electrolyte membrane fuel cells*. *Journal of Power Sources*, 2009. **193**: p. 575-579.
30. Inaba, M., T. Kinumoto, M. Kiriake, R. Umebayashi, A. Tasaka and Z. Ogumi, *Gas crossover and membrane degradation in polymer electrolyte fuel cells*. *Electrochimica Acta*, 2006. **51**: p. 5746-5753.
31. Chen, J., J.B. Siegel, T. Matsuura and A.G. Stefanopoulou, *Carbon corrosion in PEM fuel cell dead-ended anode operation*. *Journal of Electrochemistry Society*, 2011. **158**: p. B1164-B1174.
32. Panha, K., M. Fowler, X. Yuan and H. Wang, *Accelerated durability testing via reactants relative humidity cycling on PEM fuel cells*. *Applied Energy*, 2012. **93**: p. 90-97.
33. Qu, S., X. Li, M. Hou, Z. Shao and B. Yi, *The effect of air stoichiometry change on the dynamic behaviour of a proton exchange membrane fuel cell*. *Journal of Power Sources*, 2008. **185**: p. 302-310.
34. Zhang, F.Y., X.G. Yang and C.-W. Wang, *Liquid water removal from a polymer electrolyte fuel cell*. *Journal of Electrochemistry Society*, 2006. **153**: p. A225-A232.
35. Wang, C.Y., M. Groll, J.S. Rosler and C.J. Tu, *Porous medium model for two-phase flow in mini channels with applications to micro heat pipes*. *Heat Recovery Systems and CHP*, 1994. **14**: p. 377-390.
36. Wilke, C.R., *A viscosity equation for gas mixture*. *The Journal of Chemical Physics*, 1950. **18**: p. 517-519.
37. Kumar, R. and K. Scott, K, Freestanding sulfonated grapheme oxide paper: a new polymer electrolyte for polymer electrolyte fuel cells. *Chemical Communications*, 2012. **48**: p. 5584-5586.
38. Mason, T.J., J. Millichamp, T. P. Neville, P.R. Shearing, S. Simons, D.J.L. Brett, *A study of the effect of water management and electrode flooding on the dimensional change of polymer electrolyte fuel cells*. *Journal of Power Sources*, 2013. **242**: p. 70-77.
39. Xing, L., X.G. Song, K. Scott, V. Pickert and W.P. Cao, *Multi-variable*

- optimisation of PEMFC cathodes based on surrogate modelling.* International Journal of Hydrogen Energy, 2013. **38**: p. 14295-14313.
40. Zhou, Y., G. Lin, A.J. Shih and S.J. Hu, *Assembly pressure and membrane swelling in PEM fuel cells.* Journal of Power Sources, 2009. **192**: p. 544-551.
41. Iranzo, A., P. Boillat, J. Biesdorf and A. Salva, *Investigation of the liquid water distribution in a 50 cm<sup>2</sup> PEM fuel cell: effects of reactants relative humidity, current density, and cathode stoichiometry.* Energy, 2015. **82**: p. 914-921.
42. Kim, K.-H., K.-Y. Lee, S.-Y. Lee, E. Cho, T.-H. Lim, H.-J. Kim et al., *The effect of relative humidity on the performance of PEMFC MEAs with various Nafion® ionomer contents.* International Journal of Hydrogen Energy, 2010. **35**: p. 13104-13110.
43. Xing, L., S. Du, R. Chen, M. Mamlouk, M and K, Scott, *Anode partial flooding modelling of proton exchange membrane fuel cells: Model development and validation.* Energy, 2016. **96**: p. 80-95.
44. Benziger, J., E. Kimball, R. Mejia-Ariza and I. Kevrekidis, *Oxygen mass transport limitations at the cathode of polymer electrolyte membrane fuel cells.* AIChE Journal, 2011. **57**: p. 2505-2517.
45. Kulikovsky, A.A., *The effect of stoichiometric ratio  $\lambda$  on the performance of a polymer electrolyte fuel cell.* Electrochimica Acta, 2004. **49**: p. 617-625.

## Chapter 8. Cathode catalyst layer optimisation

In this chapter, five design parameter of the cathode catalyst layer, namely platinum loading ( $m_{\text{Pt}}$ ), platinum mass ratio ( $f$ ), ionomer volume fraction ( $L_M$ ), catalyst layer thickness ( $l_{\text{CL}}$ ) and agglomerate radius ( $r_{\text{agg}}$ ) are optimised by a multiple surrogate model and their sensitivities are analysed by a Monte Carlo method based approach. Two optimisation strategies, maximising the current density at a fixed cell voltage and during a specific cell voltage range, are implemented for the optima prediction.

### 8.1 Introduction

Although significant improvements on PEMFC performance have been achieved over the last ten years, the high cost associated with platinum catalyst is one of the major barriers hampering the commercial use of PEMFCs. Since platinum is dispersed within carbon black and combines with electrolyte to construct the catalyst layer, the performance depends on how effectively the platinum is dispersed, i.e. the effectiveness of the catalyst layer [1]. Accordingly, the function of different component within the catalyst layer requires the existence of triple phase boundaries (TPB) [2], where the content of ionomer (for proton transfer), void space (for gas transport) and platinum dispersed carbon (for catalysis and electron transfer) interacted [3-7]. As a result, optimisation of the composition and structure of the electrode is important.

Traditionally, the optimum composition and structure of the catalyst layer is conducted through experiments [4-7], which are expensive and time-consuming. Computer simulations facilitate the exploration of alternative designs and reduce the resource and time for producing expensive prototypes. Numerical simulations also help the design and optimisation of a fuel cell, there has been many studies in this area [8-16]. For instance, Wu *et al.* [9] investigated the optimal operating conditions of hydrogen polymer electrolyte fuel cells based on the radial basis function (RBF) surrogate model. Tirnovan *et al.* [10, 11] applied a moving least squares (MLS) model for the PEMFC, and proved that the method was suitable for predicting and describing the fuel cell behaviour in all points of the approximation domain. Zervas *et al.* [12] utilised radial basis function (RBF) neural network architecture for optimizing the operation of fuel cells systems. Wahdame *et al.* [13] reviewed design of experiment (DoE) techniques for fuel cell characterisation and development. Miao and Cheng *et al.* [14, 17] presented an

approach to improve the performance of the power density of a PEMFC based on artificial neural network (ANN) metamodel.

The design optimisation of PEMFC is challenging due to several factors: (a) fuel cell simulation is still lengthy and complicated, (b) there are many design variables to be considered, (c) design variables are interdependent, (d) multiple design objectives are desired simultaneously and multiple design constraints need to be satisfied, (e) conventional sensitivity-based optimisation method is not suitable for the local sensitivity issues. In addition, most of the aforementioned research adopted maximizing the current density at a specific voltage as the optimisation objective. However, PEMFCs do not usually work at a fixed voltage, the voltage condition always has a certain variation as the environments surrounding it and other factors, such as operating temperature [18], always change. For this reason, the present study concerns both optimisation of the PEMFC at specific voltages and within specific voltage ranges.

To solve these problems, a surrogate model technique is introduced in this chapter, which could formulate an explicit relationship between the objective/constraint functions and design variables in terms of a few computer simulations and thus it can calculate the local sensitivity quickly and efficiently. An optimisation algorithm is implemented to search for the global optimum designs and a global sensitivity analysis based on Monte Carlo (MC) method is carried out to examine the influence of design variables on the fuel cell performance.

## 8.2 Mathematical model

The mathematical model developed in [Chapter 4](#) is used to describe the mass balance and transport, reactant diffusion and reaction, water transport through the membrane, charge conservation and current distribution coupled in the PEMFCs. Water phase transfer, two-phase flow, and non-isothermal operation are not included in this model. In order to account for the liquid water generation at high current density, we assume that liquid water fills the primary pores inside the agglomerate only. The same assumption can be found from the work of Marr *et al.* [19].

Another highlighted feature of this model is the effective diffusion coefficient. In order to account for gas diffusion in anisotropic porous electrodes, the effective diffusion coefficient is corrected by the percolation theory presented by Nam and Kaviani [20] instead of the Bruggeman's factor as follow:

$$f(\varepsilon) = \varepsilon \left( \frac{\varepsilon - \varepsilon_{pc}}{1 - \varepsilon_{pc}} \right)^{\chi} \quad \chi = \begin{cases} 0.521 & \text{in-plane} \\ 0.785 & \text{through-plane} \end{cases} \quad (8-1)$$

where  $\varepsilon_{pc}$  is the percolation critical value of the porosity.  $\varepsilon_{pc} = 0.11$  reported by Pharoah *et al.* [33]. As assumed previously, the primary pores can be completely filled by liquid water. Then oxygen diffuses through the secondary pores to the outer boundary of the ionomer film. The effective diffusion coefficient of oxygen diffusion in catalyst layer is:

$$D_{O_2,CL}^{eff} = f(\varepsilon_s) D_{O_2-P}^0 \quad (8-2)$$

The effective diffusion coefficient of oxygen within agglomerate is

$$D_{O_2,agg}^{eff} = f(\varepsilon_{agg,M}) D_{O_2-M}^0 + f(\varepsilon_{agg,p}) D_{O_2-W}^0 \quad (8-3)$$

$D_{O_2-M}^0$ ,  $D_{O_2-W}^0$  and  $D_{O_2-P}^0$  ( $m^2 s^{-1}$ ), which have been explained in Chapter 3, are the intrinsic diffusion coefficients of oxygen through ionomer film, liquid water and void space, respectively.

The boundary conditions and computational process are as same as that of the two-dimensional, along-the-channel, single phase, isothermal model represented in Chapter 4.

### 8.3 Model verification and validation

#### 8.3.1 Mesh independence

Theoretically, the calculating errors in the solution related to the grid must disappear for an increasingly fine mesh. In this study, the current density at a certain cell voltage (0.7V) is taken as the parameter to evaluate six grids (see Table 8-1) and determine the influence of the number of nodes on the solution. It is clear in Figure 8-1 that the current density reaches an asymptotic value while the calculating time increases as the number of nodes increases. Having considering both the calculation time and accuracy in this work, Grid D is selected as it is considered to be sufficiently reliable to ensure mesh independence with acceptable calculating time.

Table 8-1 Characters of mesh sizes

Mesh characteristics	Number of nodes
Grid A	6894
Grid B	31490
Grid C	110290
Grid D	262055
Grid E	434290
Grid F	648265

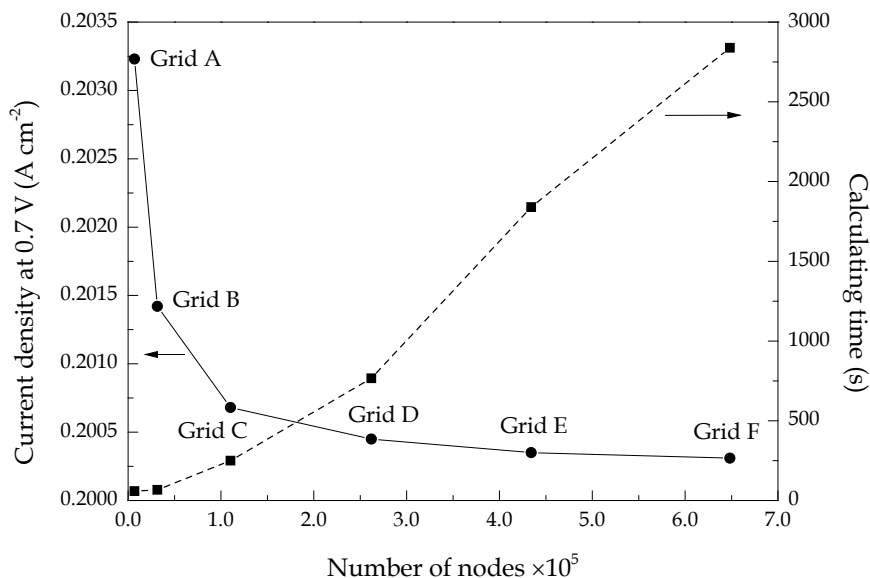


Figure 8-1 Influence of mesh characteristics on current density

### 8.3.2 Model validation

The modelling results are validated by the experimental data in Figure 4-3 of Chapter 4, in which the predicted polarisation curves agree well with the experimental data. Thus the numerical model is proven to be sufficiently accurate.

## 8.4 Global sensitivity analysis and design optimisation

Global sensitivity analysis (GSA) and design optimisation are increasingly recognized as useful tools for the analysis and design of PEMFCs. The former is able to determine the influence of design variables on a PEMFC. The latter could help identify the optimum design under different conditions. However, a global sensitivity analysis

and/or design optimisation of a fuel cell is still a challenging endeavour because the relations between design variables and design objectives/constraints are often not explicitly known. A function of a certain design can generally be found from a large number of time-consuming numerical calculations. To do this, explicitly known approximations of objective/constraint functions in terms of a few sampling data obtained from computer simulations can be used, which is called a surrogate model (also called metamodel technique).

The optimisation in this chapter adopts a widespread used surrogate model- Kriging (KRG) model- to evaluate the approximation models of the objective functions. The approximation models are then used to visualise the input-output relationship, assess the effect of each design variable and predict the optimum design of the cathode catalyst layer.

#### **8.4.1 Kriging Surrogate models**

Kriging model was originally developed for mining and geostatistical application involving spatially and temporally correlated data [21, 22]. Kriging model postulates a combination of a global model combined with departures:

$$y(\tilde{x}) = f(\tilde{x}) + Z(\tilde{x}) \quad (8-4)$$

where  $y(\tilde{x})$  is the unknown function of interest,  $f(\tilde{x})$  is a known polynomial, and  $Z(\tilde{x})$  is assumed as a Gaussian random process with mean zero and variance  $\sigma^2$  as well as a non-zero covariance to create local deviations so that Kriging model interpolates the sampled data points. The covariance matrix of  $Z(\tilde{x})$  is formulated as

$$\text{Cov}[Z(\tilde{x}^i), Z(\tilde{x}^j)] = \sigma^2 \mathbf{R} \quad \mathbf{R} = [R(\tilde{x}^i, \tilde{x}^j)] \quad (8-5)$$

where  $\mathbf{R}$  is the symmetric correlation matrix with ones along the diagonal, and  $R(\tilde{x}^i, \tilde{x}^j)$  is the correlation function between any two sampled data points  $\tilde{x}^i$  and  $\tilde{x}^j$ . The correlation function could be exponential, Gaussian, cubic or other kinds of functions. In this work, the Gaussian correlation function is assumed:

$$R(\tilde{x}^i, \tilde{x}^j) = \exp\left(-\sum_{k=1}^{n_{dv}} \theta_k |\tilde{x}_k^i - \tilde{x}_k^j|^2\right) \quad (8-6)$$

where  $n_{dv}$  is the number of design variables,  $\theta_k$  are the unknown correlation parameters used to fit the model, and  $|\tilde{x}_k^i - \tilde{x}_k^j|$  is the distance between the  $k$ -th components of sample points  $\tilde{x}^i$  and  $\tilde{x}^j$ . Once the correlation function has been selected, the estimate,  $\hat{y}$ , of the response  $y(\tilde{x})$  at untried values of  $\tilde{x}$  are given as:

$$\hat{y} = \hat{\beta} + \mathbf{r}^T(\tilde{\mathbf{x}})\mathbf{R}^{-1}(\mathbf{y} - \mathbf{f}\hat{\beta}) \quad (8-7)$$

where  $\mathbf{y}$  is the column vector of length  $n_s$  which contains the sample values of the response, and  $\mathbf{f}$  is an column vector of length  $n_s$  which is filled with ones when  $f(\tilde{x})$  is taken as constant.  $\mathbf{r}^T(\tilde{\mathbf{x}})$  is the correlation vector between a untried  $\tilde{x}$  and the sampled data points:

$$\mathbf{r}^T(\tilde{\mathbf{x}}) = [R(\tilde{x}, \tilde{x}^1), R(\tilde{x}, \tilde{x}^2), \dots, R(\tilde{x}, \tilde{x}^{n_s})]^T \quad (8-8)$$

and  $\hat{\beta}$  is estimated as

$$\hat{\beta} = (\mathbf{f}^T \mathbf{R}^{-1} \mathbf{f})^{-1} \mathbf{f}^T \mathbf{R}^{-1} \mathbf{y} \quad (8-9)$$

The estimate of variance of the sample data from the global model is

$$\hat{\sigma}^2 = \frac{(\mathbf{y} - \mathbf{f}\hat{\beta})^T \mathbf{R}^{-1} (\mathbf{y} - \mathbf{f}\hat{\beta})}{n_s} \quad (8-10)$$

where  $f(\tilde{x})$  is assumed to be the constant  $\hat{\beta}$ . The maximum likelihood estimates (i.e., “best guesses”) for  $\theta_k$  in Eq. (8-6) used to fit the model can be found by solving the following maximisation problem over the interval  $\theta_k > 0$ :

$$\max \left( -\frac{n_s \ln(\hat{\sigma}^2) + \ln|\mathbf{R}|}{2} \right) \quad (8-11)$$

where both  $\hat{\sigma}^2$  and  $|\mathbf{R}|$  are the functions of  $\theta_k$ .

#### 8.4.2 Sobol' Global sensitivity analysis

There are two kinds of sensitivities, one is called local sensitivity and the other is global sensitivity. Local sensitivity is equivalent to the partial derivative, which is

usually used to locally estimate the sensitivity of an objective to a specific design variable. On the contrary, global sensitivity characterizes the overall behaviour of a specific design variable on a system or model. GSA can increase the understanding of the relationships between design variables and design objective and classify the individual variable influence, hence help researcher to pay more attention on the design variables with large influence, and remove design variables with less influence. Among many kinds of GSA methods, Sobol' method [23, 24] is used to do it in this work. The Sobol' method is a variance-based Monte Carlo method that allows the computation of both the sensitivity indices of individual parameters,  $S_i$ , and the interactions between these parameters through the ratio of each sensitivity index to the corresponding total sensitivity index,  $S_i^{tot}$ . Specifically, considering an integrable function,  $f(\tilde{\mathbf{x}})$ , which can be written in the form:

$$f(\tilde{\mathbf{x}}) = f_0 + \sum_{s=1}^n \sum_{i_1 < \dots < i_s} f_{i_1 \dots i_s}(\tilde{x}_{i_1}, \dots, \tilde{x}_{i_s}) \quad (8-12)$$

where  $1 \leq i_1 < \dots < i_s \leq n$ ,  $f_{i_1 \dots i_s}(\tilde{x}_{i_1}, \dots, \tilde{x}_{i_s})$  is a function of a unique subset of variables from  $\tilde{\mathbf{x}}$ . The components  $f_i(\tilde{x}_i)$  are called the first order terms,  $f_{ij}(\tilde{x}_i, \tilde{x}_j)$  are the second order terms and so on. The total number of summands in Eq. (8-12) is  $2n$ . Eq. (8-12) is also called the ANOVA representation of  $f(\tilde{\mathbf{x}})$  if

$$\int_0^1 f_{i_1 \dots i_s}(\tilde{x}_{i_1}, \dots, \tilde{x}_{i_s}) d\tilde{x}_k = 0 \quad \text{for } k = i_1, \dots, i_s \quad (8-13)$$

It follows from condition Eq. (8-13) that the members in Eq. (8-12) are orthogonal and can be expressed as integrals of  $f(\tilde{\mathbf{x}})$ . Assume now that  $f(\tilde{\mathbf{x}})$  is square integrable, then all the  $f_{i_1 \dots i_s}$  in Eq. (8-13) are square integrable as well. Squaring Eq. (8-13) and integrating over the  $n$ -dimensional unit hypercube, the following equation can be obtained:

$$\tilde{D} = \int f^2(\tilde{\mathbf{x}}) d\tilde{\mathbf{x}} - f_0^2 = \sum_{s=1}^n \sum_{i_1 < \dots < i_s} \int f_{i_1 \dots i_s}^2 d\tilde{x}_{i_1} d\tilde{x}_{i_s} = \sum_{s=1}^n \sum_{i_1 < \dots < i_s} \int \tilde{D}_{i_1 \dots i_s} \quad (8-14)$$

where  $\tilde{D}_{i_1 \dots i_s}$  is the partial variance in the model response brought about by simultaneous changes in factors  $i_1$  to  $i_s$  and  $D$  is the total variance of  $f(\tilde{\mathbf{x}})$ . Then the global sensitivity indices of each variable can be calculated in terms of following equation:

$$S_{i_1 \cdots i_s} = \frac{\tilde{D}_{i_1 \cdots i_s}}{\tilde{D}} \quad (8-15)$$

This method can be extended to evaluate the global sensitivity indices of an arbitrary set of  $m$  variables. Let  $y$  denote the set of  $m$  variables ( $1 \leq m \leq n-1$ ), and  $Z$  denote the set of  $n-m$  complementary variables, thus  $\tilde{x} = (y, z)$ , let  $K = (k_1, \dots, k_m)$ . The variance corresponding to the subset  $y$  can be defined as

$$\tilde{D}_y = \sum_{s=1}^m \sum_{(i_1 < \dots < i_s) \in K} \int \tilde{D}_{i_1 \cdots i_s} \quad (8-16)$$

The sum in Eq. (8-16) is extended over all groups  $(i_1, \dots, i_s)$  where all the  $i_1, \dots, i_s$  belongs to  $K$ . Similarly, the variance  $D_z$  can be obtained. Then the total variance corresponding to the subset  $y$  is

$$\tilde{D}_y^{tot} = \tilde{D} - \tilde{D}_z \quad (8-17)$$

Note that  $\tilde{D}_y^{tot}$  is also a sum of  $S_{i_1 \cdots i_s}$ , but it is extended over all group  $(i_1, \dots, i_s)$  where at least one  $i_j \in K$ . Here  $1 \leq s \leq n$ . Therefore the individual sensitivity indices (or main sensitivity indices) and the total sensitivity indices can be calculated as follows:

$$S_y = \frac{\tilde{D}_y}{\tilde{D}} \quad (8-18)$$

$$S_y^{tot} = \frac{\tilde{D}_y^{tot}}{\tilde{D}} \quad (8-19)$$

It is obvious that  $S_y^{tot} = 1 - S_z$  and always  $0 \leq S_y \leq S_y^{tot} \leq 1$ . Then a Monte Carlo method can be conducted to calculate the sensitivity indices.

## 8.5 Optimisation formulation

The performance of a PEMFC is often characterized by its polarization behaviour, i.e. voltage versus current density. For design optimisation of a specific PEMFC, the objective is usually set to maximise the current density at given cell voltages and other constraint conditions. That is, a fixed voltage is usually assumed beforehand, and current density at this voltage is maximised by using optimisation methods. However, a PEMFC does not always work at one fixed voltage but usually works within a varying

range of cell voltage based on different environment and work conditions. This variation of the cell voltage means that the optimal design obtained based on one fixed cell voltage is not necessarily the best design for other voltages. Consequently, the so-called optimal design cannot produce the best performance when the voltage changes in the fluctuation range. To avoid this problem, a new objective function considering the average performance of a PEMFC within a given range of cell voltage is added. There are two optimisation strategies, strategy A and B, corresponding formulations in this work, which are presented as follows.

Strategy A: the common formulation at fixed cell voltage:

$$\begin{aligned} & \text{find } \tilde{\mathbf{x}}_i(m_{Pt}, f, L_M, l_{CL}, r_{agg}) \\ & \left\{ \begin{array}{l} \max. i_i (\text{at fixed } E_i) \\ \text{s.t.} \begin{cases} \varepsilon_{pc} \leq \varepsilon_{CL} \leq 1.0 \\ 0 < L_{Pt/C} < 1.0 \\ \tilde{\mathbf{x}}_{LB} \leq \tilde{\mathbf{x}}_i \leq \tilde{\mathbf{x}}_{UB} \end{cases} \end{array} \right. \end{aligned} \quad (8-20)$$

where  $i_i$  is the current density at a fixed cell voltage  $E_i$ , and integral  $i$  varies from 1 to 9, corresponding to the cell voltage from 0.2V to 1.15V (OCP at base-case conditions), respectively. There are five design variables,  $m_{Pt}$ (mg cm<sup>-2</sup>) is the platinum loading,  $f$  is the platinum mass ratio,  $L_M$  is the ionomer volume fraction in cathode catalyst layer,  $l_{CL}$ (m) is the catalyst layer thickness,  $r_{agg}$ (m) is the agglomerate radius, the bound of each variable is listed in [Table 8-2](#). In addition, other two parameters  $\varepsilon_{CL}$  and  $L_{Pt/C}$  are both constrained in the range of  $\varepsilon_{pc} \sim 100\%$  and 0~100%, respectively.

Strategy B: the new one for a specific range of cell voltage:

$$\begin{aligned} & \text{find } \tilde{\mathbf{x}}_{ij}(m_{Pt}, f, L_M, l_{CL}, r_{agg}) \\ & \left\{ \begin{array}{l} \max. \bar{i}_{ij} (\text{from } E_i \text{ to } E_j) \\ \text{s.t.} \begin{cases} \varepsilon_{pc} \leq \varepsilon_{CL} \leq 1.0 \\ 0 < L_{Pt/C} < 1.0 \\ \tilde{\mathbf{x}}_{LB} \leq \tilde{\mathbf{x}}_i \leq \tilde{\mathbf{x}}_{UB} \end{cases} \end{array} \right. \end{aligned} \quad (8-21)$$

where  $\bar{i}_{ij}$  is the average current density for the cell voltage from  $E_i$  to  $E_j$ , integral  $i$  is smaller than integral  $j$ ,  $\tilde{\mathbf{x}}_{ij}$  is the vector of the optimal design variables.

In strategies A and B, the objectives are to find the optimal design  $\tilde{\mathbf{x}}_i$  which is capable of maximising the current densities at a fixed cell voltage or during a specific cell voltage range subjected to the following constraints: (1) the catalyst layer porosity between the percolation critical value and 1; (2) the volume fraction of  $Pt/C$  between 0 and 1; 3). the design variables between the lower boundary and upper boundary.

Table 8-2 Lower and upper bound of design variables for the optimisation

Design parameters	Description (Unit)	Lower bound	Upper bound
$m_{Pt}$	Platinum loading ( $\text{mg cm}^{-2}$ )	0.1	1.0
$f$	Platinum mass ratio to $Pt/C$	0.2	0.8
$L_M$	Electrolyte volume fraction	0.05	0.5
$l_{CL}$	Catalyst layer thickness ( $\mu\text{m}$ )	5.0	30.0
$r_{agg}$	Agglomerate radius ( $\mu\text{m}$ )	0.1	1.0

## 8.6 Implementation of the optimisation process

The proposed simulation-based optimisation approach consists of the following 7 steps as shown in [Figure 8-2](#).

1. Optimisation problem, including design variables, ranges of variables, design objectives and design constraints, are defined.
2. A sampling strategy is determined and a series of sampling points are generated in the design domain, numerical simulations are carried out at these sampling points and corresponding response values are collected.
3. Constructing the surrogate models (KRG) based on the sample data. Note that the KRG model cannot be explicitly obtained as the second term in the right hand of [Eq. \(8-4\)](#) varies significantly for different estimated design.
4. Checking the accuracy of the surrogate models, if the accuracy satisfies the required criterion, then it goes to the next step, otherwise, more sampling data should be added in terms of sequential sampling strategies [25] and new surrogate models with more accuracy are constructed.
5. Combining optimisation algorithm with the surrogate models to search the optimum design under specific working condition.

6. Validating the optimisation results, the validation result can generally be satisfied if the sampling data generated above is sufficient enough and the right surrogate model is employed. However, this step remains necessary to guarantee the optimum designs have the best performance. In case of error between the predicted optimal design and validation design, new infill sampling data like those in the fourth step should be added and a new loop will stop until the validation results satisfy the desired criterion.
7. Carrying out GSAs in terms of the surrogate models to investigate the effects of design variables.

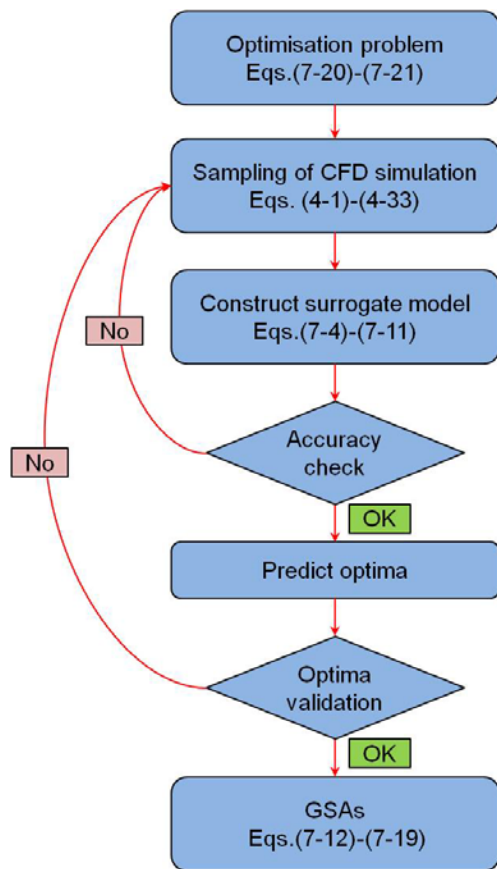


Figure 8-2 Flowchart of the optimisation process

## 8.7 Optimisation at a fixed cell voltage

The optimisation problem in Strategy A (Eq. 8-20) is solved in this section for three different cell voltages: low (0.2 V), medium (0.5 V) and high (0.8 V) which corresponds to a high, medium and low current densities. For each of these cases, the effect of structural parameters, including platinum loading, platinum mass ratio, catalyst layer thickness, ionomer volume fraction and agglomerate radius, on fuel cell performance is studied. In addition, as mentioned above, the optimal design obtained is

taken into the agglomerate model as a new design to validate the optimisation results. In this model, coordinates  $X$  and  $Y$  refer to diffusion and flow direction, respectively.

### 8.7.1 Base design

The parameters of base design are presented in [Table 8-3](#). For this initial design, the volume fractions of solid phase ( $\varepsilon_s$ ), ionomer ( $L_M$ ) and void space ( $\varepsilon_{CL}$ ) of the cathode catalyst layer are 63.5%, 20.0% and 16.5% respectively. In this situation, the current density at 0.8, 0.5 and 0.2 V are 0.05, 0.46 and 0.52 A cm<sup>-2</sup>, respectively. The optimal composition of catalyst layer is then obtained by solving the optimisation problems in [Eq. \(8-20\)](#) and [Eq. \(8-21\)](#). Then the polarisation curve, oxygen mole fraction, cathode overpotential and cathode volumetric current density for the base design in contrast to the optimal design are shown in figures from [Figure 8-3](#) to [Figure 8-5](#).

Table 8-3 Physical parameters for base-case conditions

<i>Electrode parameters</i>	<i>Value</i>
Platinum loading, $m_{Pt}$ (mg cm <sup>-2</sup> )	0.4
Platinum mass ratio, $f$	0.2
Ionomer volume fraction, $L_M$	0.2
Catalyst layer thickness, $l_{CL}$ (μm)	15.0
Agglomerate radius, $r_{agg}$ (μm)	0.2
<i>Operating conditions</i>	<i>Value</i>
Operating temperature, $T$ (K)	343
Anode pressure, $p_a$ (atm)	1.0
Cathode pressure, $p_c$ (atm)	1.0
Relative humidity, $RH$ (%)	100
Anode stoichiometric flow ratio, $\xi_a$	1.2
Cathode stoichiometric flow ratio, $\xi_c$	2.0

Five design variables, platinum loading, platinum mass ratio, ionomer volume fraction, catalyst layer thickness and agglomerate radius are abbreviated as

$\{m_{Pt}, f, L_M, l_{CL}, r_{agg}\}$ . At base design, the ionomer film thickness ( $\delta_M$ ) and agglomerate specific area ( $a_{agg}$ ) are  $1.55 \times 10^{-8}$  m and  $4.22 \times 10^7$  m<sup>-1</sup>, respectively.

### 8.7.2 Optimisation at low cell voltage

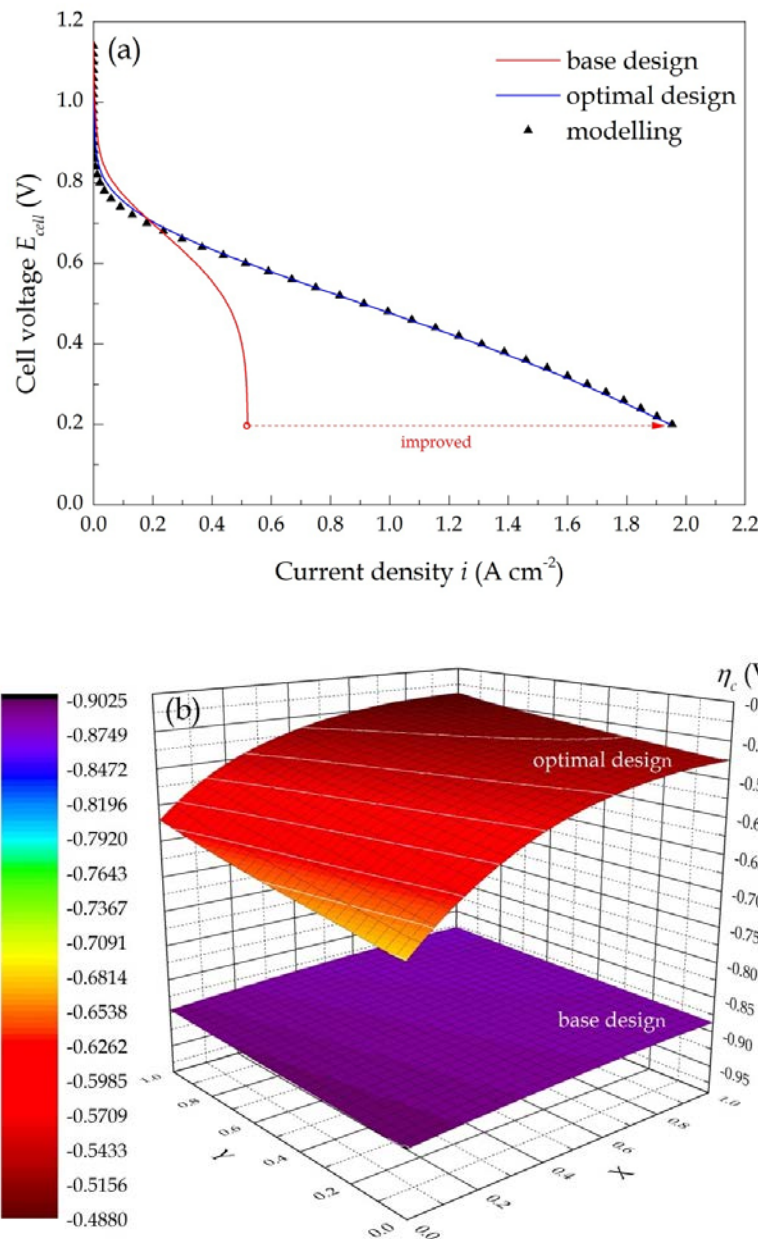
Figure 8-3 shows the polarization curve, cathode overpotential, cathode volumetric current density and oxygen mole fraction for the base design and the optimal design at 0.2 V. The simulation results, based on the agglomerate model, agree very well with the optimisation results, with a maximum error of approximately 0.3% at lower current density. It is clear in Figure 8-3(a), at 0.2 V, the current density increases from 0.52 to 1.95 A cm<sup>-2</sup> for the optimal design  $\{m_{Pt}, f, L_M, l_{CL}, r_{agg}\} = \{1.0, 80.0\%, 7.0\%, 5.0, 0.1\}$ .

For these values,  $\varepsilon_s$ ,  $L_M$  and  $\varepsilon_{CL}$  are 40.1%, 7.0% and 52.9%, respectively. Moreover, the optimal design simultaneously decrease  $\delta_M$  to  $3.16 \times 10^{-10}$  m and  $a_{agg}$  to  $3.41 \times 10^7$  m<sup>-1</sup>. The increase in current density upon optimal design is due to the decrease in the ionomer film thickness and the increases in catalyst layer porosity. This is because the dramatic fall in current density at lower cell voltages is mainly due to the oxygen transport limitation through the ionomer film [19, 26] and within the void space of the porous electrode [3].

It is clear in Figure 8-3(b) that the absolute value of cathode average overpotential decreases from 0.89 to 0.55 V, resulting in an improvement in cell performance according to Eq. (4-21). The maximum absolute value of cathode overpotential is observed at the cathode outlet adjacent to the membrane where the biggest oxygen transport resistance exists. The overpotential on the cathode is negative, which results in the second term of Eq. (3-13) much smaller than is reasonable to omit. According to Eq. (3-13), the increase in the absolute value of cathode overpotential enhances the oxygen reduction reaction (ORR), leading to a relative higher cathode volumetric current density since overpotential is the driving force for the reaction rate. However, according to Eq. (4-21), higher overpotential decreases the current density of the cell. Consequently, optimal overpotential is required for the best performance of the cell. As shown in Figure 8-3(c), for optimal design, the cathode volumetric current density increases everywhere, but is less uniform, in the cathode catalyst layer. The biggest increase occurs at the CL-membrane interface near the cathode inlet where both the oxygen concentration and proton conductivity are relatively higher. The average cathode volumetric current density increases from 282.80 to 3892.87 A cm<sup>-3</sup>. The

increase in current density can also be explained by the decrease in oxygen mole fraction as shown in Figure 8-3(d). The decrease in oxygen mole fraction and the increase in its gradient indicate a faster consumption of oxygen by applying the optimised parameters.

However, the optimal design performance is poorer than the base design at lower current densities, although it exhibits enhanced performance at higher current density which is because of the decrease in agglomerate specific area and then the decrease in ORR rate according to Eq. (3-31).



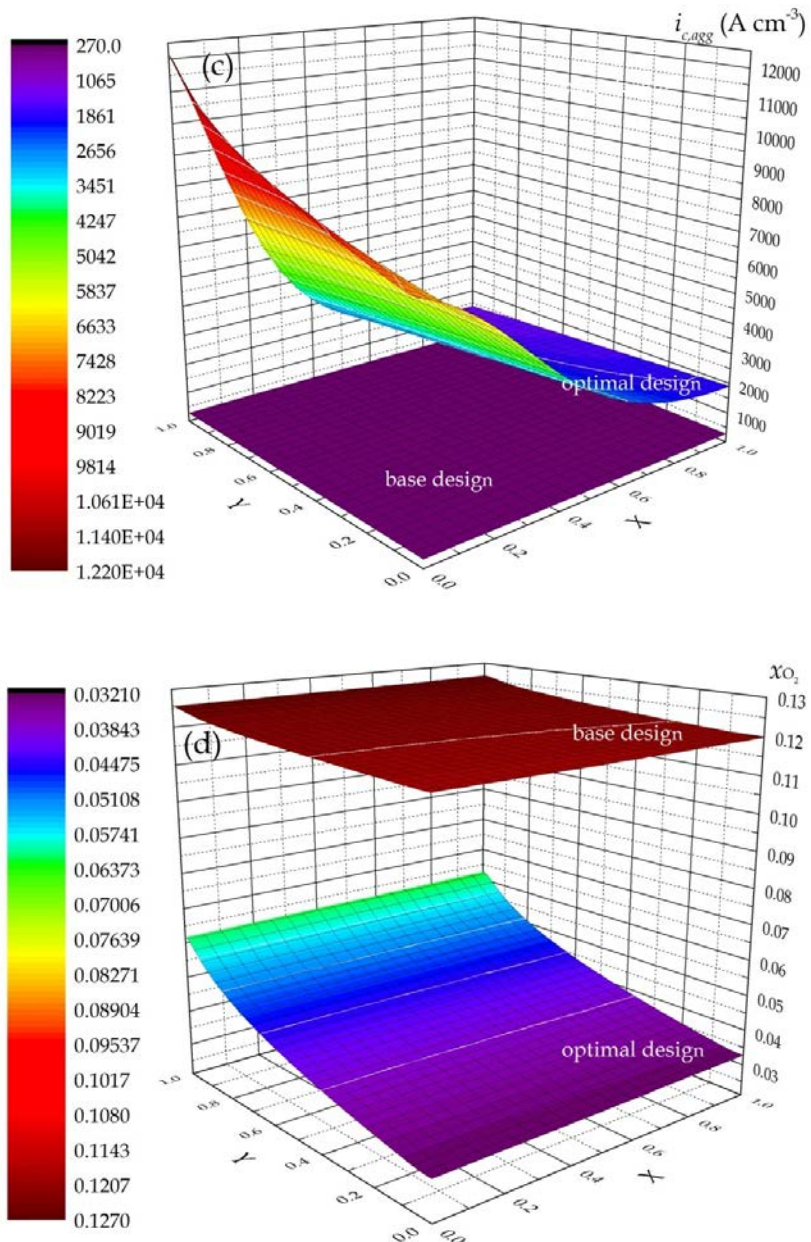
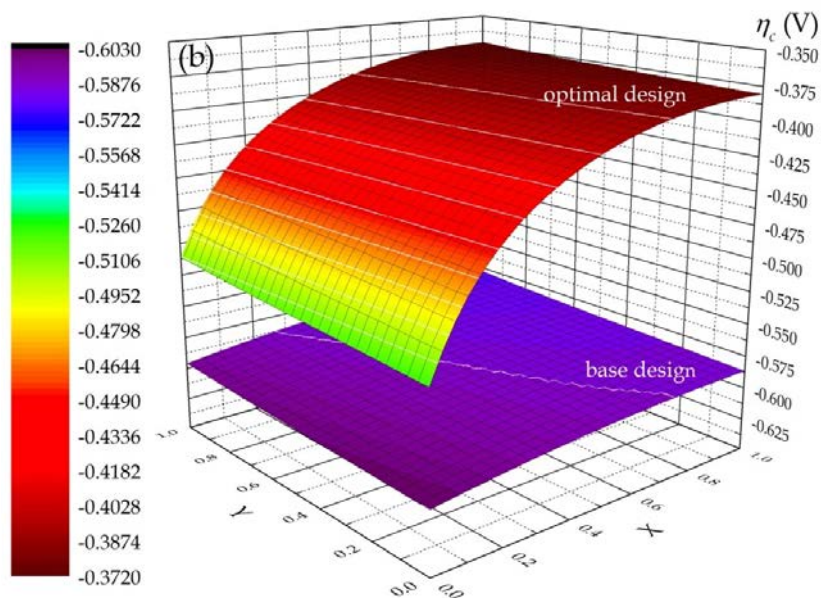
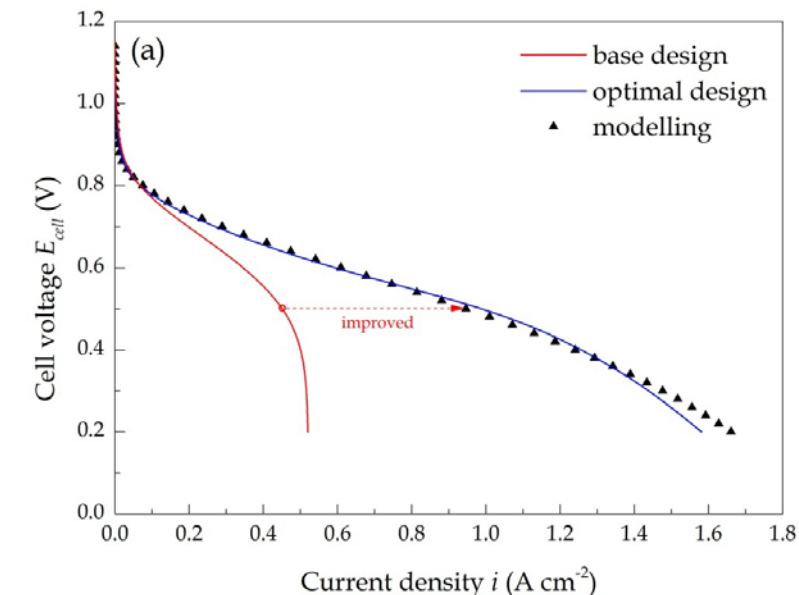


Figure 8-3 Polarisation curve (a), cathode overpotential (b), cathode volumetric current density (c) and oxygen mole fraction (d) for base design and optimal design at the cell voltage of 0.2 V

### 8.7.3 Optimisation at medium cell voltage

Figure 8-4 shows the polarisation curve, cathode overpotential, cathode volumetric current density and oxygen mole fraction for the base design and the optimal design at 0.5 V. The simulation results based on the agglomerate model agree well with the optimisation result, an approximate 4.5% maximum error is observed at the cell voltage of 0.2 V. Apparently, as shown in Figure 8-4(a), the current density increases from 0.46 to 1.02  $\text{A cm}^{-2}$  for the optimal design  $\{m_{Pt}, f, L_M, l_{CL}, r_{agg}\} = \{1.0, 31.5\%, 11.5\%, 30.0,$

0.1}. At this condition,  $\varepsilon_s$ ,  $L_M$  and  $\varepsilon_{CL}$  are 44.8%, 11.5% and 43.7%, respectively. Simultaneously, the optimal design decreases  $\delta_M$  to  $2.89 \times 10^{-9}$  m and  $a_{agg}$  to  $3.92 \times 10^7$  m<sup>-1</sup>. Note that, by optimising, these two parameters are both greater than that obtained of 0.2 V. As stated previously, at a lower cell voltage (0.2 V), the overall rate control process of the ORR is the oxygen transport rate through the ionomer film. When the cell voltage increases, the electrochemical kinetics play more important role in determining the overall rate. Consequently, both an increase in volume fraction of solid and void space gives a higher current density at medium cell voltages. By optimising, the volume fractions of solid and void space are approximate 45.0%, which results in the best performance of the cell.



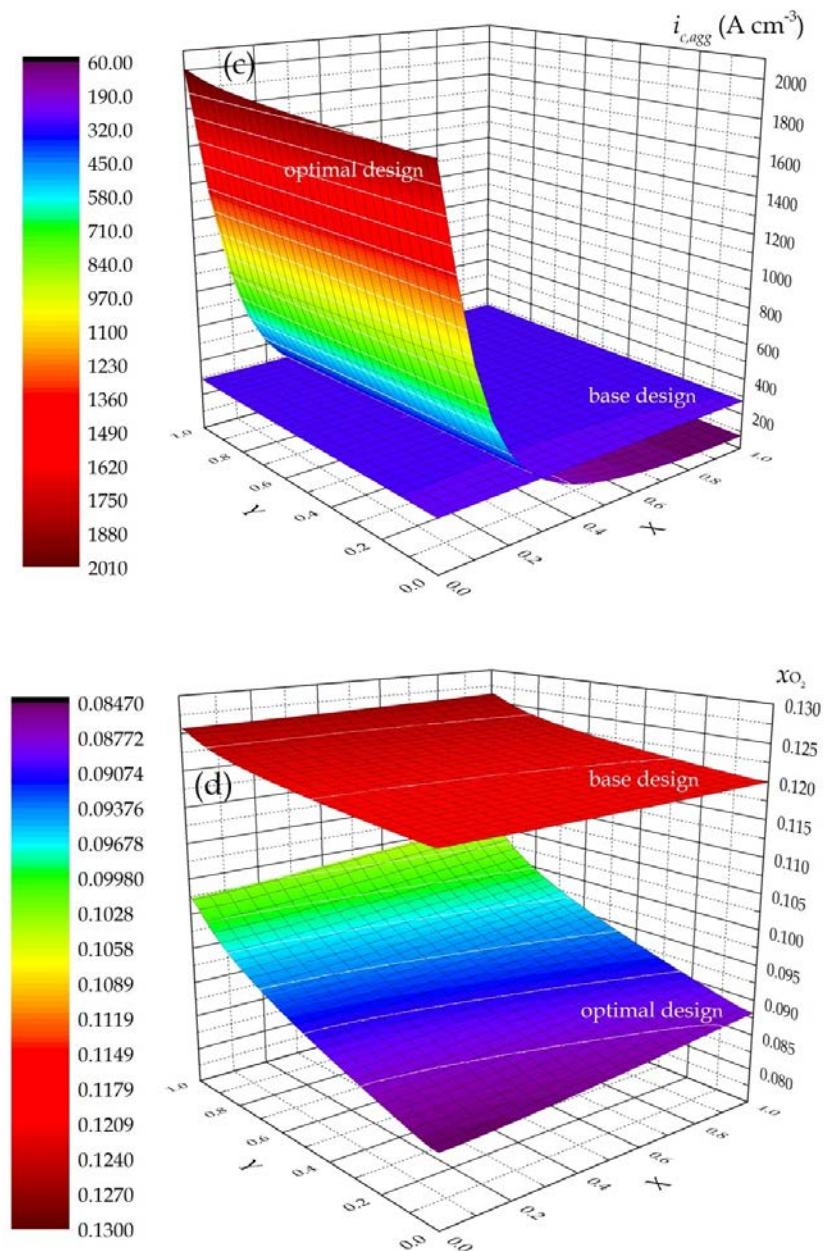


Figure 8-4 Polarisation curve (a), cathode overpotential (b), cathode volumetric current density (c) and oxygen mole fraction (d) for base design and optimal design at the cell voltage of 0.5 V

The cathode overpotential for the base design and optimal design are shown in Figure 8-4(b). After optimising, the absolute value of average cathode overpotential decreases from 0.59 to 0.41 V, which leads to an improved cell performance according to Eq. (4-21). The cathode volumetric current density is shown in Figure 8-4(c). Although the average volumetric current density increases from 280.91 to 312.97  $\text{A cm}^{-3}$  by optimisation, the volumetric current density near the CL-GDL decreases. The complicated distribution of volumetric current density can be explained by the combination of the ORR kinetics (the first term in Eq. (3-13)) and oxygen transport resistance (the second term in Eq. (3-13)). Near the CL-membrane, although the optimal

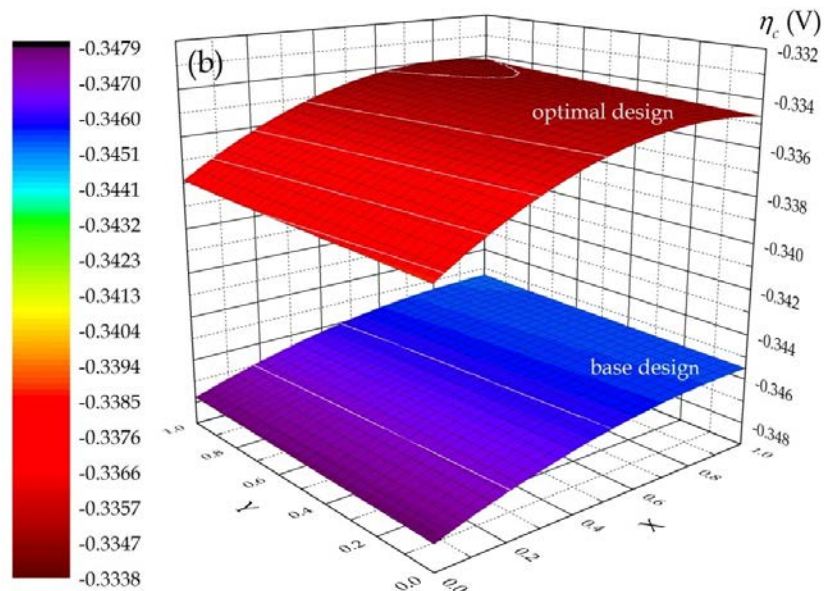
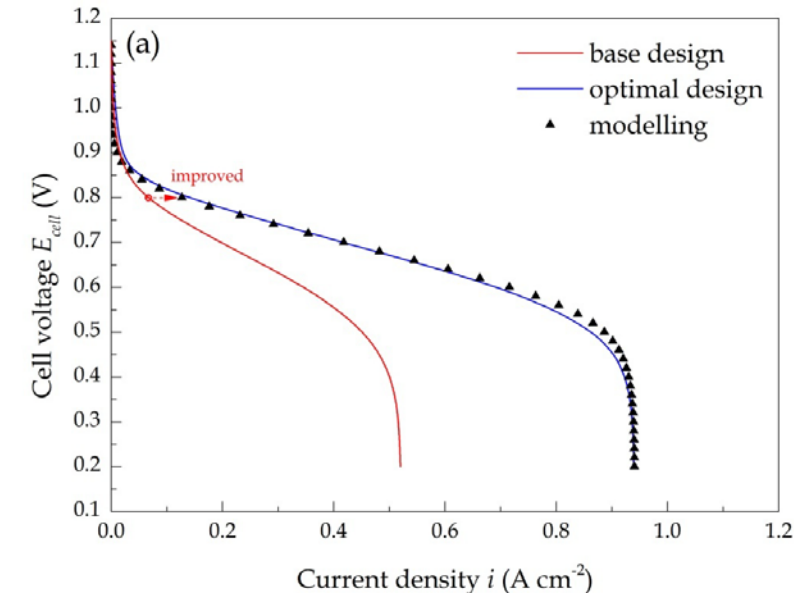
design causes a decrease in the rate coefficient of ORR by reducing the overpotential according to Eq. (3-13), the volumetric current density increases due to the decrease in ionomer film thickness according to Eq. (3-31). However, the decrease in ionomer film thickness cannot compensate the decrease in rate coefficient of the ORR near the CL-GDL, resulting in a decrease in volumetric current density. It can be concluded that, at medium cell voltages the overall rate is controlled by both the ORR kinetics and oxygen transport. The decrease in oxygen mole fraction and the increase in its gradient are observed in Figure 8-4(d). The increase in the gradient of oxygen mole fraction and overpotential increase the cathode current density by enhancing the mass and charge transport [27].

#### 8.7.4 Optimisation at high cell voltage

Figure 8-5 shows the polarization curve, cathode overpotential, cathode volumetric current density and oxygen mole fraction for the base design and the optimal design at 0.8 V. The simulation results based on the agglomerate model agree well with the optimisation result where a maximum error of approximate 1.0% is observed at higher cell voltages. It is clear in Figure 8-5(a) that the current density increases from 0.05 to 0.13 A cm<sup>-2</sup> at the cell voltage of 0.8 V with the optimal design { $m_{pt}, f, L_M, l_{CL}, r_{agg}$ } = {1.0, 35.6%, 50.0%, 30.0, 0.1}. In this situation,  $\varepsilon_s$ ,  $L_M$  and  $\varepsilon_{CL}$  are 38.0%, 50.0% and 12.0%, respectively. Unlike the situation at 0.2 and 0.5 V, the optimal design increases  $\delta_M$  to  $3.08 \times 10^{-8}$  m and  $a_{agg}$  to  $6.53 \times 10^7$  m<sup>-1</sup>.

It is expected that fuel cell performance is limited by ORR kinetics rather than oxygen transport at higher cell voltages [3, 19, 26]. In this case, the main target of the optimisation is to increase the electrochemical kinetics and this is achieved by the increase in the specific area and decrease in porosity. Note that the optimal volume fraction of the electrolyte reaches to the upper bound, 50.0%, indicating that the proton migration rate is also important in determining the overall rate at higher cell voltages. It is clear in Figure 8-5(b) that the absolute value of average cathode overpotential decreases from 0.346 V to 0.335 V at the cell voltage of 0.8 V. Compared to that of low and medium cell voltages, the change in overpotential is smaller due to the slower kinetics at high cell voltages. As shown in Figure 8-5(c), the average volumetric current density only increases from 40.11 to 42.30 A cm<sup>-3</sup> after optimisation. However, the gradient in oxygen mole fraction shown in Figure 8-5(d) increases more significant

than that of 0.2 V and 0.5 V. This is due to the decrease in catalyst layer porosity. At high cell voltages, the electrochemical kinetics is the main limitation to the overall reaction rate while the influence of oxygen diffusion rate within the pores of the porous electrode reduced.



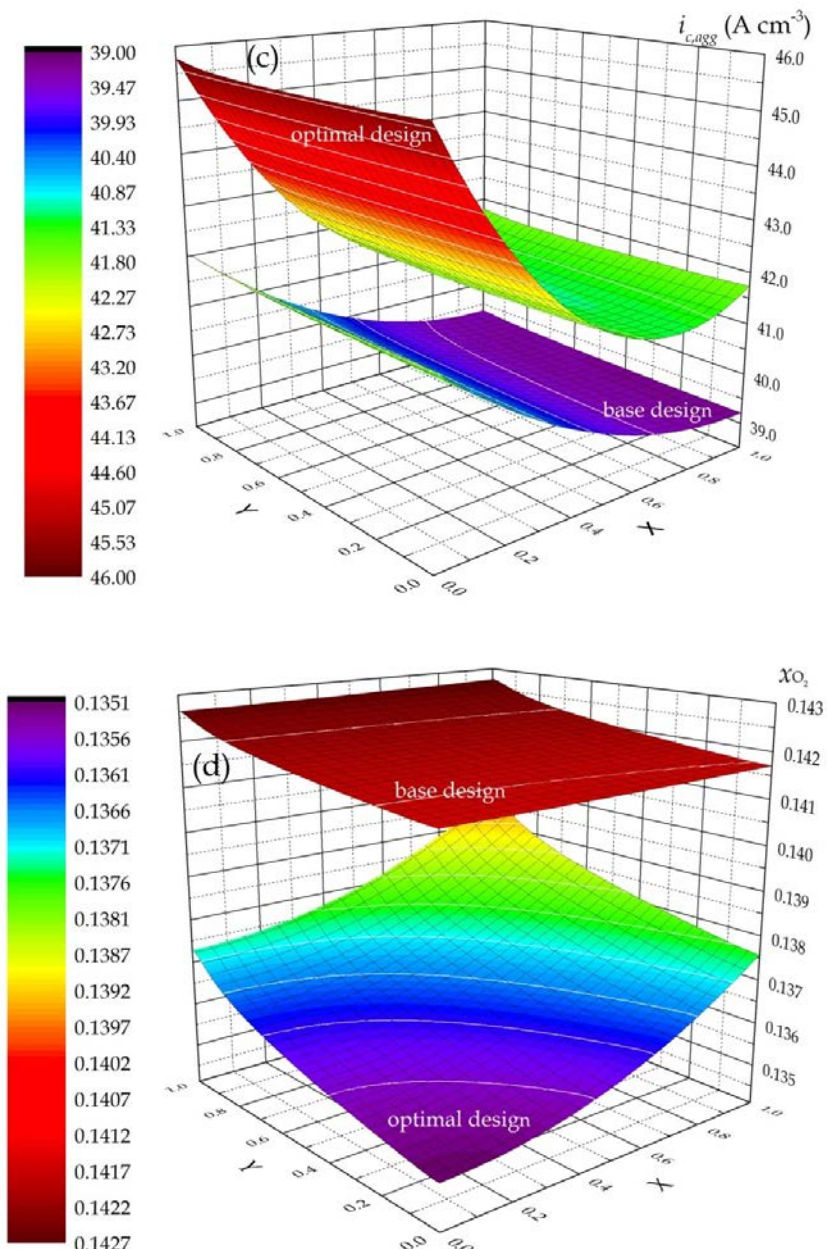


Figure 8-5 Polarisation curve (a), cathode overpotential (b), cathode volumetric current density (c) and oxygen mole fraction (d) for base design and optimal design at the cell voltage of 0.8 V

In addition, the proton conductivity of the catalyst layer is another important issue in deterring the overall reaction rate. At the cell voltage of 0.8 V, the optimal design leads to an increase in effective proton conductivity of catalyst layer (from 1.84 to  $3.96 \text{ S m}^{-1}$ ). However, the optimal designs at 0.2 and 0.5 V result in decreases (from 1.86 to 0.23 at 0.2 V and from 1.86 to 0.44 at 0.5V) in effective proton conductivity of the catalyst layer. It can be concluded that, at high cell voltages, ORR kinetics and proton conductivity of the catalyst layer both control the overall reaction rate. Consequently, the cell performance can be improved by increasing the volume fraction of solid phase

when keeping ionomer volume fraction at a sufficient level. The parameters for base design and optimal designs for different cell voltages are summarised in [Table 8-4](#).

[Table 8-4](#) Parameters for base design and optimal designs at different cell voltages

Parameters	Base design	Optimal design at different cell voltages		
		0.2 V	0.5 V	0.8 V
$\varepsilon_S$	63.5%	40.1%	44.8%	38.0%
$L_M$	20.0%	7.0%	11.5%	50.0%
$\varepsilon_{CL}$	16.5%	52.9%	43.7%	12.0%
$\delta_M$ (m)	$1.55 \times 10^{-8}$	$3.16 \times 10^{-10}$	$2.89 \times 10^{-9}$	$3.08 \times 10^{-8}$
$a_{agg}$ ( $m^{-1}$ )	$4.22 \times 10^7$	$3.41 \times 10^7$	$3.92 \times 10^7$	$6.53 \times 10^7$
$\sigma_{CL}$ ( $S m^{-1}$ )	1.84	0.23	0.44	3.96

## 8.8 Optimisation during a specific cell voltage range

The power density curves for the base design and optimal design at three cell voltages are shown in [Figure 8-6\(a\)](#). It is apparent that the optimal cell voltages are observed to the highest power density at different conditions, i.e. the optimal cell voltages are 0.54 V for base design, 0.36 V for optimal design for 0.2 V. As mentioned in [Section 8.4](#), fuel cell is often operated during a range of cell voltage close to the optimal value. Consequently, the optimisation problem in [Strategy B \(Eq. 8-21\)](#) is solved in this section for two ranges of cell voltage range: 0.3-0.6V, 0.5-0.7V. In addition, the range of 0.6-0.9 V is added to compare. For each of these cases, the parameters in [Table 8-3](#) are applied as the base design during the design optimisation process.

[Figure 8-6\(b\)-\(d\)](#) show the polarisation curves for the base case and optimal design during the cell voltage range of 0.3-0.6 V, 0.5-0.7 V and 0.6-0.9 V, respectively. The shaded areas refer to the improved output of the cell upon optimisation. It is clear that each optimal design corresponding to the specific range of cell voltage improves the cell performance. The optimal design are  $\{m_{P_t}, f, L_M, l_{CL}, r_{agg}\} = \{1.0, 34.35\%, 8.44\%, 28.92, 0.1\}$  for 0.3-0.6 V,  $\{0.959, 34.27\%, 49.46\%, 30.0, 0.1\}$  for 0.5-0.7 V and  $\{0.957, 34.59\%, 50.0\%, 30.0, 0.1\}$  for 0.6-0.9 V, respectively.

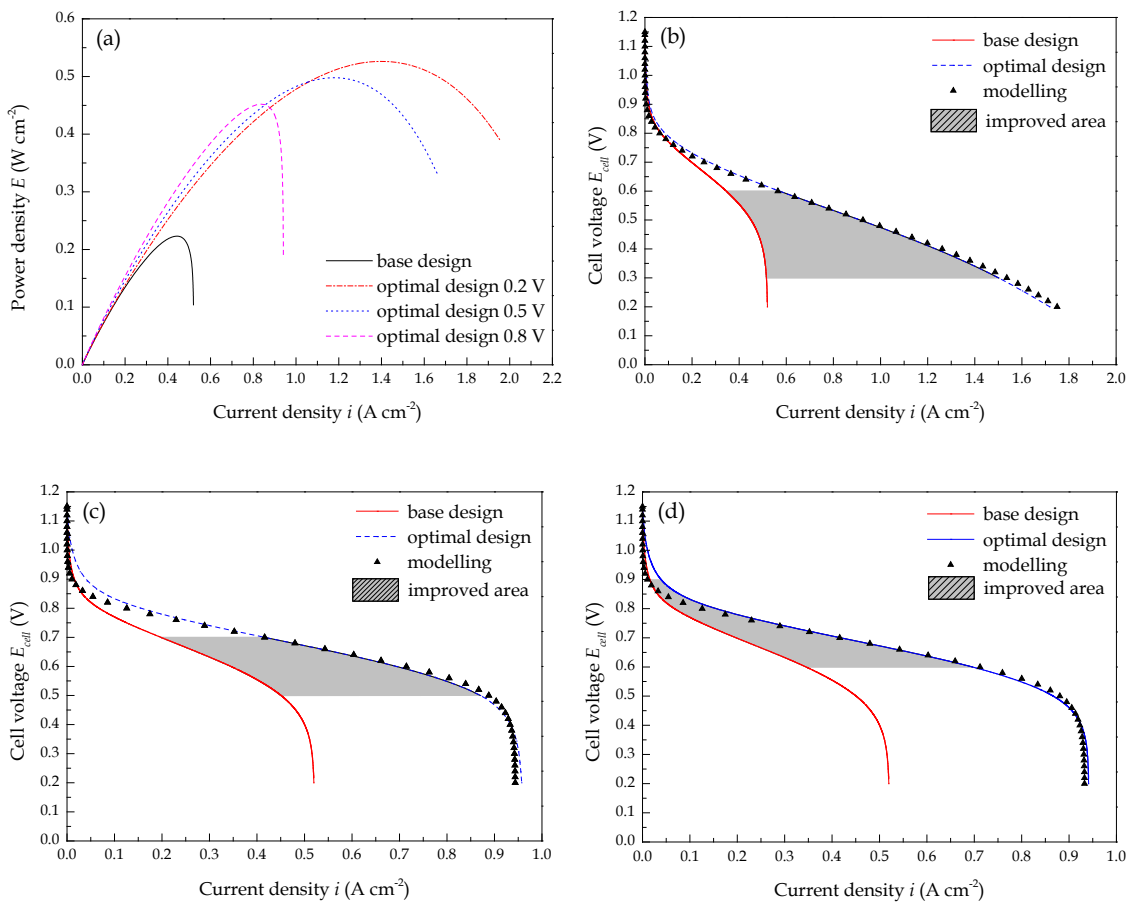


Figure 8-6 Power density curves (a) and polarisation curves during the cell voltage range of 0.3-0.6 V (b), 0.5-0.7 V (c) and 0.6-0.9 V (d) for the base design and optimal design

For these values, as shown in Table 8-5,  $\varepsilon_s$ ,  $L_M$  and  $\varepsilon_{CL}$  are 41.3%, 8.5% and 50.2% for 0.3-0.6 V, 38.5%, 49.5% and 12.0% for 0.5-0.7 V and 38.0%, 50.0% and 12.0% for 0.6-0.9 V, respectively. In addition, the optimal designs change  $\delta_M$  and  $a_{agg}$  to  $1.13 \times 10^{-9}$  m and  $3.63 \times 10^7$  m $^{-1}$  for 0.3-0.6 V,  $3.02 \times 10^{-8}$  m and  $6.41 \times 10^7$  m $^{-1}$  for 0.5-0.7 V and  $3.08 \times 10^{-8}$  m and  $6.44 \times 10^7$  m $^{-1}$  for 0.6-0.9V, respectively. The obtained mean current densities during the selected cell voltages and the relative errors between the optimisation results and the simulation results are  $1.06$  A cm $^{-2}$  and 1.16% for 0.3-0.6V,  $0.68$  A cm $^{-2}$  and 0.28% for 0.5-0.7 V, and  $0.32$  A cm $^{-2}$  and 0.51% for 0.6-0.9V, respectively.

It is obvious in Table 8-6 that the obtained parameters are very close for optimal designs for 0.5-0.7 V and 0.6-0.9V. It is also observed that the improvement in fuel cell output requires higher platinum loading and lower ionomer volume fraction during lower voltage range and it requires lower platinum loading and higher ionomer volume fraction during higher voltage range. The improvement in cell performance during

lower voltage range can be mainly explained by two reasons: the decrease in oxygen diffusion resistance through the ionomer film surrounding the agglomerate and the increase in the porosity of the catalyst layer. And the improvement in cell performance during higher voltage range can be explained by the increased specific area and proton conductivity.

Table 8-5 Parameters for base design and optimal designs for different cell voltage ranges

Parameters	Base design	Optimal design at different cell voltage ranges		
		0.3 – 0.6 V	0.5 – 0.7 V	0.6 – 0.9 V
$\varepsilon_s$	63.5%	41.3%	38.5%	38.0%
$L_M$	20.0%	8.5%	49.5%	50.0%
$\varepsilon_{CL}$	16.5%	50.2%	12.0%	12.0%
$\delta_M$ (m)	$1.55 \times 10^{-8}$	$1.13 \times 10^{-9}$	$3.02 \times 10^{-8}$	$3.08 \times 10^{-8}$
$a_{agg}$ (m <sup>-1</sup> )	$4.22 \times 10^7$	$3.63 \times 10^7$	$6.41 \times 10^7$	$6.44 \times 10^7$
$i_{mean}$ (A cm <sup>-2</sup> )	0.29	1.06	0.68	0.32

Table 8-6 Key parameters to optimal design at different cell voltages

Cell voltages	Optimal volume fraction of the component in catalyst layer					Other parameters		
	$E^{cell}$ (V)	$L_{Pt/C}$	$L_M$	$\frac{\varepsilon_{CL}}{\varepsilon_p \quad \varepsilon_s}$	$L_s$	$\delta_M$ (nm)	$a_{agg}$ (m <sup>-1</sup> )	$N_{agg}$ (m <sup>-3</sup> )
0.2	37.10%	7.00%	35.42%	17.48%	3.00%	0.316	$3.407 \times 10^7$	$1.880 \times 10^{20}$
0.5	41.82%	11.50%	27.57%	16.11%	3.00%	2.894	$3.924 \times 10^7$	$1.773 \times 10^{20}$
0.8	35.00%	50.00%	4.06%	7.95%	3.00%	30.828	$6.525 \times 10^7$	$9.494 \times 10^{19}$
0.3 - 0.6	38.33%	8.40%	32.88%	17.35%	3.00%	1.129	$3.628 \times 10^7$	$1.839 \times 10^{20}$
0.5 - 0.7	35.55%	49.50%	4.12%	7.87%	3.00%	30.186	$6.408 \times 10^7$	$9.644 \times 10^{19}$
0.6 - 0.9	35.00%	50.00%	4.06%	7.94%	3.00%	30.826	$6.436 \times 10^7$	$9.495 \times 10^{19}$

It is also clear in Table 8-6 that the optimal volume fraction of the secondary pores at lower cell voltages is approximate 20% and the optimal ionomer volume fraction is approximate 50% when cell voltage is higher than 0.5 V, which agree with the previous work by Bernardi *et al.* [3] and Sun *et al.* [26].

## 8.9 Global sensitivity analysis

The good agreement of the result of predicted optimal design and the validation result indicates that the approximate model obtained with the Kriging surrogate model is sufficiently accurate. Therefore, it can be used for the GSAs of these design variables. In this work, the Sobol' indices are computed based on the surrogate models to obviate the problem of expensive computation. A total of 50,000 Monte Carlo (MC) simulations are conducted for one indices calculation. [Figure 8-7](#) shows the individual and total sensitivity indices for each design variable at different cell voltages.

As shown in [Figure 8-7](#), the significance of variables is determined by ranking the total sensitivity indices over the 50,000 MC simulations, as the total sensitivity indices takes into account not only the contribution of the individual effect of a design variable but also the contribution of interactions between variables. Assuming the minimum error to be 2.0%, then it can be concluded that the catalyst layer thickness has no measurable effect on the fuel cell performance at most voltage condition except at 0.8V. It is also found that three variables, i.e., platinum loading, platinum mass ratio, and ionomer volume fraction, play very significant roles on the performance at low and medium voltage, but the effect of ionomer volume fraction decreases sharply at high voltage. Ionomer volume fraction plays most important role at the lower cell voltages due to its significant effect on the ionomer film thickness and then the oxygen diffusion resistance. At higher cell voltages, the importance of platinum loading and platinum mass ratio increase as ORR kinetics becomes to the rate control process. The importance of ionomer volume fraction decreases at higher cell voltages, but it is still important due to its strong effect on the proton conductivity. Platinum loading has an important effect at every cell voltage because it greatly affects the volume fraction solid phase and specific area of agglomerates according to [Eq. \(3-39\)](#) and [Eq. \(3-68\)](#).

Note that the rankings of individual and total sensitivities are same at low and medium cell voltages, but different at high cell voltages. In specific, catalyst layer thickness is negligible at low and medium cell voltages, but no variable can be neglect at high cell voltages. The GSAs of the 5 variables can be used to reduce the size of the problem in subsequent research, neglecting the design variables with unimportant impact. For instance, just use the top 4 relatively important variables in subsequent work and freeze the relatively unimportant variable (catalyst layer thickness) at their nominal values.

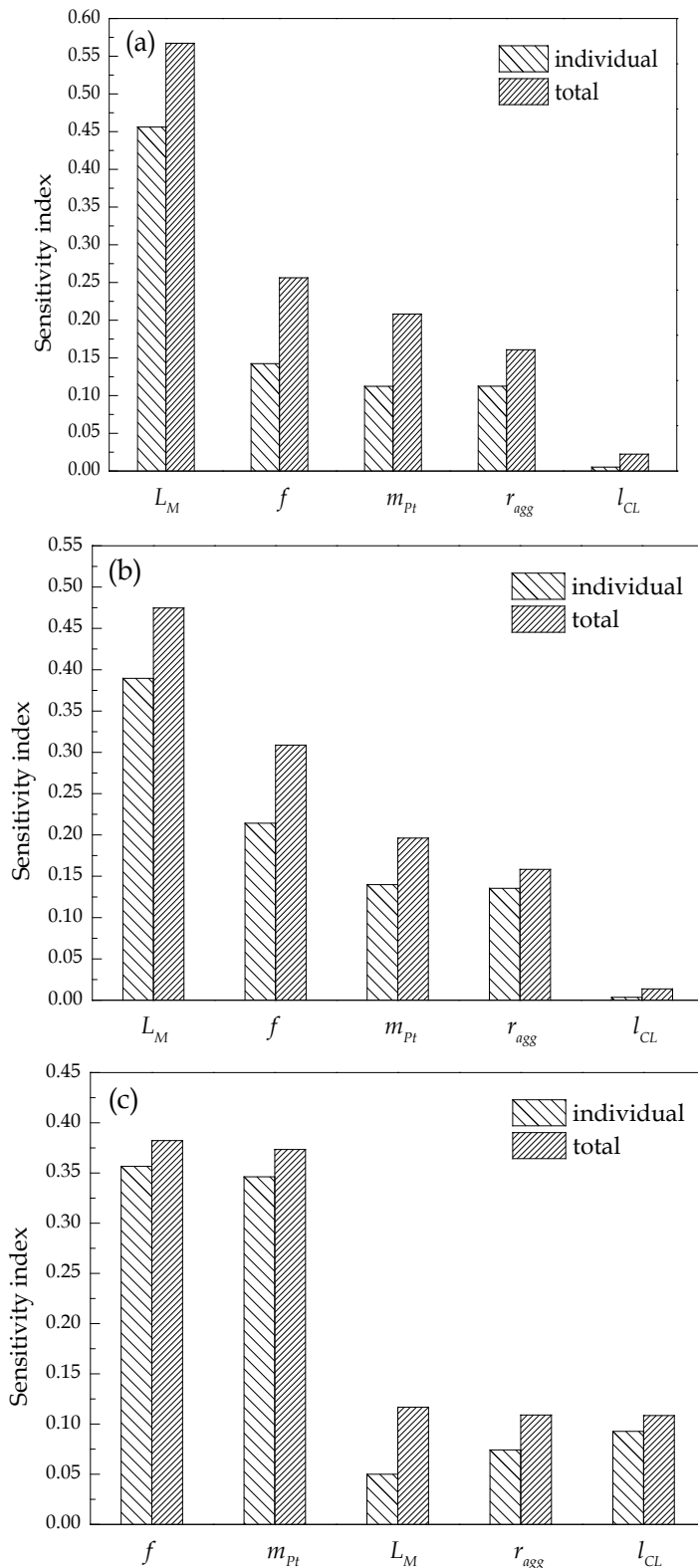


Figure 8-7 Sensitivity indices of the five variables at 0.2V (a), 0.5V (b) and 0.8V (c)

## 8.10 Final remarks

At three fixed voltages, the optimal value of platinum loading is its upper bound, 1.0 mg cm<sup>-2</sup>, and the agglomerate radius is its lower bound, 0.1 μm. This is because,

according to Eq. (3-39), the approximate ten times bigger in density of platinum than that of carbon results in a more significant effect on volume fraction of  $Pt/C$  when changing platinum loading. Moreover, the specific area of agglomerate is proportional to platinum loading according to Eq. (3-68). Consequently, as stated in the work of Secanell *et al.* [8], the maximum platinum loading is required to ensure the maximum value of specific area of agglomerate at every cell voltage. Due to the relationship between agglomerate radius and ionomer film thickness according to Eq. (3-60), the minimum agglomerate radius should be adopted in order to maintain the lowest mass transport resistance of oxygen diffusion through the electrolyte coating. In addition, the number of agglomerate per unit (agglomerate density) increases by applying smaller agglomerate radius according to Eq. (3-50).

As discussed in Section 8.8, the thickness of catalyst layer has least important effect on the cell performance. According to Eq. (3-42), the increase in porosity is result from the thicker catalyst layer. Consequently, the optimal catalyst layer thickness is almost at the upper bound value, 30  $\mu m$  except for the cell voltage of 0.2 V. This is because the increase in porosity is resulted from the increase in platinum mass ratio at 0.2 V. It is clear in Figure 7-7 that the effect of platinum mass ratio is more obvious than catalyst layer thickness. According to Eq. (3-66), the increase in platinum mass ratio leads to the decrease in reaction surface area per unit platinum mass, then the decrease in specific area of agglomerate. Moreover, the optimal platinum loading obtained at its upper bound is because of the omission of the effectiveness factor and the cost of platinum in the current optimisation target.

## 8.11 Conclusions

A design method to obtain the optimal parameters for PEMFC cathodes containing a two-dimensional, steady-state and an isothermal model, finite element method (FEM) analysis and surrogate model based optimisation has been presented. An improved cathode numerical approach, considering the volume fraction of all components, is conducted to simulate and investigate the effect of cathode platinum loading, platinum mass ratio, ionomer volume fraction, catalyst layer thickness and agglomerate radius on the polarisation curves of PEMFC. Reactant flow in flow channels, species transport in porous media and water transport through the membrane are included in the numerical model. A surrogate model-based optimisation method is adopted to build the approximate model of the cell response with respect to 5 design variables and to predict

the optimal design based on two optimisation strategies. The first strategy maximises the current densities at fixed cell voltages commonly used in previous work, and the second strategy is modified from the first strategy to maximise the current densities within a specific range of cell voltages. The final surrogate model-based GSAs provide an insight into the effect of each design variable on the PEMFC performance, and help reduce the design dimensions in the subsequent work. It is found that, porosity is important to the performance of PEMFCs operated at lower cell voltages, ionomer volume fraction is important to the performance of fuel cells operated at higher cell voltages and platinum loading is important at a full range of cell voltage.

## 8.12 References

1. Kamarajugadda, S. and S. Mazumder, *Numerical investigation of the effect of cathode catalyst layer structure and compositon on polymer electrolyte membrane fuel cell performance*. Journal of Power Sources, 2008. **183**: p. 629-642.
2. O'Hayre, R, D.M. Barnett and F.B. Prinz, *The triple phase boundary - A mathematical model and experimental investigations for fuel cells*. Journal of Electrochemistry Society, 2005. **152**: p. A439-A444.
3. Bernardi, D.M. and M.W. Verbrugge, *A mathematical model of the solid-polymer-electrolyte fuel cell*. Journal of Electrochemistry Society, 1992. **139**: p. 2477-2491.
4. Xie, Z., T. Navessin, K. Shi, R. Chow, Q. Wang, D. Song, B. Andreaus, M. Eikerling, Z. Liu and S. Holdcroft, *Functionally graded cathode catalyst layers for polymer electrolyte fuel cells*. Journal of Electrochemistry Society, 2005. **152**: p. A1171-A1179.
5. Wu, X. and K. Scott, *The effects of ionomer content on PEM water electrolyser membrane assembly performance*. International Journal of Hydrogen Energy, 2010. **35**: p.12029-12037.
6. Suzuki, A, U. Sen, T. Hattori, R. Miura, R. Nagum, H. Tsuboi, N. Hatakeyama, A. Endou, H. Takaba, M.C. Willams and A. Miyamoto. *Electrolyte content in the catalyst layer of polymer electrolyte electrolyte fuel cell (PEMFC): Effect on diffusion and performance*. International Journal of Hydrogen Energy, 2011. **36**: p. 2221-2229.
7. Hwang, D.S., C.S. Park, S.C. Yi, Y.M. Lee, *Optimal catalyst layer structure of polymer electrolyte membrane fuel cell*. International Journal of Hydrogen Energy,

2011. **36**: p. 9876-9885.
8. Secanell, M., R. Songprakorp, N. Djilali and A. Suleman, *Optimisation of a proton exchange membrane fuel cell membrane electrode assembly*. Structural Multidisciplinary Optimization, 2010. **40**: p. 563-583.
  9. Wu, J., Q. Liu and H. Fang, *Toward the optimisation of operating conditions for hydrogen polymer electrolyte fuel cells*. Journal of Power Sources, 2006. **156**: p. 388-399.
  10. Tirnovan, R., S. Giurgea, A. Miraoui and M. Cirrincione, *Surrogate model for proton exchange membrane fuel cell (PEMFC)*. Journal of Power Sources, 2008. **175**: p. 773-778.
  11. Tirnovan, R., S. Giurgea, A. Miraoui and M. Cirrincione, *Proton exchange membrane fuel cell modelling based on a mixed moving least squares technique*. International Journal of Hydrogen Energy, 2008. **33**: p. 6232-6238.
  12. Zervas, P.L., A. Tatsis, H. Sarimveis and N.C.G. Markatos, *Development of a novel computational tool for optimizing the operation of fuel cells systems: Application for phosphoric acid fuel cells*. Journal of Power Sources, 2008. **185**: p. 345-355.
  13. Wahdame, B., D. Candusso, X. François, F. Harel, J.M. Kauffmann and G. Coquery, *Design of experiment techniques for fuel cell characterisation and development*. International Journal of Hydrogen Energy, 2009. **34**: p. 967-980.
  14. Miao, J.M., S.J. Cheng and S.J. Wu, *Metamodel based design optimisation approach in promoting the performance of proton exchange membrane fuel cells*. International Journal of Hydrogen Energy, 2011. **36**: p. 15283-15294.
  15. Shokuhi-Rad A., A. Jamali, M. Naghashzadegan, N. Nariman-zadeh and A. Hajiloo, *Optimum Pareto design of non-linear predictive control with multi-design variables for PEM fuel cell*. International Journal of Hydrogen Energy, 2012. **37**: p. 11244-11254.
  16. Peksen, M., L. Blum and D. Stolten, *Optimisation of a solid oxide fuel cell reformer using surrogate modelling, design of experiments and computational fluid dynamics*. International Journal of Hydrogen Energy, 2012. **37**: p. 12540-12547.
  17. Cheng, S.J., J.M. Miao and S.J. Wu, *Use of metamodeling optimal approach*

- 
- promotes the performance of proton exchange membrane fuel cell (PEMFC).* Applied Energy, 2013. **105**: p. 161-169.
18. Riascos, L.A. and D.D. Pereira, *Limit Operating Temperature in Polymer Electrolyte Membrane Fuel Cells*. Journal of Electrochemistry Society, 2009. **156**: p. B1051-B1058.
  19. Marr, C. and X. Li, *Composition and performance modelling of catalyst layer in a proton exchange membrane fuel cell*. Journal of Power Sources, 1999. **77**: p. 17-27.
  20. Nam, J.H. and M. Kaviany, *Effective diffusivity and water-saturation distribution in single- and two-layer PEMFC diffusion medium*. International Journal of Heat and Mass Transfer, 2003. **46**: p. 4595-4611.
  21. Matheron, G., *Principles of geostatistics*. Economic Geology, 1963. **58**: p. 1246-1266.
  22. Sacks, J., W.J. Welch, T.J. Mitchell and H.P. Wynn, *Design and analysis of computer experiments*. Statistical Science, 1989. **4**: p. 409-423.
  23. Sobol's, I.M., *Global sensitivity indices for nonlinear mathematical models and their Monte Carlo estimates*. Mathematics and Computers in Simulation, 2001. **55**: p.271-280.
  24. Sobol's I.M. and S.S. Kucherenko, *On global sensitivity analysis of quasi-Monte Carlo algorithms*. Monte Carlo Methods and Applications, 2005. **1**: p. 1-9.
  25. Jin, R., W. Chen and A. Sudjianto, *On sequential sampling for global metamodeling in engineering design*. Proceedings of DETC, 2002. **2**: p. 539-548.
  26. Sun, W., B.A. Peppley and K. Karan, *An improved two-dimensional agglomerate cathode model to study the influence of catalyst layer structural paramets*. Electrochimica Acta, 2005. **50**: p. 3359-3374.
  27. Sun, Y.P., L. Xing and K. Scott, *Analysis of the kinetics of methanol oxidation in a porous Pt-Ru anode*. Journal of Power Sources, 2010. **195**: p. 1-10.

## Chapter 9. Summary, Conclusions and Perspective

### *Summary and conclusions*

The rapid development of the current economy requires an increasing consumption of energy, which will eventually result in the depletion of limited fossil energy resources, e.g. coal and oil, and the environmental problems. As one of the most important renewable energy, hydrogen is suggested as the ideal energy carrier for the future because it is abundant, clean and can be easily produced by other energy sources. Proton exchange membrane fuel cells (PEMFCs), using hydrogen or methanol as the fuel, is proved to be an efficient and reliable electrochemical device that converts chemical energy directly into electricity. Nafion® membrane is usually used as the electrolyte in PEMFCs, which is strongly dependent on water to conduct protons. As a consequence of this fact water management, including the dissolved water transport through the membrane and ionomer and liquid water transport in the porous electrode, is of vital importance to a successful fuel cell operation.

Due to the limitation of the experimental measurement, computational modelling plays an important role in studying the water formation, phase transfer and transport in PEMFCs. The mathematical models developed in this book are typically mechanistic, i.e. all physical and chemical phenomena in the fuel cell are described by algebraic and differential equations based on the properties of the species and processes. COMSOL Multiphysics®, a commercial computational fluid dynamics (CFD) software, is used to solve these equations based on the finite element method (FEM). Three outstanding features are presented namely (1). an agglomerate catalyst layer. The catalyst layer is constructed by spherical agglomerates, which consists of platinum dispersed carbon ( $Pt/C$ ), ionomer and void space. The primary pores are the void space inside the agglomerates and the secondary pores are the void space between the agglomerates. The ionomer firstly fills part of the primary pores of the agglomerate then the remainder covers the agglomerate to form a thin film surrounding the agglomerates. Liquid water occupies the secondary pores to form a liquid water film on the outer boundary of the ionomer film. The properties of the catalyst layer, e.g. porosity, agglomerate density, specific area, ionomer and liquid water film thicknesses, can be algebraically calculated. (2). a combinational water phase transfer and transport mechanism. Water phase

transfer between water vapour, dissolved water and liquid water is considered in the model. The dissolved water transport through the membrane and ionomer under the driving forces of electro-osmotic drag (EOD), back diffusion and hydraulic permeation are accounted for. (3). the majority of the parameters used are treated as functions of temperature, pressure and/or water content. As a result of these features the model is capable of performing several tests at a variety of operating conditions and analysing the parameters which are hard to be obtained by experiment.

A two-dimensional, along-the-channel, steady-state, single-phase flow and isothermal model based on an agglomerate catalyst layer structure is developed. The properties of the catalyst layer, such as porosity, agglomerate density, specific area and ionomer film thickness, are quantitatively represented. The increase in oxygen mass transport resistance through the ionomer film surrounding the agglomerate is proved to be critical for the rapid decrease in the predicted current density at lower cell voltages. Higher platinum loading and carbon loading improve the cell performance at higher cell voltages. However, the effectiveness factor is decreased, leading to a poor utilisation of the platinum particles near the membrane. Too much platinum and carbon loadings rather than improve the cell performance at higher current densities can waste expensive catalyst.

A two-dimensional, across-the-channel, steady-state, two-phase flow and isothermal model based on an agglomerate catalyst layer structure is presented. The water phase transfer between water vapour, dissolved water and liquid water is addressed and the dissolved water transport through the membrane and ionomer according to a combinational mechanism is included. Moreover, the membrane and ionomer swelling associating with the non-uniform water distribution are taken into account. By accounting for the increase in mass transport resistance resulting from membrane and ionomer swelling and considering the void space loss due to liquid water occupation (flooding), the two-phase flow model gives a greater accuracy in validating the experimental data in comparison with the single-phase flow model.

The modelling results show that the non-uniform distribution of the membrane and ionomer water content is a consequence of the electro-osmotic drag (EOD) and water absorption (water uptake) of the membrane and ionomer. In the case of lower current density and higher relative humidity, the membrane and ionomer water absorption is the main mechanism in determining the water content of the membrane and ionomer.

However, the effect of EOD is pronounced with lower relative humidity and higher current density, especially the portion of the catalyst layer close to the membrane.

Combining the simulation results from the along-the-channel model and across-the-channel model, the higher membrane/ionomer water content is predicted near the cathode CL-GDL boundary along the air flow direction on the region under the bipolar current collector. The membrane swelling increases the portion of GDL bulged into flow channel while the ionomer swelling decreases the catalyst layer porosity and increases the ionomer film thickness. For the purpose of the best fuel cell performance, the optimal dry ionomer loading (initial ionomer content) is from 0.2 to 0.3 mg cm<sup>-2</sup> and the optimal cathode relative humidity is around 60%.

A two-dimensional, across-the-channel, steady-state model for a PEMFC is developed in which the non-isothermal model for temperature distribution, the two-phase flow model for liquid water transport and the agglomerate model for oxygen reduction reaction (ORR) are fully coupled. It is observed that cell performance is increased when non-isothermal conditions are used in the simulation. This is due to the increases in some important electrochemical parameters and transport properties, e.g. the exchange current density, transfer coefficient, and species effective diffusivity, and the decrease in liquid water saturation resulting from the temperature increase in the MEA, the cathode catalyst layer in particular.

At a fixed current density, the increase in operating temperature increases the water carrying capacity (WCC) which is of benefit to the membrane and ionomer water content and cell performance. Water molecules migrate through the membrane from anode to cathode associating with the proton transport. Due to this fact, applying higher temperatures on the anode could improve the cell performance at higher current densities. Applying higher temperatures on the cathode increases the ORR kinetics. However, higher inlet temperatures on the cathode decrease the oxygen mole fraction at a fixed relative humidity, which probably leads to an oxygen depletion that then limits the cell performance. Heat accumulates inside the cathode catalyst layer on the region under the channel. Applying higher temperatures on the anode and lower temperatures on the cathode could optimise the temperature distribution in the MEA and avoid hot spots within the cathode catalyst layer and membrane. Enlarging the width ratio of the channel/rib also improve the cell performance. However, the improvement is limited by the sluggish ORR.

A two-dimensional, along-the-channel, two-phase flow, non-isothermal, computational fluid dynamics (CFD) model based on agglomerate catalyst layer structure is developed to study the distributions of liquid water and heat and catalyst layer effectiveness factors within the MEA and channels for a low temperature PEMFC. Liquid water flooding at the anode side is taken into account. The model fully couples seven sub-models: (1) agglomerate models for gas transport resistance in CLs, (2) two-phase flow models for liquid water saturation, (3) combinational diffusion models for dissolved water transport through the membrane, (4) non-isothermal models for heat transport in MEA and channels, (5) computational fluid dynamic (CFD) models for gas transport along the channels, (6) multicomponent diffusion of reactant gases in gas mixture, and (7) ionomer swelling due to non-uniform distribution of water content.

The modelling results reveal that the increase in GDL thickness and channel depth lead to a monotonically decrease in cell performance in a large range of current densities while contact angle and channel length almost had no effect on the cell performance at low current densities. At high current densities, liquid water flooding can be mitigated when electrodes with larger contact angle, lower porosity and low platinum loading are used. In the meanwhile, liquid water saturations can be reduced by shorter and deeper flow channels. The optimal relative humidity depends on the cell current density. At low current densities, low relative humidity is of benefit to the cell performance. At medium and high current densities, the optimal cathode relative humidity increases as the anode relative humidity decreases. The anode relative humidity is vital important to a high performance fuel cell due to the proportional relationship between anode relative humidity and the membrane/ionomer water content at the anode side. Therefore, fully humidified anode gas is required of maintaining the membrane/ionomer hydration. The optimal cathode relative humidity depends on anode relative humidity, channel length and current density. At medium current densities, as the anode relative humidity decreases from 100% to 50%, the optimal cathode relative humidity increases from 80% to 90% for channel length varies from 1.0 cm to 10 cm. On the contrary, at high current densities, the optimal cathode relative humidity increases from 30% to 70% for a 1.0 cm channel and increases from 40% to 70% for a 10 cm channel. Liquid water flooding cannot be avoided at the cathode using fully humidified gas, resulting in high cathode relative humidity an undesirable operating condition in full range of current densities. However, too low cathode relative humidity is hard to maintain the hydrated membrane/ionomer at the cathode side, resulting in a

decrease in cell performance at medium and high current densities. At medium current densities, with fully humidified anode gas, the optimal cathode relative humidity is 80% for different lengths of channel of 1.0 and 10 cm. At high current densities, the optimal cathode relative humidity is 30% and 40% for 1.0 cm and 10 cm channel, respectively.

The increase in stoichiometric flow ratios at both the anode and cathode almost has no effect on the cell performance at low current densities. At medium and high current densities, the initial increase in the cathode stoichiometric flow ratio improves the cell performance, e.g. the limiting current densities at various relative humidity. However, the further increase larger than 2.0 leads to limited contributions. The increase in stoichiometric flow ratio shortens the water flooding region and mitigates the degree of flooding in the channel, resulting in a more significant improvement of limiting current density for longer channel. The effect of anode stoichiometric flow ratio on cell performance can be omitted.

The Peclet number indicates that advection almost has no effect on the liquid water transport in the porous electrode, which is mainly governed by the capillary diffusion mechanism. On the contrary, advection contributes approximate 10% of heat transport inside the gas diffusion layer at limiting current densities. In flow channels, the heat removal ability of cathode gas is reduced as the stoichiometric flow ratio decreases.

The temperature rise is sharp near the cathode inlet and the temperature slowly increases along the air flow to the outlet. The increase in GDL thickness could mitigate the temperature rise within the MEA but it is at an expense of the effectiveness factor of the catalyst layers due to the increased mass transport resistance. The flow channel of 1 cm is found to be the optimal length to the cell performance at high current densities. A new channel design featured with multi- outlets and inlets along-the-channel is capable of mitigating the water flooding and improving the cell performance.

Five key parameters of the cathode catalyst layer, namely platinum loading, platinum mass ratio, ionomer volume fraction, catalyst layer thickness and agglomerate radius, are investigated and optimised by a multiple surrogate model and their sensitivities are analysed by a Monte Carlo method based approach. Maximising the current densities at a fixed cell voltage and during a specific cell voltage range are the two optimisation strategies implemented for the optima prediction. The improvement in cell performance is analysed in terms of ionomer film thickness, specific area, proton conductivity, overpotential, volumetric current density and oxygen mole fraction inside the cathode catalyst layer. It is found that the catalyst layer porosity is important to the cell

performance at higher current densities while the ionomer volume fraction is important to the cell performance at lower current densities and platinum loading is important during a full range of cell voltages.

### ***Perspective***

This book contributes to a better understanding of the physical and electrochemical processes within a PEM fuel cell, especially the water formation, phase change and transport. The developed models are believed to be useful tools to analyse the transport and electrochemical reaction processes involved in the fuel cell operation and predict the cell performance. However, in order to improve the modelling reliability and compatibility, further works have to be done on several aspects.

1. Species crossover, such as, hydrogen, oxygen and nitrogen transport through the membrane have to be considered. Even though the amount of species crossover is small, it has significant effect on the PEMFCs degradation.
2. The steady-state models for water generation, phase change and transport have to be extended to the dynamic models, which is capable of predicting the time-dependent behaviour of water and coupling the degradation processes of the PEMFCs.
3. For the purposes of fully representing and better understanding the physical and electrochemical behaviours in the practical fuel cells, the current two-dimensional models have to be extended to three-dimensional models.
4. Catalyst degradation, carbon corrosion and membrane degradation by chemical process to predict loss of fuel cell performance with time could be performed over a three-dimensional domain.
5. Different three-dimensional flow fields, such as interdigitated, serpentine and pin-type, have to be developed.
6. The mathematical model developed for the low temperature PEMFC should be extended to study the fuel cells with high temperature proton exchange membrane (HTPEM) and alkaline membrane.